Damage and recovery of visual and motor central nervous system pathways investigated with structural and functional magnetic resonance imaging

Ahmed Tahir Toosy

A thesis submitted to the University of London for the degree of

Doctor of Philosophy

2005

NMR Research Unit

Department of Headache, Brain Injury and Rehabilitation

Institute of Neurology

Queen Square

London, WC1N 3BG

United Kingdom

ProQuest LLC
789 East Eisenhower Parkway
P.O. Box 1346
Ann Arbor, MI 48106-1346

Abstract

The investigations in this thesis applied magnetic resonance imaging (MRI) techniques to study structural and functional aspects of central nervous system (CNS) damage and recovery. The principal disease model investigated was optic neuritis (ON) for the visual system. A longitudinal study of acute optic neuritis was performed, in which patients were studied over one year. Functional and optic nerve structural MRI were performed, along with detailed clinical assessments. Analysis of the functional MRI (fMRI) data revealed differential deactivation behaviours outside the occipital cortex in ON patients when compared with healthy controls. Further correlation analyses, in which fMRI and optic nerve structure data were combined, presented evidence for adaptive cortical plasticity in higher visual processing areas early after optic neuritis onset.

Diffusion tensor imaging (DTI) was then introduced as a potentially valuable technique for investigating white matter structure. It was applied to the corticospinal pathways of amyotrophic lateral sclerosis patients, which showed reduced fractional anisotropy (FA), a measure of white matter structural integrity, when compared with healthy controls. DTI tractography, an exciting development of DTI, was subsequently used to develop probabilistic mapping of white matter tracts (including visual and motor pathways) for multiple subjects.

This methodology was applied to a group of subjects who also underwent fMRI scanning for the visual system. The integration of DTI tractography and fMRI derived information discovered a function-structure gradient within the posterior visual pathways: the visual cortex fMRI response correlated with the FA of the probabilistically segmented optic radiations. Finally, a preliminary study of ON patients applied this novel methodology to investigate their posterior visual function-structure gradients and found differences, compared with controls.

Acknowledgments

The work in this thesis was conducted in the NMR Research Unit, Institute of Neurology, which was generously funded by the MS Society of Great Britain and Northern Ireland. My research post was funded by the Brain Research Trust, Barnwood House Trust and the Mrs FB Laurence Charitable Trust.

I am extremely grateful for the tireless and enthusiastic support of Professor Alan Thompson, my principal research supervisor. His patience during the gestation of this thesis is also much appreciated. I am also very grateful to Professor Gareth Barker, my second supervisor, for his help in many aspects of this thesis' work, especially its technical issues. Many thanks to Professor David Miller and Professor Ian McDonald for their supportive advice and interest during my research period.

I extend a warm thanks to Olga Ciccarelli for her support and generosity with all aspects of this thesis, especially the DTI related studies. Our collaborations helped to produce results of great interest. I also warmly thank Claudia Wheeler-Kingshott for advice and for helping to implement the DTI and fMRI acquisition protocols.

The longitudinal optic neuritis study was organized by Simon Hickman who arranged subject recruitment and follow up. I am grateful for his help and generosity in providing data and support during the analysis.

I also thank Gordon Plant who ran the Moorfield's Eye Clinic, from which the optic neuritis patients were recruited and Geoff Parker for developing the DTI fibre tracking algorithms. Professor Karl Friston and his colleagues at the Wellcome Department of Imaging Neuroscience provided valuable and much appreciated advice for SPM analysis. I warmly thank Martin King for performing the

statistical analysis for chapter 4 and Dan Altmann for his valuable statistical advice and interesting discussions.

Katherine Miszkiel contributed to the analysis of optic nerve structural imaging and Stephen Jones kindly performed visual evoked potentials on the optic neuritis patients. Thanks also to Chris Benton, Ros Gordon and David MacManus for their assistance with subject MRI scanning and to other members of the NMR Research Unit for general support and advice. I also thank the patients and controls who gave up their time to participate in the studies described in this thesis.

David Werring helped introduce me to and taught me about DTI, fMRI and clinical methodology during the early stages of my research period. I am also grateful to Charles Clarke for his support throughout my time in neurology.

Finally, I thank my wife, Hina, for her patience and encouragement, and my children, Shehzad, Sofiyah and Mikaeel.

Publications associated with this thesis' work

Ciccarelli O, Parker GJ, **Toosy AT**, Wheeler-Kingshott CA, Barker GJ, Boulby PA, Miller DH, Thompson AJ. From diffusion tractography to quantitative white matter tract measures: a reproducibility study. *NeuroImage*. 18(2):348-59, 2003.

Toosy AT, Werring DJ, Orrell RW, Howard RS, King MD, Barker GJ, Miller DH, Thompson AJ. Diffusion tensor imaging detects corticospinal tract involvement at multiple levels in amyotrophic lateral sclerosis. *Journal of Neurology Neurosurgery and Psychiatry*. 74(9):1250-7, 2003.

Ciccarelli O*, **Toosy AT***, Parker GJ, Wheeler-Kingshott CA, Barker GJ, Miller DH, Thompson AJ. Diffusion tractography based group mapping of major white-matter pathways in the human brain. *NeuroImage*. 19(4):1545-55, 2003.

* Joint first authors.

Hickman SJ, **Toosy AT**, Jones SJ, Altmann DR, Miszkiel KA, MacManus DG, Barker GJ, Plant GT, Thompson AJ, Miller DH. Serial magnetization transfer imaging in acute optic neuritis. *Brain*. 127(Pt 3):692-700, 2004.

Toosy AT, Ciccarelli O, Parker GJ, Wheeler-Kingshott CA, Miller DH, Thompson AJ. Characterizing function-structure relationships in the human visual system with functional MRI and diffusion tensor imaging. *NeuroImage*. 21(4):1452-63. 2004.

Hickman SJ, **Toosy AT**, Miszkiel KA, Jones SJ, Altmann DR, MacManus DG, Plant GT, Thompson AJ, Miller DH. Visual recovery following acute optic neuritis--a clinical, electrophysiological and magnetic resonance imaging study. *Journal of Neurology*. 251(8):996-1005, 2004.

Hickman SJ, **Toosy AT**, Jones SJ, Altmann DR, Miszkiel KA, MacManus DG, Barker GJ, Plant GT, Thompson AJ, Miller DH. A serial MRI study following optic nerve mean area in acute optic neuritis. *Brain*. 127(Pt 11):2498-505, 2004.

Ciccarelli O, **Toosy AT**, Hickman SJ, Parker GJ, Wheeler-Kingshott CA, Miller DH, Thompson AJ. Optic radiation changes after optic neuritis detected by tractography-based group mapping. *Human Brain Mapping*. Apr 15, 2005; [Epub ahead of print]

Toosy AT, Hickman SJ, Miszkiel KA, Jones SJ, Plant GT, Altmann DR, Barker GJ, Miller DH, Thompson AJ. Adaptive cortical plasticity in higher visual areas after acute optic neuritis. *Annals of Neurology*. 57(5):622-633, 2005.

Toosy AT, Hickman SJ, Plant GT, Altmann DR, Barker GJ, Miller DH, Thompson AJ. A longitudinal study of the functional MRI response to photic stimulation after optic neuritis. *NeuroImage*., 2005 (to be submitted).

Table of Contents

List of Figures

CHAPTER 2

CHAPTER 3

CHAPTER 4

CHAPTER 5

CHAPTER 6

APPENDIX A

List of Tables

CHAPTER 3

CHAPTER 4

CHAPTER 5

Abbreviations

ADC	Apparent diffusion coefficient
AION	Anterior ischaemic optic neuropathy
ALS	Amyotrophic lateral sclerosis
BOLD	Blood oxygen level dependent
BW	Bandwidth
CBF	Cerebral blood flow
CBV	Cerebral blood volume
CMRO2	Oxygen consumption rate
CNS	Central nervous system
CSF	Cerebrospinal fluid
DCM	Dynamic causal modelling
DeoxyHb	Deoxyhaemoglobin
DSI	Diffusion spectrum imaging
DTI	Diffusion tensor imaging
EC	Euler characteristic
EfMRI	Event-related fMRI
EPI	Echo planar imaging
ETL	Echo train length
FA	Fractional Anisotropy
FEF	Frontal eye field
FFX	Fixed effects
FMRI	Functional magnetic resonance imaging
FMT	Fast marching tractography
FOV	Field of view
GABA	Gamma-aminobutyric acid
GE	Gradient echo

GRE	Gradient recalled echo
GRFT	Gaussian random field theory
HLA	Human Leukocyte Antigen
HMD	Humphrey mean deviation
HRF	Haemodynamic response function
ICA	Independent components analysis
IPS	Intraparietal sulcus
LFP	Local field potential
LO	Lateral occipital
LOC	Lateral occipital complex
LTD	Long term depression
LTP	Long term potentiation
MAR	Multivariate autoregressive
MD	Mean diffusivity
MNI	Montreal Neurological Institute
MRI	Magnetic resonance imaging
MS	Multiple sclerosis
MT	Magnetization transfer
MUA	Multi unit activity
NAA	N-acetyl-aspartate
NEX	Number of excitations
NMDA	N-methyl-d-aspartate
NMR	Nuclear magnetic resonance
NPL	No perception of light
OEF	Oxygen extraction fraction
OFC	Orbitofrontal cortex
ONTT	Optic Neuritis
ONTT	Optic Neuritis Treatment Trial
OxyHb	Oxyhaemoglobin
PB	Partial brain

PCA	Principal components analysis
PDF	Probability distribution function
PE	Parameter estimate
PET	Positron emission tomography
PICo	Probabilistic index of connectivity
QBI	Q-ball imaging
RF	Radiofrequency
RFX	Random effects
RMS	Root mean square
RNFL	Retinal nerve fibre layer
ROI	Region of interest
RPT	Refractory period of transmission
SE	Spin echo
SEM	Structural equation model
SNR	Signal to noise
SOA	Stimulus onset asynchrony
SPM	Statistical parametric mapping
TMS	Transcranial magnetic stimulation
VC	Visual cortex
VEP	Visual evoked potential
WB	Whole brain

CHAPTER 1

INTRODUCTION

1.1 Overview

The brain is a highly complex organ able to process neural signals that code for information about the environment (from the past, in the present and for the future). In recent years there have been great advances in understanding how the brain works. This has led to an increasing realization of the complexity that exists within the brain at many levels. Scientific methodology has generally employed a *reductionist* approach which assumes that there is a chain of hierarchical modules of structure and function running from the lowest to the highest levels of description. Higher level processes or structures can be explained and understood in terms of lower level ones. This approach has been very productive in helping to understand the brain and has successfully investigated the structural and functional aspects of brain organization. Functional neuroimaging is an important example of this form of scientific approach and has been instrumental in exploring the phenomenon of functional segregation, in which neurophysiology is characterized in terms of regionally specific responses. An alternative approach has been to employ a *holistic* view to model brain function. In this, the brain is considered to be a parallel processing system with properties of mass action or global function. Research into artificial neural networks have, with the aid of complexity theory, demonstrated the emergence of self-organizing principles and spatio-temporal patterns of activity. These are properties of non-linear dynamical systems, thought to be exemplified by real neural networks and serve as examples of functional integration.

In reality, there is evidence for the co-existence of both functional segregation and functional integration in the central nervous system. It has been demonstrated that neural complexity is

greatest for systems that combine both local specialization with global integration (Tononi et al, 1998). Conversely, complexity is low for systems that comprise completely independent parts (maximally segregated) or systems that have completely homogeneous behaviour (maximum integration). The central nervous system (CNS) is therefore thought to have a hierarchical organization of structural levels ranging from neurons to networks to systems, which at each level are organized into regionally specific modules with multiple interconnections. This gives it parallel distributive properties while concomitantly demonstrating regional segregation.

Both regional specificity of brain function and the interactions between functionally segregated areas have been successfully investigated with functional neuroimaging techniques such as positron emission tomography (PET) and functional magnetic resonance imaging (fMRI). In particular, functional neuroimaging has been applied to study the phenomenon of *cortical plasticity or adaptation*, referring to the dynamic changes in the functional organization of the cerebral cortex that may occur in response to CNS insult. Great advances in the structural organization of the brain have also been made with MRI techniques. Diffusion tensor imaging (DTI) is a development of MRI, which is able to characterize indices of white matter architecture and is potentially sensitive to quantifying the degree of white matter coherence in disease. A recent innovation from DTI is DTI tractography, which can provide maps of white matter tracts and indicate connectivity between different structures of the brain.

An exciting prospect is to marry the functional and structural aspects of CNS organization. Correlating structure with function would allow greater insight into the mechanisms of CNS biology and pathology. This thesis investigates CNS structure and function using MRI. It uses functional MRI to investigate the role of cortical plasticity in the visual system and DTI to study structural degenerative changes that occur in the motor system white matter. Finally, functional fMRI and DTI (with DTI tractography) are applied and combined to study how damage to the optic radiations may affect the functional organization of the visual cortex.

The remainder of this chapter will describe optic neuritis, the model of visual pathology that was investigated, and then introduce some basic concepts about cortical plasticity. The following chapter will describe the basic principles of functional MRI and its analysis, DTI and tractography. Chapter three will describe the results of a serial study of optic neuritis that was performed with functional MRI. For the motor system, amyotrophic lateral sclerosis, a condition characterized by motor tract degeneration, was chosen to investigate changes in white matter structure using DTI. This will be detailed in chapter four. Chapter five will discuss the methodology of combining functional and structural measures of CNS organization derived from MR techniques and apply it to a group of patients with optic neuritis. Chapter Six will discuss the overall findings of this thesis and comment on future directions.

1.2 Acute idiopathic demyelinating optic neuritis

Optic neuritis (ON) can be used to refer to any inflammatory optic neuropathy but usually it signifies an acute condition of the optic nerve that is characterized by focal inflammation associated with demyelination and will be used as such for the purposes of this thesis (Hickman et al, 2002). It may be isolated, recurrent and it may be associated with multiple sclerosis.

1.2.1 Historical Perspective

Optic nerve disorders were not diagnosed reliably until ophthalmoscopy became a routine part of the ophthalmic examination during the late nineteenth century. In ancient times, eye diseases were divided into "ophthalmia" – visible pathology of the conjunctiva or cornea, and "blindness" – visual loss not attributable to ophthalmia. The earliest references to optic nerve dysfunction causing visual loss are found in Arabic texts of ophthalmology written in the ninth century. Hunain Ibn Is-Haq (Meyerhoff 1928) described eye paralysis involving perception, eye motion or both. He also references pain and heaviness, "swelling" of the optic nerve and the afferent pupillary defect.

In literature, 'The case of Augustus d'Este' describes how the author, Augustus d'Este (1794-1848), the illegitimate grandson of King George III, develops in 1822 probable optic neuritis and later progresses to multiple sclerosis (Firth 1948).

The invention of the ophthalmoscope by Helmholtz in 1845 allowed ophthalmologists to identify optic nerve and retinal pathology. Optic neuritis was first described by von Graefe in 1860 (von Graefe 1860) and by Nettleship in 1884 (Nettleship 1884). In particular, Nettleship described the following features based on a series of 28 patients:

"They are characterized by failure of sight limited to one eye, often accompanied by neuralgic pain about the temple and orbit and by pain in moving the eye; many recover but permanent damage and even total blindness may ensue; there is at first little, sometimes no, ophthalmoscopic change, but the disc often becomes more or less atrophic in a few weeks, and occasionally there are slight retinal changes."

He noted that orbital pain may predate visual loss, that the maximum visual field deficit tends to be central and that recovery usually takes 4 to 6 weeks. He also distinguished between optic neuritis and papilloedema secondary to raised intracranial pressure as distinct causes of optic nerve head swelling.

Over the next few years, further contributions were made by Parinaud (Parinaud 1884), Uhthoff (Uhthoff 1890), Buzzard (Buzzard 1893) and Gunn (Gunn 1897) to the description of optic neuritis, which consolidated on the earliest accounts.

1.2.2 Epidemiology

Acute demyelinating optic neuritis is the most common optic neuropathy and has an estimated annual incidence of 1-5 per 100,000 (Jin et al, 1998; Kinnunen 1983; MacDonald et al, 2000; Rodriguez et al, 1995). Most patients are between 20 and 50 years of age, with a mean age of 30-35 years (Beck 1995). Despite this, cases during childhood (Riikonen et al, 1988) and later in adult life during the 6th and 7th decades (Perkin and Rose 1979) have also been described. Females are more commonly affected than males and there is a Caucasian preponderance (Beck 1988).

1.2.3 Symptoms

Patients typically present with blurred vision and monocular pain.

1.2.3.1 Visual loss

This is the major symptom and has been reported in over 90% of patients (Optic Neuritis Study Group 1991). It usually develops over several hours to several days. Most patients report diffuse monocular blurring or fogging of vision. The severity of visual loss varies widely and can be complete with no perception of light (Optic Neuritis Study Group 1991; Perkin and Rose 1979). Colour vision is affected early, with colours appearing broken up, dull and washed out.

1.2.3.2 Orbital or ocular pain

Pain in or around the eye is usually mild, but may be extremely severe and has been reported in 90% of patients. It may precede or begin concomitantly with the onset of visual dysfunction. It is usually exacerbated by ocular movement and settles after several days (Optic Neuritis Study Group 1991; Compston 1992; McDonald and Barnes 1992; Perkin and Rose 1979). Different theories have been proposed for the aetiology of pain. It may be caused by inflammation within the optic nerve sheaths

that are innervated by the trigeminal (Rose 1972); alternatively inflammation of the optic nerve at the orbital apex where the extra-ocular muscles are attached may be involved (Swartz et al, 1995). Meningeal stretching of the optic nerve, particularly on eye movement has also been proposed as a contributing factor (Liu et al, 1992). The presence of pain may help to differentiate optic neuritis from other conditions such as anterior ischaemic optic neuropathy.

1.2.3.3 Positive visual phenomena

'Photopsias' (positive visual phenomena) were reported by 30% of patients in the optic neuritis treatment trial (ONTT) (Optic Neuritis Study Group 1991). These comprise spontaneous flashing black squares, flashes of light or showers of sparks (Davis 1976). They may be precipitated by eye movement or certain sounds (McDonald and Barnes 1992; Page et al, 1982).

1.2.4 Signs

The signs of optic neuritis include reduced visual acuity, contrast sensitivity and colour vision. Visual field loss is variable but commonly includes a central scotoma. A relative afferent pupillary defect is usually present. Disc swelling is sometimes seen (with ophthalmoscopy) but peripapillary haemorrhages are uncommon.

1.2.4.1 Visual Acuity

Central vision presentation may vary from normal visual acuity (6/6 or 20/20) or better to no perception of light (NPL). In the ONTT, only 11% of patients presented with normal visual acuity (6/6) and 15% had finger counting visual acuity or worse (Optic Neuritis Study Group 1991). In patients with normal visual acuities other tests (e.g. contrast sensitivity, colour vision, electrophysiology) may indicate optic nerve abnormalities (Frederiksen et al, 1991).

1.2.4.2 Colour Vision

Colour vision is nearly always abnormal in optic neuritis and tends to be affected early. The degree of colour vision dysfunction may be out of proportion to the degree of visual acuity loss. Colour vision can be tested with the Ishihara pseudoisochromatic plates (Kanehara and Co. Ltd., Tokyo, Japan). These have been reported to detect abnormalities of colour vision in almost 90% of cases in the ONTT (Optic Neuritis Study Group 1991). Other tests of colour vision include the Hardy-Rand-Rittler (HRR) pseudoisochromatic plates (Steinmetz and Kearns 1956) and the Farnsworth-Munsell 100-Hue test (Optic Neuritis Study Group 1991).

1.2.4.3 Visual Field

Although central and paracentral scotomas were originally thought to comprise the dominant field defects in optic neuritis (Marshall 1950, Miller 1982), it has since become clear that almost any type of field defect can occur, including an arcuate defect, a centrocaecal scotoma, a superior or inferior altitudinal defect and a left or right hemianopic defect. In the ONTT, visual field loss was predominantly focal in 52% and diffuse in 48% (Keltner et al, 1993) of patients at baseline. 8% of patients had central or centrocaecal defects, 20% had focal nerve fibre bundle type defects (altitudinal, arcuate and nasal step) and the remaining 24% had a variety of other defects, including hemianopias in 5% (Keltner et al, 1993).

1.2.4.4 Pupillary Reactions

A relative afferent pupillary defect (RAPD) of the affected eye has been shown in most cases of optic neuritis (Cox et al, 1981; Ellis 1979). Its absence may indicate subclinical or previous optic neuritis in the contralateral eye or mild involvement of the ipsilateral eye.

1.2.4.5 Fundus appearance

In most studies, 20-40% of patients with acute optic neuritis have optic disc swelling on ophthalmoscopy (Optic Neuritis Study Group 1991; Perkin and Rose 1979). The degree of disc swelling is generally associated with severity of visual dysfunction at presentation (Perkin and Rose 1979). The evolution of disc change begins with venous engorgement, followed by disc oedema initially of the nasal side (Berliner 1935). Fluorescin angiography confirms leakage of dye first occurring at the nasal margin (Carroll 1935). Sheathing of retinal veins has also been described especially in association with multiple sclerosis and sarcoidosis (Birch et al, 1966; Lightman et al, 1987). Disc or peripapillary haemorrhages are rare in optic neuritis and were present in 6% of cases in the ONTT (Optic Neuritis Study Group 1991). They are much more common in anterior ischaemic optic neuropathy.

1.2.5 Fellow eye involvement

Asymptomatic concomitant visual dysfunction in the fellow eye has been reported by several studies (Optic Neuritis Study Group 1991; Beck et al, 1993b; Wakakura et al, 1999). In the ONTT contralateral eye abnormalities were found with quantification of visual acuity in 13.8%, contrast sensitivity in 15.4%, colour vision in 21.7% and visual fields in 48% of patients (Optic Neuritis Study Group 1991). These abnormalities were not associated with a previous history of multiple sclerosis or brain MRI lesion load, suggesting that demyelinating disease dissemination was not responsible. These abnormalities did however recover over several months, suggesting that subclinical acute demyelination of the contralateral optic nerve may be responsible (Beck et al, 1993b).

1.2.6 Visual recovery

Patients tend to worsen for several days to two weeks following the onset of acute optic neuritis (Beck 1998). Vision then tends to recover in two phases. There is an initial rapid improvement which

levels off, followed by a slower improvement that can continue up to 1 year after onset (Beck et al, 1993b; Beck et al, 1994; Beck 1998; Perkin and Rose 1979). In the placebo arm of the ONTT, visual acuity began to improve within three weeks of onset in 79% of patients. Recovery for most patients was nearly complete by five weeks after onset and at one year, more that 90% of patients had visual acuities better that 20/40 (Beck 1998).

Visual improvement does seem to be weakly correlated with the initial degree of visual acuity loss. Despite this, most patients tend to make a good clinical recovery. In the ONTT, for example, 64% of 28 patients whose visual acuities were perception of light or worse, recovered to 20/40 or better (Beck et al, 1994; Beck and Cleary 1993; Perkin and Rose 1979). The final visual outcome appears to be unrelated to factors such as age, gender, the appearance of the optic disc at presentation, abnormal MRI, concurrent multiple sclerosis or intravenous corticosteroid treatment (Beck et al, 1994; Bradley and Whitty 1967; Kapoor et al, 1998; Perkin and Rose 1979). A poorer visual prognosis, however, has been associated with long lesions of the optic nerve on MRI (Miller et al, 1988) particularly when the lesion is intracanicular.

1.2.7 Residual visual deficits

Although parameters of visual function tend to recover in parallel following an attack of optic neuritis, and there is usually a significant degree of recovery, residual deficits may still persist. These include disturbances of visual acuity (15-30%), contrast sensitivity (63-100%), colour vision (33-100%), visual field (62-100%), stereopsis (89%), pupillary reaction (55-92%) and visual evoked potentials (63-100%) (Beck 1998). In one study involving 93 patients, the most common findings after an attack of acute optic neuritis were optic atrophy, defective colour vision, abnormal pupillary reactions and abnormal visual evoked potentials (VEPs) (Kirkham and Coupland 1981). Psychophysical studies have explored the relative contributions of parvo- and magno-cellular pathway damage to visual deficit. The parvocellular pathway detects chromatic stimuli of low to medium spatial frequency, achromatic stimuli of high spatial frequency and constitutes about 80% of optic nerve fibres. The magnocellular

pathway detects achromatic stimuli of low to medium spatial frequency and comprises about 10% of optic nerve fibres (Caruana et al, 2000; Silveira and Perry 1991). Some studies have reported a predilection for magnocellular pathway involvement in optic neuritis and multiple sclerosis (Phillips et al, 1994; Regan et al, 1991) whereas others have demonstrated greater parvocellular dysfunction (Caruana et al, 2000; Flanagan and Markulev 2005; Mullen and Plant 1986; Porciatti and Sartucci 1996; Wall 1990) or non-selective loss of luminance and chromatic function (Dain et al, 1990; Mason et al, 1982; Russell et al, 1991; Vleugels et al, 1998). Optic disc pallor is often present even when recovery is excellent (Lynn 1959; Perkin and Rose 1979; Wybar 1952). It tends to be temporal but may be generalized. In the ONTT, at six months follow up, colour vision was still abnormal in 40% of patients, visual fields deficits (measured by the mean deviation using Humphrey 30-2 perimetry) were present in 32%, contrast sensitivity was abnormal (measured with the Pelli-Robson Chart) in 56% and optic disc pallor was detectable in 63% (Beck et al, 1992).

1.2.7.1 Subjective visual symptoms

Despite the return of normal visual acuity, many patients may still experience difficulties with vision. They may feel that their vision is still not quite back to normal or is "fuzzy". This may be related to persistent abnormalities of other measurements of optic nerve function e.g. colour vision, visual evoked potentials (Bynke et al, 1980; Fleishman et al, 1987). Subjectively abnormal vision may also occur in spite of normal clinical parameters. Subtle abnormalities of the visual field that are undetectable by conventional visual field perimetry have been suggested as a contributory factor although, in reality the cause in unclear (Beck 1998).

1.2.7.2 Uhthoff's phenomenon

This phenomenon tends to appear during recovery. Patients describe transient visual blurring during exercise, during a hot bath or when under emotional stress (Goldstein and Cogan 1964; Perkin and Rose 1979; Uhthoff 1890). It was reported by about 10% of patients after six months in the ONTT

(Beck 1998). It tends to be associated with multiple sclerosis (McAlpine and Compston 1952) but can also occur in optic neuropathies other than optic neuritis (Nelson et al, 1958). Several hypotheses exist to explain the phenomenon. The most commonly described one suggests that a small rise in body temperature may inhibit nerve conduction within the affected optic nerve by inducing a reversible conduction block of the demyelinated nerve fibres which leads to visual blurring (Beck 1998).

1.2.7.3 Visual-Evoked Potentials (VEPs)

Stimulation of the optic nerve by an alternating pattern of light and dark squares produces a reproducible occipital potential with a well defined latency in normal individuals (Halliday et al, 1972; Sokol 1976). The VEP is used as an objective measure of conduction in the afferent visual system. Following resolution of acute optic neuritis most patients still demonstrate delayed latency, indicating impaired optic nerve conduction. The frequencies of these cases from previous studies range from 63-100% (Arden and Gucukoglu 1978; Halliday et al, 1972; Shahrokhi et al, 1978). Halliday (1978) reported that even when visual acuity returned to 20/20 the VEP amplitude was often normal but the latency was nearly always delayed.

1.2.8 Neurological Prognosis

The recurrence of optic neuritis and its association with multiple sclerosis are discussed below. Rarely, optic neuritis may be part of the demyelinating syndrome, "Devic's disease" or "neuromyelitis optica", and it also occurs in primary demyelinating conditions, myelinoclastic diffuse sclerosis (Schilder's disease) and encephalitis periaxialis concentrica (Beck 1998). These will not be discussed in this thesis.

1.2.8.1 Optic Neuritis Recurrence

The risk of recurrence has been reported as being 10-25% (Optic Neuritis Study Group 1997; Hutchinson 1976; Perkin and Rose 1979). In particular the ONTT reported a 5 year risk of developing recurrent optic neuritis as 19% in the affected eye and 17% in the fellow eye.

1.2.8.2 Relationship with Multiple Sclerosis

The association between optic neuritis and multiple sclerosis (MS) has been appreciated for a long time. In 1893, Buzzard reported five patients with a history of MS that had episodes of optic neuritis (Buzzard 1893). It is thought MS and optic neuritis share the same pathophysiological mechanisms. Some consider optic neuritis to be a limited form of MS (Ebers 1985). About 20% of patients with MS present with optic neuritis (Beck 1998). The occurrence of an isolated episode of optic neuritis increases the risk of progression to MS. This risk has been assessed in several studies. Early retrospective studies reported MS in 40-60% of unilateral optic neuritis patients after at least a decade (Compston et al, 1978; Francis et al, 1987). Rodriguez et al (1995) showed in a prospective study that among 95 cases of optic neuritis, the estimated risk of developing MS was 39% by 10 years, 49% by 20 years, 54 % by 30 years and 60% by 40 years (Rodriguez et al, 1995). In contrast, another prospective population based study followed up 86 optic neuritis patients and reported an estimated 15 year risk of 40% for developing MS with a minimal increase in risk at 30 years following optic neuritis (Nilsson et al, 2005).

The risk of progression appears to depend upon the presence of MRI lesions at presentation. In the ONTT the cumulative risk of progression to MS within 4 years of the onset of optic neuritis was 13% in patients with normal MR imaging, 35% in patients with one or two lesions and 50% in patients with three or more lesions (Beck and Trobe 1995). A 14 year longitudinal study reported the risk of developing MS following an acute clinically isolated syndrome (optic neuritis, spinal cord or brainstem syndrome) (Brex et al, 2002). 71 patients were followed up out of the original cohort of 109.

Overall, 68% had developed clinically definite MS. In patients with normal MRI scans at baseline, 19% had progressed to MS whereas in patients with abnormal baseline MRI scans 88% had clinically definite MS at 14 years. Disability at 14 years was moderately correlated with the change in lesion volume on MRI over the first five years (r=0.61) and the MRI lesion volume at 5 years (r=0.60). Another study investigated 127 patients, originally enrolled in the ONTT, who had developed MS and found that most (65%) had low disability after 10 years (Beck et al, 2004).

Other possible risk factors, that may influence the development of MS following optic neuritis, have also been studied. For example, a younger age for optic neuritis has been found by some studies to signify a greater risk of developing MS (Kahana et al, 1976; Mapelli et al, 1986; Rizzo, III and Lessell 1988). There have been conflicting reports for the effect of gender. Some studies have found no difference in the incidence of MS after optic neuritis (Beck and Trobe 1995; Bradley and Whitty 1967; Mapelli et al, 1986; Rodriguez et al, 1995) whereas others report an increased risk associated with women (Hely et al, 1986; Rizzo, III and Lessell 1988; Sandberg-Wollheim et al, 1990). The occurrence of optic neuritis during winter months may predispose to developing MS (Compston et al, 1978; Nilsson et al, 2005). Two year data from the ONTT suggests that Caucasians are at higher risk than African-Americans (Beck et al, 1993a). This difference was still present at four years (Beck and Trobe 1995).

Clinical features of optic neuritis that may influence the development of MS have not been thoroughly studied. In one study, MS developed in 13% of 45 patients with anterior optic neuritis, compared with 60% of 30 patients with retrobulbar neuritis (Kahana et al, 1976). These findings are consistent with results from the ONTT, which suggest that the presence of severe disc swelling reduces the subsequent likelihood of MS (Beck et al, 1993a). Generally it is believed that the severity of visual loss and the final visual acuity outcome have no effect on the development of MS (Bradley and Whitty 1967; Perkin and Rose 1979). Reports concerning the risk of MS following recurrent optic neuritis are mixed with some demonstrating an increased risk (Rodriguez et al, 1995; Sandberg-

Wollheim et al, 1990) and others showing no increased risk (Francis et al, 1987; Rizzo, III and Lessell 1988). The ONTT does not show a strong relationship between recurrent optic neuritis and subsequent MS (Beck and Trobe 1995). Patients with bilateral simultaneous optic neuritis are said to have the same risk of developing MS as unilateral optic neuritis (Morrissey et al, 1995) although one report suggested an increased risk when the second eye became affected within 2 weeks of the first eye (Hutchinson 1976).

Immunological abnormalities within the cerebrospinal fluid (CSF) are common in patients with optic neuritis. In the ONTT, 83 patients with isolated optic neuritis underwent a lumbar puncture within 24 hours of presentation (Rolak et al, 1996). A pleocytosis was present in the CSF of 36% of patients; elevated myelin basic protein in 18%; increased IgG synthesis in 44%; oligoclonal bands in 50% and kappa-light chains in 27%. The predictive power of CSF abnormalities at determining the future risk of developing MS has been reported with variable results. The studies have indicated that about 10-50% of patients with acute isolated optic neuritis and normal CSF may still develop MS after many years, whereas about 25-50% of patients with optic neuritis and abnormal CSF avoid progression to MS (Anmarkrud and Slettnes 1989; Sandberg-Wollheim et al, 1990; Stendahl-Brodin and Link 1983).

Genetic studies have determined that certain Human Leukocyte Antigen (HLA) typing patterns influence the development of MS. In Northern Europeans the A3, B7 and DR2 alleles are more commonly found in MS patients (Francis et al, 1987; Sandberg-Wollheim 1975). Certain haplotypes such as DR2 and DR3 may weakly influence the risk of developing MS in patients with acute isolated optic neuritis (Francis et al, 1987; Hely et al, 1986). HLA BT101 may also play a role (Compston et al, 1978).

1.2.9 Pathology

There are few histopathological studies of the optic nerve in patients with acute optic neuritis. Published studies of the optic nerves from patients with acute MS have found active demyelinating plaques similar to those found in the brain (Lumsden 1970; McDonald 1974; Prineas 1975). These plaques demonstrate inflammation or degeneration. The inflammatory response was characterized by perivascular cuffing, T-cells and plasma cells. As inflammation subsides there is fat-laden macrophage infiltration and glial proliferation. Degenerating plaques exhibit axonal loss.

One post-mortem study, published in 1953, examined 14 eyes from 10 patients with advanced multiple sclerosis (Gartner 1953). Only optic atrophy was found, mainly in the temporal part of the optic nerve. There was also increased glial cell cellularity within the nerve, gliosis on the surface of the optic disc, retinal atrophy and sclerosed blood vessels on and around the disc.

A study employing electron and light microscopy reported ultrastructural findings in a patient who developed Schilder's disease and bilateral disseminated optic neuritis (de Preux and Mair 1974). Areas of patchy and complete demyelination were seen in both optic nerves. Some oligodendrocytes were seen in areas of partial demyelination but there were no oligodendrocytes in regions of complete demyelination. Increased numbers of fibrous astrocytes were seen in all areas. Some axonal destruction was also noted.

Evangelou published a post-mortem study that compared the anterior visual pathways (optic nerves, optic tracts and lateral geniculate nuclei) of eight MS patients with eight controls (Evangelou et al, 2001). The optic nerves and optic tracts tended to be smaller in the patients ($p=0.08$) and also had significantly lower axonal densities (optic nerves – MS 1.1×10^5 /mm^2, controls 1.7×10^5 /mm^2; optic tracts – MS 1.4×10^5 /mm^2, controls 1.8×10^5 /mm^2, $P=0.006$). The parvocellular cells of the lateral geniculate nuclei were smaller and showed greater variation in size in the MS group (mean size: MS 226 μm^2, controls 230 μm^2). These findings supported preferential atrophy of smaller axons. Several

mechanisms were postulated for the lateral geniculate findings including the presence of neurotoxic inflammatory factors, retrograde injury with Wallerian degeneration and trans-synaptic degeneration in the MS patients.

Axonal loss and, in particular, axonal transection was found to be a consistent feature of demyelination in the brains of 11 patients with multiple sclerosis and was present in both active and chronic lesions (Trapp et al, 1998)

Animal models (experimental allergic optic neuritis) have also provided insight into the pathology of optic neuritis. A study which investigated the optic neuritis model in guinea pigs reported mononuclear cell infiltrates with multiple foci of axial and periaxial demyelination (Rao et al, 1977). Another study, which examined rhesus monkeys with experimental allergic encephalomyelitis, revealed inflammatory infiltrates, extensive demyelination and axon degeneration (Hayreh et al, 1981). MR imaging of adult guinea pigs sensitized for acute experimental allergic encephalomyelitis showed leakage of gadolinium in the optic nerves and chiasm as early as 5 to 8 days after antigenic stimulation. Pathologically no demyelination was observed in the optic nerves although a few perivascular inflammatory foci were present. This supported a role for increased permeability of the blood-optic nerve barrier early in autoimmune demyelination (Guy et al, 1990). A further study used the microinjection of polyclonal rabbit anti-galactocerebroside antibody and guinea pig complement to induce localized demyelination in the rat optic nerve (Zhu et al, 1999). It reported local cyoskeletal changes within the demyelinated axons and suggested that this may enhance axonal damage.

1.2.10 Pathophysiology

The mechanisms that underlie the pathophysiology of optic neuritis and multiple sclerosis are very similar and may be divided into those that account for negative symptoms or loss of function,

recovery of function and positive phenomena. In addition, potential roles for optic nerve atrophy and remyelination have been investigated in longer term follow up studies.

1.2.10.1 Negative symptoms

1.2.10.1.1 Effects of demyelination

Negative symptoms are primarily due to the loss of conduction within the optic nerve. A major cause is axonal conduction block, in which the transmission of electrical impulse trains along the axon is interrupted, and this has been reliably localized to the sites of demyelination (McDonald and Sears 1969; McDonald and Sears 1970). Under experimental conditions, following segmental demyelination of the sciatic nerve, spinal roots or dorsal columns, conduction block tends to persist for the first few days (Smith and McDonald 1999) and this is thought to be related to an initial paucity of sodium channels in the underlying axolemma (Waxman and Ritchie 1993). Widening of the nodal gap may also cause conduction block and this is thought to arise from a reduction in the safety factor[1] for conduction (Tasaki 1953). This reduction is due to an increase in nodal membrane area, which will raise the electrical capacitance and will also dissipate the local depolarizing nodal currents (Smith 1994).

1.2.10.1.2 Effects of inflammation

---

[1] The safety factor for conduction is the ratio of the actual local action current that depolarizes a node to the minimum current that is necessary to do so. It is around three to five in normal axons but in demyelinated axons it is near unity, making conduction less reliable.

Inflammation has also been implicated in contributing to conduction block in acute optic neuritis. A strong relationship was demonstrated between contrast enhancement on MR imaging of the optic nerve and reduced VEP amplitude during the acute phase when vision was poor (Youl et al, 1991). One month later, after visual recovery, the VEP amplitude had returned towards normal, indicating partial recovery of conduction block. In addition contrast enhancement on MR imaging was no longer evident however VEP delay was still present, consistent with persistent demyelination. This suggested that the onset and resolution of inflammation contributes to the onset and recovery of conduction block (and visual dysfunction).

It is thought that pro-inflammatory cytokines may mediate the mechanisms that contribute to conduction block. The cytokines, tumour necrosis factor-α (TNF-α) and interferon-γ (IFN-γ), have been implicated and although direct effects on axonal conduction have been difficult to detect (Dugandzija-Novakovic and Shrager 1995) they are known to promote the expression of the inducible form of nitric oxide synthase (iNOS) (Goureau et al, 1997; Hu et al, 1995). Evidence for the putative role of NO in mediating the inflammatory process is strengthened by the finding that its synthesis is raised in MS and in inflammatory lesions (Bo et al, 1994; Giovannoni et al, 1997). In addition, physiological levels of NO have been shown to cause conduction block in both normal (Redford et al, 1997; Shrager et al, 1998) and demyelinated axons (Redford et al, 1997). Potential therapies could attempt to reduce NO levels in the future. For example, the animal model of experimental autoimmune encephalomyelitis has demonstrated the benefit of using NOX-100, an NO scavenger, which greatly reduces disease progression in combination with the immunosuppressant ciclosporin A in mice (Jolivalt et al, 2003).

Inflammation may also alter glial cell properties, in particular those of astrocytes and microglia, which could contribute to neurological dysfunction (Chao et al, 1995; Ridet et al, 1997). Astrocytes are thought to regulate chemical factors in the brain and are physically associated with neurons, dendrites, synapses and nodes of Ranvier (Sims et al, 1991).

1.2.10.2 Recovery of function

1.2.10.2.1 Conduction recovery in demyelinated axons

Studies of experimentally demyelinated central axons have shown that conduction tends to recover within two to three weeks of demyelination (Felts et al, 1997). It is believed that this recovery is helped by the appearance of sodium channels along the demyelinated axolemma (Felts et al, 1998) and also by the restored conduction being more continuous, as is the case with peripheral demyelinated axons (Bostock and Sears 1976), rather than saltatory. Conduction recovery should therefore be assisted by small axon diameters (Bostock 1994) and small internodes (Waxman and Brill 1978) which are found in the optic nerve and may account for the rapid and good recovery of vision following optic neuritis.

1.2.10.2.2 Resolution of inflammation

Clinical recovery following optic neuritis is associated with a concomitant reduction of contrast enhancement on optic nerve MR imaging, which suggests that it may be influenced by the resolution of inflammation (Youl et al, 1991). Further supportive evidence is provided by the observation that NO induced conduction block is reversed when the agent is removed (Redford et al, 1997).

1.2.10.2.3 Role of remyelination

Remyelination is common in MS (Prineas et al, 1993; Prineas and Connell 1979) and is effective at restoring conduction (Felts and Smith 1992; Smith et al, 1981) however the newly myelinated internodes are shorter and thinner than normal. Despite this, the conduction efficacy is thought to be reasonably well maintained at physiological frequencies (Jeffery and Blakemore 1997).

Although remyelination is known to start within a few days of the inflammatory lesion onset there is evidence that, in optic neuritis, remyelinating processes may continue for more than 2 years. A recent paper reported the findings of one cross-sectional and two longitudinal studies (Jones and Brusa 2003) and described how the VEP latencies continued to shorten over the next 2-3 years despite negligible improvements in visual recovery. The long term VEP latency evolution was attributed to myelin repair processes that may protect the demyelinated axons from subsequent degeneration. They also noted an asymptomatic deterioration in the VEPs of the fellow eyes, possibly due to latent demyelination or axonal degeneration.

1.2.10.2.4 Role of cortical adaptation?

Excellent visual recovery has been noted in optic neuritis even with marked retinal fibre layer loss (a marker for optic nerve axonal density), optic atrophy or persistent VEP delay (Halliday et al, 1972; MacFadyen et al, 1988; Steel and Waldock 1998). It has been suggested that compensatory processes involving the cerebral cortex may therefore be involved in contributing to visual recovery.

Other studies suggest this possibility. In one study, visual recovery in cats was monitored after experimentally induced lesions of the intracranial optic nerve (Jacobson et al, 1979). Following the lesion, a rapid recovery was initially seen in parallel with resolution of local oedema. A second slower recovery phase was demonstrated over the next few months. This occurred even when up to 77% of optic nerve axons were destroyed and therefore alluded to recovery mechanisms that did not involve the anterior visual pathways.

Another study that addressed this question was reported by Werring et al (1999) who applied fMRI with a photic stimulation paradigm to a group of seven patients who had made excellent clinical recoveries following acute unilateral optic neuritis (Werring et al, 2000). The optic neuritis patients showed areas of brain activity outside the visual cortex in regions not normally associated with visual

processing e.g. insula, lateral temporal cortex, corpus striatum. A correlation between the extent of extra-occipital activation and the VEP latency of the affected eyes was also demonstrated.

1.2.10.3 Conduction characteristics following recovery

1.2.10.3.1 Conduction slowing

Although recovery of conduction is common following demyelination, the restored conduction itself is neither as fast nor as robust as normal. The low conduction velocity is restricted to the demyelinated portions of the axon and affects the conduction latency (McDonald and Sears 1970). This, along with a reduction in the number of conducting axons, produces latency and waveform changes with VEP testing (Halliday et al, 1972) following acute optic neuritis.

1.2.10.3.2 Conduction refractory period of transmission (RPT)

Restored conduction also remains susceptible to conduction block due to a prolonged RPT (McDonald and Sears 1970). This is the maximum interval between two supramaximal stimuli for which the second action potential fails to propagate through the lesion. Repetitively firing impulse trains are attenuated when propagated through the demyelinated lesion, which therefore acts as a reducing frequency filter. This phenomenon may account for the blurring or 'fading' of vision sometimes described with fixated gaze (Waxman 1981).

1.2.10.3.3 Temperature effects

Temperature sensitive symptomatology is well known following demyelination (Uhthoff's phenomenon). Deleterious changes in visual symptoms occur with warming (Perkin and Rose 1979) and conversely improvements in vision with cooling (e.g. cold drinks) are well described (Hopper et al, 1972). The neurophysiological basis for the beneficial effects of cooling is thought to derive from a

small prolongation in action potential duration (Paintal 1966), itself a consequence of the temperature coefficient for sodium channel inactivation being larger than that for sodium channel activation (Davis and Schauf 1981). In the node prior to the demyelinated region, prolonged action current potentials will encourage depolarization of the demyelinated axon and so enhances nerve conduction.

1.2.10.4 Positive symptoms

Demyelinated axons can become hyperexcitable and spontaneously generate impulse trains at the site of demyelination which propagate in both directions in experimental models (Smith and McDonald 1980; Smith and McDonald 1982). Several mechanisms have been described which may account for this hyperexcitability. A slow inward sodium current can appear at the sites of demyelination (Kapoor et al, 1997; Rizzo et al, 1996) and a prolonged, inward potassium current resulting from an accumulation of potassium ions outside the axons has also been reported (Kapoor et al, 1993). In optic neuritis, patients may experience the perception of flashes of light or other phosphenes upon eye movements (Davis et al, 1976), which are thought to result from mechanosensitive hyperexcitable properties of demyelinated axons. These axonal properties are also thought to mediate L'hermitte's phenomenon, sensory symptoms, especially 'electric shock' like sensations, that radiate down the limbs in MS patients on neck flexion.

1.2.10.5 Mechanisms of persistent deficit

1.2.10.5.1 Axonal loss and optic atrophy

Axonal loss is a common feature in all types of MS lesions (Trapp et al, 1998). Clinically, the later stages of MS are characterized by progressive disability and several lines of evidence support the view that axonal loss is probably a major determinant for this. For example, a strong correlation exists between spinal cord atrophy and clinical disability (Losseff et al, 1996). Various MR imaging modalities

have made important contributions towards determining the mechanisms of atrophy in MS. The interested reader is referred to two recent comprehensive reviews by DH Miller and others which cover this topic (Miller et al, 2002; Miller 2004). Another imaging technique, MR spectroscopy, has shown reduced NAA (N-acetyl aspartate, which is a marker of neuronal dysfunction or loss) in MS lesions and normal appearing white matter (De Stefano et al, 1998; Fu et al, 1998; Matthews et al, 1996). Correlations between NAA, clinical function and cerebellar volumes in MS patients have also been shown (Davie et al, 1995). Recent evidence suggests that cerebral atrophy may occur early following a clinically isolated syndrome. In a group of 55 patients with clinically isolated syndromes, ventricular enlargement occurred in the 18 patients who developed clinical MS, and in the 40 patients with abnormal brain MRI at presentation over one year. No change in ventricular volume was noted in the 15 patients with normal imaging (Dalton et al, 2002). Atrophy has also been found early in the disease course of relapsing-remitting MS (Chard et al, 2002). The mechanisms responsible for direct chronic axonal loss are not fully understood but the severity of early inflammation (Perry and Anthony 1999) and also continuing inflammatory processes (Trapp et al, 1998) are thought to be factors particularly in relapsing remitting and secondary progressive MS .

In optic neuritis, there is also evidence for optic atrophy which can continue three years after the inflammatory episode. In a serial MRI study, the optic nerve cross-sectional areas were measured in patients 20 months after optic neuritis and one year later (Hickman et al, 2001). The mean area of the affected optic nerve decreased over one year from 11.1 to 10.2 mm^2 ($p<0.01$). Poor visual acuity and reduced VEP amplitude was associated with optic atrophy. The recently introduced non-invasive technique, optical coherence tomography, has been used to quantify axonal loss of the retinal nerve fibre layer (RNFL) after optic neuritis (Trip et al, 2005). RNFL thickness was significantly reduced in the affected patients' eyes compared with healthy volunteers' and clinically unaffected eyes. There were also significant relationships among RNFL thickness and visual acuity, visual field, colour vision and VEP amplitude. In addition, a putative role for NO has been suggested in axon degeneration following acute inflammation. Acute Wallerian degeneration has been found in axons of the rat dorsal

root ganglion, electrically stimulated at physiological frequencies whilst exposed to low concentrations of NO (Smith et al, 2001). Furthermore, a recent study discovered higher plasma biomarkers of axonal injury and higher nitric oxide metabolites in patients with acute optic neuritis when compared with healthy volunteers (Petzold et al, 2004).

1.2.10.5.2 Persistent conduction block

This is known to occur in chronic demyelinating peripheral neuropathy (Lewis et al, 1982) and is likely to occur in central demyelinating disease. For instance, if the safety factor in demyelinated axons is around unity, in some axons it will be below unity and this will impose a conduction block that may manifest as persistent clinical deficit.

1.3 Cortical Plasticity

Functional improvement is often seen following acute brain injury; however certain aspects of recovery cannot be explained by structural mechanisms such as the resolution of inflammation or oedema. FMRI has presented the opportunity to measure changes, relating to interactions at the level of large neuronal populations that follow neural insult (cortical plasticity). The term cortical plasticity has been defined as the "reorganisation of distributed patterns of normal task-associated brain activity that accompany action, perception, and cognition and that compensate impaired function resulting from disease or brain injury." (Frackowiak 1997).

Ultimately, plasticity in neuroscience research is thought to be related to lower levels of neural organization and may include axonal/neuronal (e.g. reflecting changes in sodium channel expression (Waxman 2001) or dendritic arborisation (Jones and Schallert 1992)) and synaptic (e.g. indicating changes in synaptic density, distribution or strength (Jacobs and Donoghue 1991)) mechanisms. For example, dendritic spines have been posited as the primary sites of synaptic plasticity (Calverley and Jones 1990). The synaptic channels covering dendritic trees operate on different time scales and with

a range of activity-dependent sensitivities which facilitate sophisticated neuronal plasticity (Harris 1999; Johansson 2004). This was illustrated by a study that imaged pyramidal neurons in the mouse barrel cortex with a fluorescent-protein labelling technique over several weeks (Trachtenberg et al, 2002). Although dendritic structure was stable, spines appeared and disappeared with varying lifetimes. About 50% of the population persisted for at least a month, whereas the rest were present for several days at most. Electron microscopy of dendritic segments revealed that spine sprouting and retraction are associated with synapse formation and elimination respectively. Whisker trimming induced rapid and robust remodelling of whisker representation, with an increase in the pool of transient spines. Thus, experience dependent plasticity was associated with increased synapse turnover (Trachtenberg et al, 2002).

Activity-dependent modification of synaptic connections is also thought to involve long term potentiation (LTP) and long term depression (LTD). The detailed mechanisms remain unclear, however LTP is accompanied by an enhanced local excitability of pyramidal neuron dendrites (Frick et al, 2004). The excitatory neurotransmitter, glutamate is thought to play a major role – cortical reorganization is prevented by blockade of NMDA glutamatergic receptors in the primate somatosensory cortex (Garraghty and Muja 1996). Other diffuse neuromodulatory systems have also been implicated, originating in subcortical regions, based on norepinephrine, acetylcholine, dopamine and serotonin. These are thought to alter the threshold for activity-dependent synaptic plasticity (Gu 2002) perhaps through the facilitation of a NMDA receptor gated process. Studies have also implicated GABA-A receptors (Hess et al, 1996) and nitric oxide (Centonze et al, 2003) as influencing LTP and LTD.

Synaptic plasticity is not the only mode of modulating information processing in the brain. The regulation of ionic conductance within the dendrites, cell body and axon may affect intrinsic neuronal excitability especially in cortical, hippocampal and cerebellar neurons. Changes in the properties or

densities of ionic channels (voltage gated Ca^{2+}, K^+ and Na^+ channels) near the synapse could influence the spread of neuronal information (Daoudal and Debanne 2003; Debanne et al, 2003).

Non-neuronal cells may also be involved in plasticity. Astrocytes in particular help to maintain the synaptic environment and provide neurotrophic and neurotransmitter support thereby influencing neuronal signalling and synaptic density (Johansson 2004).

Neural stem cells are present in the hippocampus and subventricular zone of adult human brains (Eriksson et al, 1998; Gage 2000). These are progenitor cells with the capacity to differentiate into neurons (neurogenesis). Animal models have shown neurogenesis stimulated by trophic factors, hormones, environment and brain lesions (Johansson 2004). For example, mice exposed to an enriched environment showed 15% more granule cell neurons in the dentate gyrus of the hippocampus than littermates housed in standard cages, presumably as a result of neurogenesis (Kempermann et al, 1997).

Although the capacity for cortical plasticity is at its greatest during the early years of CNS development, it appears to persist throughout life. The behavioural effects of cortical reorganization following CNS insult may be divided into different categories which describe, for example, *adaptive* and *maladaptive* processes. Adaptive cortical reorganization implies that the redistribution of neural processing in some way contributes to the mechanisms involved in clinical recovery or helps to maintain a degree of clinical function in the presence of structural damage. At least four forms of adaptive plasticity have been suggested (Grafman and Litvan 1999): (i) *Homologous area adaptation* – implies that the damaged brain region can be compensated for by transferring the neural operations to other unaffected brain modules (usually in the homologous region of the opposite hemisphere). (ii) *Cross-modal reassignment* – occurs when cortical modules usually devoted to processing particular sensory inputs, now accept inputs from another sensory modality. (iii) *Map expansion* – is the enlargement of a functional cortical region in response to frequent stimulus exposure or following

adjacent cortical injury. (iv) *Compensatory masquerade* – is the novel allocation of a cognitive strategy to perform a task that otherwise would depend on another cognitive process which is now impaired.

However, cortical reorganization may not necessarily contribute to recovery of clinical function. It may also reflect the recruitment of unusual distributed neural networks purely as a 'stress' response to CNS injury implying that it can be *non-adaptive.*

Indeed, plastic changes, in response to injury, may also have deleterious behavioural effects resulting in functional loss rather than gain. This form of plasticity is termed *maladaptive* and is, for example, thought to account for phantom limb pain following amputation (Lotze et al, 2001).

1.4 Conclusions

It should be appreciated that several pathophysiological mechanisms determine the visual deficit seen at any one time following isolated optic neuritis. The acute phase of clinical recovery is known to be influenced by structural factors within the optic nerve that include the resolution of inflammation and recovery of conduction. This is followed by a second phase during which visual recovery may continue at a much slower rate. Pathophysiological structural processes of the optic nerve, following the acute phase, such as remyelination and axonal degeneration may influence visual outcome. However, it is possible that visual recovery may also be affected by cortical adaptive processes. The nature of the possible role for cortical adaptation will therefore need to be assessed in the context of the stage of clinical recovery and also the different structural pathophysiological processes that help to determine visual outcome.

1.5 References

The clinical profile of optic neuritis. Experience of the Optic Neuritis Treatment Trial. Optic Neuritis Study Group. *Arch Ophthalmol.* 1991. **109**(12), 1673-8.

The 5-year risk of MS after optic neuritis. Experience of the optic neuritis treatment trial. Optic Neuritis Study Group. *Neurology.* 1997. **49**(5), 1404-13.

Anmarkrud, N and Slettnes, ON. Uncomplicated retrobulbar neuritis and the development of multiple sclerosis. *Acta Ophthalmol (Copenh).* 1989. **67**(3), 306-9.

Arden, GB and Gucukoglu, AG. Grating test of contrast sensitivity in patients with retrobulbar neuritis. *Arch Ophthalmol.* 1978. **96**(9), 1626-9.

Beck, RW. The Optic Neuritis Treatment Trial. *Arch Ophthalmol.* 1988. **106**(8), 1051-3.

Beck, RW. The optic neuritis treatment trial: three-year follow-up results. *Arch Ophthalmol.* 1995. **113**(2), 136-7.

Beck, RW. Optic Neuritis. In: Miller, NR and Newman, NJ. Walsh and Hoyt's Clinical Neuro-ophthalmology. Baltimore; Williams and Wilkins, 1998: 599-647.

Beck, RW and Cleary, PA. Recovery from severe visual loss in optic neuritis. *Arch Ophthalmol.* 1993. **111**(3), 300.

Beck, RW, Cleary, PA, Anderson, MM, Jr., Keltner, JL, Shults, WT, Kaufman, DI, Buckley, EG, Corbett, JJ, Kupersmith, MJ, Miller, NR, and . A randomized, controlled trial of corticosteroids in the treatment of acute optic neuritis. The Optic Neuritis Study Group. *N.Engl.J Med.* 1992. **326**(9), 581-8.

Beck, RW, Cleary, PA, and Backlund, JC. The course of visual recovery after optic neuritis. Experience of the Optic Neuritis Treatment Trial. *Ophthalmology*. 1994. **101**(11), 1771-8.

Beck, RW, Cleary, PA, Trobe, JD, Kaufman, DI, Kupersmith, MJ, Paty, DW, and Brown, CH. The effect of corticosteroids for acute optic neuritis on the subsequent development of multiple sclerosis. The Optic Neuritis Study Group. *N.Engl.J Med.* 1993a. **329**(24), 1764-9.

Beck, RW, Kupersmith, MJ, Cleary, PA, and Katz, B. Fellow eye abnormalities in acute unilateral optic neuritis. Experience of the optic neuritis treatment trial. *Ophthalmology*. 1993b. **100**(5), 691-7.

Beck, RW, Smith, CH, Gal, RL, Xing, D, Bhatti, MT, Brodsky, MC, Buckley, EG, Chrousos, GA, Corbett, J, Eggenberger, E, Goodwin, JA, Katz, B, Kaufman, DI, Keltner, JL, Kupersmith, MJ, Miller, NR, Moke, PS, Nazarian, S, Orengo-Nania, S, Savino, PJ, Shults, WT, Trobe, JD, and Wall, M. Neurologic impairment 10 years after optic neuritis. *Arch.Neurol.* 2004. **61**(9), 1386-9.

Beck, RW and Trobe, JD. What we have learned from the Optic Neuritis Treatment Trial. *Ophthalmology*. 1995. **102**(10), 1504-8.

Berliner, MD. Acute optic neuritis in demyelinating diseases of the nervous system. *Arch Ophthalmol.* 1935. **13**, 83-98.

Birch, MK, Barbosa, S, Blumhardt, LD, and et al. Retinal venous sheathing and the blood-retinal barrier in multiple sclerosis. *Arch Ophthalmol.* 1966. **114**, 34-9.

Bo, L, Dawson, TM, Wesselingh, S, Mork, S, Choi, S, Kong, PA, Hanley, D, and Trapp, BD. Induction of nitric oxide synthase in demyelinating regions of multiple sclerosis brains. *Ann.Neurol.* 1994. **36**(5), 778-86.

Bostock, H. The pathophysiology of demyelination. In: Herndon, RM and Seil, FJ. Multiple Sclerosis: Current status of research and treatment. New York; Demos Publications, Inc., 1994: 89-112.

Bostock, H and Sears, TA. Continuous conduction in demyelinated mammalian nerve fibers. *Nature*. 1976. **263**(5580), 786-7.

Bradley, WG and Whitty, CW. Acute optic neuritis: its clinical features and their relation to prognosis for recovery of vision. *J Neurol.Neurosurg.Psychiatry*. 1967. **30**(6), 531-8.

Brex, PA, Ciccarelli, O, O'Riordan, JI, Sailer, M, Thompson, AJ, and Miller, DH. A longitudinal study of abnormalities on MRI and disability from multiple sclerosis. *N.Engl.J Med*. 2002. **346**(3), 158-64.

Buzzard, T. Atrophy of the optic nerve as a symptom of chronic disease of the central nervous system. *BMJ*. 1893. **2**, 779-84.

Bynke, H, Rosen, I, and Sandberg-Wollheim, M. Correlation of visual evoked potentials, ophthalmological and neurological findings after unilateral optic neuritis. *Acta Ophthalmol.(Copenh)*. 1980. **58**(5), 673-87.

Calverley, RK and Jones, DG. Contributions of dendritic spines and perforated synapses to synaptic plasticity. *Brain Res.Brain Res.Rev*. 1990. **15**(3), 215-49.

Carroll, FD. Retrobulbar optic neuritis: Observations on hundred cases. *Arch Ophthalmol*. 1935. **24**, 44-54.

Caruana, PA, Davies, MB, Weatherby, SJ, Williams, R, Haq, N, Foster, DH, and Hawkins, CP. Correlation of MRI lesions with visual psychophysical deficit in secondary progressive multiple sclerosis. *Brain*. 2000. **123 (Pt 7)**, 1471-80.

Centonze, D, Gubellini, P, Pisani, A, Bernardi, G, and Calabresi, P. Dopamine, acetylcholine and nitric oxide systems interact to induce corticostriatal synaptic plasticity. *Rev.Neurosci.* 2003. **14**(3), 207-16.

Chao, CC, Hu, S, and Peterson, PK. Glia, cytokines, and neurotoxicity. *Crit Rev.Neurobiol.* 1995. **9**(2-3), 189-205.

Chard, DT, Griffin, CM, Parker, GJ, Kapoor, R, Thompson, AJ, and Miller, DH. Brain atrophy in clinically early relapsing-remitting multiple sclerosis. *Brain.* 2002. **125**(Pt 2), 327-37.

Compston, A. Cellular organisation of the optic nerve and the implications for optic neuritis. *Eye.* 1992. **6 (Pt 2)**, 123-8.

Compston, DA, Batchelor, JR, Earl, CJ, and McDonald, WI. Factors influencing the risk of multiple sclerosis developing in patients with optic neuritis. *Brain.* 1978. **101**(3), 495-511.

Cox, TA, Thompson, HS, and Corbett, JJ. Relative afferent pupillary defects in optic neuritis. *Am.J Ophthalmol.* 1981. **92**(5), 685-90.

Dain, SJ, Rammohan, KW, Benes, SC, and King-Smith, PE. Chromatic, spatial, and temporal losses of sensitivity in multiple sclerosis. *Invest Ophthalmol.Vis.Sci.* 1990. **31**(3), 548-58.

Dalton, CM, Brex, PA, Jenkins, R, Fox, NC, Miszkiel, KA, Crum, WR, O'Riordan, JI, Plant, GT, Thompson, AJ, and Miller, DH. Progressive ventricular enlargement in patients with clinically isolated syndromes is associated with the early development of multiple sclerosis. *J Neurol Neurosurg.Psychiatry.* 2002. **73**(2), 141-7.

Daoudal, G and Debanne, D. Long-term plasticity of intrinsic excitability: learning rules and mechanisms. *Learn.Mem.* 2003. **10**(6), 456-65.

Davie, CA, Barker, GJ, Webb, S, Tofts, PS, Thompson, AJ, Harding, AE, McDonald, WI, and Miller, DH. Persistent functional deficit in multiple sclerosis and autosomal dominant cerebellar ataxia is associated with axon loss. *Brain.* 1995. **118 (Pt 6)**, 1583-92.

Davis, FA, Bergen, D, Schauf, C, McDonald, I, and Deutsch, W. Movement phosphenes in optic neuritis: a new clinical sign. *Neurology.* 1976. **26**(11), 1100-4.

Davis, FA and Schauf, CL. Approaches to the development of pharmacological interventions in multiple sclerosis. *Adv.Neurol.* 1981. **31**, 505-10.

de Preux, J and Mair, WG. Ultrastructure of the optic nerve in Schilder's disease, Devic's disease and disseminated sclerosis. *Acta Neuropathol.(Berl).* 1974. **30**(3), 225-42.

De Stefano, N, Matthews, PM, Fu, L, Narayanan, S, Stanley, J, Francis, GS, Antel, JP, and Arnold, DL. Axonal damage correlates with disability in patients with relapsing-remitting multiple sclerosis. Results of a longitudinal magnetic resonance spectroscopy study. *Brain.* 1998. **121 (Pt 8)**, 1469-77.

Debanne, D, Daoudal, G, Sourdet, V, and Russier, M. Brain plasticity and ion channels. *J.Physiol Paris.* 2003. **97**(4-6), 403-14.

Dugandzija-Novakovic, S and Shrager, P. Survival, development, and electrical activity of central nervous system myelinated axons exposed to tumor necrosis factor in vitro. *J Neurosci.Res.* 1995. **40**(1), 117-26.

Ebers, GC. Optic neuritis and multiple sclerosis. *Arch Neurol.* 1985. **42**(7), 702-4.

Ellis, CJ. The afferent pupillary defect in acute optic neuritis. *J Neurol.Neurosurg.Psychiatry.* 1979. **42**(11), 1008-17.

Eriksson, PS, Perfilieva, E, Bjork-Eriksson, T, Alborn, AM, Nordborg, C, Peterson, DA, and Gage, FH. Neurogenesis in the adult human hippocampus. *Nat.Med.* 1998. **4**(11), 1313-7.

Evangelou, N, Konz, D, Esiri, MM, Smith, S, Palace, J, and Matthews, PM. Size-selective neuronal changes in the anterior optic pathways suggest a differential susceptibility to injury in multiple sclerosis. *Brain.* 2001. **124**(Pt 9), 1813-20.

Felts, PA, Baker, TA, and Smith, KJ. Conduction in segmentally demyelinated mammalian central axons. *J Neurosci.* 1997. **17**(19), 7267-77.

Felts, PA, Deecinek, TJ, Ellisman, MH, Levinson, SR, Schwarz, TL, and Smith, KJ. Sodium and potassium channel immunolocalisation in demyelinated and remyelinated central axons. *Neuropathol.Appl.Neurobiol.* 1998. **24**, 154-5.

Felts, PA and Smith, KJ. Conduction properties of central nerve fibers remyelinated by Schwann cells. *Brain Res.* 1992. **574**(1-2), 178-92.

Firth, D. The case of Augustus d'Este. Cambridge; Cambridge University Press, 1948.

Flanagan, P and Markulev, C. Spatio-temporal selectivity of loss of colour and luminance contrast sensitivity with multiple sclerosis and optic neuritis. *Ophthalmic Physiol Opt.* 2005. **25**(1), 57-65.

Fleishman, JA, Beck, RW, Linares, OA, and Klein, JW. Deficits in visual function after resolution of optic neuritis. *Ophthalmology.* 1987. **94**(8), 1029-35.

Frackowiak, RS. The Cerebral Basis of Functional Recovery. In: Frackowiak, RS, Friston, KJ, Frith, CD, Dolan, RJ, and Mazziotta, JC. Human Brain Function. San Diego; Academic Press, 1997: 275-99.

Francis, DA, Compston, DA, Batchelor, JR, and McDonald, WI. A reassessment of the risk of multiple sclerosis developing in patients with optic neuritis after extended follow-up. *J.Neurol.Neurosurg.Psychiatry*. 1987. **50**(6), 758-65.

Frederiksen, JL, Larsson, HB, Ottovay, E, Stigsby, B, and Olesen, J. Acute optic neuritis with normal visual acuity. Comparison of symptoms and signs with psychophysiological, electrophysiological and magnetic resonance imaging data. *Acta Ophthalmol.(Copenh)*. 1991. **69**(3), 357-66.

Frick, A, Magee, J, and Johnston, D. LTP is accompanied by an enhanced local excitability of pyramidal neuron dendrites. *Nat.Neurosci.* 2004. **7**(2), 126-35.

Fu, L, Matthews, PM, De Stefano, N, Worsley, KJ, Narayanan, S, Francis, GS, Antel, JP, Wolfson, C, and Arnold, DL. Imaging axonal damage of normal-appearing white matter in multiple sclerosis. *Brain*. 1998. **121 (Pt 1)**, 103-13.

Gage, FH. Mammalian neural stem cells. *Science*. 2000. **287**(5457), 1433-8.

Garraghty, PE and Muja, N. NMDA receptors and plasticity in adult primate somatosensory cortex. *J.Comp Neurol.* 1996. **367**(2), 319-26.

Gartner, S. Optic neuropathy in multiple sclerosis: Optic neuritis. *Arch Ophthalmol.* 1953. **50**, 718-26.

Giovannoni, G, Heales, SJ, Silver, NC, O'Riordan, J, Miller, RF, Land, JM, Clark, JB, and Thompson, EJ. Raised serum nitrate and nitrite levels in patients with multiple sclerosis. *J Neurol Sci.* 1997. **145**(1), 77-81.

Goldstein, JE and Cogan, DG. Exercise and the optic neuropathy of multiple sclerosis. *Arch Ophthalmol.* 1964. **72**, 168-70.

Goureau, O, Amiot, F, Dautry, F, and Courtois, Y. Control of nitric oxide production by endogenous TNF-alpha in mouse retinal pigmented epithelial and Muller glial cells. *Biochem.Biophys.Res.Commun.* 1997. **240**(1), 132-5.

Grafman, J and Litvan, I. Evidence for four forms of neuroplasticity. In: Grafman, J and Christen, Y. Neuronal Plasticity: Building a bridge from the laboratory to the clinic (research and perspectives in neurosciences). Berlin Heidelberg; Springer-Verlag, 1999: 131-9.

Gu, Q. Neuromodulatory transmitter systems in the cortex and their role in cortical plasticity. *Neuroscience.* 2002. **111**(4), 815-35.

Gunn, RM. Discussion on retro-ocular neuritis. *Trans Ophthal Soc UK.* 1897. **17**, 107-217.

Guy, J, Fitzsimmons, J, Ellis, EA, and Mancuso, A. Gadolinium-DTPA-enhanced magnetic resonance imaging in experimental optic neuritis. *Ophthalmology.* 1990. **97**(5), 601-7.

Halliday, AM, McDonald, WI, and Mushin, J. Delayed visual evoked response in optic neuritis. *Lancet.* 1972. **1**(7758), 982-5.

Harris, KM. Structure, development, and plasticity of dendritic spines. *Curr.Opin.Neurobiol.* 1999. **9**(3), 343-8.

Hayreh, SS, Massanari, RM, Yamada, T, and Hayreh, SM. Experimental allergic encephalomyelitis. I. Optic nerve and central nervous system manifestations. *Invest Ophthalmol Vis.Sci.* 1981. **21**(2), 256-69.

Hely, MA, McManis, PG, Doran, TJ, Walsh, JC, and McLeod, JG. Acute optic neuritis: a prospective study of risk factors for multiple sclerosis. *J Neurol.Neurosurg.Psychiatry.* 1986. **49**(10), 1125-30.

Hess, G, Aizenman, CD, and Donoghue, JP. Conditions for the induction of long-term potentiation in layer II/III horizontal connections of the rat motor cortex. *J.Neurophysiol.* 1996. **75**(5), 1765-78.

Hickman, SJ, Brex, PA, Brierley, CM, Silver, NC, Barker, GJ, Scolding, NJ, Compston, DA, Moseley, IF, Plant, GT, and Miller, DH. Detection of optic nerve atrophy following a single episode of unilateral optic neuritis by MRI using a fat-saturated short-echo fast FLAIR sequence. *Neuroradiology.* 2001. **43**(2), 123-8.

Hickman, SJ, Dalton, CM, Miller, DH, and Plant, GT. Management of acute optic neuritis. *Lancet.* 2002. **360**(9349), 1953-62.

Hopper, CL, Matthews, CG, and Cleeland, CS. Symptom instability and thermoregulation in multiple sclerosis. *Neurology.* 1972. **22**(2), 142-8.

Hu, S, Sheng, WS, Peterson, PK, and Chao, CC. Differential regulation by cytokines of human astrocyte nitric oxide production. *Glia.* 1995. **15**(4), 491-4.

Hutchinson, WM. Acute optic neuritis and the prognosis for multiple sclerosis. *J Neurol.Neurosurg.Psychiatry.* 1976. **39**(3), 283-9.

Jacobs, KM and Donoghue, JP. Reshaping the cortical motor map by unmasking latent intracortical connections. *Science.* 1991. **251**(4996), 944-7.

Jacobson, SG, Eames, RA, and McDonald, WI. Optic nerve fibre lesions in adult cats: pattern of recovery of spatial vision. *Exp.Brain Res.* 1979. **36**(3), 491-508.

Jeffery, ND and Blakemore, WF. Locomotor deficits induced by experimental spinal cord demyelination are abolished by spontaneous remyelination. *Brain.* 1997. **120 (Pt 1)**, 27-37.

Jin, YP, Pedro-Cuesta, J, Soderstrom, M, Stawiarz, L, and Link, H. Incidence of optic neuritis in Stockholm, Sweden 1990-1995: I. Age, sex, birth and ethnic-group related patterns. *J Neurol.Sci.* 1998. **159**(1), 107-14.

Johansson, BB. Brain plasticity in health and disease. *Keio J.Med.* 2004. **53**(4), 231-46.

Jolivalt, CG, Howard, RB, Chen, LS, Mizisin, AP, and Lai, CS. A novel nitric oxide scavenger in combination with cyclosporine A ameliorates experimental autoimmune encephalomyelitis progression in mice. *J.Neuroimmunol.* 2003. **138**(1-2), 56-64.

Jones, SJ and Brusa, A. Neurophysiological evidence for long-term repair of MS lesions: implications for axon protection. *J Neurol Sci.* 2003. **206**(2), 193-8.

Jones, TA and Schallert, T. Overgrowth and pruning of dendrites in adult rats recovering from neocortical damage. *Brain Res.* 1992. **581**(1), 156-60.

Kahana, E, Alter, M, and Feldman, S. Optic neuritis in relation to multiple sclerosis. *J Neurol.* 1976. **213**(2), 87-95.

Kapoor, R, Li, YG, and Smith, KJ. Slow sodium-dependent potential oscillations contribute to ectopic firing in mammalian demyelinated axons. *Brain.* 1997. **120 (Pt 4)**, 647-52.

Kapoor, R, Miller, DH, Jones, SJ, Plant, GT, Brusa, A, Gass, A, Hawkins, CP, Page, R, Wood, NW, Compston, DA, Moseley, IF, and McDonald, WI. Effects of intravenous methylprednisolone on outcome in MRI-based prognostic subgroups in acute optic neuritis. *Neurology.* 1998. **50**(1), 230-7.

Kapoor, R, Smith, KJ, Felts, PA, and Davies, M. Internodal potassium currents can generate ectopic impulses in mammalian myelinated axons. *Brain Res.* 1993. **611**(1), 165-9.

Keltner, JL, Johnson, CA, Spurr, JO, and Beck, RW. Baseline visual field profile of optic neuritis. The experience of the optic neuritis treatment trial. Optic Neuritis Study Group. *Arch Ophthalmol.* 1993. **111**(2), 231-4.

Kempermann, G, Kuhn, HG, and Gage, FH. More hippocampal neurons in adult mice living in an enriched environment. *Nature.* 1997. **386**(6624), 493-5.

Kinnunen, E. The incidence of optic neuritis and its prognosis for multiple sclerosis. *Acta Neurol.Scand.* 1983. **68**(6), 371-7.

Kirkham, TH and Coupland, SG. Multiple regression analysis of diagnostic predictors in optic nerve disease. *Can.J Neurol.Sci.* 1981. **8**(1), 67-72.

Lewis, RA, Sumner, AJ, Brown, MJ, and Asbury, AK. Multifocal demyelinating neuropathy with persistent conduction block. *Neurology.* 1982. **32**(9), 958-64.

Lightman, S, McDonald, WI, Bird, AC, Francis, DA, Hoskins, A, Batchelor, JR, and Halliday, AM. Retinal venous sheathing in optic neuritis. Its significance for the pathogenesis of multiple sclerosis. *Brain.* 1987. **110 (Pt 2)**, 405-14.

Liu, C, Youl, B, and Moseley, I. Magnetic resonance imaging of the optic nerve in extremes of gaze. Implications for the positioning of the globe for retrobulbar anaesthesia. *Br.J Ophthalmol.* 1992. **76**(12), 728-33.

Losseff, NA, Webb, SL, O'Riordan, JI, Page, R, Wang, L, Barker, GJ, Tofts, PS, McDonald, WI, Miller, DH, and Thompson, AJ. Spinal cord atrophy and disability in multiple sclerosis. A new reproducible and sensitive MRI method with potential to monitor disease progression. *Brain.* 1996. **119 (Pt 3)**, 701-8.

Lotze, M, Flor, H, Grodd, W, Larbig, W, and Birbaumer, N. Phantom movements and pain. An fMRI study in upper limb amputees. *Brain.* 2001. **124**(Pt 11), 2268-77.

Lumsden, GE. The neuropathology of multiple sclerosis. In: Vinken, PJ and Bruyn, GW. Handbook of Clinical Neurology. Amsterdam; North Holland Publishing, 1970: 217-309.

Lynn, BH. Retrobulbar neuritis: A survey of the present condition of cases occurring over the last fifty-six years. *Trans Ophthalmol Soc UK.* 1959. **79**, 701-16.

MacDonald, BK, Cockerell, OC, Sander, JW, and Shorvon, SD. The incidence and lifetime prevalence of neurological disorders in a prospective community-based study in the UK. *Brain.* 2000. **123 (Pt 4)**, 665-76.

MacFadyen, DJ, Drance, SM, Douglas, GR, Airaksinen, PJ, Mawson, DK, and Paty, DW. The retinal nerve fiber layer, neuroretinal rim area, and visual evoked potentials in MS. *Neurology.* 1988. **38**(9), 1353-8.

Mapelli, G, De Palma, P, Sebastiani, A, Fini, M, and Franco, F. Risk of multiple sclerosis in optic neuritis. A prospective study. *Acta Neurol.(Napoli).* 1986. **8**(6), 619-25.

Mason, RJ, Snelgar, RS, Foster, DH, Heron, JR, and Jones, RE. Abnormalities of chromatic and luminance critical flicker frequency in multiple sclerosis. *Invest Ophthalmol.Vis.Sci.* 1982. **23**(2), 246-52.

Matthews, PM, Pioro, E, Narayanan, S, De Stefano, N, Fu, L, Francis, G, Antel, J, Wolfson, C, and Arnold, DL. Assessment of lesion pathology in multiple sclerosis using quantitative MRI morphometry and magnetic resonance spectroscopy. *Brain.* 1996. **119 (Pt 3)**, 715-22.

McAlpine, D and Compston, N. Some aspects of the natural history of disseminated sclerosis. *QJM.* 1952. **21**, 135-67.

McDonald, WI. Pathophysiology in multiple sclerosis. *Brain.* 1974. **97**(1), 179-96.

McDonald, WI and Barnes, D. The ocular manifestations of multiple sclerosis. 1. Abnormalities of the afferent visual system. *J.Neurol.Neurosurg.Psychiatry.* 1992. **55**(9), 747-52.

McDonald, WI and Sears, TA. Effect of demyelination on conduction in the central nervous system. *Nature.* 1969. **221**(176), 182-3.

McDonald, WI and Sears, TA. The effects of experimental demyelination on conduction in the central nervous system. *Brain.* 1970. **93**(3), 583-98.

Meyerhoff, M. The book of the ten treatises of the eye ascribed to Hunain Ibn Is-Haq. The earliest systematic textbook of ophthalmology. Cairo; Government Press, 1928.

Miller, DH. Biomarkers and surrogate outcomes in neurodegenerative disease: Lessons from multiple sclerosis. *NeuroRx.* 2004. **1**(2), 284-94.

Miller, DH, Barkhof, F, Frank, JA, Parker, GJ, and Thompson, AJ. Measurement of atrophy in multiple sclerosis: pathological basis, methodological aspects and clinical relevance. *Brain.* 2002. **125**(Pt 8), 1676-95.

Miller, DH, Newton, MR, van der Poel, JC, du Boulay, EP, Halliday, AM, Kendall, BE, Johnson, G, MacManus, DG, Moseley, IF, and McDonald, WI. Magnetic resonance imaging of the optic nerve in optic neuritis. *Neurology.* 1988. **38**(2), 175-9.

Morrissey, SP, Borruat, FX, Miller, DH, Moseley, IF, Sweeney, MG, Govan, GG, Kelly, MA, Francis, DA, Harding, AE, and McDonald, WI. Bilateral simultaneous optic neuropathy in adults: clinical, imaging, serological, and genetic studies. *J.Neurol.Neurosurg.Psychiatry*. 1995. **58**(1), 70-4.

Mullen, KT and Plant, GT. Colour and luminance vision in human optic neuritis. *Brain*. 1986. **109 (Pt 1)**, 1-13.

Nelson, D, Jeffreys, WH, and McDowell, F. Effect of induced hyperthermia on some neurological diseases. *Arch Neurol Psychiat*. 1958. **79**, 31-9.

Nettleship, E. On cases of retro-ocular neuritis. *Trans Ophthal Soc UK*. 1884. **4**, 186-226.

Nilsson, P, Larsson, EM, Maly-Sundgren, P, Perfekt, R, and Sandberg-Wollheim, M. Predicting the Outcome of Optic Neuritis Evaluation of risk factors after 30 years of follow-up. *J.Neurol*. 2005. **252**(4), 396-402.

Page, NG, Bolger, JP, and Sanders, MD. Auditory evoked phosphenes in optic nerve disease I. *J Neurol.Neurosurg.Psychiatry*. 1982. **45**(1), 7-12.

Paintal, AS. The influence of diameter of medullated nerve fibres of cats on the rising and falling phases of the spike and its recovery. *J Physiol*. 1966. **184**(4), 791-811.

Parinaud, H. Troubles oculaires de la sclerose en plaques. *J Sante*. 1884. **3**, 3-5.

Perkin, GD and Rose, FC. Optic Neuritis and its differential diagnosis. Oxford; Oxford University Press, 1979.

Perry, VH and Anthony, DC. Axon damage and repair in multiple sclerosis. *Philos.Trans R.Soc Lond B Biol.Sci.* 1999. **354**(1390), 1641-7.

Petzold, A, Rejdak, K, and Plant, GT. Axonal degeneration and inflammation in acute optic neuritis. *J.Neurol.Neurosurg.Psychiatry.* 2004. **75**(8), 1178-80.

Phillips, ML, Foster, DH, Honan, WP, Edgar, GK, and Heron, JR. Optic neuritis. Differential losses of luminance and chromatic function near a scotoma. *Brain.* 1994. **117 (Pt 4)**, 767-73.

Porciatti, V and Sartucci, F. Retinal and cortical evoked responses to chromatic contrast stimuli. Specific losses in both eyes of patients with multiple sclerosis and unilateral optic neuritis. *Brain.* 1996. **119 (Pt 3)**, 723-40.

Prineas, J. Pathology of the early lesion in multiple sclerosis. *Hum.Pathol.* 1975. **6**(5), 531-54.

Prineas, JW, Barnard, RO, Kwon, EE, Sharer, LR, and Cho, ES. Multiple sclerosis: remyelination of nascent lesions. *Ann.Neurol.* 1993. **33**(2), 137-51.

Prineas, JW and Connell, F. Remyelination in multiple sclerosis. *Ann.Neurol.* 1979. **5**(1), 22-31.

Rao, NA, Tso, MO, and Zimmerman, EL. Experimental allergic optic neuritis in guinea pigs: preliminary report. *Invest Ophthalmol.Vis.Sci.* 1977. **16**(4), 338-42.

Redford, EJ, Kapoor, R, and Smith, KJ. Nitric oxide donors reversibly block axonal conduction: demyelinated axons are especially susceptible. *Brain.* 1997. **120 (Pt 12)**, 2149-57.

Regan, D, Kothe, AC, and Sharpe, JA. Recognition of motion-defined shapes in patients with multiple sclerosis and optic neuritis. *Brain.* 1991. **114 (Pt 3)**, 1129-55.

Ridet, JL, Malhotra, SK, Privat, A, and Gage, FH. Reactive astrocytes: cellular and molecular cues to biological function. *Trends Neurosci.* 1997. **20**(12), 570-7.

Riikonen, R, Ketonen, L, and Sipponen, J. Magnetic resonance imaging, evoked responses and cerebrospinal fluid findings in a follow-up study of children with optic neuritis. *Acta Neurol.Scand.* 1988. **77**(1), 44-9.

Rizzo, JF, III and Lessell, S. Risk of developing multiple sclerosis after uncomplicated optic neuritis: a long-term prospective study. *Neurology.* 1988. **38**(2), 185-90.

Rizzo, MA, Kocsis, JD, and Waxman, SG. Mechanisms of paresthesiae, dysesthesiae, and hyperesthesiae: role of Na+ channel heterogeneity. *Eur.Neurol.* 1996. **36**(1), 3-12.

Rodriguez, M, Siva, A, Cross, SA, O'Brien, PC, and Kurland, LT. Optic neuritis: a population-based study in Olmsted County, Minnesota. *Neurology.* 1995. **45**(2), 244-50.

Rolak, LA, Beck, RW, Paty, DW, Tourtellotte, WW, Whitaker, JN, and Rudick, RA. Cerebrospinal fluid in acute optic neuritis: experience of the optic neuritis treatment trial. *Neurology.* 1996. **46**(2), 368-72.

Rose, FC. The aetiology of optic neuritis. *Monogr Hum.Genet.* 1972. **6**, 196.

Russell, MH, Murray, IJ, Metcalfe, RA, and Kulikowski, JJ. The visual defect in multiple sclerosis and optic neuritis. A combined psychophysical and electrophysiological investigation. *Brain.* 1991. **114 (Pt 6)**, 2419-35.

Sandberg-Wollheim, M. Optic neuritis: studies on the cerebrospinal fluid in relation to clinical course in 61 patients. *Acta Neurol.Scand.* 1975. **52**(3), 167-78.

Sandberg-Wollheim, M, Bynke, H, Cronqvist, S, Holtas, S, Platz, P, and Ryder, LP. A long-term prospective study of optic neuritis: evaluation of risk factors. *Ann.Neurol.* 1990. **27**(4), 386-93.

Shahrokhi, F, Chiappa, KH, and Young, RR. Pattern shift visual evoked responses. Two hundred patients with optic neuritis and/or multiple sclerosis. *Arch Neurol.* 1978. **35**(2), 65-71.

Shrager, P, Custer, AW, Kazarinova, K, Rasband, MN, and Mattson, D. Nerve conduction block by nitric oxide that is mediated by the axonal environment. *J Neurophysiol.* 1998. **79**(2), 529-36.

Silveira, LC and Perry, VH. The topography of magnocellular projecting ganglion cells (M-ganglion cells) in the primate retina. *Neuroscience.* 1991. **40**(1), 217-37.

Sims, TJ, Gilmore, SA, and Waxman, SG. Radial glia give rise to perinodal processes. *Brain Res.* 1991. **549**(1), 25-35.

Smith, KJ. Conduction properties of central demyelinated and remyelinated axons, and their relation to symptom production in demyelinating disorders. *Eye.* 1994. **8 (Pt 2)**, 224-37.

Smith, KJ, Blakemore, WF, and McDonald, WI. The restoration of conduction by central remyelination. *Brain.* 1981. **104**(2), 383-404.

Smith, KJ, Kapoor, R, Hall, SM, and Davies, M. Electrically active axons degenerate when exposed to nitric oxide. *Ann.Neurol.* 2001. **49**(4), 470-6.

Smith, KJ and McDonald, WI. Spontaneous and mechanically evoked activity due to central demyelinating lesion. *Nature.* 1980. **286**(5769), 154-5.

Smith, KJ and McDonald, WI. Spontaneous and evoked electrical discharges from a central demyelinating lesion. *J.Neurol.Sci.* 1982. **55**(1), 39-47.

Smith, KJ and McDonald, WI. The pathophysiology of multiple sclerosis: the mechanisms underlying the production of symptoms and the natural history of the disease. *Philos.Trans.R.Soc.Lond B Biol.Sci.* 1999. **354**(1390), 1649-73.

Sokol, S. Visually evoked potentials: theory, techniques and clinical applications. *Surv.Ophthalmol.* 1976. **21**(1), 18-44.

Steel, DH and Waldock, A. Measurement of the retinal nerve fibre layer with scanning laser polarimetry in patients with previous demyelinating optic neuritis. *J Neurol.Neurosurg.Psychiatry.* 1998. **64**(4), 505-9.

Steinmetz, R and Kearns, TP. H-R-R pseudoisochromatic plates: As a diagnostic aid in retrobulbar neuritis of multiple sclerosis. *Am J Ophthalmol.* 1956. **41**, 833-7.

Stendahl-Brodin, L and Link, H. Optic neuritis: oligoclonal bands increase the risk of multiple sclerosis. *Acta Neurol.Scand.* 1983. **67**(5), 301-4.

Swartz, NG, Beck, RW, Savino, PJ, Sergott, RC, Bosley, TM, Lam, BL, Drucker, M, and Katz, B. Pain in anterior ischemic optic neuropathy. *J.Neuroophthalmol.* 1995. **15**(1), 9-10.

Tasaki, I. Nervous Transmission. Springfield; Charles C. Thomas, 1953.

Tononi, G, McIntosh, AR, Russell, DP, and Edelman, GM. Functional clustering: identifying strongly interactive brain regions in neuroimaging data. *Neuroimage.* 1998. **7**(2), 133-49.

Trachtenberg, JT, Chen, BE, Knott, GW, Feng, G, Sanes, JR, Welker, E, and Svoboda, K. Long-term in vivo imaging of experience-dependent synaptic plasticity in adult cortex. *Nature*. 2002. **420**(6917), 788-94.

Trapp, BD, Peterson, J, Ransohoff, RM, Rudick, R, Mork, S, and Bo, L. Axonal transection in the lesions of multiple sclerosis [see comments]. *N Engl J Med*. 1998. **338**(5), 278-85.

Trip, SA, Schlottmann, PG, Jones, SJ, Altmann, DR, Garway-Heath, DF, Thompson, AJ, Plant, GT, and Miller, DH. Retinal nerve fiber layer axonal loss and visual dysfunction in optic neuritis. *Ann.Neurol.* 2005. **58**(3), 383-91.

Uhthoff, W. Untersuchungen uber die bei der multiplen herdsklerose vorkommenden augenstorungen. *Arch Psychiat Nervenkrankheiten*. 1890. **21**, 55-116.

Vleugels, L, van Nunen, A, Lafosse, C, Ketelaer, P, and Vandenbussche, E. Temporal and spatial resolution in foveal vision of multiple sclerosis patients. *Vision Res*. 1998. **38**(19), 2987-97.

von Graefe, A. Ueber complication von sehnervenentzundung mit gehirnkrankheiten. *Archiv Ophthalmologie*. 1860. **1**, 58-71.

Wakakura, M, Minei-Higa, R, Oono, S, Matsui, Y, Tabuchi, A, Kani, K, Shikishima, K, Kawai, K, Nakao, Y, Tazawa, Y, Kiyosawa, M, Abe, H, Ohba, N, Yago, K, Maeda, S, Sugita, M, and Ishikawa, S. Baseline features of idiopathic optic neuritis as determined by a multicenter treatment trial in Japan. Optic Neuritis Treatment Trial Multicenter Cooperative Research Group (ONMRG). *Jpn.J Ophthalmol.* 1999. **43**(2), 127-32.

Wall, M. Loss of P retinal ganglion cell function in resolved optic neuritis. *Neurology*. 1990. **40**(4), 649-53.

Waxman, SG. Clinicopathological correlations in multiple sclerosis and related diseases. *Adv.Neurol.* 1981. **31**, 169-82.

Waxman, SG. Acquired channelopathies in nerve injury and MS. *Neurology.* 2001. **56**(12), 1621-7.

Waxman, SG and Brill, MH. Conduction through demyelinated plaques in multiple sclerosis: computer simulations of facilitation by short internodes. *J Neurol Neurosurg.Psychiatry.* 1978. **41**(5), 408-16.

Waxman, SG and Ritchie, JM. Molecular dissection of the myelinated axon. *Ann.Neurol.* 1993. **33**(2), 121-36.

Werring, DJ, Bullmore, ET, Toosy, AT, Miller, DH, Barker, GJ, MacManus, DG, Brammer, MJ, Giampietro, VP, Brusa, A, Brex, PA, Moseley, IF, Plant, GT, McDonald, WI, and Thompson, AJ. Recovery from optic neuritis is associated with a change in the distribution of cerebral response to visual stimulation: a functional magnetic resonance imaging study. *J Neurol.Neurosurg.Psychiatry.* 2000. **68**(4), 441-9.

Wybar, KC. The ocular manifestations of disseminated sclerosis. *Proc Roy Soc Med.* 1952. **45**, 315-9.

Youl, BD, Turano, G, Miller, DH, Towell, AD, MacManus, DG, Moore, SG, Jones, SJ, Barrett, G, Kendall, BE, and Moseley, IF. The pathophysiology of acute optic neuritis. An association of gadolinium leakage with clinical and electrophysiological deficits. *Brain.* 1991. **114 (Pt 6)**, 2437-50.

Zhu, B, Moore, GR, Zwimpfer, TJ, Kastrukoff, LF, Dyer, JK, Steeves, JD, Paty, DW, and Cynader, MS. Axonal cytoskeleton changes in experimental optic neuritis. *Brain Res.* 1999. **824**(2), 204-17.

CHAPTER 2

FUNCTIONAL MRI AND DIFFUSION TENSOR IMAGING

2.1 MRI basic principles

2.1.1 Nuclear magnetic resonance

MRI is based on the principle of nuclear magnetic resonance (NMR) which measures the magnetic properties of a substance in the presence of a strong magnetic field. It is based on a fundamental property of nature called 'spin' possessed by electrons, protons and neutrons. Atomic nuclei with unpaired nucleons (protons or neutrons) have net spin and can classically be considered as small magnets represented by vector notation as *magnetic dipoles moments*. This latter property is possessed by several elements but the nucleus of the hydrogen isotope (the proton), ^{1}H, is the most relevant for MRI because of its high abundance in biological tissues. In the presence of a static magnetic field, B_0, proton magnetic dipoles line up in one of two energy configurations - parallel to the field (lower energy) and antiparallel (higher energy). There is a slight fractional excess of protons with the lower energy configuration (about 1 in 100 000 for 1.5T) which imposes a bulk magnetic moment, M_0, on the sample. The proton magnetic dipoles also precess around the field's direction at a frequency given by the Larmor relationship:

$$f = \frac{\gamma B_0}{2\pi} \qquad (2.1)$$

Where f is the precession frequency (Hz), γ is a constant called the gyromagnetic ratio that is specific for the isotope and B_0 is the magnetic field strength (T). f is also the resonance frequency which determines the specific energy, E, for a photon that can be absorbed by a proton to change its spin from a lower to a higher energy state.

$$E = hf \qquad (2.2)$$

Where h is Planck's constant (6.626×10^{-34} Js). The application of an oscillating magnetic field (B_1) at the resonant frequency (induced by a radiofrequency (RF) pulse perpendicular to B_0) will produce energy transitions between spin states from low to high energy levels with two consequential effects:

1) The protons will start to precess in phase (achieving *phase coherence*), creating a bulk rotating transverse magnetization moment (M_{xy}) perpendicular to B_0.
2) The longitudinal magnetization moment (M_z) is reduced as more protons achieve the antiparallel (higher energy) configuration.

These effects result in a spiral motion (called *nutation*) of the net magnetization vector from the z axis (aligned with B_0) towards the orthogonal xy plane. The degree to which this occurs is termed the *flip angle* (and is proportional to RF pulse amplitude x RF pulse duration). For a 90^0 RF pulse, the magnetization vector M_0 is flipped completely into the xy plane, resulting in the complete loss of longitudinal magnetization (M_z). The magnitude of M_{xy} then equals M_0. A 90^0 RF effectively equalizes the number of protons with parallel and antiparallel spins. A 180^0 RF pulse inverts the longitudinal magnetization vector to $-M_z$.

2.1.2 Relaxation processes

When the RF pulse is turned off, the spins continue to precess in the transverse plane. The resulting oscillating transverse electromagnetic field can induce a receiver RF coil voltage and forms the basis for MRI signal acquisition. This phenomenon was originally described in 1946 (Bloch et al, 1946; Purcell et al, 1946). The protons now experience the longitudinal magnetic field only and gradually return to equilibrium, emitting energy at the same RF frequency. The spins also exchange energy with each other, losing phase coherence. These two processes are termed relaxation; the former is known as T_1 (longitudinal) relaxation, the latter as T_2 (transverse) relaxation.

2.1.2.1 T1 (longitudinal or spin-lattice) Relaxation

T1 relaxation refers to the reestablishment of M_z through the release of energy from the protons to the surrounding lattice as their spins regain equilibrium along B_0. The rate of longitudinal relaxation depends upon the time constant, T1, and is governed by the following equation following a 90^0 RF pulse (see also figure 2.1):

$$M_Z(t) = M_0(1 - e^{-t/T_1}) \qquad (2.3)$$

T_1 is governed by the intrinsic properties of the lattice which can vary between different tissue types. Differences in T_1 constants between tissue types can provide contrast in T_1 weighted imaging.

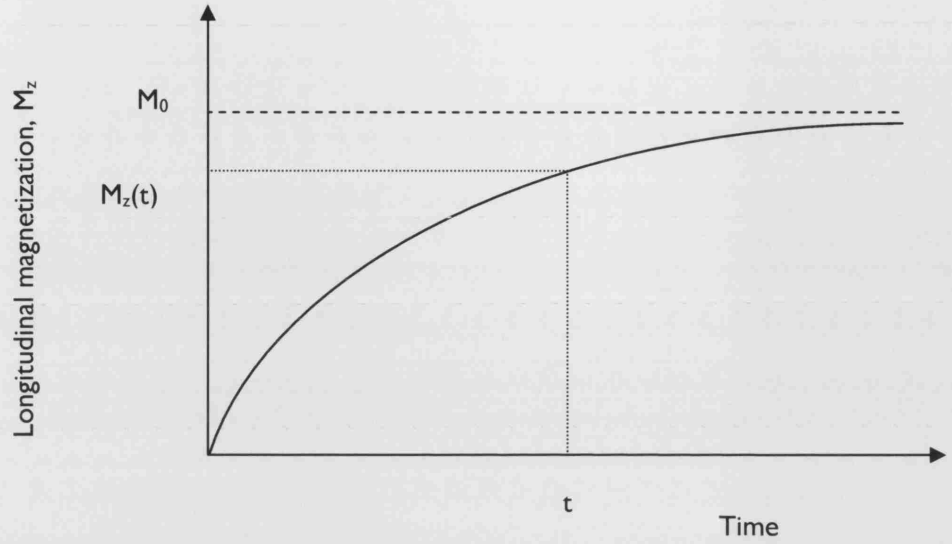

Figure 2.1. T1 relaxation.

2.1.2.2 T_2 and T_2^* Relaxation

After the 90^0 RF pulse, the spins undergo *phase decoherence* which results in the decay of M_{xy} (transverse magnetization moment). This decay is determined by two phenomena:

1) **Spin-spin interactions** – Quantum effects induce random field variations between protons and, as a result of mutual spin-spin interactions, will alter the frequency of the protons' precession, resulting in loss of phase coherence and transverse magnetization. The spin-spin interactions are inherent to every tissue and are governed by the time constant, T_2, which dictates the rate of transverse magnetization decay (figure 2.2):

$$M_{xy}(t) = M_0 e^{-t/T_2} \qquad (2.4)$$

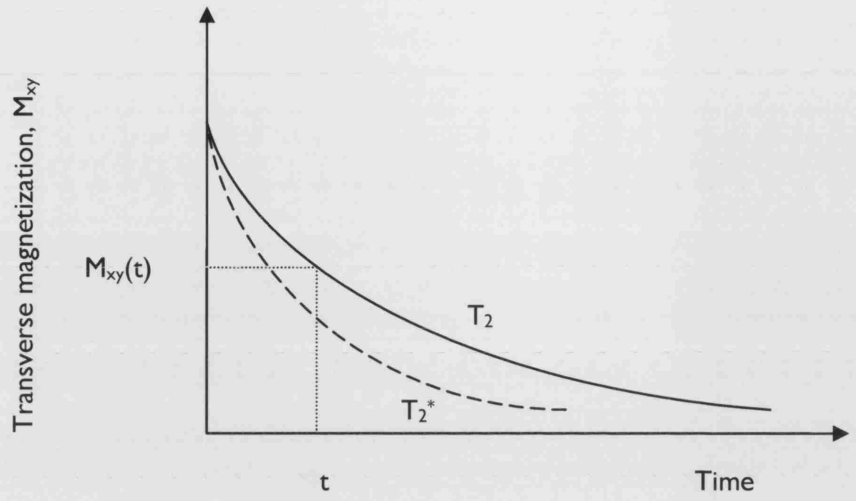

Figure 2.2. T2 relaxation

2) **External magnetic field inhomogeneities** – In reality there is an additional effect that contributes to phase decoherence. T_2 actually refers to spin-spin relaxation within a perfectly homogeneous magnetic field, however this is impossible in practice. Local magnetic field inhomogeneities unavoidably cause additional dephasing. This results in a more rapid loss of transverse magnetization which is governed by the time constant. T_2^* (figure 2.2). The relationship between T_2 and T_2^* is as follows:

$$1/T_{2^*} = 1/T_2 + 1/T_{inh} \qquad (2.5)$$

Where $1/T_{inh}$ is the relaxation rate due to the magnetic field inhomogeneities.

The actual signal measured immediately after the 90^0 RF pulse is switched off, results from T_2^* effects and takes the form of a decaying sinusoidal waveform (figure 2.3). It is called the free induction decay (FID) and is mathematically described as:

$$M_{xy}(t) = M_0 e^{-t/T_{2^*}} (\cos 2\pi f_0 t) \qquad (2.6)$$

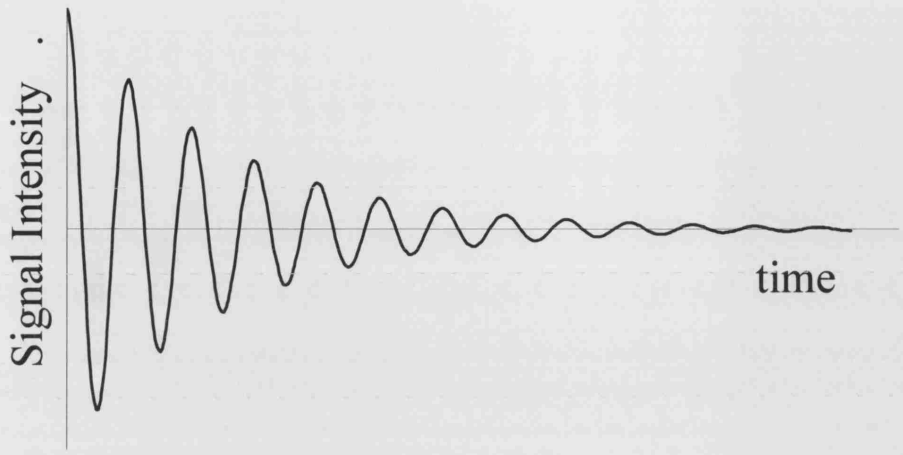

Figure 2.3. Free Induction Decay.

2.1.3 Image contrast

During an MRI image acquisition 90^0 RF pulses are repeated many times. The time interval between two successive 90^0 RF pulses is the *TR* (*repetition time*). In a "gradient echo" (GE) scan, the MR signal is collected a short period of time after the RF pulse at the *TE* (*echo time*). The resultant signal intensity depends upon the TR, TE and the number of proton spins within the tissue sample:

$$S \propto \rho(1-e^{-TR/T_1})e^{-TE/T_2^*} \qquad (2.7a)$$

where ρ is the proton spin density. In a "spin echo" (SE) sequence an additional 180^o pulse is used to remove the effects of local field inhomogeneities and the signal becomes:

$$S \propto \rho(1-e^{-TR/T_1})e^{-TE/T_2} \qquad (2.7b)$$

Contrast between different tissue types is generated by using the TR and TE to exploit tissue differences in T_1, T_2 and T_2^*.

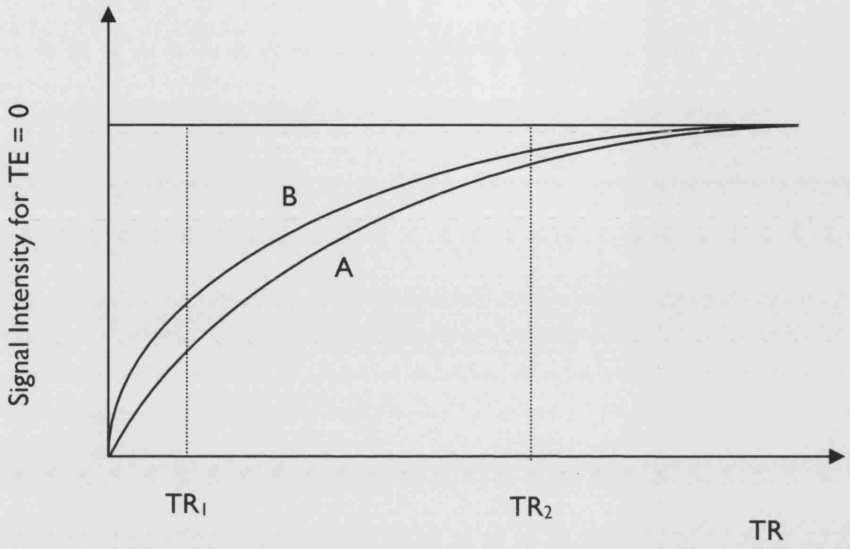

Figure 2.4. T_1 contrast.

Figure 2.4 above provides an example for two tissue types A and B where the T_1 of B is smaller than the T_1 of A i.e. the longitudinal relaxation is faster for B than for A. The signal contrast between tissues A and B (illustrated by the difference between curves for A and B) then is smaller for longer TRs (cf. TR_2 with TR_1). Therefore a relatively short TR (as long as it is not so short as to lead to near zero signal for one or both tissues) will enhance the T_1 contrast. A similar principle can be applied for T_2 (SE) and T_2^* (GE) tissue contrast:

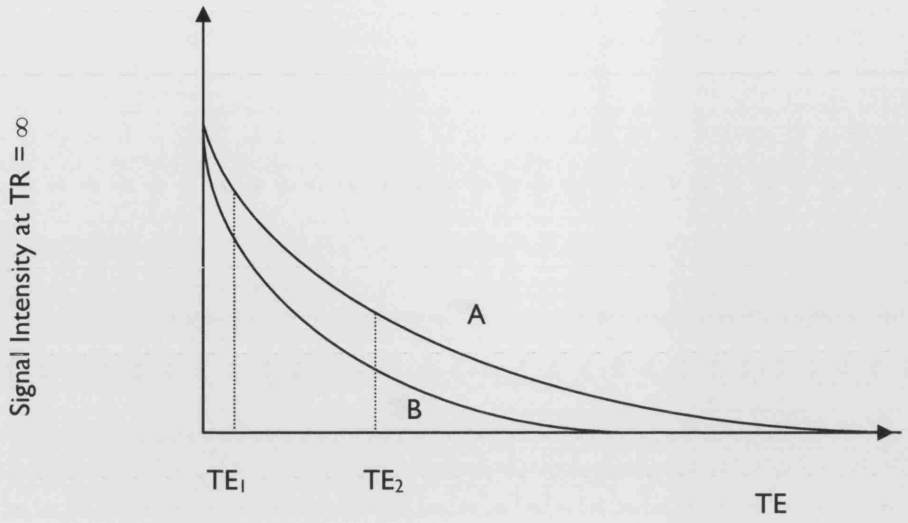

Figure 2.5. T_2 or T_2^* contrast.

In figure 2.5 tissue A has a longer T_2 (or T_2^*) constant than tissue B. If the TE is very short (TE_1) then the signal contrast will be small. Thus a short TE reduces the T_2 (or T_2^*) contrast and a longer TE will increase the contrast (as long as it is not too so long as to lead to near zero signal for one or both tissues).

In conclusion, a short TR with a short TE will enhance T_1 contrast and a long TR with a long TE will enhance T_2 or T_2^* contrast (for SE or GE sequences, respectively). A long TR with a short TE will reduce both T_1 and T_2 (and/or T_2^*) effects resulting in a signal that depends only upon the proton spin density i.e. the image becomes *proton density weighted*. The T_1 and T_2 properties of protons tend to vary together. In biological tissues, T1 is usually of the order 300 to 2000ms and T2 30 to 150ms. Mobile protons tend to take longer to relax, so that cerebrospinal fluid (CSF) has a long T_1 and a long T_2. More structured tissues contain protons that are less mobile and readily exchange energy with their surroundings, so that protein, lipid and other macromolecules have a short T_1 and a short T_2.

2.1.4 Imaging principles

2.1.4.1 Spatial encoding

The localization of the MR signal is achieved by spatially encoding it with frequency information related to magnetic field gradients applied in the z (slice selective), y (frequency encoding) and x (phase encoding) axes (Lauterbur 1973).

The slice selective gradient (G_z) imposes a linearly varying magnetic field in the z direction. This aligns the proton spins whose precession frequencies will also vary in accordance with the Larmor relationship depending upon where they are located within G_z. An RF pulse with a certain range of frequencies (*bandwidth*) will then excite the corresponding bandwidth of proton spins in a slice of a certain thickness. The slice thickness can be decreased by reducing the RF pulse bandwidth or increasing the slice selective gradient.

The frequency encoding gradient (G_x) is applied after the slice selective gradient in the x axis direction, resulting in different precession frequencies along this axis. It is applied during the time the echo is received and the MR signal digitally sampled. Each of the resulting signals of different frequencies will contribute to the net MR signal emitted by the slice. The different frequencies from protons at different positions along the x axis are derived using *Fourier transform* theory. This converts the signal from the *time domain* to the *frequency domain* by representing complex waveforms in terms of its component frequencies.

The phase encoding gradient (G_y) is applied briefly between the application of G_z and G_x. This results in a different precession frequency along the y axis. When this gradient is switched off the protons will precess again at the same frequency, but have now undergone a phase shift, allowing their y axis positions to be differentiated (those protons that experienced the highest magnetic field will have

precessed through a larger phase angle). If this phase encoding process is repeated (typically 128 or 256 times) then the phase differences can be extracted using a Fourier transform.

After phase and frequency encoding, the protons in each spatial position have a distinct frequency and phase, which uniquely encode for the x and y coordinates of that spatial position. This information is extracted using a 2 dimensional digital Fourier transform. In conventional imaging G_x (or the readout gradient) is applied during signal acquisition, whilst G_y (phase encoding gradient) is applied in increments between the 90^0 RF pulse and each echo. Each TR interval contains one phase encoding step and is repeated N_y (number of phase encodes) until the required spatial information in the x and y axes of the image slice is collected. The whole process may be repeated to increase Signal to Noise (SNR) (ie signal averaging); the number of averages is often referred to as the 'Number of Exctitations' (NEX).

2.1.4.2 K space

For an image slice with N_xN_y pixels, N_x points are sampled during each readout gradient (G_x) and this process is repeated N_y times for each the phase encoding gradient (G_y) increment. The acquired N_xN_y data matrix consists of data samples acquired at different points in k-space, ie after they have experienced different combinations of dephasing by the gradients applied in the x and y directions. A 2 dimensional Fourier transform of k space will generate the desired image. The centre of k space determines the SNR of the image. This is because the middle column in k space corresponds to the centre of each individual echo (at maximal rephasing) and the middle row is obtained with no phase encoding gradient (and therefore no additional dephasing). Sampling more points farther away from the centre encodes the image's details and increases image resolution.

2.1.5 Echo Planar Imaging (EPI)

In conventional MRI for each RF excitation, one phase encoded line of k space is recorded every TR. The whole filling of k space therefore requires N_y excitations. EPI (Mansfield 1977) is an MRI acquisition technique that permits substantially faster data making it particularly suitable for fMRI and DTI. In single shot EPI, an entire image is acquired following a single excitation pulse by collecting the complete k space dataset within the short time that the FID is detectable i.e. a whole image volume can be acquired every TR. Refocusing in EPI is usually achieved by multiple gradient reversals in the phase (G_y) and frequency (G_x) encoding directions. If this is done without a refocusing pulse then the sequence is called *gradient recalled echo (GRE)* EPI, and gives T_2^* contrast. If a refocusing pulse is used the resulting *spin echo (SE)* EPI gives T_2 contrast. An oscillating G_x gradient generates a train of echoes which are simultaneously sampled. Rapidly changing G_y gradients allow different k space lines to be selected. K space can be sampled in many ways. A common scheme is a zigzag pattern as shown in figure 2.6.

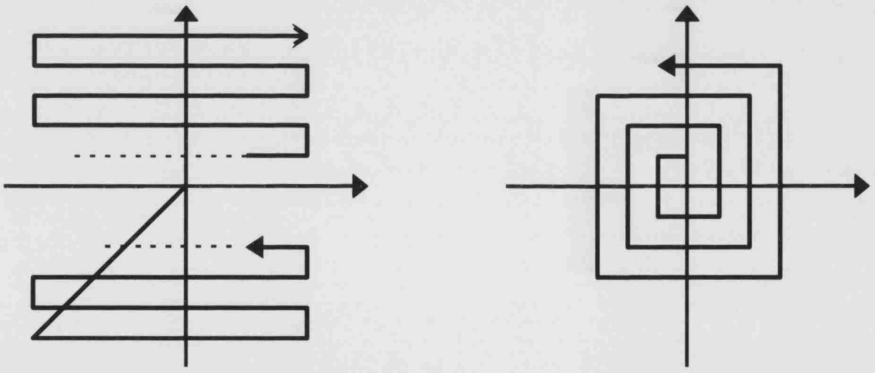

Figure 2.6. Two types of k space trajectories for EPI. A) Blipped EPI in which the TE is defined as the time from the RF pulse to the centre of k space. B) Spiral acquisition.

The TE in EPI is in the order of tens of milliseconds and the TR usually a few seconds although it is possible to reduce the TR to the order of 100 ms with appropriate hardware and implementation. Image resolution is typically around 64 x 64 or 128 x 128 with a whole volume scan in 2 to 4 seconds.

One of the limiting factors with EPI is the generation of eddy currents in neural tissue caused by the rapid switching of gradients, which can lead to peripheral nerve stimulation. Other disadvantages of EPI include 'ghost' artefacts along the phase axis as a result of phase errors from the multiple positive and negative passes through k space which can be induced by magnetic field inhomogeneities or eddy currents. These Nyquist ghosts (N/2 ghosts) can be minimized by comparing a non-phase encoded data set (a reference data set) acquired previously to the EPI data set (Bruder et al, 1992). The required corrections can alternatively be estimated from the image data set itself (Buonocore and Gao 1997). Diamagnetic susceptibility artefacts may also occur at tissue interfaces especially between air and bone and manifest as signal dropout or geometric distortion.

2.1.6 Image Optimization

Image contrast depends upon scanning parameters such as TR, TE and flip angle mentioned previously. Image quality is determined by the signal to noise ratio (SNR) which is itself influenced by the parameters chosen for image contrast, coverage, resolution, NEX and bandwidth. For a field of view with dimensions FOV_x x FOV_y and a slice thickness Δz the SNR is given by:

$$SNR = (FOV_x / N_x)(FOV_y)\Delta z \sqrt{\frac{NEX}{N_y BW}} \qquad (2.8)$$

where NEX equals the number of excitations and BW is the receiving bandwidth. Reducing the bandwidth increases SNR at the price of increased sampling time. The SNR is also influenced by the strength of B_0 and increases in an approximately linear fashion with increasing field strength. The image resolution is determined by the volume covered divided by the number of image points sampled (i.e. voxel volume). The latter equals N_x x N_y x Δz. If N_y is increased, for example, while FOV_y remains the same, then the voxel volume is reduced at the expense of SNR. Increasing the

voxel volume will increase SNR at the price of partial volume effect. The acquisition time (for a simple, non-EPI scan) equals TR x N_y x NEX. Hence, if NEX is increased then the SNR goes up at the expense of a longer acquisition time. Increasing the TR has the following effects: increased SNR (according to the T_1 relaxation curve), increased coverage (more slices), reduced T_1 weighting, increased scan time. Increasing the TE has the following effects: increased T_2 weighting, increased dephasing (in a GE scan) and reduced SNR (according to the T_2 relaxation curve), decreased number of slices possible in a given TR.

2.2 Functional MRI (FMRI)

FMRI can non-invasively localize and measure regional brain activity in response to experimental manipulation. It does this by utilizing knowledge about the well established interrelationships between neuronal activation, energy consumption and local cerebral haemodynamics. The brain itself, although only 2% of the total body mass, consumes around 20% of the oxygen entering the body (Siesjo 1978). About 90% of the brain's energy utilization occurs via the aerobic metabolism of glucose. This accounts for its dependence upon oxygen and also means that brain activity is proportional to its oxygen consumption rate ($CMRO_2$) (Logothetis 2002). Local oxygen and glucose delivery are controlled by elaborate mechanisms that orchestrate cerebral blood flow (CBF) and volume (CBV), which, necessarily, are coupled to neural activity.

2.2.1 Historical perspective

The first report of neural activity-haemodynamic coupling was published in 1881 when Angelo Mosso noticed an increase in local pulsations when a patient, with a permanent skull defect over the frontal lobes, was asked to perform arithmetic (Mosso 1881). This pulsation increase was presumed to be due to an increase in CBF. Experimental evidence in animal models was provided by Roy and Sherrington who concluded that local brain activity released metabolic products with vasomotor effects that altered the regional vascular supply (Roy and Sherrington 1890). Years later the

neurosurgeon, John Fulton, described audible increases in local blood flow associated with visual stimulation in a patient with a bony defect over the occipital lobe (Fulton 1928).

The introduction of 2-deoxyglucose autoradiographic techniques applied in animals quantitatively established a clear relationship between glucose consumption and local cerebral activity (Sokoloff 1977). The development of PET (positron emission tomography) followed and allowed the spatial mapping of injected radionuclide markers within the brain (Phelps et al, 1975; Ter Pogossian et al, 1975). PET demonstrated the regional effects of cerebral activity on CBF, CBV and blood oxygenation (Fox et al, 1986; Fox et al, 1988; Fox and Raichle 1986). Other methods of monitoring brain activity either directly or indirectly developed over the years include SPECT (single photon emission computed tomography), optical imaging, electroencephalography and magnetoencephalography. In recent years MRI has been adapted to measure blood oxygenation changes that accompany neuronal activity changes (described as the *BOLD* or blood oxygenation level dependent phenomenon). This introduced fMRI which provided the opportunity to investigate brain function with high temporal and spatial resolution.

2.2.2 The BOLD effect

In the present model of the haemodynamic response, an increase in neural activity results in an initial increase in oxygen consumption due to increased metabolic demand. This increases the deoxyhaemoglobin and decreases the oxyhaemoglobin concentrations within the local vasculature (Vanzetta and Grinvald 1999). The increased neuronal activity also triggers, after a delay of a few seconds, a large increase in local CBF. The increased CBF is associated with an approximately proportional increase in glucose consumption, but there is an oversupply of oxyhaemoglobin delivery relative to its extraction by the activated neural tissue (Fox and Raichle 1986). The increased CBF also causes vasodilation of the local venous system, because of its balloon-like elasticity, resulting in an increase in blood volume (CBV) (Buxton et al, 1998). Our present understanding therefore implies that the BOLD effect depends upon dynamic interactions between neural activity with its

associated oxygen utilization (characterized by $CMRO_2$) and local haemodynamics (CBF and CBV) resulting in an imbalance between oxygen delivery and extraction. This is explained below in greater detail.

2.2.2.1 Oxygen Limitation Model

Fick's principle was first described by the German physiologist A.E. Fick in 1870. He used the conservation of mass to state that the oxygen consumption of the body (derivable from inspired and expired gases) is equivalent to the rate of blood flow through the lungs multiplied by the difference in oxygen concentration between arterial and venous blood. When applied to the brain, at steady state, it can be written thus:

$$CMRO_2 = CBF \times 4[Hb^{TOT}] \times (Y_a - Y_v) \qquad (2.9)$$

Where $[Hb^{TOT}]$ is the total haemoglobin concentration, with each Hb molecule capable of binding four oxygen molecules; Y_a and Y_v are the arterial and venous oxygen saturations (usually ≈ 1 and ≈ 0.6 respectively). $(Y_a - Y_v)$ is approximately equivalent to the oxygen extraction fraction (OEF). Changes in $CMRO_2$, corresponding to changes in brain activation, can be described by considering Y_a and Hb^{TOT} to be fixed and differentiating this equation to:

$$\frac{\Delta CMRO_2}{CMRO_2} = \frac{\Delta CBF}{CBF} + \frac{\Delta OEF}{OEF} \qquad (2.10)$$

This relationship can be used along with the oxygen limitation model to explain the disproportionate relationship between CBF changes and $CMRO_2$ first reported in the 1980s (Fox and Raichle 1986). These observations noted that large increases in CBF and glucose consumption rate were accompanied by only modest increases in $CMRO_2$ during brain activation. This, it was felt, provided

evidence for significant anaerobic metabolism of glucose (glycolysis) by brain tissue during activation i.e. an uncoupling of flow and oxidative metabolism (Fox et al, 1988).

More recently, alternative explanations have been proposed for the CBF-$CMRO_2$ mismatch whilst maintaining a tight coupling between the two. These *oxygen limitation models* explain the mismatch as a necessary consequence of how oxygen is delivered to the tissues. A disproportionately large increase in CBF is necessary to support a required increase in $CMRO_2$ because oxygen extraction from blood, occurring by passive diffusion, is less efficient at high flow rates (Buxton and Frank 1997; Gjedde et al, 1991). For example, by making certain assumptions about oxygen extraction and capillary flow changes, Buxton et al. proposed that an increase in CBF leads to reduced OEF due to the decreased capillary transit time (Buxton and Frank 1997). Consequently, the oxygen delivery rate ($CMRO_2$) which is proportional to the product of CBF and OEF (equation 2.9) increases much less than the CBF itself. A simple expression for the OEF under activated conditions was calculated and can be substituted into equation 2.10 to yield (Jezzard and Ramsey 2003):

$$\frac{CMRO_2}{CMRO_{2_0}} = \frac{CBF}{CBF_0} \times \frac{\left(1-\left(1-OEF_0\right)^{CBF_0/CBF}\right)}{OEF_0} \qquad (2.11)$$

Here the presence and absence of the "0" suffix denotes resting and active conditions respectively. This results in an approximately linear but disproportionate relationship between positive increases in $CMRO_2$ and CBF for various assumed values of OEF_0 (figure 2.7) and has been supported by experimental evidence (Hoge et al, 1999).

This model can explain how, during brain activation, the CBF increases but the OEF decreases, which results in an increase in blood oxygenation (or Y_v, the venous oxygen saturation). This effect is used in BOLD fMRI which is sensitized to such changes.

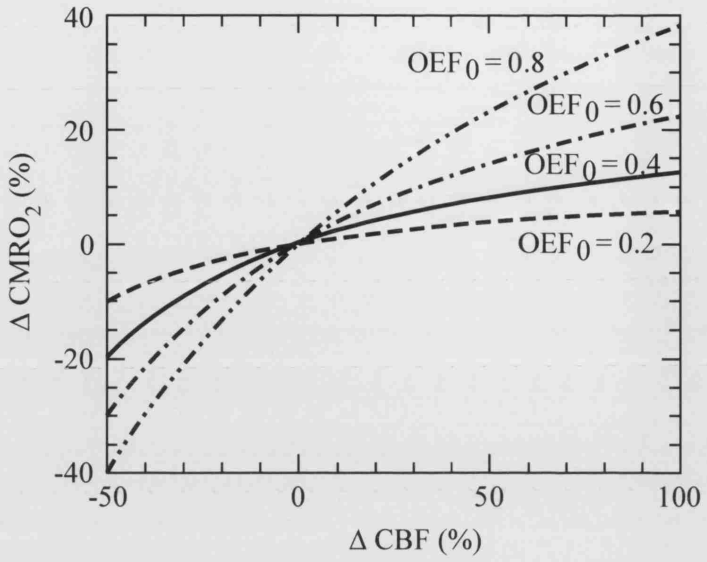

Figure 2.7. The % change in oxygen metabolism (Δ $CMRO_2/CMRO_{20}$) vs the required % change in cerebral blood flow (Δ CBF/CBF_0) simulated for several OEF_0 values using equation 2.11. At OEF_0 = 0.6, a CBF increase of 50% is required for a $CMRO_2$ increase of 10-15%. Reproduced with permission from Jezzard and Ramsey (2003).

2.2.2.2 *MRI characteristics of the BOLD response*

2.2.2.2.1 Background

The MRI basis of the BOLD effect relies upon the different magnetic properties of oxyhaemoglobin (oxyHb) and deoxy-haemoglobin (deoxyHb). DeoxyHb is paramagnetic relative to surrounding tissue whilst oxyHb is isomagnetic (Pauling and Coryell 1936). Paramagnetic materials have greater magnetic flux. Therefore increases in deoxyHb concentrations will distort local magnetic fields and shorten the T_2 constant of blood and the T_2^* of the imaging voxel, resulting in a reduction of MRI signal (Thulborn et al, 1982).

The first true BOLD contrast imaging experiments were described by Ogawa et al in MRI rodent studies where GE-EPI signal alterations in response to blood oxygenation changes were observed (Ogawa et al, 1990a; Ogawa et al, 1990b; Ogawa and Lee 1990). Similar effects were subsequently reported for cats under conditions of oxygen deprivation (Turner et al, 1991). During brain activation the BOLD signal increases due to a reduction in the OEF, as described above. This was

independently demonstrated in 1992 in humans by three groups (Bandettini et al, 1992; Kwong et al, 1992; Ogawa et al, 1992).

2.2.2.2.2 *Intravascular and extravascular effects*

The BOLD signal is caused by contributions from water molecules both within the blood vessels (intravascular) and within the surrounding tissue (extravascular). During neural activity only signal changes related to the draining capillaries and venous vessels need to be considered because the arterial oxygenation remains unchanged.

The intravascular BOLD signal is mainly determined by T_2 effects of the blood. The precise mechanisms are still undetermined but are thought to arise from spin-spin interactions between water molecules as they diffuse through local magnetic field environments that fluctuate in time and space as the red blood cells and plasma travel through the blood vessels (Matthews 2001). When blood oxygenation decreases, the magnetic field differences increase, resulting in greater phase decoherence and signal loss (i.e. a shorter blood T_2). This is thought to mediate T_2 contrast between different blood oxygenation states. In addition, some T_2^* effects may also contribute to the intravascular BOLD signal. These occur because vessels of differing orientations and oxygenation will establish different local magnetic field gradients which may influence neighbouring intravascular spins. In an imaging voxel therefore, the interactions between many vessels with random orientations will exacerbate phase decoherence following RF excitation i.e. will produce T_2^* decay (Jezzard and Ramsey 2003).

Extravascular water molecule spin dephasing is mediated by T_2^* effects produced by local magnetic field gradients that extend outside vessels. The magnitudes of these local magnetic fields will depend upon the proximity and relative orientations of the vessels and the oxygenation state of the blood (Ogawa et al, 1993). Vessel size is also an important influence. For small vessels such as capillaries

(radius $\leq$ 8μm) the BOLD contribution to T_2^* effects scales quadratically with increasing static field strength, and for larger vessels such as venules and veins it scales in a linear fashion.

Only 3-5% of a grey matter voxel resides in the intravascular space. It might be expected therefore that the intravascular BOLD signal contributions would be negligible. However this is not the case (at 1.5T) because the T_2 and T_2^* of blood are quite long compared with tissue and also the extravascular effects are quite localized around the vessels. Simulation studies have predicted that at 1.5 T as much as 60% of the BOLD signal may arise from the intravascular space (capillaries and venules) (Boxerman et al, 1995) (figure 2.8). With higher magnetic field strengths, a reduced intravascular contribution is expected because the T_2 and T_2^* of blood decrease significantly.

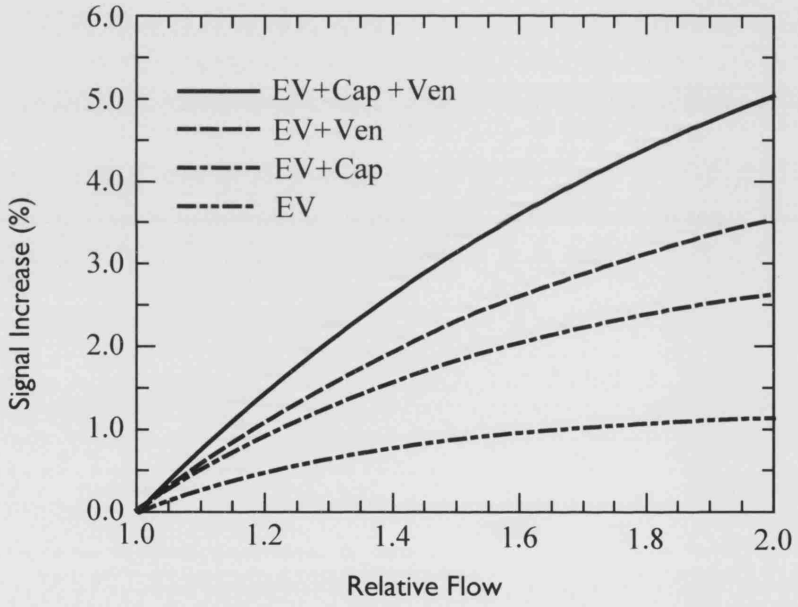

Figure 2.8. Theoretical dependence of the extravascular (EV) and intravascular (Cap = capillary, Ven = venule) BOLD signal contributions as a function of CBF at 1.5T. Most signal arises from intravascular contributions. Reproduced with permission from Jezzard and Ramsey (2003).

2.2.2.2.3 Spin echo vs gradient echo sequences

Although most fMRI is conducted using gradient echo (GE) EPI, spin echo sequences can also detect BOLD signal changes. Spin echo (SE) uses a second RF pulse following the initial excitatory RF pulse to refocus the signal into an echo and effectively compensates for signal dephasing effects due to

macroscopic magnetic field inhomogeneities. This sensitizes it to T_2 effects but at the same time removes T_2^* effects (mainly extravascular), causing spin echo sequences to exhibit a smaller BOLD effect for a given TE. This implies also, that spin echo may be used to localize the intravascular capillary compartment provided that flow-crushing principles (Boxerman et al, 1995) are adopted to suppress the intravascular signal from the larger draining veins. In practice however, adequate BOLD sensitivity with spin echo may only be realistically possible at high static field strengths.

2.2.2.2.4 *Temporal characteristics and the balloon model*

The BOLD response to a period of neuronal stimulation (e.g. induced by visual stimulation) evolves over a much longer time scale than the underlying electrical activity and is sometimes called the *haemodynamic response function* (HRF). It has certain features detailed below in figure 2.9. After the commencement of neural activity an 'initial dip' is sometimes observed, thought to result from increasing metabolic demand ($CMRO_2$) producing transient deoxygenation, before the CBF rise (Menon et al, 1995). This is followed by a rise in the BOLD signal over five to eight seconds to a plateau which is sometimes associated with a positive overshoot and corresponds to the increasing CBF and CBV. After stimulus cessation the BOLD response drops back to baseline often accompanied with a 'post-stimulus undershoot'. The positive BOLD response is usually detected in fMRI studies (corresponding to 1-3% signal change at 1.5T with GE-EPI in the visual cortex).

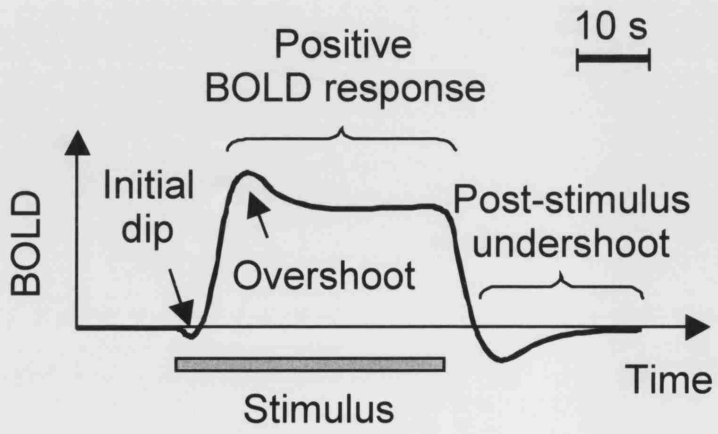

Figure 2.9. The temporal characteristics of the BOLD response to a prolonged input stimulus function. Adapted from Jezzard and Ramsey (2003).

In fact, the initial dip, stimulus overshoot and post-stimulus undershoot are transient features of the BOLD signal that can be explained by two models. The first postulates transient decoupling between flow and oxygen metabolism and is presently the favoured explanation for the initial dip (see above). The second is the *balloon model* which invokes a simple biomechanical model for blood volume changes by imparting the venous compartment with elastic properties, whilst maintaining a tight coupling between CBF and $CMRO_2$ (Buxton et al, 1998). Venous elasticity will therefore induce transient mismatches between CBF and CBV. This is the favoured explanation for the post-stimulus undershoot which results from a slowly resolving CBV (after the CBF has returned to baseline) which contains diluted dHb.

2.2.2.3 *Neurophysiological basis of the BOLD response*

Interpretation of the BOLD signal generally assumes the linear transform model (Boynton et al, 1996; Friston et al, 1994), which states that "the fMRI signal is approximately proportional to a measure of local neural activity, averaged over a spatial extent of several millimetres and over a time period of several seconds" (Heeger and Ress 2002). This model implies that it is possible to estimate the underlying neuronal activity from the fMRI response. The relationship would be characterized by the HRF resulting from a brief pulse of neuronal activity (figure 2.10).

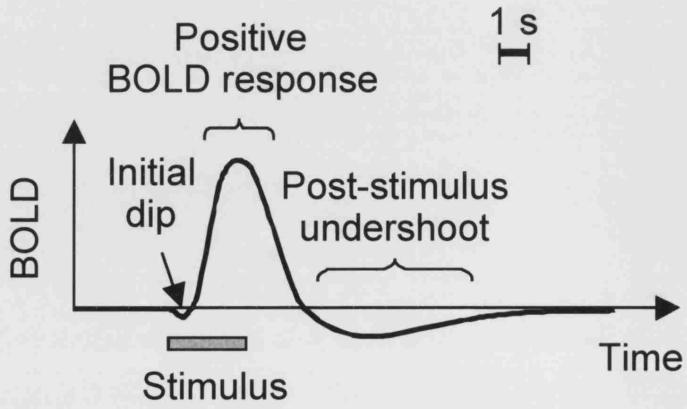

Figure 2.10. BOLD response to a brief period of neuronal stimulation. Adapted from Jezzard and Ramsey (2003).

One implication of the linear transform model is that of temporal summation, which means that the response to a long stimulus presentation can be predicted by the summation of responses to its component stimuli of shorter duration. This is a good approximation in most situations although it appears to break down in certain cases. Studies have demonstrated that although longer duration stimuli behave in a linear fashion, shorter stimuli produce responses larger than those predicted from linear models (Birn et al, 2001; Boynton et al, 1996; Friston et al, 1998; Vazquez and Noll 1998). These nonlinear BOLD responses could arise from nonlinearities in the neuronal response (Albrecht et al, 1984; Muller et al, 2001; Ohzawa et al, 1982) or from nonlinearities in the haemodynamic response resulting, for example, from BOLD saturation effects (Miller et al, 2001) or from a combination of both.

The neurophysiological basis of the BOLD response has been investigated by several studies. The results of two studies indirectly support a proportional interspecies relationship between the BOLD signal and average neuronal firing rates by successfully correlating human fMRI data with monkey single-unit recordings from visual areas V5 (Rees et al, 2000) and V1 (Heeger et al, 2000).

A recent study performed by Logothetis et al performed simultaneous intracortical recordings of neural and fMRI signals in response to visual stimulation in the visual cortices of monkeys (Logothetis et al, 2001). Neuronal activity was recorded from V1 with microelectrodes during BOLD fMRI acquisition. Several experiments were performed at different recording sites. The raw electrophysiological data were decomposed into signals representing local field potential (LFP) and multi unit activity (MUA)[2] and examined to ascertain how well they could predict the BOLD signal,

[2] The MUA is thought to represent the spiking activity of neurons within the vicinity of the electrode tip (100-300μm) (Legatt et al, 1980) whereas the LFP is believed to originate from synchronized synaptic activity of dendritic trees summated over a larger volume (0.5-3 mm) (Logothetis 2002; Mitzdorf 1987). MUA was extracted from the raw signal by bandpass filtering between 400 and a few thousand Hz, whereas LFP information was obtained by lower frequency bandpass filtering (10 and 300 Hz). LFPs are thought to reflect

assuming the linear transform model. The results showed some variability between recording sites in the predictive ability of the neurophysiological signal to estimate the BOLD response. At sites where predictive power was strong, both LFP and MUA data tended to vary together (Heeger and Ress 2002) although LFPs were slightly better predictors (accounting for 7.6% more variance of the fMRI response than MUA). This difference related to the transient nature of the MUA signal whereas LFP and BOLD signals were sustained for the duration of the visual stimuli. The study concluded that BOLD fMRI signals "reflect the input and intracortical processing of a given area rather than its spiking output." This was found to correlate quite well with the output spiking activity (MUA) in this particular study, but under certain conditions the relationship between input processing and output spiking may decouple. For example, LFP increases may be caused by greater synchronized yet subthreshold synaptic activity resulting from simultaneous excitation and inhibition or modulatory inputs, which will result in a haemodynamic response without neuronal spiking activity (Mathiesen et al, 1998). Logothetis et al also reported a monotonic but nonlinear relationship between the fMRI and neural responses as the stimulus contrast was increased from 12.5% to 100%. At a contrast of 12.5% the BOLD signal reached 50% of its measured amplitude at 100% contrast (maximum amplitude) whilst the LFP and MUA were at 10-20% of their maximum (measured at 100% contrast). This discrepancy shortened with increasing stimulus contrast and implied that at lower contrast intensities the fMRI response has more variance that is unexplained by the LFP/MUA measurements e.g. the fMRI signal might include a contribution from asynchronous subthreshold activity that would not be detected by LFP or MUA measurements (Heeger and Ress 2002).

2.2.3 FMRI acquisition

GRE based EPI is commonly used to acquire fMRI data because it is a fast acquisition technique with moderately good spatial resolution that is sensitive to T_2^* and hence BOLD effects. Fast acquisition is

---

inputs and intracortical activity and are often, though not always, correlated with output spiking activity (MUA) (Heeger and Ress 2002).

desirable because the BOLD effect may be confounded by signal instabilities originating from cardiac and respiratory cycles or head motion. Typical brain volumes can be acquired in a few seconds and each slice in tens of milliseconds at a spatial resolution of a few millimetres at 1.5T.

2.2.3.1 MRI optimization

The MRI signal from a voxel acquired with a GE-EPI sequence will decay as a function of TE with the time constant T_2^*. The T_2^* value depends on the magnetic field variations within the voxel as well as a T_2 contribution and will be altered by oxygenation state of the blood. The optimum BOLD contrast (or *BOLD sensitivity*) is therefore determined by the TE that maximizes the difference between the two exponential decay rates of active and resting conditions. This occurs when TE ≈ resting T_2^*. For small changes in T_2^* the fractional change in signal can be given by:

$$\frac{\Delta S}{S} \approx -TE\Delta R_{2^*} \qquad (2.12)$$

where R_2^* is $1/T_2^*$ and describes the decay rate. T_2^* decreases with increasing static field strength and demonstrates spatial variability within the brain.

Voxel size is also an important consideration. Although larger voxels increase the MR SNR, the T_2^* tends to shorten which will reduce the BOLD sensitivity for a given TE. Isotropic voxels are usually considered desirable as thick slices will exacerbate these T_2^* shortening effects and matching the voxel size to the cortical thickness, 3mm is a common choice.

The TR choice usually depends on the number of slices required and the slice acquisition rate. Shorter TRs are advantageous for temporally characterizing the HRF following brief stimuli. However, TRs less than about 1 second may make the image sensitive to flow velocity (Lai et al, 1993) especially with larger flip angles (inflow effects). As a consequence, changes in blood velocity in supplying arteries and draining veins may show spurious activations. Inflow effects may be obviated by

reducing the flip angle or increasing the TR. They can also be removed by the application of out of volume RF saturation pulses (Duyn et al, 1994) or reduced by diffusion weighting which rapidly dephases the moving intravascular spins (Boxerman et al, 1995; Song et al, 1996).

Higher static field strengths will tend to spatially localize the BOLD signal towards the capillary bed more than venous vessels and also enhance extravascular effects. The image SNR increases linearly with field strength and the BOLD sensitivity increase (i.e. activation induced BOLD signal change) is also approximately linear (Gati et al, 1997). Another consequence is a reduction in the optimum TE resulting from the shorter T_2^* constant. Higher field strengths, however, encourage more artefacts, which are produced by bulk susceptibility differences around tissue-air interfaces e.g. with the air-filled sinuses or ear canals.

2.2.3.2 *Experimental design*

During an fMRI experiment, the subject is typically exposed to multiple conditions one of which is used as a baseline. The other conditions usually involve a goal directed behavioural task or exposure to sensory stimulus. FMRI analysis employs signal averaging techniques to compare the BOLD response between conditions e.g. between visual stimulation and darkness. Several independent classification systems can be used to describe the experimental paradigms: 1) Conditions may be categorical or parametric. 2) They may be single- or multi-factorial. 3) They may be presented in epochs or as events.

2.2.3.2.1 Categorical and parametric designs

Categorical designs are used to contrast different experimental conditions. Their interpretation assumes that differences between the experimental conditions represent separable cognitive or sensorimotor processes, and that the differences in the BOLD response identify the corresponding functionally responsible areas. Parametric designs vary the sensorimotor or cognitive load for a

condition in a systematic way and assume that the resulting brain activity will respond in a corresponding fashion e.g. this can be used to discern brain regions that respond to increasing word presentation rates for an auditory stimulus paradigm.

2.2.3.2.2 *Single and multi-factorial presentations*

Experimental designs whose conditions possess more than one experimental factor may be used to investigate interactions between factors. If two experimental factors are being assessed, then the interaction can be determined by examining the response in the presence of both factors together. For example if one of the factors is time then the condition by time interaction may represent physiological adaptation (e.g. habituation or learning).

2.2.3.2.3 *Epoch and event-related paradigms*

A common format for the presentation of an experimental condition is in blocks or discrete *epochs* of time. An example of an epoch based paradigm is a simple categorical ON-OFF paradigm for photic stimulation, which is used in this thesis (figure 2.11). The optimum experimental period should theoretically match the HRF's temporal characteristics as lower and higher frequency components (representing experimental noise) will be filtered out during experimental analysis. This suggests an optimum frequency of about 0.03 Hz corresponding to periods of about 32 seconds (16 second epochs) (Friston 2004).

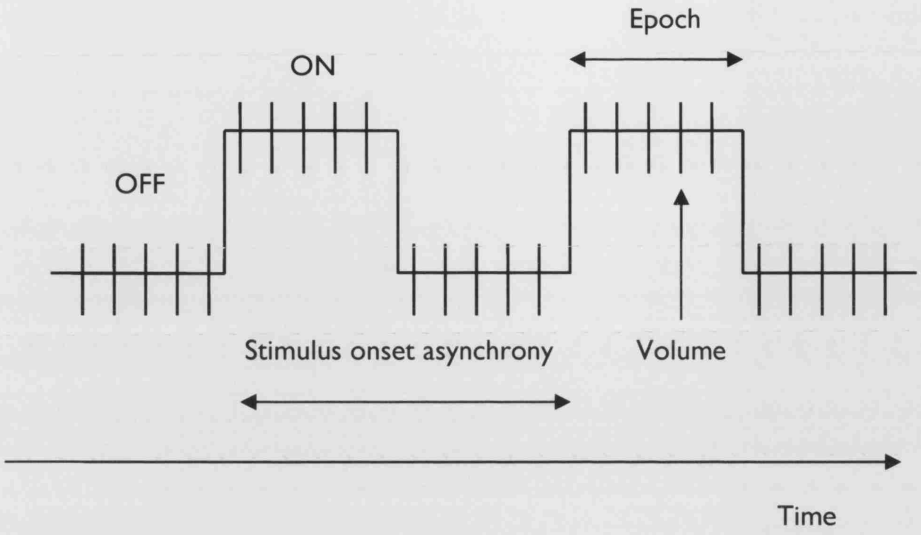

Figure 2.11. A categorical epoch based paradigm for photic stimulation. Five volumes are acquired during each epoch (shown as vertical lines). The experimental period (interstimulus interval) is called the stimulus onset asynchrony (SOA).

Alternatively, experimental conditions may be presented as *events* or brief stimuli (*event-related fMRI*), which offers several advantages. 1) The order of trials can be randomized which can avoid adaptive or learning confounds. 2) Trials can be categorized or parameterized post hoc depending upon the subject's performance. 3) Some experiments involve events that cannot be blocked e.g. unpredictable events or 'oddball' paradigms. 4) The temporal characteristics of the BOLD response can be investigated.

The distribution of the interstimulus intervals or SOAs (stimulus onset asynchrony) in event-related fMRI (efMRI) strongly influences BOLD detection power and estimation efficiency. Since the HRFs detected with efMRI result from tasks of brief duration, the ability to detect activation (called detection power) is much less than with epoch-based fMRI designs. The ability to characterize the shape of the HRF is conversely much better (called estimation efficiency) with efMRI when compared with epoch designs. In the design of efMRI experiments calculations have shown a trade-off between estimation efficiency and detection power (Liu et al, 2001). That is, designs which achieve maximum detection power necessarily have minimum estimation efficiency and vice versa. In addition, for a varying interstimulus interval, the optimum estimation accuracy or maximum detectability can be

achieved when the number of time points for the task and control states are evenly balanced (Birn et al, 2002). Designs with high detection power tend to approximate epoch based paradigms with stimuli segregated into blocks. Another way of improving the estimation accuracy is to 'jitter' the SOA or TR with respect to each other which allows distributed sampling of the HRF (Dale 1999). This can be ensured when the SOA and TR are not integer multiples of each other and means that the temporal relationship between stimulus presentation and scan acquisition is distributed (not fixed) (Price et al, 1999). EfMRI is becoming increasingly popular, especially with cognitive fMRI because it can offer several advantages over epoch-based fMRI as mentioned above. However, since detection power is compromised, in certain conditions epoch-based fMRI is considered more useful. This was felt to be the case for the fMRI studies performed for this thesis where using epoch based fMRI maximized our ability to detect fMRI responses following neurological insult.

2.2.4 FMRI Analysis (Statistical Parametric Mapping – SPM99)

The aim of fMRI data analysis is to make regionally specific inferences about brain activity. SPM99 is one of several analysis packages that achieve this by using the general linear model (*GLM*) on a mass univariate (voxel by voxel) scale. The GLM framework assumes that the BOLD-related signal changes, caused by the task or stimulus, can be modelled as a linear combination of known experimental variables. Raw fMRI data also includes signal changes unrelated to the experimental design which may swamp the small expected BOLD changes of a few percent. A significant portion of this noise can be 'removed' by SPM99 before the data is modelled. Some aspects of fMRI noise contributions will be discussed below. Following this, fMRI analysis will be discussed (in the context of SPM99) and divided into three sections: spatial preprocessing, model estimation and statistical inference.

2.2.4.1 Sources of fMRI noise

MRI instrument related noise is usually 'white' or random and appears uniformly across the image. In fMRI time series, other random and non-random noise components are noticeable. Their sources include head motion, cardiac pulsations, respiratory oscillations and slow global variations in the BOLD signal.

Head motion is a major source of statistical confounds and can lead to the false detection of both activity and no activity (type I and type II errors). Fortunately most motion effects can be removed by realignment procedures described below.

Cardiac pulsations can cause periodic blood flow effects and bulk motion due to mechanical effects. Respiration can cause general periodic variation of blood oxygenation, head motion and changes in venous sinus pressure. Changes in chest cavity volume and oxygenation may also influence the B_0 field. The effects on the measured fMRI signal depend in part on the acquisition sampling rate (or TR). For example, with short TRs (<< 1 second), the cardiorespiratory effects will manifest as periodic fluctuations. If a long TR is used (e.g. 6 seconds) and approximately matches the respiratory cycle (e.g. 6.1 seconds) then aliasing effects may occur resulting in low frequency artefactual signal variations (Turner et al, 1998).

Another source of low frequency signal variation is thought to be related to intrinsic autoregulatory feedback mechanism of cerebrovascular tone which result in slow periodic haemodynamic changes (Biswal et al, 1995). These make significant contributions to the low frequency components of fMRI noise and assume a 1/f noise spectrum appearance (Turner and Ordidge 2000).

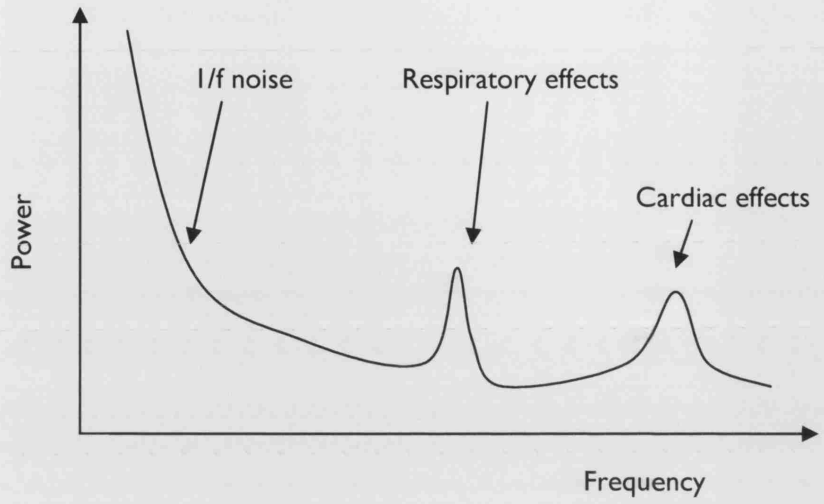

Figure 2.12. Example of a noise spectrum for fMRI data acquired with very short TR (so that no aliasing occurs with cardiac or respiratory effects).

2.2.4.2 *Spatial Preprocessing*

The spatial preprocessing steps after fMRI image reconstruction typically consist of (optional) slice timing correction, realignment, spatial normalization and smoothing. The aims are to remove unwanted variance components from the data, to transform the data into a standard reference, to improve the signal to noise and compensate for interindividual differences in anatomy.

2.2.4.2.1 *Slice Timing Correction*

FMRI analysis assumes that all brain slices were acquired simultaneously. This is typically not the case and may result in suboptimal model fitting. Slice timing correction aims to addresses this by phase shifting the voxels' time series from each slice to a reference slice (by using sinc interpolation techniques). Slice timing becomes more important for the temporal dynamics of efMRI and is more accurate for smaller TRs. Longer TRs may result in interpolation errors.

2.2.4.2.2 *Realignment*

Head motion during an fMRI session can produce unwanted changes in signal in a particular voxel location from scan to scan and consequently can confound fMRI analysis. Basic realignment removes much of this unwanted signal variance by first estimating six parameters (three translations, three rotations) of a rigid-body transformation that minimize the sums of squares differences between each scan and a reference scan (usually either the first scan of the time series or the mean scan). These parameters are then applied by resampling the data (using tri-linear, sinc or spline interpolation). Although this procedure can align scans very well, certain effects may still result in movement-related signal variance some of which may be partially correctable. These effects include 1) subject movement during a volume acquisition (Grootoonk et al, 2000), 2) nonlinear distortions due to interactions with B_0 inhomogeneities (Andersson et al, 2001), 3) interpolation artefacts, 4) spin-excitation history effects (Friston et al, 1996b).

2.2.4.2.3 *Spatial Normalization*

Spatial normalization matches brain volumes from different individuals to a standard template. This procedure partially compensates for interindividual anatomical variability and therefore allows the comparison of anatomically homologous regions among subjects. The template used for normalization is usually an averaged image derived from a number of normal subjects. In SPM99 the templates have been provided by the Montreal Neurological Institute (MNI) (Collins et al, 1994) and are similar to the atlas of Talairach and Tournoux (Talairach and Tournoux 1988). Spatial normalization firstly estimates the parameter set that transforms the original image to the anatomical template. This is a two step procedure: (i) a linear transformation that uses a 12 parameter affine transformation matrix, (ii) a non-linear transformation that is parameterized using low frequency basis spatial functions (Ashburner and Friston 1999). The transformations can be constrained by penalizing unlikely warps (called regularization). The optimum parameter set is estimated by minimizing the sums of squared differences between the two images whilst simultaneously maximizing the smoothness of the transformation. The estimated normalization parameters are used to write out the normalized image usually with bilinear or sinc interpolation methods.

2.2.4.2.4 *Spatial Smoothing*

This is performed after spatial normalization and replaces each voxel intensity with a weighted average of itself and its neighbours. The weights are defined by a smoothing kernel. This is usually Gaussian with (in SPM) a full width half maximum (FHWM) at least 2-3 times the original voxel size for optimal results. Spatial smoothing has several consequences: (i) It increases signal to noise by the matched filter theorem if the size of the region over which a BOLD effect is expected is similar to the kernel size. (ii) It renders the errors more normal in their distribution through the central limit theorem thereby increasing the validity of parametric statistics. (iii) It fulfils the requirements of techniques used to correct for multiple comparisons in fMRI data which assumes that the error terms represent a reasonable lattice approximation to an underlying smooth Gaussian random field. (iv) It allows intersubject averaging of homologous functional anatomy to validate the statistical interpretation of groups of subjects.

2.2.4.3 *Model Estimation*

Most fMRI analyses (including SPM) use the general linear model (GLM). This is applied in a univariate (voxel by voxel) manner to estimate parameters that can explain the BOLD response (Friston et al, 1995). The data are modelled to partition the observed neurophysiological responses into effects of interest and confounds (with a residual error term). The GLM uses the following equation to model the fMRI response at each voxel:

$$Y = X\beta + \varepsilon \qquad (2.13)$$

Here Y is the observed response, X the explanatory variable, β is the parameter estimate (effectively response magnitude) and ε is an error term (residual) that is assumed to be independently and identically distributed (i.i.d). In SPM, X is expressed as a design matrix which consists of columns representing the explanatory variables (effects of interest or confounds). The effects of interest are convolved with an HRF (usually the canonical form). This process assumes the linear transform

model described above (chapter 2.2.2.3) and characterizes the input-output behaviour of the system at each voxel. General signal drift can be removed by introducing low frequency drift terms into the design matrix (as hidden confounds).

The residual error terms tend to have temporal autocorrelations, most likely caused by some influence of preceding time points on the current time point. It is therefore important to model the error term. In SPM99 this is performed by 'precolouring' or temporally smoothing the data (and the model). This imposes a known temporal autocorrelation structure on the error terms and reduces the effective degrees of freedom of the model. It also results in an unbiased estimator of ε, but with slightly increased variance.

The estimation of β is performed by using ordinary least squares regression fitting methods in the context of matrix mathematics. From equation 2.13, if the error term is omitted then:

$$X^{-1}Y = X^{-1}X\beta = \beta \qquad (2.14)$$

where X^{-1} is the inverse matrix of X. With real data (which includes the residual error terms), the least squares estimator of β is that value which minimizes the sum of squared errors in equation 2.13. It can be shown that:

$$\hat{\beta} = X^{+}Y = ((X^{T}X)^{-1}X^{T})Y \qquad (2.15)$$

Where $\hat{\beta}$ is the estimation of β. X^{+} is denotes the psuedoinverse, the 'best possible' inverse that minimizes the sum of squares error. X^{+} can be derived from X and X^{T} (transposed X) as shown in the right hand side of the equation. The estimation of β fits the model to the data.

2.2.4.4 Statistical inference

2.2.4.4.1 T and F contrasts

The detection of a significant BOLD response is made by statistically comparing the effect of interest with its variance. The particular differences of the parameter estimates, $\hat{\beta}$, that constitute the effect of interest are specified by a contrast vector, c, which comprises a linear combination of the parameter estimates, $c'\hat{\beta}$. The simplest contrast involves only one explanatory variable, for example, to test for activation in a photic stimulation paradigm (versus rest) the contrast vector used is c'= [1] where the baseline has been implicitly modelled. So the estimated effect size is $\hat{\beta}$. To test for a difference between two explanatory variables with parameter estimates $\hat{\beta}_1$ and $\hat{\beta}_2$ the contrast vector c'= [1 -1] is used. A T statistic can be obtained by dividing the contrast weighted parameter estimates by the standard error of that compound:

$$T = \frac{c'\hat{\beta}}{\sqrt{\hat{Var}(c'\hat{\beta})}} \qquad (2.16)$$

Where the denominator denotes the estimated standard error of the effect.

T tests in SPM99 are one sided. Two tailed tests or simultaneous tests of several contrasts can be made using an F contrast. This is specified using a *matrix* of contrast weights rather than a *vector* as with T contrasts.

2.2.4.4.2 Multiple comparisons correction

The test statistics (T or F scores) are calculated for every voxel within the image volume resulting in a generation of an SPM (statistical parametric map) which can comprise tens of thousands of

statistics. This introduces a multiple comparisons problem when deciding whether there is a significant effect if the precise location of the effect is unknown (i.e. if the hypothesis is anatomically open). Hypothesis testing compares the test statistic with its null distribution (the distribution of test statistics if there were no effect) to decide how likely it is that the test statistic has arisen by chance. Conventionally a threshold of 5% (or α value of 0.05) is used to decide whether test statistics are significant i.e. 5% is the type I error rate (false positive rate). In a large volume of test statistics this can result is high numbers of falsely activated voxels.

Ideally the family wise error (FWE) needs to be controlled which specifies the likelihood that the family (volume) of test statistics could have arisen by chance. Appropriate thresholding of the test statistic magnitude ('height thresholding') can achieve this and provide localizing power i.e. allow voxel specific inferences, but the number of tests must be taken into account. One way of achieving this is to perform a Bonferroni correction. This states that:

$$P^{FWE} = 1-(1-\alpha^{n}) \qquad (2.17)$$

Where P^{FWE} is the probability of one or more test statistics being greater than α and n is the number of tests. The small size of α means that this approximates to:

$$P^{FWE} \leq n\alpha \qquad (2.18)$$

This can be solved to:

$$\alpha = P^{FWE}/n \qquad (2.19)$$

In a brain volume of 100,000 voxels for example, and for a desired FWE rate of 0.05 the required probability threshold is 0.0000005. This allows one to conclude that significant test statistics have only a 5% chance of arising anywhere within the whole brain volume. A disadvantage of the Bonferroni correction in functional neuroimaging is that the tests are assumed to be independent.

This is not the case as some degree of spatial correlation is nearly always present, mostly as a result of smoothing, which makes this type of correction very conservative (because it overestimates the number of independent elements).

Gaussian Random Field theory (GRFT) has been applied in SPM99 to overcome this problem (Worsley et al, 1996). It deals with multiple comparisons in the context of continuous, spatially extended fields and expresses the search volume in terms of resels (resolution elements corresponding to the units of independent observations) each of which may consist of many spatially correlated voxels. As the number of resels will be fewer than the number of test statistics, GRF theory is more sensitive than the Bonferroni correction at detecting significant effects. The application of GRF theory relies upon first estimating the smoothness (spatial correlation) of the statistical map and then determining the expected Euler characteristics (ECs) for the smooth statistical map at different thresholds. It is beyond the scope of this thesis to discuss the EC in detail but it should be noted that the expected EC gives the expected number of clusters above a given threshold which, in turn gives the desired height threshold for a desired FWE rate. GRF correction relies on some assumptions which may be violated if: (i) the data are not smoothed, violating the assumption that the error fields are a reasonable approximation to an underlying random multivariate Gaussian field. (ii) the statistical model is incorrectly specified so that the residual errors are not normally distributed.

Anatomical hypotheses are 'open' if the expected spatial locations for the experimental effects are unknown. In these cases, after SPM thresholding (using GRFT), inferences can be made at: (i) *set level* – the number of activated regions, (ii) *cluster level* – the number of activated voxels within a region and (iii) *voxel level* – the p value for each suprathreshold (activated) voxel (Friston et al, 1996a). If the anatomical hypothesis is closed (i.e. if there is an *a priori* hypothesis about where to expect significant experimental effects) then a correction for the entire brain is inappropriate. In this case, a small volume can be specified and GRF correction applied (Worsley et al, 1996). The reduced volume will

lower the number of resels and improve inference sensitivity. An alternative approach is to use the uncorrected p value based on the spatial extent of the nearest cluster (Friston 1997).

2.2.4.5 *Group inferences*

Methods that allow statistical inferences for groups of subjects constitute *second level analyses* and depend upon both *within subject variability* (between scan variability in fMRI) and *between subject variability*. The consideration of the latter requires the treatment of each subject as a random effect i.e. it assumes that the subjects have been randomly drawn from the population at large. This takes into account appropriate sampling variability and allows assumptions to be made about the population from which the subjects were drawn. In SPM99 this is conducted using a *random effects or RFX analysis* (strictly speaking a *mixed effects analysis*). In early fMRI (and especially PET) studies, *fixed effects analyses* (*FFX*) were performed which only considered within subject (between scan) variability. This is appropriate for case studies and group conjunction analyses. Formal population level inferences about averaged group effects derived from a FFX analysis however are not valid i.e. the results pertain only to the specific group of subjects that was analysed.

RFX analyses are implemented in SPM99 using a 'summary statistic' approach. The contrasts of parameters estimated at the first level (fixed effects) analysis are entered into a second level (random effects) analysis. Hence there is only one observation per subject (i.e. contrast) per subject and the error variance is estimated using the between subject variability. If the design matrices between subjects are similar, then the second level variance estimator possesses the right mixture of variance at the first level (within subject) and at the second level (between subject). The analysis consequently emulates a full mixed effects analysis. The second level design matrix can implement the general linear model to perform for example one sample or two sample t-tests, ANOVA or linear regression.

2.3 Diffusion Tensor Imaging (DTI) and Diffusion Tractography

DTI was developed to characterize the three dimensional water diffusion properties within the brain at the imaging scale of the voxel. This is used to indirectly provide insight into the geometric properties of neural tissue. This is possible because water diffusion *in vivo* is affected by microstructural cellular architecture, the presence of non-permeable membranes and cellular transport between different subcompartments of brain tissue. Diffusion tractography has recently evolved from DTI and exploits the directional information about bulk fibre orientation within the imaging voxels to infer anatomical connections between brain regions. The principles of DTI are summarized below before a brief discussion of DT-tractography is presented.

2.3.1 Physical principles of DTI

Diffusion is the random translational motion of molecules in a fluid system and generally refers to the mixing of different molecular species via Brownian motion.[3] As a result of thermal agitation, collisions occur between molecules which provoke random displacements for each one ('random walk'). The overall displacement magnitude can be quantified for a group of molecules over a time interval as the root mean square (rms) displacement. In DTI, the measured process is the diffusion of water within water or its *self-diffusion.*

2.3.1.1 Fick's laws of diffusion

Fick formulated his first law of diffusion in 1855 by supposing that the rate of flow of a tracer within a medium would be proportional to its concentration gradient thus:

[3] First described by Robert Brown in 1827 as the random movement of microscopic particles suspended in fluid.

$$F = -D\frac{\delta C}{\delta x} \tag{2.20}$$

where F is the rate of transfer of the tracer substance along a particular direction, C is the concentration and x is the spatial co-ordinate along the same direction. D is the constant of proportionality and is called the *diffusion coefficient* or *constant* (mm^2s^{-1}). From this equation, Fick's second law of diffusion can be derived by using the conservation principles of tracer flow as shown:

$$\frac{\delta C}{\delta t} = -\frac{\delta F}{\delta x} \tag{2.21}$$

This states that the local rate of increase in tracer concentration equals the rate at which the tracer flow decreases with distance. Fick's second law of diffusion is valid for constant values of D and one dimensional diffusion processes and states:

$$\frac{\delta C}{\delta t} = D\frac{\delta^2 C}{\delta x^2} \tag{2.22}$$

With *isotropic* diffusion, where diffusion occurs equally in all directions, the probability of a certain displacement after a time interval can be modelled as a multivariate Gaussian distribution. Although equation 2.22 pertains to the diffusion of tracer substances, an analogous result can be derived for self-diffusion, which describes the probability of displacement (rather than concentration) after a certain time interval.

2.3.1.2 The diffusion tensor

Anisotropic media have different diffusion properties in different directions. With the assumption that the probability of displacement after a certain time interval still follows a multivariate Gaussian distribution, the diffusion process can be represented as a 3 x 3 tensor matrix:

$$D = \begin{pmatrix} D_{xx} & D_{xy} & D_{xz} \\ D_{yx} & D_{yy} & D_{yz} \\ D_{zx} & D_{zy} & D_{zz} \end{pmatrix} \tag{2.23}$$

The diagonal elements, D_{xx}, D_{yy} and D_{zz} represent the diffusion coefficients in the three main perpendicular axes (x, y and z). The off diagonal elements effectively represent how strongly the diffusion coefficients are correlated in the x, y and z directions. If the off diagonal elements are zero then diffusion is either isotropic or parallel to the x, y or z axis. Fick's second law of diffusion (2.22) can be extended to incorporate the diffusion tensor:

$$\frac{\delta C}{\delta t} = \sum_{i,j} D_{i,j} \frac{\delta^2 C}{\delta i \delta j} \tag{2.24}$$

$D_{i,j}$ are the elements of the diffusion tensor. For uncharged water molecules the diffusion tensor is symmetric i.e. $D_{i,j} = D_{j,i}$ and as a result can be completely defined by the six elements D_{xx}, D_{yy}, D_{zz}, D_{xy}, D_{xz}, D_{yz}.

2.3.2 MRI application of diffusion measurement

2.3.2.1 *Measurement of diffusion (diffusion weighted imaging)*

The Bloch equations used in MRI (e.g. equations 2.3, 2.4, 2.7) can be extended to include effects that may affect transverse magnetization, M_{xy}, such as diffusion. This was done by Torrey to produce the Bloch-Torrey equation (Torrey 1956). Further work was performed by Stejskal and Tanner who proposed a practical scheme to introduce diffusion weighting into an MRI sequence (Stejskal and Tanner 1965). The basic principle is to sensitize the NMR signal to diffusive motion which results in additional dephasing and corresponding attenuation of M_{xy}. The degree of signal attenuation depends upon the TE, T_2, the diffusion coefficient of the sample as well as the *gradient b-factor*, a user specified factor that describes properties of the diffusion sensitizing gradients (including magnitude, separation and duration). In biological tissues the diffusion coefficient is referred to as the *ADC* or *apparent diffusion coefficient.* This is because tissue microstructure will tend to restrict and hinder water diffusion resulting in a calculated diffusion coefficient that does not represent true free water diffusion. The ADC can be calculated by obtaining MRI signal intensities at different b-values (degrees of diffusion sensitization) and simultaneously solving the resulting Bloch-Torrey equations. Two b-values can be used to derive the ADC, usually b_{max} and b_{min} (or b_0 which denotes the absence of a diffusion sensitizing gradient). In this case:

$$\frac{S(TE, b_{\max})}{S(TE, b_{\min})} = e^{([b_{\max} - b_{\min}]D)} \qquad (2.25)$$

This can be solved for D:

$$D = \frac{1}{b_{\max} - b_{\min}} \ln \frac{S(b_{\max})}{S(b_{\min})} \qquad (2.26)$$

Consequently, voxel by voxel calculations for D (or ADC) can produce quantitative diffusion maps of ADC values, where each voxel value is the average ADC of tissue contained within that voxel.

2.3.2.2 *Derivation of the diffusion tensor (DTI)*

ADC measurements inherently provide one dimensional information whilst DT gives three dimensional information about water diffusion. The DT is also independent of sample orientation within the scanner. Using MRI, the DT can be calculated from a non-diffusion weighted image (b=0) plus diffusion weighted measurements along six or more non-collinear directions (Basser et al, 1994). Diffusion weighting along different directions is achieved by simultaneously applying diffusion weighting along combinations of the x, y and z axes e.g. x, y, z, xy, xz, yz directions would provide the minimum number of directions to define the DT. In the presence of two b factors – b_{max} and b_0, the DT can be derived from:

$$\ln\frac{S(TE,b)}{S(TE,b)} = -b : DT \qquad (2.27)$$

Where b is the matrix of elements $b_{i,j}$ (i,j are combinations of the x, y and z axes) and ":" is the matrix dot product between b and DT. After the DT is calculated, matrix diagonalization is performed to convert it into another tensor DT', with the off diagonal elements reduced to zero:

$$DT' = \begin{pmatrix} \lambda_1 & 0 & 0 \\ 0 & \lambda_2 & 0 \\ 0 & 0 & \lambda_3 \end{pmatrix} \begin{pmatrix} \varepsilon_1 \\ \varepsilon_2 \\ \varepsilon_3 \end{pmatrix} \qquad (2.28)$$

ε_1, ε_2 and ε_3 are called the *eigenvectors* of the DT and are unit vectors representing the three orthogonal directions of water diffusion within the scanner reference frame. λ_1, λ_2 and λ_3 are called the *eigenvalues* and correspond to the ADC values for the respective eigenvectors. Conventionally,

the eigenvalues are listed numerically in decreasing magnitude such that $\lambda_1 > \lambda_2 > \lambda_3$. In white matter, for example, λ_1 represents the diffusion coefficient along the fibre direction, whilst λ_2 and λ_3 represent the mutually perpendicular transverse diffusion coefficients (i.e. $\lambda_1 >> \lambda_2 \approx \lambda_3$). From the diagonalized DT, various scalar parameters can be calculated that characterize certain aspect of water diffusion properties within each voxel and are *rotationally invariant* (i.e. are independent of sample orientation within the scanner).

2.3.2.3 Scalar invariants of the diffusion tensor

Maps can be produced from the diagonalized DT demonstrating the eigenvalues and the eigenvectors at each voxel. In addition, voxelwise calculations can produce maps of scalar parameters.

2.3.2.3.1 Mean Diffusivity (MD)

This summarizes the diffusion properties within each voxel and is the simple arithmetical mean of the three eigenvalues. Sometimes a Trace D (Tr(D)) is reported which is the sum of the three eigenvalues (equivalent to 3MD).

2.3.2.3.2 Mean ADC

This averages the ADC measurements taken along the three principle axes (x, y and z). The mean ADC is approximately the same as the MD, and differs only when the effects on (uncompensated) imaging gradients (and cross terms between these and the applied diffusion gradients) are non-negligible.

2.3.2.3.3 Diffusion ellipsoid

This allows a visually qualitative interpretation of diffusion characteristics in each voxel by displaying ellipsoids with the axis directions defined by the eigenvectors and the axis magnitudes by the eigenvalues. The eccentricity of an ellipsoid indicates the degree of anisotropy e.g. a sphere represents isotropic diffusion whilst a cigar shaped ellipsoid indicates very anisotropic diffusion preferentially along one direction. The size of the ellipsoid is proportional to the product of the eigenvalues. Although, quite informative, diffusion ellipsoids are only useful for qualitative display. Several quantitative measures have been developed to characterize *in vivo* tissue anisotropy. The most frequently used one is fractional anisotropy.

2.3.2.3.4 Fractional Anisotropy (FA)

This estimates the proportion of the 'magnitude' of the DT that is due to anisotropic diffusion. It is derived from the ratio between the variance of the eigenvalues and the sum of squares of the eigenvalues:

$$FA = \frac{\sqrt{(\lambda_1 - MD)^2 + (\lambda_2 - MD)^2 + (\lambda_3 - MD)^2}}{\sqrt{\lambda_1^{\,2} + \lambda_2^{\,2} + \lambda_3^{\,2}}} \qquad (2.30)$$

It varies from 0 to 1, with higher values denoting greater anisotropy. One of its limitations is the influence of noise at low levels of true FA which may bias the calculation and result in higher that expected FA values (Pierpaoli and Basser 1996).

2.3.2.4 DTI acquisition

Diffusion weighted imaging uses the *pulsed field gradient* method, originally suggested by Stejskal and Tanner (Stejskal and Tanner 1965). This applies specific gradients in order to provide further signal attenuation and is typically used in the context of spin echo or single shot EPI sequences for DTI. Certain factors need consideration when optimizing DTI sequences.

2.3.2.4.1 Motion artefacts

Large diffusion gradients are usually applied to sensitize the DTI sequence to bulk water molecule motion. As a result, macroscopic motion artefacts can arise from motion of the head or pulsations within the brain. This can be partly compensated for by using motion correction techniques (Ordidge et al, 1994) or implementing fast acquisition techniques. However ultrafast acquisition techniques such as EPI have certain disadvantages such as poor SNR, distortions and signal drop out due to magnetic susceptibility artefacts and eddy currents (see also 2.1.5).

2.3.2.4.2 SNR considerations

The use of magnitude images may lead to non-zero signal intensity in regions of pure noise and increased signal in low SNR area which can lead to errors in the ADC calculations unless compensated for (Wheeler-Kingshott et al, 2002). A further issue, called the 'sorting bias' may lead to imprecise and inaccurate FA measurements at low SNR (Pierpaoli and Basser 1996).

2.3.2.4.3 Acquisition time

ADC calculations for a single direction require a minimum of two images with different diffusion weightings e.g. b=0 and b_{max}. The measurement of the DT requires at least seven measurements (e.g. b=0 and six non-collinear directions) which will prolong the total acquisition time. Ultrafast imaging techniques such as single shot EPI significantly reduce imaging time but at the cost of SNR or image resolution, so signal averaging (or the collection of more than seven measurement directions) is usually required. Typically, total data acquisition at 1.5T with 2-3mm resolution should take approximately 20-25 minutes (Jones et al, 1999).

2.3.2.4.4 Cerebrospinal fluid (CSF) pulsation artefacts

Macroscopic motion artefacts may arise from CSF pulsations synchronized with the heart beat. These can be minimized by cardiac 'gating' which allows image acquisition only during diastole (cardiac relaxation). Hence the TR (expressed as number of RR intervals) may vary between subjects and within the sequence itself. This makes the acquisition less time efficient than sequences with no cardiac gating and can also lead to differential T_1 weighting for each b-value or gradient direction.

2.3.2.4.5 *Diffusion and perfusion*

In grey matter, perfusion effects may interact with diffusion effects to affect the signal decay at low b-values, resulting in the measurement of a *pseudo*diffusion coefficient, some 10 times higher that the ADC of water in tissue (Le Bihan 1990). This effect has been explained by the intravoxel incoherent motion model (Turner et al, 1990) and can be reduced by using a non-zero b_{min} value.

2.3.2.4.6 *Optimum b-values and their calculations*

The signal decay curve may be estimated by fitting signal results from more than one b-factor. In the past several b-factors were used with the hope of providing a better fit. However, it has become increasingly apparent that, if only a single component of the decay curve is to be investigated, two points are better in terms of SNR per unit acquisition time (Jones et al, 1999).

Also, with careful sequence design, the effect of imaging gradients (i.e. all the non-diffusion encoding gradients within the sequence) can be minimised and a more accurate calculation of the diffusion parameters can be achieved by including all the sequence gradients in the b-factor calculations (Mattiello et al, 1997).

2.3.2.4.7 *Diffusion gradient directions*

A minimum of six diffusion encoding directions are required to derive the DT. Although this is adequate and relatively straightforward to implement, this acquisition is biased towards the chosen directions (*directional bias*). Voxels with principle directions of diffusion aligned with one of the chosen directions will have different SNR properties to voxels with different principle diffusion directions. The complex propagation of noise through the calculations may lead to differences in the parameter estimates between the different types of voxels. The most obvious way to overcome directional bias is to sample many more diffusion encoded directions. This can now be achieved with sequences which sample 60 or more directions, and also provide providing good SNR and image resolution.

2.3.3 DTI-based fibre tractography

DTI provides voxelwise information about the degree of anisotropy and its orientation. This information can be expressed in terms of eigenvectors (ε_1, ε_2, ε_3) and eigenvalues (λ_1, λ_2, λ_3). It is assumed the orientation of ε_1 is collinear with the principal orientation of the fibre bundles within each voxel. High diffusion anisotropy is felt to reflect underlying highly coherent nerve fibre bundles, for example in white matter. Over recent years, techniques able to infer fibre connectivity between voxels have been developed that have allowed the 3D visualization of fibre tracts

Two main classes of tractography software have been developed. The first is based on line propagation techniques that utilize local tensor information for each step of the propagation. The second is based on global energy minimization to find the energetically most favourable paths between voxels.

2.3.3.1 Line propagation techniques

These use the principal eigenvector, ε_1, of the DT to provide a propagation direction for each voxel along the path. They are generally analogous to methods for determining streamlines in fluid

dynamics. They usually use techniques to interpolate the eigenvector fields or DTs to allow smooth propagation (Basser et al, 2000; Conturo et al, 1999) although non-interpolated variants have also been developed (Mori et al, 1999; Mori et al, 2000; Xue et al, 1999). Termination criteria, such as low anisotropy values or very large path angle deviations between voxels, are usually employed with line propagation techniques to prevent tracking where DTI Gaussian assumptions may be violated.

The DTI eigenvector field contains noise and, as a consequence, the derived vector direction may not be congruent with the real bundle fibre direction. With linear propagation models, noise errors tend to accumulate with greater distances and appear to be dependent upon the shape of the trajectory, anisotropy, resolution and the particular method used (Mori and van Zijl 2002). This noise effect can be reduced by using smoothing (or interpolation) techniques that average tensor or eigenvector information among neighbouring voxels at the cost of lower effective resolution. Other approaches include an approximation of the tensor field based on B-spline fitting (Basser et al, 2000) and 'regularization' of the tensor field based upon a 'low curvature hypothesis' (Poupon et al, 2000). Other disadvantages particular to linear tracking methods include the intrinsic inability to account for branching white matter fibres and the inability to assign connectivity indices that score the confidence of connection between voxels.

2.3.3.1.1 PICo (Probabilistic index of Connectivity) algorithm

This tractography algorithm is able to partly tackle the last limitation mentioned in the previous paragraph. It is based on linear tracking techniques, but provides probabilistic indices of anatomical connectivity between voxels (Parker et al, 2003). Two orders of uncertainty, based on ε_1 orientation, are introduced: a 0^{th} order, assigning uncertainty using the anisotropy of the tensor; and a 1^{st} order, assigning uncertainty using the relative magnitudes of ε_2 and ε_3 and the orientations of their associated eigenvectors. Probability distribution functions (PDFs) are generated based on this information. These reflect the best estimate of the tissue microstructure responsible for a give DT profile. Streamline propagation is then repeated *N* times in a Monte Carlo fashion using the derived

PDFs, thus establishing the confidence of connection to the start point to a distributed area, from a fundamentally linear process. The number of occasions that each voxel is crossed by a streamline over *N*, the number of iterations, is used to define a map of the probability of connection to the start point. A limitation of this technique is that the probability of connection in any experiment generally decreases with distance from the start point. This is due to the cumulative effect of the uncertainties in propagation direction at each step in the streamline process.

2.3.3.2 *Energy minimization techniques*

These attempt to overcome some of the limitations of conventional linear propagation techniques.

2.3.3.2.1 Fast Marching Tractography (FMT)

This estimates the degree of connectivity between all voxels in the brain (or predefined volume) and a seed voxel or region. It achieves this with a region-growing step based on the orientation of the ε_1, followed by pathway generation via a gradient descent through the propagation field of the region-growing process (Parker et al, 2002b; Parker et al, 2002a). It can be visualized by imagining ink dropped onto cloth (or some anisotropically variable medium). The speed at which the ink front propagates will depend upon the underlying substructure of the medium. High spreading speeds will occur where the propagating direction is collinear with the principle eigenvectors. Multiple contour lines can be calculated, each representing the shape of the propagating front at different time points. Maps of a connectivity metric can subsequently be defined, allowing putative connections to be ranked between the seed voxel and every voxel within the analysis volume (Ciccarelli et al, 2003). One advantage of FMT is the provision to allow the branching of the estimated white matter tracts. As a result, however it is prone to false positive results.

2.3.3.2.2 Simulated annealing methods

These use energy minimization algorithms to generate paths, the shapes of which depend upon a balance between the 'stiffness' of the lines and their alignment to the underlying vector fields (Tuch et al, 2001). For example, if the connection to be determined (between two voxels) is allowed to be very flexible then numerous solutions will result in low energy. With an appropriate amount of allowed stiffness, an anatomically realistic pathway can be determined. The simulated annealing refers to a technique that can minimize noise in a global fashion. This approach can be used to generate anatomical connectivity maps.

2.3.4 Conclusions

Both DTI and its derivation, diffusion tractography are potentially powerful tools able to probe CNS structure. In this thesis, DTI was used to explore corticospinal tract pathology in ALS (amyotrophic lateral sclerosis) which is detailed in chapter 4. A further development of DTI analysis is outlined in chapter 5 in which group specific inferences are made from DTI tractography. This enabled us to combine fMRI and DTI tractography derived data in a multi-subject level analysis (also in chapter 5).

In spite of their usefulness, DTI and DTI tractography rely on several assumptions and have limitations which will be discussed in later chapters. Future directions that may evolve from DTI will also be discussed later (chapter 6).

2.4 References

Albrecht, DG, Farrar, SB, and Hamilton, DB. Spatial contrast adaptation characteristics of neurones recorded in the cat's visual cortex. *J Physiol.* 1984. **347**, 713-39.

Andersson, JL, Hutton, C, Ashburner, J, Turner, R, and Friston, K. Modeling geometric deformations in EPI time series. *Neuroimage.* 2001. **13**(5), 903-19.

Ashburner, J and Friston, KJ. Nonlinear spatial normalization using basis functions. *Hum.Brain Mapp.* 1999. **7**(4), 254-66.

Bandettini, PA, Wong, EC, Hinks, RS, Tikofsky, RS, and Hyde, JS. Time course EPI of human brain function during task activation. *Magn Reson Med.* 1992. **25**(2), 390-7.

Basser, PJ, Mattiello, J, and LeBihan, D. Estimation of the effective self-diffusion tensor from the NMR spin echo. *J.Magn Reson.B.* 1994. **103**(3), 247-54.

Basser, PJ, Pajevic, S, Pierpaoli, C, Duda, J, and Aldroubi, A. In vivo fiber tractography using DT-MRI data. *Magn Reson.Med.* 2000. **44**(4), 625-32.

Birn, RM, Cox, RW, and Bandettini, PA. Detection versus estimation in event-related fMRI: choosing the optimal stimulus timing. *Neuroimage.* 2002. **15**(1), 252-64.

Birn, RM, Saad, ZS, and Bandettini, PA. Spatial heterogeneity of the nonlinear dynamics in the fmri bold response. *Neuroimage.* 2001. **14**(4), 817-26.

Biswal, B, Yetkin, FZ, Haughton, VM, and Hyde, JS. Functional connectivity in the motor cortex of resting human brain using echo-planar MRI. *Magn Reson.Med.* 1995. **34**(4), 537-41.

Bloch, F, Hansen, WW, and Packard, M. The nuclear induction experiment. *Phys.Rev.* 1946. **70**, 474-85.

Boxerman, JL, Bandettini, PA, Kwong, KK, Baker, JR, Davis, TL, Rosen, BR, and Weisskoff, RM. The intravascular contribution to fMRI signal change: Monte Carlo modeling and diffusion-weighted studies in vivo. *Magn Reson.Med.* 1995. **34**(1), 4-10.

Boynton, GM, Engel, SA, Glover, GH, and Heeger, DJ. Linear systems analysis of functional magnetic resonance imaging in human V1. *J.Neurosci.* 1996. **16**(13), 4207-21.

Bruder, H, Fischer, H, Reinfelder, HE, and Schmitt, F. Image reconstruction for echo planar imaging with nonequidistant k-space sampling. *Magn Reson Med.* 1992. **23**(2), 311-23.

Buonocore, MH and Gao, L. Ghost artifact reduction for echo planar imaging using image phase correction. *Magn Reson.Med.* 1997. **38**(1), 89-100.

Buxton, RB and Frank, LR. A model for the coupling between cerebral blood flow and oxygen metabolism during neural stimulation. *J.Cereb.Blood Flow Metab.* 1997. **17**(1), 64-72.

Buxton, RB, Wong, EC, and Frank, LR. Dynamics of blood flow and oxygenation changes during brain activation: the balloon model. *Magn Reson.Med.* 1998. **39**(6), 855-64.

Ciccarelli, O, Parker, GJ, Toosy, AT, Wheeler-Kingshott, CA, Barker, GJ, Boulby, PA, Miller, DH, and Thompson, AJ. From diffusion tractography to quantitative white matter tract measures: a reproducibility study. *Neuroimage.* 2003. **18**(2), 348-59.

Collins, DL, Neelin, P, Peters, TM, and Evans, AC. Automatic 3D intersubject registration of MR volumetric data in standardized Talairach space. *J Comput.Assist.Tomogr.* 1994. **18**(2), 192-205.

Conturo, TE, Lori, NF, Cull, TS, Akbudak, E, Snyder, AZ, Shimony, JS, McKinstry, RC, Burton, H, and Raichle, ME. Tracking neuronal fiber pathways in the living human brain. *Proc.Natl.Acad.Sci.U.S.A.* 1999. **96**(18), 10422-7.

Dale, AM. Optimal experimental design for event-related fMRI. *Hum.Brain Mapp.* 1999. **8**(2-3), 109-14.

Duyn, JH, Moonen, CT, van Yperen, GH, de Boer, RW, and Luyten, PR. Inflow versus deoxyhemoglobin effects in BOLD functional MRI using gradient echoes at 1.5 T. *NMR Biomed.* 1994. **7**(1-2), 83-8.

Fox, PT, Mintun, MA, Raichle, ME, Miezin, FM, Allman, JM, and Van Essen, DC. Mapping human visual cortex with positron emission tomography. *Nature.* 1986. **323**(6091), 806-9.

Fox, PT and Raichle, ME. Focal physiological uncoupling of cerebral blood flow and oxidative metabolism during somatosensory stimulation in human subjects. *Proc Natl.Acad.Sci.U.S.A.* 1986. **83**(4), 1140-4.

Fox, PT, Raichle, ME, Mintun, MA, and Dence, C. Nonoxidative glucose consumption during focal physiologic neural activity. *Science.* 1988. **241**(4864), 462-4.

Friston, KJ. Testing for anatomically specified regional effects. *Hum.Brain Mapp.* 1997. **5**(2), 133-6.

Friston, KJ. Experimental Design and Statistical Parametric Mapping. In: Frackowiak, RSJ, Friston, KJ, Frith, CD, Dolan, RJ, Price, CJ, Zeki, S, Ashburner, J, and Penny, W. Human Brain Function. London; Elsevier Science, 2004: 599-632.

Friston, KJ, Holmes, A, Poline, JB, Price, CJ, and Frith, CD. Detecting activations in PET and fMRI: levels of inference and power. *Neuroimage.* 1996a. **4**(3 Pt 1), 223-35.

Friston, KJ, Holmes, AP, Worsley, KJ, Poline, JB, Frith, CD, and Frackowiak, RSJ. Statistical parametric maps in functional imaging: A general linear approach. *Hum.Brain Mapp.* 1995. **2**, 189-210.

Friston, KJ, Jezzard, P, and Turner, R. The analysis of functional MRI time series. *Hum Brain Mapp.* 1994. **1**, 153-71.

Friston, KJ, Josephs, O, Rees, G, and Turner, R. Nonlinear event-related responses in fMRI. *Magn Reson.Med.* 1998. **39**(1), 41-52.

Friston, KJ, Williams, S, Howard, R, Frackowiak, RS, and Turner, R. Movement-related effects in fMRI time-series. *Magn Reson.Med.* 1996b. **35**(3), 346-55.

Fulton, JF. Observations upon the vascularity of the human occipital lobe during visual activity. *Brain.* 1928. **51**, 310-20.

Gati, JS, Menon, RS, Ugurbil, K, and Rutt, BK. Experimental determination of the BOLD field strength dependence in vessels and tissue. *Magn Reson.Med.* 1997. **38**(2), 296-302.

Gjedde, A, Ohta, S, Kuwabara, H, and Meyer, E. Is oxygen diffusion limiting for blood-brain transfer of oxygen? In: Lassen, NA, Ingvar, DH, Raichle, ME, and Friberg, L. Brain, Work and Mental Acitivity. Munksgaard, Copenhagen; Alfred Benson Symposium 31, 1991: 177-84.

Grootoonk, S, Hutton, C, Ashburner, J, Howseman, AM, Josephs, O, Rees, G, Friston, KJ, and Turner, R. Characterization and correction of interpolation effects in the realignment of fMRI time series. *Neuroimage.* 2000. **11**(1), 49-57.

Heeger, DJ, Huk, AC, Geisler, WS, and Albrecht, DG. Spikes versus BOLD: what does neuroimaging tell us about neuronal activity? *Nat.Neurosci.* 2000. **3**(7), 631-3.

Heeger, DJ and Ress, D. What does fMRI tell us about neuronal activity? *Nat.Rev.Neurosci.* 2002. **3**(2), 142-51.

Hoge, RD, Atkinson, J, Gill, B, Crelier, GR, Marrett, S, and Pike, GB. Linear coupling between cerebral blood flow and oxygen consumption in activated human cortex. *Proc Natl.Acad.Sci.U.S.A.* 1999. **96**(16), 9403-8.

Jezzard, P and Ramsey, NF. Functional MRI. In: Tofts, P. Quantitative MRI of the Brain - Measuring changes caused by disease. London; John Wiley and Sons, Ltd, 2003: 413-53.

Jones, DK, Horsfield, MA, and Simmons, A. Optimal strategies for measuring diffusion in anisotropic systems by magnetic resonance imaging. *Magn Reson.Med.* 1999. **42**(3), 515-25.

Kwong, KK, Belliveau, JW, Chesler, DA, Goldberg, IE, Weisskoff, RM, Poncelet, BP, Kennedy, DN, Hoppel, BE, Cohen, MS, Turner, R, and . Dynamic magnetic resonance imaging of human brain activity during primary sensory stimulation. *Proc.Natl.Acad.Sci.U.S.A.* 1992. **89**(12), 5675-9.

Lai, S, Hopkins, AL, Haacke, EM, Li, D, Wasserman, BA, Buckley, P, Friedman, L, Meltzer, H, Hedera, P, and Friedland, R. Identification of vascular structures as a major source of signal contrast in high resolution 2D and 3D functional activation imaging of the motor cortex at 1.5T: preliminary results. *Magn Reson Med.* 1993. **30**(3), 387-92.

Lauterbur, PC. Image formation by induced local interactions: examples employing nuclear magnetic resonance. *Nature.* 1973. **242**, 190-1.

Le Bihan, D. Magnetic resonance imaging of perfusion. *Magn Reson Med.* 1990. **14**(2), 283-92.

Legatt, AD, Arezzo, J, and Vaughan, HG, Jr. Averaged multiple unit activity as an estimate of phasic changes in local neuronal activity: effects of volume-conducted potentials. *J Neurosci.Methods.* 1980. **2**(2), 203-17.

Liu, TT, Frank, LR, Wong, EC, and Buxton, RB. Detection power, estimation efficiency, and predictability in event- related fMRI. *Neuroimage.* 2001. **13**(4), 759-73.

Logothetis, NK. The neural basis of the blood-oxygen-level-dependent functional magnetic resonance imaging signal. *Philos.Trans R.Soc Lond B Biol.Sci.* 2002. **357**(1424), 1003-37.

Logothetis, NK, Pauls, J, Augath, M, Trinath, T, and Oeltermann, A. Neurophysiological investigation of the basis of the fMRI signal. *Nature.* 2001. **412**(6843), 150-7.

Mansfield, P. Multi-planar image formation using N.M.R. spin echoes. *J.Phys.C.* 1977. **10**, L55-L58.

Mathiesen, C, Caesar, K, Akgoren, N, and Lauritzen, M. Modification of activity-dependent increases of cerebral blood flow by excitatory synaptic activity and spikes in rat cerebellar cortex. *J Physiol.* 1998. **512 (Pt 2)**, 555-66.

Matthews, P. An introduction to functional magnetic resonance imaging of the brain. In: Jezzard, P, Matthews, P, and Smith, SM. Functional MRI. An Introduction to Methods. Oxford; Oxford University Press, 2001: 3-34.

Mattiello, J, Basser, PJ, and Le Bihan, D. The b matrix in diffusion tensor echo-planar imaging. *Magn Reson.Med.* 1997. **37**(2), 292-300.

Menon, RS, Ogawa, S, Hu, X, Strupp, JP, Anderson, P, and Ugurbil, K. BOLD based functional MRI at 4 Tesla includes a capillary bed contribution: echo-planar imaging correlates with previous optical imaging using intrinsic signals. *Magn Reson.Med.* 1995. **33**(3), 453-9.

Miller, KL, Luh, WM, Liu, TT, Martinez, A, Obata, T, Wong, EC, Frank, LR, and Buxton, RB. Nonlinear temporal dynamics of the cerebral blood flow response. *Hum.Brain Mapp.* 2001. **13**(1), 1-12.

Mitzdorf, U. Properties of the evoked potential generators: current source-density analysis of visually evoked potentials in the cat cortex. *Int.J Neurosci.* 1987. **33**(1-2), 33-59.

Mori, S, Crain, BJ, Chacko, VP, and van Zijl, PC. Three-dimensional tracking of axonal projections in the brain by magnetic resonance imaging. *Ann.Neurol.* 1999. **45**(2), 265-9.

Mori, S, Kaufmann, WE, Pearlson, GD, Crain, BJ, Stieltjes, B, Solaiyappan, M, and van Zijl, PC. In vivo visualization of human neural pathways by magnetic resonance imaging. *Ann.Neurol.* 2000. **47**(3), 412-4.

Mori, S and van Zijl, PC. Fiber tracking: principles and strategies - a technical review. *NMR Biomed.* 2002. **15**(7-8), 468-80.

Mosso, A. Über den Kreislauf des Blutes im menschlichen Gehirn. Leipzig; Verlag von Veit, 1881.

Muller, JR, Metha, AB, Krauskopf, J, and Lennie, P. Information conveyed by onset transients in responses of striate cortical neurons. *J Neurosci.* 2001. **21**(17), 6978-90.

Ogawa, S and Lee, TM. Magnetic resonance imaging of blood vessels at high fields: in vivo and in vitro measurements and image simulation. *Magn Reson Med.* 1990. **16**(1), 9-18.

Ogawa, S, Lee, TM, Kay, AR, and Tank, DW. Brain magnetic resonance imaging with contrast dependent on blood oxygenation. *Proc.Natl.Acad.Sci.U.S.A.* 1990a. **87**(24), 9868-72.

Ogawa, S, Lee, TM, Nayak, AS, and Glynn, P. Oxygenation-sensitive contrast in magnetic resonance image of rodent brain at high magnetic fields. *Magn Reson Med.* 1990b. **14**(1), 68-78.

Ogawa, S, Menon, RS, Tank, DW, Kim, SG, Merkle, H, Ellermann, JM, and Ugurbil, K. Functional brain mapping by blood oxygenation level-dependent contrast magnetic resonance imaging. A comparison of signal characteristics with a biophysical model. *Biophys.J.* 1993. **64**(3), 803-12.

Ogawa, S, Tank, DW, Menon, R, Ellermann, JM, Kim, SG, Merkle, H, and Ugurbil, K. Intrinsic signal changes accompanying sensory stimulation: functional brain mapping with magnetic resonance imaging. *Proc Natl Acad Sci U S A.* 1992. **89**(13), 5951-5.

Ohzawa, I, Sclar, G, and Freeman, RD. Contrast gain control in the cat visual cortex. *Nature.* 1982. **298**(5871), 266-8.

Ordidge, RJ, Helpern, JA, Qing, ZX, Knight, RA, and Nagesh, V. Correction of motional artifacts in diffusion-weighted MR images using navigator echoes. *Magn Reson Imaging.* 1994. **12**(3), 455-60.

Parker, GJ, Haroon, HA, and Wheeler-Kingshott, CA. A framework for a streamline-based probabilistic index of connectivity (PICo) using a structural interpretation of MRI diffusion measurements. *J Magn Reson Imaging.* 2003. **18**(2), 242-54.

Parker, GJ, Stephan, KE, Barker, GJ, Rowe, JB, MacManus, DG, Wheeler-Kingshott, CA, Ciccarelli, O, Passingham, RE, Spinks, RL, Lemon, RN, and Turner, R. Initial demonstration of in vivo tracing of axonal projections in the macaque brain and comparison with the human brain using diffusion tensor imaging and fast marching tractography. *Neuroimage.* 2002a. **15**(4), 797-809.

Parker, GJ, Wheeler-Kingshott, CA, and Barker, GJ. Estimating distributed anatomical connectivity using fast marching methods and diffusion tensor imaging. *IEEE Trans Med.Imaging.* 2002b. **21**(5), 505-12.

Pauling, L and Coryell, C. The magnetic properties and structure of hemoglobin, oxyhemoglobin and carbonmonoxyhemoglobin. *Proc Natl Acad Sci U S A.* 1936. **22**, 210-6.

Phelps, ME, Hoffman, EJ, Mullani, NA, and Ter Pogossian, MM. Application of annihilation coincidence detection to transaxial reconstruction tomography. *J Nucl.Med.* 1975. **16**(3), 210-24.

Pierpaoli, C and Basser, PJ. Toward a quantitative assessment of diffusion anisotropy. *Magn Reson.Med.* 1996. **36**(6), 893-906.

Poupon, C, Clark, CA, Frouin, V, Regis, J, Bloch, I, Le Bihan, D, and Mangin, J. Regularization of diffusion-based direction maps for the tracking of brain white matter fascicles. *Neuroimage.* 2000. **12**(2), 184-95.

Price, CJ, Veltman, DJ, Ashburner, J, Josephs, O, and Friston, KJ. The critical relationship between the timing of stimulus presentation and data acquisition in blocked designs with fMRI. *Neuroimage.* 1999. **10**(1), 36-44.

Purcell, EM, Torrey, HC, and Pound, CV. Resonance absorption by nuclear magnetic moments in a solid. *Physiol.Rev.* 1946. **64**, 37-8.

Rees, G, Friston, K, and Koch, C. A direct quantitative relationship between the functional properties of human and macaque V5. *Nat.Neurosci.* 2000. **3**(7), 716-23.

Roy, CS and Sherrington, CS. On the regulation of the blood supply of the brain. *J Physiol (Lond).* 1890. **11**, 85-108.

Siesjo, BK. Brain Energy Metabolism. New York; John Wiley and Sons, 1978.

Sokoloff, L. Relation between physiological function and energy metabolism in the central nervous system. *J Neurochem.* 1977. **29**(1), 13-26.

Song, AW, Wong, EC, Tan, SG, and Hyde, JS. Diffusion weighted fMRI at 1.5 T. *Magn Reson.Med.* 1996. **35**(2), 155-8.

Stejskal, EO and Tanner, JE. Spin diffusion measurements: spin-echo in the presence of a time dependent field gradient. *J Chem Phys.* 1965. **42**, 288-92.

Talairach, J and Tournoux, P. Co-planar stereotaxic atlas of the human brain. New York; Thieme Medical, 1988.

Ter Pogossian, MM, Phelps, ME, Hoffman, EJ, and Mullani, NA. A positron-emission transaxial tomograph for nuclear imaging (PETT). *Radiology.* 1975. **114**(1), 89-98.

Thulborn, KR, Waterton, JC, Matthews, PM, and Radda, GK. Oxygenation dependence of the transverse relaxation time of water protons in whole blood at high field. *Biochim.Biophys.Acta.* 1982. **714**(2), 265-70.

Torrey, HC. Bloch equations with diffusion terms. *Phys.Rev.* 1956. **104**(3), 563-5.

Tuch, DS, Wiegell, MR, Reese, TG, Belliveau, JW, and Wedeen, VJ. Measuring cortico-cortical connectivity matrices with diffusion spectrum imaging. *Proceedings of the 9th Scientific Meeting of the International Society for Magnetic Resonance in Medicine*. 2001. 502.

Turner, R, Howseman, A, Rees, GE, Josephs, O, and Friston, K. Functional magnetic resonance imaging of the human brain: data acquisition and analysis. *Exp.Brain Res.* 1998. **123**(1-2), 5-12.

Turner, R, Le Bihan, D, Maier, J, Vavrek, R, Hedges, LK, and Pekar, J. Echo-planar imaging of intravoxel incoherent motion. *Radiology*. 1990. **177**(2), 407-14.

Turner, R, Le Bihan, D, Moonen, CT, DesPres, D, and Frank, J. Echo-planar time course MRI of cat brain oxygenation changes. *Magn Reson Med*. 1991. **22**(1), 159-66.

Turner, R and Ordidge, RJ. Technical challenges of functional magnetic resonance imaging. *IEEE Eng Med Biol.Mag*. 2000. **19**(5), 42-54.

Vanzetta, I and Grinvald, A. Increased cortical oxidative metabolism due to sensory stimulation: implications for functional brain imaging. *Science*. 1999. **286**(5444), 1555-8.

Vazquez, AL and Noll, DC. Nonlinear aspects of the BOLD response in functional MRI. *Neuroimage*. 1998. **7**(2), 108-18.

Wheeler-Kingshott, CA, Parker, GJ, Symms, MR, Hickman, SJ, Tofts, PS, Miller, DH, and Barker, GJ. ADC mapping of the human optic nerve: increased resolution, coverage, and reliability with CSF-suppressed ZOOM-EPI. *Magn Reson.Med*. 2002. **47**(1), 24-31.

Worsley, KJ, Marrett, S, Neelin, P, Vandal, AC, Friston, KJ, and Evans, AC. A unified statistical approach for determining significant signals in images of cerebral activation. *Hum.Brain Mapp.* 1996. **4**, 58-73.

Xue, R, van Zijl, PC, Crain, BJ, Solaiyappan, M, and Mori, S. In vivo three-dimensional reconstruction of rat brain axonal projections by diffusion tensor imaging. *Magn Reson.Med.* 1999. **42**(6), 1123-7.

CHAPTER 3

A LONGITUDINAL STUDY OF THE FUNCTIONAL MRI RESPONSE TO PHOTIC STIMULATION FOLLOWING ACUTE OPTIC NEURITIS

This chapter describes the results of a study conducted in an acute optic neuritis (ON) patient cohort followed up over one year. By performing a longitudinal study, it was possible to observe the dynamics of the fMRI response to visual stimulation during the recovery process and consequently to investigate in greater detail the role of cortical plasticity following optic nerve insult.

3.1 Introduction

3.1.1 Cortical plasticity

Functional improvement is often seen following acute brain injury; however certain aspects of recovery cannot be explained by structural mechanisms such as the resolution of inflammation or oedema. FMRI has presented the opportunity to measure changes, relating to interactions at the level of large neuronal populations that follow neural insult (cortical plasticity). The term cortical plasticity has been defined as the "reorganisation of distributed patterns of normal task-associated brain activity that accompany action, perception, and cognition and that compensate impaired function resulting from disease or brain injury." (Frackowiak 1997). Plasticity in neuroscience research may also relate to lower levels of neural organization and may include axonal/neuronal (e.g. reflecting changes in sodium channel expression (Waxman 2001) or dendritic arborisation (Jones and Schallert

1992)) and synaptic (e.g. indicating changes in synaptic density, distribution or strength (Jacobs and Donoghue 1991)) mechanisms.

Although the capacity for cortical plasticity is at its greatest during the early years of CNS development, it appears to persist throughout life. The behavioural effects of cortical reorganization following CNS insult may be divided into different categories which describe, for example, *adaptive* and *maladaptive* processes. Adaptive cortical reorganization implies that the redistribution of neural processing in some way contributes to the mechanisms involved in clinical recovery or helps to maintain a degree of clinical function in the presence of structural damage. At least four forms of adaptive plasticity have been suggested (Grafman and Litvan 1999): (i) *Homologous area adaptation* – implies that the damaged brain region can be compensated for by transferring the neural operations to other unaffected brain modules (usually in the homologous region of the opposite hemisphere). (ii) *Cross-modal reassignment* – occurs when cortical modules usually devoted to processing particular sensory inputs, now accept inputs from another sensory modality. (iii) *Map expansion* – is the enlargement of a functional cortical region in response to frequent stimulus exposure or following adjacent cortical injury. (iv) *Compensatory masquerade* – is the novel allocation of a cognitive strategy to perform a task that otherwise would depend on another cognitive process which is now impaired.

However, cortical reorganization may not necessarily contribute to recovery of clinical function. It may also reflect the recruitment of unusual distributed neural networks purely as a 'stress' response to CNS injury implying that it can be *non-adaptive*.

Indeed, plastic changes, in response to injury, may also have deleterious behavioural effects resulting in functional loss rather than gain. This form of plasticity is termed *maladaptive* and is, for example, thought to account for phantom limb pain following amputation (Lotze et al, 2001).

3.1.2 Functional MRI in demyelinating disease

A principal challenge of functional neuroimaging is to determine the role of cortical plasticity in neurological disease. Although this thesis focuses upon ON, previous studies have already been performed to investigate how the brain possibly adapts to neurological damage in demyelinating disease. These studies have mostly employed experimental paradigms for the visual and the motor systems and can be categorized into those that address (i) clinically isolated syndromes e.g. ON, (ii) relapsing remitting MS (iii) secondary progressive MS and (iv) primary progressive MS.

3.1.2.1 Clinically isolated syndromes

Previous visual fMRI studies have been mainly cross-sectional and have studied patients with previous ON (Rombouts et al, 1998; Russ et al, 2002; Toosy et al, 2002a; Werring et al, 2000). The main findings have been reduced fMRI visual cortex activation with occasional evidence for correlations between fMRI activity and visual function or VEP data. In particular, Werring et al (Werring et al, 2000) studied a group of seven patients who had recovered from a single episode of acute ON and demonstrated an extensive extra-occipital pattern of activation (that included the insula, lateral temporal cortex, inferior parietal cortex, orbitofrontal cortex and corpus striatum). The volume of extra-occipital activation correlated with the VEP latency in the patients. These extra-occipital regions are known to have connections with primary visual areas in animal models and some are thought to be involved in multimodal sensory integration. It was suggested that their activity might represent an adaptive response to a persistently abnormal visual input. An interesting finding from this study was the observation that the extra-occipital activation correlated inversely with the experimental paradigm i.e. that they were deactivations. This was confirmed in a follow up study on the same patients in which the photic stimulation epoch length was doubled (Toosy et al, 2002a).

Motor fMRI studies have also been applied to clinically isolated syndromes. One study conducted proton magnetic resonance spectroscopy as well as upper limb motor fMRI sequences (Rocca et al,

2003b). Patients, recruited within three months of symptom onset, had greater activation of the contralateral sensorimotor cortex, secondary somatosensory cortex and inferior frontal gyrus compared with controls ($P<0.05$, voxel level corrected). They also had reduced whole brain N-acetylaspartate concentrations (indicating axonal injury) which were inversely correlated with the contralateral sensorimotor cortex fMRI response. As the task performance was matched between patients and controls, it was suggested that the correlation may reflect adaptive cortical plasticity to maintain normal clinical function in the presence of brain neuronal injury.

Another motor fMRI study examined 10 patients who had recovered from a previous episode of hemiparesis and reported greater activation extents within regions such as the lateral premotor cortex, inferior parietal lobule and insula ($P<0.001$, uncorrected) compared with 10 controls, regardless of whether the affected or unaffected hands were examined (Pantano et al, 2002a). A follow up study compared three groups using upper limb motor fMRI – 10 patients with previous hemiparesis, 10 patients with previous ON and 10 controls (Pantano et al, 2002b). The hemiparetic patients demonstrated greater ipsilateral activation within the sensorimotor cortex, parietal cortex and insula and greater contralateral activation in the motor cortex ($P<0.05$, cluster level corrected). There was also a positive correlation between markers of damage for the corticospinal tracts (T2 and T1 lesion loads) and activation of several motor related areas from both hemispheres. The ON group also showed increased activation compared with controls in some contralateral regions (sensorimotor cortex, lateral premotor cortex, insula, lentiform) but statistical threshold used was quite lenient ($P<0.01$, uncorrected) to minimize the type I family wise error rate and so these results should be interpreted with caution.

Single episode spinal cord relapses (myelitis) have also been investigated using fMRI. A recent study investigated 14 patients with previous cervical myelitis and normal upper limb function (Rocca et al, 2003c). Upper limb motor FMRI and DTI of the brain were conducted as well as magnetization transfer imaging and conventional MRI of the cervical cord and brain. Compared with healthy

volunteers, the myelitis patients had significantly greater activations in the ipsilateral primary sensorimotor cortex, supplementary motor area and middle frontal gyrus. The average cervical cord magnetization transfer ratio was inversely correlated with activations within the middle frontal and ipsilateral postcentral gyri suggesting a possible role for adaptive cortical plasticity.

3.1.2.2 Relapsing remitting multiple sclerosis

Several motor fMRI studies have investigated cortical reorganization in MS. An early study serially scanned a relapsing remitting MS patient during the recovery period of a right hemiplegic relapse which was associated with a left hemisphere demyelinating lesion (Reddy et al, 2000b). MR spectroscopy and fMRI were performed over six months following presentation. The NAA concentration in the affected corticospinal tract increased in parallel with clinical recovery. The fMRI activation was larger at three and six weeks, compared with controls, in contra- and ipsi-lateral motor areas whereas at six months it had returned to control levels. Clinical function had recovered by six weeks and remained stable thereafter. This study demonstrated dynamic changes in the motor fMRI response following acute subcortical injury even after the completion of clinical recovery.

In a follow up study by Lee et al, greater ipsilateral motor cortex activation was demonstrated in a group of 12 MS patients compared with 12 healthy controls (Lee et al, 2000). A lateralization index was calculated to quantify the contralateral bias and was found to inversely correlate with disease burden as measured by the T2 lesion load. In particular, greater ipsilateral supplementary motor cortex activation extent positively correlated with lesion load. A posterior shift in the activation centre by 8.8 mm of the contralateral supplementary motor cortex in patients relative to controls was also reported. The authors surmised that these results could reflect adaptive cortical plasticity.

Some studies have used MS patients with normal upper limb function in an attempt to avoid confounding influences of differences between patient and control performance. Reddy et al compared nine MS patients who had unimpaired upper limb hand function with eight normal controls

(Reddy et al, 2000a). The authors demonstrated a fivefold increase in sensorimotor cortex activation for the MS patients relative to normal controls. They also reported a significant correlation between the volume of ipsilateral sensorimotor cortex activation and the central white matter NAA (σ =-0.93, P=0.001). It was felt that, although the corticospinal tracts were not selectively sampled, the central white matter NAA measurements still reflected corticospinal tract pathology. The authors suggested that adaptive cortical reorganization had occurred to compensate for axonal injury presumably to the corticospinal tracts in order to maintain hand function. In another study 15 non-disabled relapsing remitting patients were compared with 14 controls using a simple motor task. In addition to fMRI, patients underwent DTI and magnetization transfer imaging. MS patients showed greater activation in regions including the contralateral primary sensorimotor cortex, secondary somatosensory cortex and intraparietal sulcus as well as bilateral supplementary motor areas and the cingulated motor area ($P<0.05$, corrected). Strong correlations were found between the spatial extents of fMRI activation and several structural brain metrics derived from DTI and magnetization transfer imaging. This, the authors suggested, could be explained by adaptive reorganization of the motor network in MS to limit the functional effect of the diffuse brain injury.

Another study attempted to avoid task performance confounds by comparing the activation between non-disabled relapsing remitting MS patients and controls in response to a simple upper limb motor paradigm (Rocca et al, 2002). The authors also acquired magnetization transfer and diffusion tensor images to provide crude indices of structural brain pathology. The MS patients (median T2 lesion load 9.4 ml (range 1.2–41.7 ml)) showed increased activity in several mainly contralateral regions, including the primary sensorimotor cortex, the secondary somatosensory cortex and the intraparietal sulcus. There was also greater activation bilaterally in the supplementary motor area and the cingulated motor area. The authors noted some correlations between the extent of fMRI activations and several MR derived indices of structural brain pathology and postulated a process of adaptive functional reorganization that acts to limit the clinical impact of MS.

A further study carefully selected 12 right handed relapsing remitting MS patients with no upper limb disability (EDSS range 0-6.0) and conventional MRI head scans within normal limits (i.e. $\leq$ 3 lesions) (Rocca et al, 2003d). There were no intracranial lesions along the pyramidal tracts or corpus callosa although multiple spinal cord abnormalities were identified in three of the patients. Motor fMRI and DTI were performed and the results compared with 12 right handed healthy volunteers. The MS patients demonstrated greater activation in the ipsilateral supplementary motor area, superior frontal sulcus and contralateral superior temporal gyrus and thalamus. The SMA fMRI response was correlated with the peak height and position of the mean diffusivity histogram of the segmented normal appearing grey matter. The healthy controls showed greater activation in the contralateral parieto-occipital fissure and ipsilateral sensorimotor cortex. The latter difference was explained by deactivation within this area for the MS group and the authors speculated that this could result from altered 'transcallosal inhibition' (Liepert et al, 2001), a phenomenon thought to control homologous hand muscles during unilateral movements.

Clinical disability itself is known to be associated with altered patterns of cortical activation. This relationship may simply reflect the expected dependence of disability on structural brain injury but it may also be directly related to disability, such as altered patterns of use. An upper limb motor fMRI study was designed to investigate this by selecting three groups of (Reddy et al, 2002) patients with relapsing-remitting or relapsing-progressive MS: (i) Group 1 – Normal hand function and low levels of white matter injury. (ii) Group 2 – Normal hand function and higher levels of white matter injury. (iii) Group 3 – Reduced hand function and higher levels of white matter injury. Groups 1 and 2 were matched for hand function whereas groups 2 and 3 were matched for white matter injury. The latter was estimated from N-acetylaspartate to creatine ratios, derived from MR spectroscopy, of the central brain. Contrasts between groups 2 and 1 showed greater activation within the supplementary motor area bilaterally and premotor cortex ipsilaterally for group 2. A comparison between groups 2 and 3 revealed greater primary and secondary somatosensory, as well as parietal cortex activation, in group 3. This was interpreted as a disability related reorganization of brain function and the authors

felt therefore that both clinical disability and structural brain injury may contribute to changes in the patterns of movement-associated brain activation.

In addition to motor fMRI, cognitive tasks have been investigated using fMRI in MS. Staffen et al found greater activation for frontal and parietal areas in relapsing remitting MS patients with mild disability (Staffen et al, 2002) compared with controls during the Paced Visual Serial Addition Task. They felt that this represented compensatory cortical plasticity for the MS patients, possibly as a result of raised cerebral effort.

3.1.2.3 Secondary progressive multiple sclerosis

Rocca et al recently published a study looking at both right upper and lower limb motor fMRI tasks in 13 patients with secondary progressive MS (Rocca et al, 2003a). They selected patients with clinically unaffected right limbs to avoid task performance confounds. DTI was also performed and showed reduced grey and white matter measures of FA and diffusivity in patients compared with 15 healthy volunteers. With the upper limb task (finger extension-flexion), compared with controls, the MS patients demonstrated greater activation in the ipsilateral inferior frontal gyrus, middle frontal gyrus, bilaterally and contralateral intraparietal sulcus. For the lower limb task (ankle flexion-extension) the MS patients showed more activation of the contralateral sensorimotor cortex and thalamus and of the ipsilateral sylvian fissure. Some strong correlations were found between the several DTI measures and both motor tasks in the frontal lobes.

3.1.2.4 Primary progressive multiple sclerosis

Primary progressive MS is characterized by the accumulation of progressive clinical deficit. Affected patients tend to have lower MRI lesion loads although several structural measures of normal appearing brain tissue have pointed towards a more prominent role for axonal degeneration (Filippi and Comi 2002).

FMRI studies with primary progressive MS patients have involved motor paradigms. One study investigated the fMRI response to simple and complex motor tasks in 30 primary progressive patients. The functional response of clinically unaffected limbs was compared with that from 15 healthy volunteers. In the MS group, the simple motor task activated more in the contralateral supplementary motor area, the secondary somatosensory cortex and other frontal and temporal regions, including the insula and superior temporal gyrus. This widespread cortical pattern involved some regions thought to be associated with multimodal integration (Mesulam 1998). With the more complex motor task, MS patients exhibited more activation in the ipsilateral thalamus, middle frontal gyrus, bilaterally and other regions including the ipsilateral visual cortex. It was felt that this could reflect enhanced visual-sensory interactions in the primary progressive group.

A further study applied fMRI, DTI magnetization transfer and cord imaging in primary progressive MS patients with normal right upper limb function (Filippi et al, 2002). It reported correlations between the extent of fMRI activation in sensorimotor areas and several measures of brain and cord structural pathology, suggesting the existence of attempted compensatory mechanisms within the brain to preserve clinical function in response to structural damage.

3.1.2.5 Interpretational issues with cortical adaptation

There are some interpretational caveats that may limit the inferences about the functional nature of cortical reorganization after neurological insult. Firstly, there is an implicit assumption, when comparing neurological disease with healthy controls, that the neurovascular coupling mechanisms generating the BOLD response are similar. This may not be the case e.g. for example, it is possible that vasoactive substances derived from inflammatory lesions could alter the spatiotemporal dynamics of the BOLD response. In practice, it tends not to be considered important and may be more relevant with event-related fMRI studies and with diffuse (as opposed to focal) neurological disease.

Secondly, with motor tasks, there should be careful control of task performance between individuals as it is well known that task complexity (Catalan et al, 1998; Wexler et al, 1997) and effort (Ward and Frackowiak 2003) will affect the resulting brain activation patterns. A related issue concerns the decision to control for absolute or relative biomechanical parameters (e.g. with movement frequency and amplitude or force generation). Although the studies described in the previous sections tended to control for absolute mechanical parameters (in particular movement frequency), Ward et al have controlled for individual relative effort. They reason that patients, with impaired motor performance, who are asked to perform a motor task with the same absolute parameters as controls will find the task more effortful or cognitively complex resulting in differences in activation secondary to differences in relative effort. This argument has greater applicability in patients with impaired function.

Thirdly, most of the correlations described previously between fMRI activation and diffuse brain structural integrity, although presumed to be adaptive, may yet be non-adaptive. They may constitute a 'stress' or hyperexcitable response of certain cortical regions to diffuse brain injury. In addition, it is difficult to exclude non-adaptive reorganization because the structural integrity of the specific corticospinal pathways involved in the limb movements that were studied, was not specifically investigated. Measures of diffuse brain integrity were assumed to directly reflect pyramidal tract pathology. It is therefore possible that preserved limb function could be accounted for by its subserving structurally intact corticospinal pathways in the presence of brain pathology elsewhere, which may then be detected.

Finally, it has been shown that the fMRI response to upper limb motor tasks may be altered in patients who have had neurological insults to other systems (e.g. visual) or to the lower limbs (Pantano et al, 2002b). This could make interpretation of the reorganized response difficult because, although most motor fMRI studies in MS have controlled for upper limb motor function, it is not

apparent that the severity of involvement of other neurological systems (e.g. visual, cerebellar, cognitive) or of the lower limbs has been controlled for. Thus the altered fMRI activation may represent a non-adaptive response to damage of non upper limb related neural pathways e.g. those subserving lower limb or visual function.

In reality, it is likely that functional reorganization following neurological injury may comprise a mixture of both adaptive and non-adaptive components. These will be complex, dynamic and dependent upon complex interrelationships both within the reorganized networks and between other neurological subsystems with their cortical substrates and will also be influenced by the structural integrity of the specifically involved neural pathways.

3.1.3 Outline of longitudinal fMRI study in acute ON

The objectives of the study, to be described below, were to follow up on the findings of Werring et al which showed reduced visual cortex activation associated with an extra-occipital network of (de-)activations in seven patients following a single episode of ON (Werring et al, 2000). The regions involved (which included the insula, lateral temporal cortex, corpus striatum, orbitofrontal and inferior parietal cortices) are known to have connections with visual processing areas and some of them have been proposed as areas of multimodal sensory integration (Mesulam 1998). In order to investigate the potential roles that these areas play after ON, we examined the temporal relationship of the visual fMRI response within these regions to functional recovery in a longitudinal study in which we recruited patients with acute ON and followed them over one year. The study was split into two analyses. Both used the same recruited subjects and image acquisition (see 3.2.1 and 3.2.2). The first compared ON patients with controls (see 3.2.3 for statistical analysis, 3.3 for results and appendix A) whereas the second comprised correlations to determine the nature of fMRI activation within ON patients (see 3.4). Both analyses are finally discussed to conclude this chapter (see 3.5).

3.2 Methods

3.2.1 Subjects

Patients – 21 subjects (baseline characteristics – mean age 33.8 years, 9 men, 12 women) with their first episode of typical acute unilateral ON were recruited from Moorfield's Eye Hospital, London, within three weeks of symptom onset. Ethical approval was obtained as was informed consent in writing from each subject, according to the Declaration of Helsinki. They were studied at the following time points following recruitment: baseline, 2 weeks, 1 month, 2 months, 3 months, 6 months and 1 year.

Controls – 46 healthy volunteers (mean age 32.0 years, 24 men, 22 women) underwent fMRI scanning at least once. Of these, 26 were scanned twice or more to investigate intersessional variability. 11 of these 26 controls were scanned three times, in total, over the course of one year to investigate longitudinal changes.

Clinical Examination – At each time point patients were clinically assessed. Best visual acuity was measured (unaided, with appropriate spectacle correction or with pinhole correction) using a retro-illuminated ETDRS (Early Treatment Diabetic Retinopathy Study) chart and recorded as the 4m logMAR visual acuity and Snellen equivalent (Ferris, III et al, 1982). When no letters could be correctly identified a score of 1.7 was assigned (Optic Neuritis Study Group, 1991). The central 30° of the visual field was analysed using the 30-2 program on the Humphrey field analyser (Allergan-Humphrey Inc., San Leandro, CA, USA). The overall field mean deviation was compared with a reference field derived from control data provided by the manufacturer. A mean deviation of -35dB was assigned when vision was too poor to attempt the test (Kupersmith et al, 2002). LogMAR acuity and Humphrey mean field deviation (HMD) were chosen because they are continuous variables and are amenable to statistical analysis.

Whole field pattern-reversal visual evoked potentials (VEP) were also obtained for each patient at baseline, 1 month, 3 months and 1 year (Brusa et al, 2001). The VEPs were recorded such that the screen subtended 28° horizontally x 20° vertically and the check size was 40'.

3.2.2 Image acquisition

MR images were acquired using a 1.5 Tesla GE Signa Horizon Echospeed system (General Electric, Milwaukee, Wisconsin, United States) with a standard quadrature head coil.

3.2.2.1 Structural imaging and post-processing

Brain imaging was performed at baseline and at 1 year using an axial-oblique dual echo fast spin echo (FSE) sequence (TR 2000ms, TEef 19/95ms, 2 excitations, echo-train length[ETL] 8, matrix size 256x256, field of view(FOV) 24x18cm, 5mm contiguous slices). Total T2-weighted lesion loads for each brain and the optic radiations were then determined by an experienced observer (SJH) using a semi-automated contouring method (DispImage) (Plummer 1992). Optic nerve imaging was performed for patients and comprised: 1) sTE fFLAIR sequence at each time point (coronal-oblique, TR 2740ms, TE 16ms, TI 1072ms, NEX 6, ETL 6, matrix size 512x384, FOV 24x18cm, 3mm contiguous slices). The mean cross-sectional area of the intra-orbital portion of each optic nerve was calculated by an experienced observer (SJH) blinded to image identity and acquisition order from five consecutive 3mm slices anteriorly from the orbital apex using a previously described technique (Hickman et al, 2001). 2) Coronal-oblique fat-saturated T_1-weighted spin-echo post triple-dose gadolinium sequence (TR 600ms, TE 20ms, matrix size 256x192, FOV 24x18cm, 16 contiguous 3mm slices) at baseline. A blinded radiologist (KAM) determined the enhanced lesion lengths.

3.2.2.2 *Functional imaging*

The study began with an fMRI acquisition that provided partial brain (PB) coverage. Later, the acquisition was extended to allow whole brain coverage (WB) and this was implemented during the course of study on subsequent new patients and controls (see table 3.1). The results from both WB and PB acquisitions were combined in the subsequent statistical analysis.

Partial brain (PB) acquisition - 120 T2*-weighted single-shot EPI images depicting blood oxygenation level dependent (BOLD) contrast were acquired in each 8 minute experiment at each of 11 near-axial 5mm thick slices through visual cortex approximately parallel to the AC-PC line (TE 40 ms; TR 4000ms; FOV 24cm; matrix 96x96; acquisition in-plane resolution, 2.5x2.5mm (1.88x1.88mm after reconstruction at 128x128 matrix size); interslice gap, 0.5mm).

Whole brain (WB) acquisition - 150 T2* weighted images depicting BOLD contrast were acquired in each 10 minute experiment at each of 27 near-axial slices of the whole brain (TE 40ms, TR 4000ms, field of view, 38x19cm, matrix size, 128x64, in-plane resolution 3x3mm, slice thickness 3.6mm, interslice gap 0.4mm).

Experimental design - Subjects passively viewed a visual display which alternated periodically between 20 second epochs of two contrasting conditions: (A) red 8 Hz photic stimulation to the whole visual field was presented to one eye using lightproof goggles (Grass Instruments, Quincy, MA, USA Model SV10SB) whereas the other eye received no visual stimulation; (B) no visual stimulation (darkness) was presented to both eyes; condition B (no stimulation) was always presented first. Each subject was studied twice, once for each eye. Each experiment lasted 8 (PB) or 10 (WB) minutes and the order of side of monocular stimulation was randomly decided.

3.2.3 Statistical analysis – Comparisons between ON patients and controls

Statistical parametric mapping software (SPM99, Wellcome Department of Cognitive Neurology, London, UK) was used. Each fMRI time series was realigned, normalized to a standard stereotactic MNI (Montreal Neurological Institute) space and smoothed (8mm isotropic Gaussian kernel). The general linear model (Friston et al, 1995) was implemented to determine the main effect of photic stimulation, with realignment parameters entered as covariates of no interest. For every subject one fixed effects analysis was performed for each eye. Two contrasts were consequently obtained for each subject, representing the fMRI response for the left and right eye.

3.2.3.1 Control data investigation

This was performed to test the assumptions for the subsequent analyses. Four sub-analyses were conducted independently for left and right eye control contrasts. Statistical inferences were made on the derived SPM(T) maps thresholded at $p<0.05$ corrected at the voxel level across the whole search volume.

a) Longitudinal assessment – 11 controls that had three fMRI sessions over 1 year were entered into a random effects analysis (RFX) in a one-way ANOVA model to assess differences in the fMRI response between any of the three sessions.

b) Between session variability – For 26 controls that were scanned twice, each fMRI session was divided equally into 2 subsessions. This created 4 subsessions per control. Their order of acquisition was randomized for each subject (see figure 3.1) and the resulting 4 groups were assessed for differences again using a RFX one-way ANOVA model in SPM99.

c) Age and gender regression – Age and gender effects were assessed in the control group with a multiple regression RFX model in SPM.

d) FMRI protocol and side – The effects of partial vs whole brain acquisition and left vs right side were tested with a multiple regression RFX model in SPM.

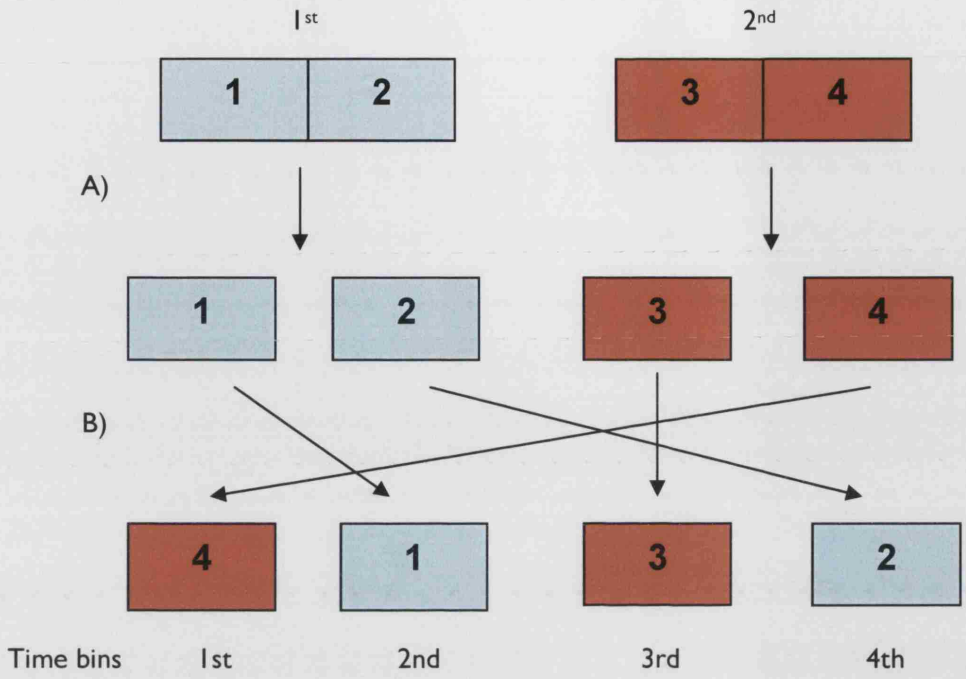

Figure 3.1. 26 controls underwent two fMRI sessions. This figure shows how the sessions were split for one subject. (A) Each of the two sessions was divided into two halves which created four subsessions. (B) The order of these subsessions was then randomized into a new order which was reassigned to four time bins. These would be matched to the patients' four time bins, to be described in the 'hierarchical regression analysis' section below.

3.2.3.2 Hierarchical regression analysis

This investigated how gradual changes over time in the functional response to photic stimulation differed between patients and controls during the first six months following recruitment. A balanced design was necessary to compare patients with controls. To achieve this, the following steps were taken. 1) The seven time points for 17 patients were collapsed into 4 time bins: 0-2 weeks, 1-2, 3 and 6 months. For the first two time bins, patient sessions were randomly selected to ensure an even selection across the group (see table 3.1). For the last two time bins, every patient contributed an fMRI session (for each eye). Thus, for each of 17 patients four fMRI sessions were chosen (for each eye) to represent the fMRI response in patients across 6 months. 2) The first half of each selected patient fMRI session was entered into the regression analysis. 3) At the first level of fMRI analysis, each patient's selected subsessions (four) were entered into a fixed effects model, from which contrasts that represented a) mean activation (1 1 1 1), b) linear changes (-3 -1 1 3) and c) second

order changes (1 -1 -1 1), were derived (figure 3.2). 4) Equivalent contrasts were also generated for the 24 controls whose studies had been divided and randomized into four subsessions (see above 'control data investigation' paragraph b)). 5) The patient and control contrast images were compared using one-way ANOVA models.

Patient	Age	Sex	fMRI	Side	Visual Acuity Affected side						
					First	2 wks	1 mth	2 mth	3 mth	6 mth	1 yr
1	28	M	PB	L(+R)	**6/75**	6/15	**6/11**	6/8	**6/7**	**6/7**	6/5
2	42	F	PB	L	6/10	**6/10**	6/7	**6/7**	**6/6**	**6/6**	6/5
3	38	F	PB	L	**6/79**	6/11	**6/8**	6/7	**6/6**	**6/7**	6/5
4	26	F	PB	L	HM	**6/300**	**6/83**		**6/15**	**6/8**	
5	53	F	PB	L	**6/104**	6/55	6/40	**6/30**	**6/26**	**6/25**	6/25
6	27	M	PB	L	**6/5**		**6/5**		**6/5**	**6/5**	6/4
7	33	F	PB	R	6/8	**6/5**	6/5	**6/5**	**6/6**	**6/5**	6/5
8	24	F	PB	R	6/10	**6/8**	6/7	**6/8**	**6/7**	**6/5**	6/5
9	46	M	WB	L	**6/48**	6/208	**6/100**	6/17	**6/14**	**6/22**	6/20
10	34	M	WB	L	CF	**6/21**	6/8	**6/6**	**6/6**	**6/6**	6/5
11	30	F	WB	R(+L)	**6/120**		**6/6**		**6/5**	**6/4**	6/5
12	27	F	WB	R	6/13	**6/10**	6/8	**6/8**	**6/8**	**6/5**	6/5
13	29	F	WB	R	**6/14**		**6/6**	6/5	**6/5**	**6/4**	6/4
14	22	M	WB	R(+L)	HM	**6/181**		**6/19**	**6/40**	**6/109**	6/69
15	44	M	WB	R	**6/8**		**6/12**	6/15	**6/12**	**6/12**	6/15
16	35	F	WB	R	**HM**		6/7	**6/6**	**6/5**	**6/6**	6/5
17	23	F	WB	R	**6/125**	6/20	**6/15**	6/15	**6/10**	**6/8**	6/8
18	30	M	PB	R	6/218	6/12	6/6				
19	41	M	PB	L	6/13		6/20			6/6	6/6
20	47	F	PB	R	6/79						
21	31	M	WB	R	CF						

Time bin divisions 1st 2nd 3rd 4th

Table 3.1. Patient characteristics for age, sex, acquisition protocol, affected side and visual acuity for affected eye. Note that three patients suffered contralateral optic neuritis following recruitment – patient 1 at 12 wks, patient 11 at 22 wks and patient 14 at 11 wks. Fellow visual acuities are not shown. The sessions chosen for the regression analysis are highlighted in grey. The time bin divisions are shown below the table. The sessions chosen for the cross-sectional analysis (described below) are in red font. Four time bins were extracted (17 sessions per bin) into the regression analysis. Note that most patients had made a good recovery by 3 months. PB = partial brain, WB = whole brain.

Each model comprised four groups to represent PB vs WB acquisitions and patients vs controls. This ensured that comparisons between patients and controls were matched for PB or WB acquisition. The control groups were also matched for side of stimulation.

3.2.3.3 Cross-sectional analysis

This enabled us to investigate dynamic differences between patients and controls. In order to make comparable inferences between time points we selected the most number of patients that attended the most number of time points. As a result, we excluded data from 2 weeks and 2 months from further analysis. 17 patients were chosen from the baseline, 1 month and 6 month time points and 16 patients were chosen from the 3 month and 1 year time points. Contrast images, that represented the fMRI response to photic stimulation, were generated for every patient and control session. The control contrast images were divided into four groups for PB left (33 sessions), PB right (33 sessions), WB left and WB right eye stimulation (50 sessions per side) and were subsequently averaged to create four contrast images. These estimated the population fMRI response for each of the four categories. For every patient contrast image, a further image was then generated that showed the differences between the patient contrast and the corresponding control average (matched for side of stimulation and acquisition protocol). These 'diffcon' images were grouped into the five time points for affected and fellow eyes and represented the group difference between patients and controls after correcting for side of stimulation and acquisition protocol. Random effects analyses using one-sample t-tests were conducted at each time point for the diffcon images to test for differences between patients and controls.

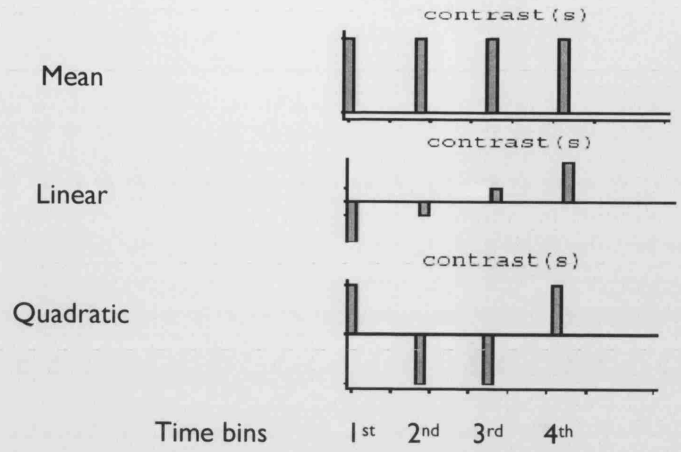

Figure 3.2. Hierarchical regression analysis. At the first level a fixed effects analysis was performed for each subject into which was entered the four subsessions. Three contrasts were derived per subject as shown above.

3.2.3.4 Statistical Inferences

Previous studies have investigated the possible role of functional reorganization following recovery from demyelination. This allowed us to generate an *a priori* hypothesis that we used to focus on specific regions of interest when comparing patients with controls. The regions of particular interest were - insula, corpus striatum, lateral temporal cortex, orbitofrontal cortex, inferior parietal and visual cortex. Unless stated otherwise, every statistical inference for regionally specific differences between patients and controls was conducted using small volume correction (SVC) with a 10-15 mm radius sphere on uncorrected t-contrast maps ($p<0.001$) at predesignated co-ordinates (table 3.2).

Region	X	Y	Z	SVC radius
Visual Cortex	0	-86	0	15
Insula	±34	10	-2	10
Lateral Temporal	±60	-24	4	12
Corpus Striatum	±14	8	0	10
Orbitofrontal	±14	40	-6	12
Posterior Parietal	±48	-24	20	12

Table 3.2. Voxel co-ordinates (in MNI space) for regions of interest that were investigated with small volume correction (SVC) for multiple comparisons on the uncorrected t-contrast maps thresholded at $p<0.001$. The radius for the spherical volume, that was used, is shown in mm for each region.

3.3 Results

3.3.1 Control data assessment

Longitudinal assessment – No significant longitudinal effects were found for the controls that were assessed across one year for both left and right eye stimulation. This enabled us to randomize sessions acquired at different times for the control group in the regression analysis.

Between session variability – No significant differences were obtained when comparing between the randomized groups of control subsessions.

Age and gender regression – There were no significantly detectable age or gender effects within the control group (age range 17-71 years). This allowed us to omit age and gender when matching the control groups with the patients.

FMRI protocol and side – Significant effects were found for side of stimulation (left vs right) within the occipital cortex and fMRI protocol (partial vs wholebrain). The controls were consequently matched for these two variables.

3.3.2 Regression analysis

Figure 3.3 shows the results from the regression analysis for comparisons of the mean, 1st and 2nd order effects over the first six months following recruitment. There is an overall reduction in fMRI activity in the visual cortex of ON patients compared with controls. In addition, ON patients have a greater positive slope for fMRI activity than controls within the visual cortex over the six months.

3.3.3 Cross-sectional analysis

Table 3.3 and table 3.4 summarize the results. Differences in activation were considered significant with $p<0.05$ (corrected for multiple comparisons). P values between 0.05 and 0.1 were considered to provide weak evidence for a difference in fMRI activity between patients and controls. Results are

also displayed graphically after the tables (figure 3.4). The main findings from the cross-sectional results will be summarized after figure 3.4.

	Affected eye		Unaffected eye	
	Pat>Con	Con>Pat	Pat>Con	Con>Pat
MEAN	-	Visual Cortex P<0.001 Z=4.68 k 869	-	-
LINEAR	Visual Cortex P=0.034 Z=3.56 k 58	-	-	-
QUADRATIC	R Lat Temp Cortex P=0.05 Z=3.33 k 9	-	-	-

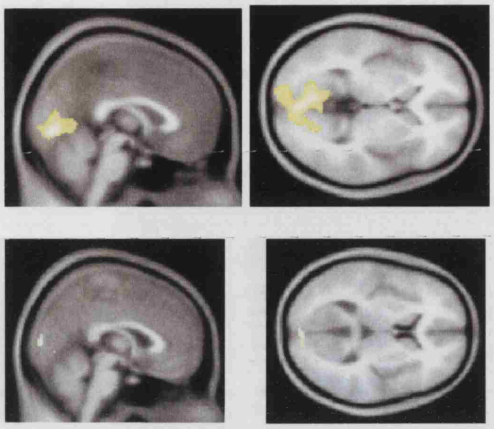

Figure 3.3. Regression analysis results. In the fellow eye, no differences were found between patients and controls for mean, linear effects and 2nd order effects. With the affected eye, the mean level of activation was greater in controls that ON patients with p<0.001 corrected, peak Z 4.68. There was also a linear effect over time (p=0.034, peak Z 3.56) which could reflect the functional recovery of the visual cortex as patients recover. The results overlaid onto structural templates are shown to the right of the table. There were also some minor 2nd order effects greater in patients than controls. K = number of suprathreshold voxels within the SVC used.

Time points		First	1 mth	3 mths	6 mths	1 yr
Degrees of freedom		16	16	15	16	15
Affected	Insula	R ++	R ++	R +	-	L+
	Lat Temp	R+ L+	R++ L++	L+	-	R++
	Corpus Striatum	R++	L++ R++	R++ L+	-	L+
	Orbitofrontal	-	R+ L++	L+	-	R+
	Inf Parietal	-	-	L++	-	L+
Fellow	Insula	R++ L+	R++ L++	L++	-	-
	Lat Temp	R+ L+	R++ L++	R++ L++	-	R++ L++
	Corpus Striatum	R++	R++ L++	R++ L++	-	R++
	Orbitofrontal	-	R++	-	-	R++
	Inf Parietal	-	L++	-	-	L ++

Table 3.3. (Above) Cross-sectional results where patients > controls. The regions where patients activated more than controls are shown for stimulation of the affected and fellow eyes. The regions of interest defined by the a priori hypothesis are listed on the left of the table (see also table 2). All inferences were made after correction for multiple comparisons to protect against type I errors (i.e. protect against false positives). The significance of each region is shown at every time point in the study. P values <0.05 were considered significant and designated by "++"; P values between 0.05 and 0.1 were considered as weak evidence and assigned as "+". For example, significant differences in the insula appear to subside after 3 mths. The degrees of freedoms (df) for the one sample t-tests are shown along the second row. The overall impression from the table is that extra-occipital differences in activation appear early and then subside by 6 mths. There is weak evidence for the reappearance of some differences at 1 year.

Time points		First	1 mth	3 mths	6 mths	1 yr
Degrees of freedom		16	16	15	16	15
Affected	Visual Cortex	++	++	++	++	++
Fellow	Visual Cortex	-	-	-	-	-

Table 3.4. Cross-sectional results where controls were found to activate more than patients. These differences were confined to the visual cortical areas and were present at every time point for the stimulation of the affected eye. There were no differences between patients and controls in the visual cortex for stimulation of the fellow eyes.

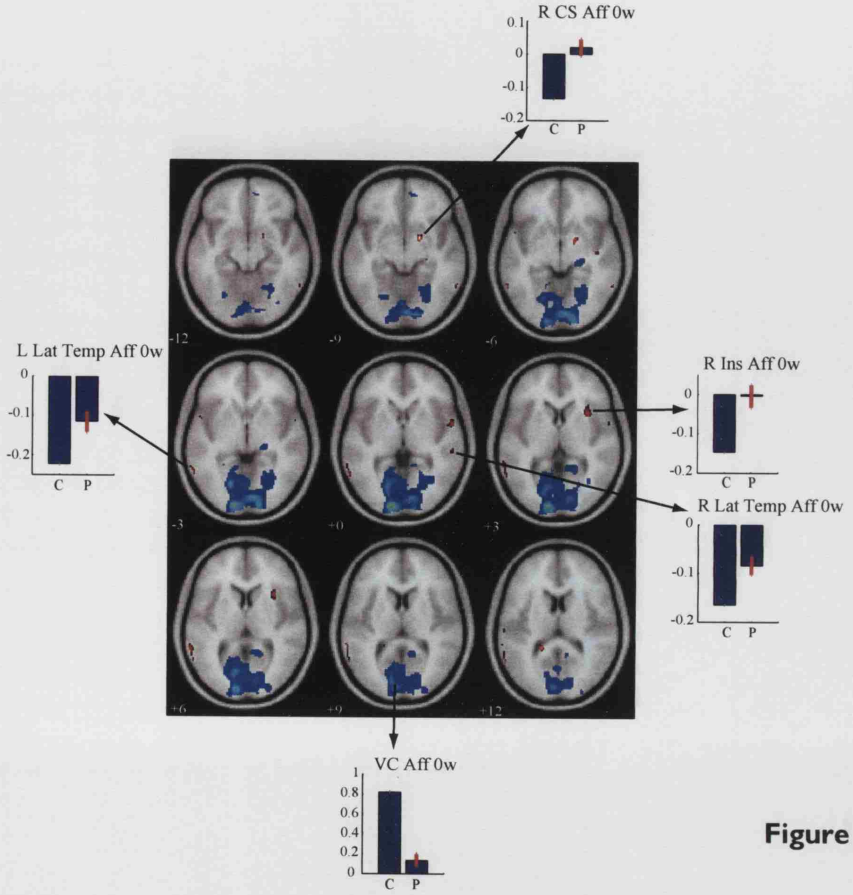

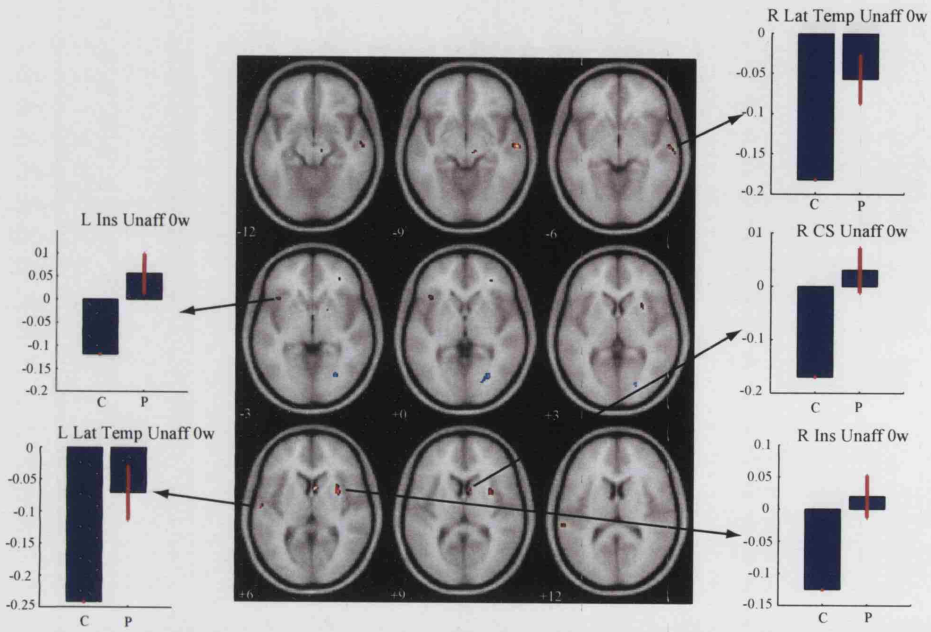

Figure 3.4. A) Baseline.

Aff Baseline

Visual Cortex
R Insula
L and R Lat Temp Cortex
R Corpus Striatum

Fell Baseline

L and R Insula
L and R Lat Temp Cortex
R Corpus Striatum

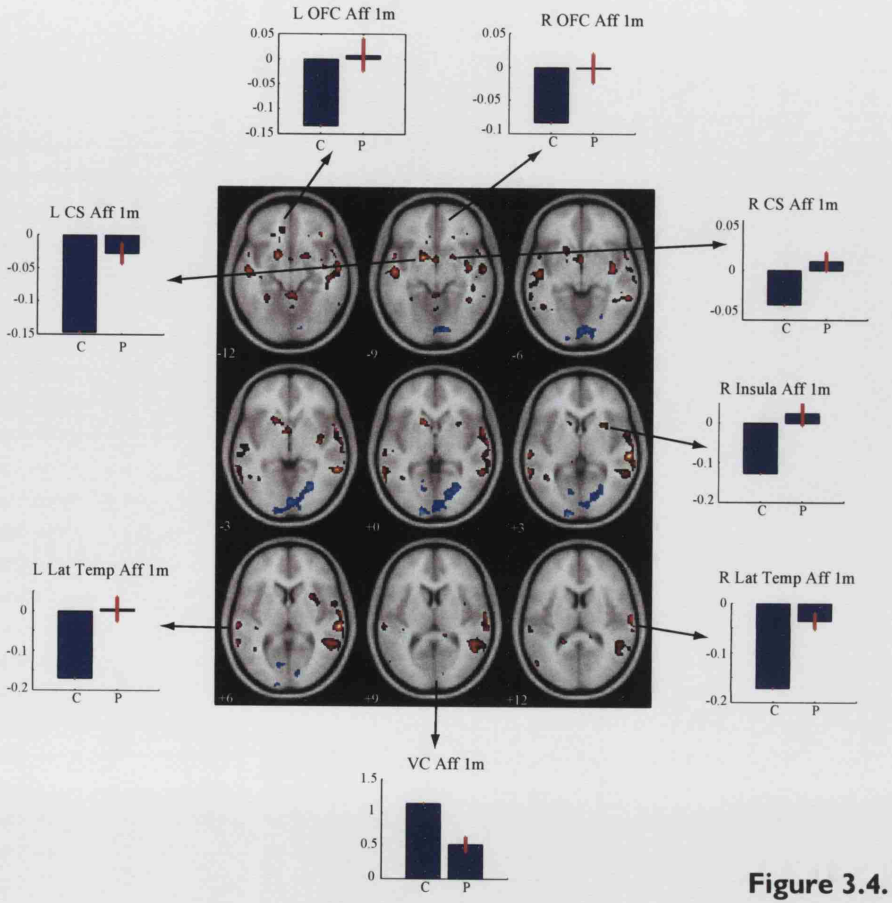

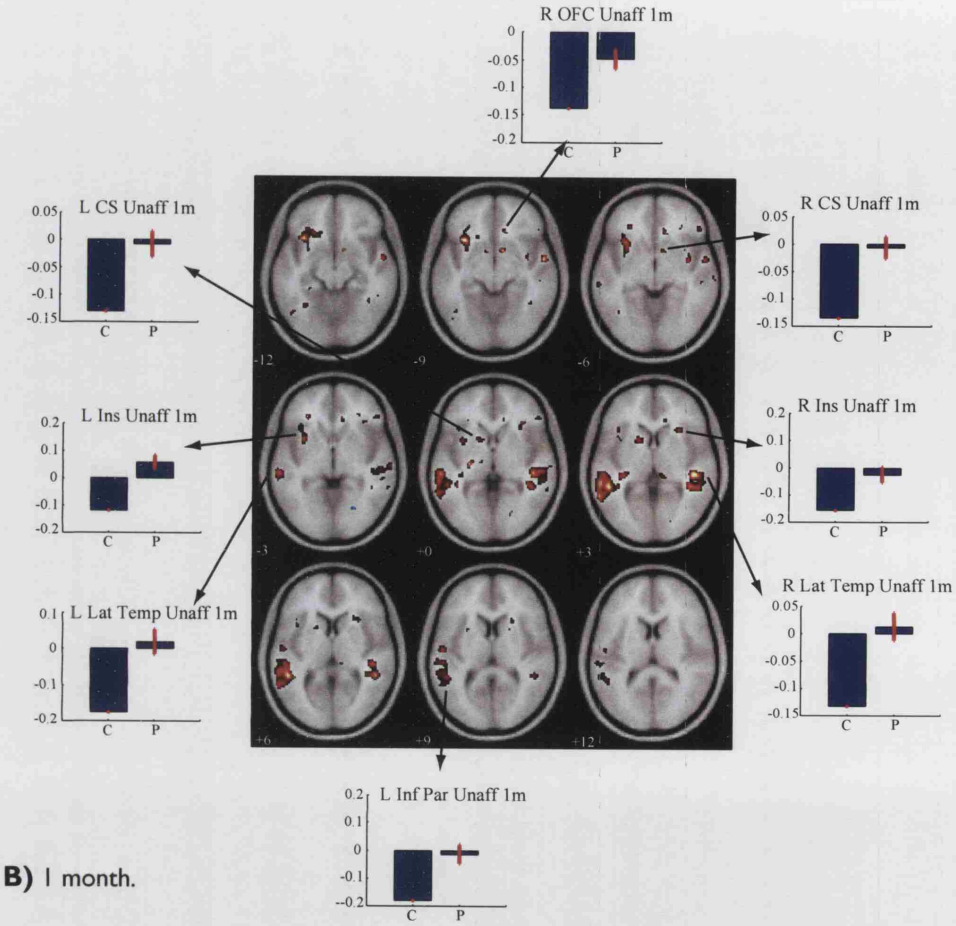

Figure 3.4. B) 1 month.

Aff 1 month

Visual Cortex
R Insula
L and R Lat Temp Cortex
R Corpus Striatum
L and R OFC

Fell 1 month

L and R Insula
L and R Lat Temp Cortex
L and R Corpus Striatum
R OFC
L Inf Par

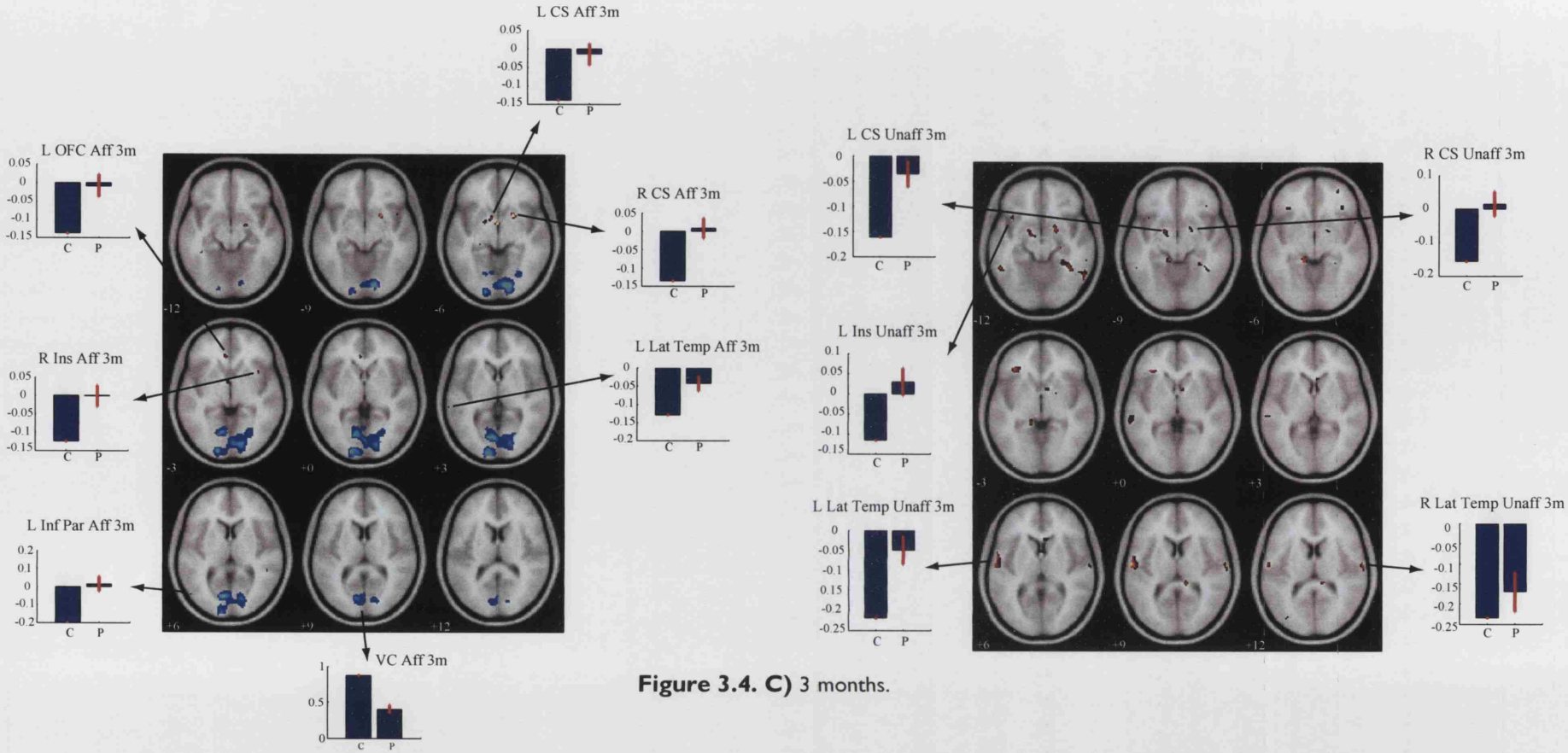

Figure 3.4. C) 3 months.

Aff 3 months

Visual Cortex
R Insula
L Lat Temp Cortex
L and R Corpus Striatum
L OFC
L Inf Par

Fell 3 months

L Insula
L and R Lat Temp Cortex
L and R Corpus Striatum

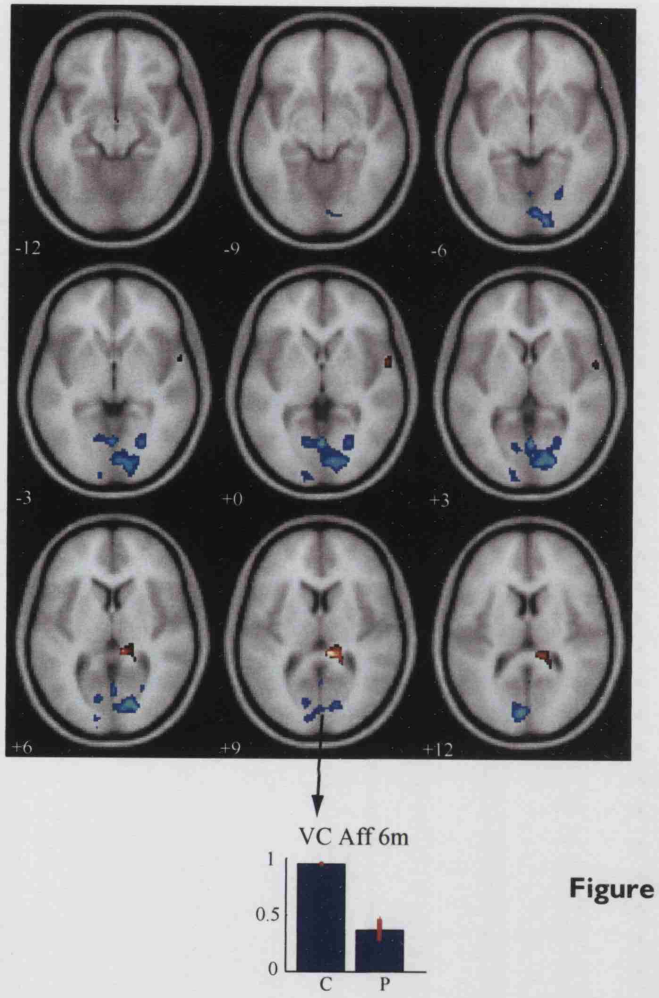

Figure 3.4. D) 6 months.

Aff 6 months
Visual Cortex

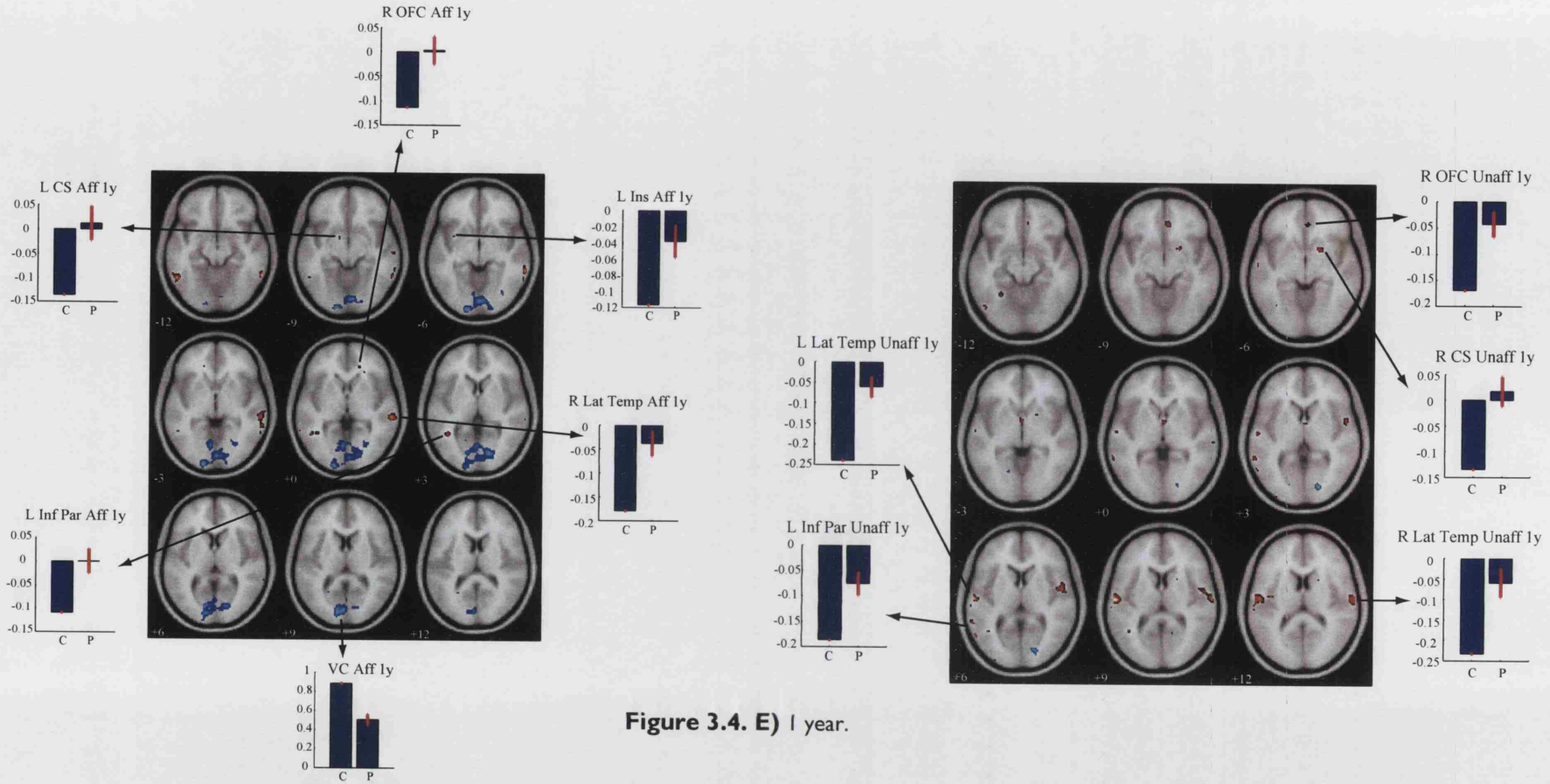

Figure 3.4. E) 1 year.

Aff 1 year

Visual Cortex
L Insula
R Lat Temp
L Corpus Striatum
R OFC
L Inf Par

Fell 1 year

L and R Lat Temp
R Corpus Striatum
R OFC
L Inf Par

Figure 3.4. The above figures (A to E) graphically display the differences between patients and controls from the cross-sectional analysis at baseline, 1 month, 3 months, 6 months and 1 year. Affected eye (aff) results are shown on the left and fellow (fell) on the right. The differences are displayed as T contrast maps ($p<0.001$ uncorrected) overlaid onto a T1 structural template. The hot colour scale represents where patient activity was greater than controls and the blue colour scale shows where controls activated more than patients. The regional differences are listed below the figures and in fact correspond to those shown in tables 3.3 and 3.4. In addition the fMRI parameter estimates (PEs) for the local maxima of the regional differences for both patients (P) and controls (C) have been derived and plotted as bar graphs. The fellow eye results are not shown for 6 months because there were no differences. L = left. R = right. Lat Temp = Lateral Temporal. OFC = Orbitofrontal Cortex. Inf Par = Inferior Parietal. CS = Corpus Striatum.

Several observations should be noted from these results. Firstly, there was a marked discrepancy between the affected and fellow eyes for the visual cortex differences. Controls activated more than patients at all time points when the affected eyes were compared whereas there were no significant differences at any time point for the fellow eyes within the visual cortex. Secondly, when the results for greater patient activation were considered, they showed an approximate symmetry for the affected and fellow eyes whereby both eyes had similar activation patterns at each time point. Thirdly, these extra-occipital activation differences predominated early on during the ON recovery process (baseline, 1 month and 3 months) before subsiding at six months. There is then some evidence for their re-emergence at one year. Finally, when the parameter estimates (PEs) are inspected, it appears that most of the extra-occipital differences could be accounted for by differences in patient and control deactivation i.e. the magnitude of control deactivation was greater than patient deactivation. This last observation was very intriguing because it implied that the controls demonstrated deactivation behaviour outside the visual cortex with parameter estimates approximately 5-10 times less than those for visual cortex activation. In order to help explain the extra-occipital differences, it was felt necessary to investigate the deactivation behaviour in normal controls (see discussion 3.5.1).

3.4 Correlation analyses

3.4.1 Introduction

The results from the cross-sectional analysis demonstrated regionally specific extra-occipital differences between the ON patients and healthy controls that appeared to be particularly prominent during the early recovery phase following the episode. These differences were noted when both the affected and the fellow eyes were stimulated. Correlation analyses were subsequently performed with the aims: (i) To investigate the direct relationships between optic nerve structure, visual function and functional activation and their variation over time. (ii) To apply a novel technique that related fMRI to clinical function after accounting for any confounding structural influences thereby effectively searching for true adaptive cortical reorganization. (iii) To investigate whether the rate of early clinical recovery was related to the corresponding fMRI response.

3.4.2 Methods

The following were investigated in the ON group:

1) Clinical function – for the affected eyes: (i) LogMAR visual acuity, for central vision, and (ii) 30-2 Humphrey visual field mean deviation scores (HMD), for central and peripheral vision. Worse vision was indicated by more positive logMAR and more negative HMD.

2) Optic nerve structure – for the affected eyes: (i) The optic nerve mean area, measured by fat-saturated short echo fast fluid-attenuated inversion recovery sequence (sTE fFLAIR) - larger areas were interpreted as more swollen optic nerves early after the episode (Hickman et al, 2004a). By one year lower areas were felt to signify greater atrophy (Hickman et al, 2001; Hickman et al, 2002; Hickman et al, 2004a). (ii) The baseline gadolinium-enhanced lesion length which has been correlated with poorer visual function acutely (Kupersmith et al, 2002) and chronically (Hickman et al, 2004b).

We used the same sessions as in the cross-sectional analysis (see 3.1.2.3 and table 3.1) to make qualitative inferences between time points whilst optimizing degrees of freedom. FMRI contrasts for both affected and fellow eyes were examined. This was because we identified alterations in the cortical response external to the occipital cortex when either eye was stimulated, implying that the extra-occipital fMRI differences for the fellow eye may be influenced by the affected optic nerve.

3.4.2.1 Direct correlations for fMRI versus affected side

For each chosen time point (baseline, 1 month, 3 months, 6 months and 1 year), separate models were specified in SPM99 with each of the four markers of clinical function or structure as explanatory variables and affected or fellow eye fMRI contrasts as dependent variables. Side of stimulation (left vs right) and fMRI protocol (PB vs WB) were always entered as covariates of no interest. Two additional explanatory variables were also explored for each time point – the T_2 brain and optic radiation lesion loads. Cluster-level inferences (Friston et al, 1994; Friston et al, 1996; Poline et al, 1997; Worsley 2004) were made, corrected across the whole brain (peak threshold $p<0.001$ and spatial extent $p<0.01$).

3.4.2.2 Indirect correlations

Inferences about adaptive plasticity from direct correlations are limited by confounding interrelationships between functional activation, clinical function and structural integrity. We developed a novel methodology to deal with this. We reasoned that variation in clinical function at a time point should be explained by both variation in functional activation and optic nerve structure. This can be simply modeled in a general linear framework:

$$Y = S + F + \varepsilon_1$$

Y represents clinical function, *S* indicates structural integrity, *F* is the fMRI response and ε_1 is the error variance. It is then possible to determine how much functional activation explains clinical function over and above that which is explained by structural factors. SPM cannot directly implement the above equation because it requires *F* to be the dependent variable. This issue can be solved in two stages. The first stage explores the relationship between Y and S:

$$Y = S + \varepsilon_2$$

ε_2, represents the unexplained variance in *Y* after accounting for the relationship between *S* and *Y*. This residual variance, ε_2, can then be correlated with *F* using SPM in the second stage:

$$F \propto \varepsilon_2$$

A significant positive relationship implies that some aspect of clinical function is explained by functional activation after taking into account the role of structure in the relationship and consequently suggests a role for adaptive cortical reorganization.

For each chosen time point we initially performed two principal components analyses using SPSS 11.0, one for logMAR acuity and HMD and the other for optic nerve area and baseline gadolinium-enhanced lesion length. The first principal component for each analysis was taken to represent *Y* and *S* respectively. This significantly reduced the number of correlations to be performed later. A linear regression analysis was then specified (using SPSS 11.0) with *Y* and *S* chosen as the dependent and explanatory variables respectively (first stage). The standardized residuals for *Y* were saved (*ResY*). A covariates model was then adopted in SPM99 for affected or fellow eye fMRI response with *ResY* as an explanatory variable and side of stimulation (left vs right) and type of fMRI protocol (partial vs whole brain) as covariates of no interest (second stage). Cluster-level inferences were made on SPM(T) maps corrected across the whole brain with a peak threshold of $p<0.001$ and spatial extent of $p<0.05$. The spatial extent threshold was more lenient than that used in the direct correlations because we felt the effects would be more subtle.

3.4.2.3 *Recovery Rates*

We investigated whether visual recovery rate at baseline was related to fMRI activation. Recovery was modeled separately for logMAR acuity and HMD as previously described (figure 3.5) (Hickman et al, 2004b). Two models were fitted in SPM99, for baseline logMAR acuity and HMD recovery rate to determine their effects on affected eye fMRI. Side of stimulation and fMRI protocol were again covariates of no interest and statistical inferences were made at cluster-level corrected across the whole brain (peak threshold $p<0.001$, spatial extent $p<0.05$).

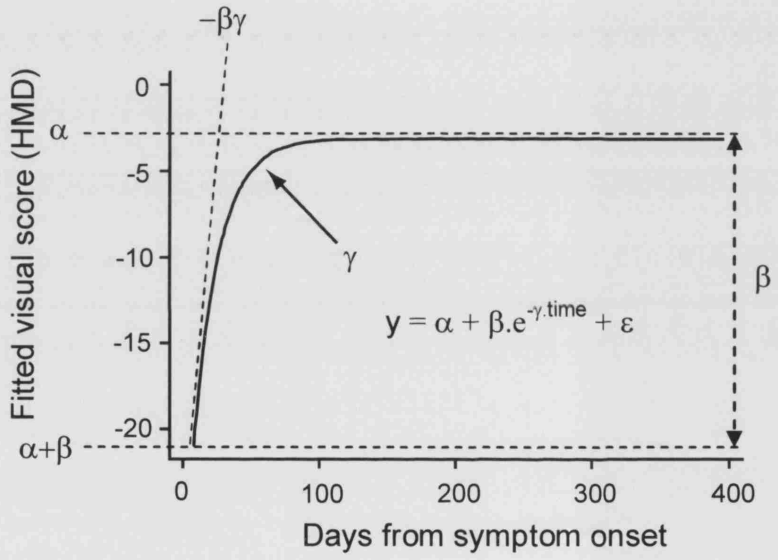

Figure 3.5. An idealized fitted visual recovery curve for HMD against time. y is visual function, α is the 'asymptote', the value which the recovery eventually settles on, β is the 'recovery climb', the extent of improvement from baseline to asymptote. In a curve going up β is negative, hence $\alpha + \beta$ is the baseline value. γ controls how sharp the bend is and *time* is time from onset. ε is the random error. $-\beta.\gamma$ (baseline recovery rates) could be estimated for 14 patients and was used in the recovery rate analysis.

3.4.3 Results

The selected sessions are shown in table 3.1. Table 3.5 shows the clinical, electrophysiological and structural characteristics of the selected patients. By one year, one patient had developed clinically definite MS and one had developed clinically probable MS.

	Baseline	1 month	3 months	6 months	1 year
No. of patients	17	17	16	17	16
Days from onset	14.7 (5.2)	43.2 (6.6)	99.2 (10.5)	203.8 (15.3)	371.4 (8.5)
LogMAR acuity affected eye	0.71 (0.36)	0.30 (0.41)	0.12 (0.21)	0.06 (0.23)	0.03 (0.25)
Humphrey Mean deviation affected eye	-18.3 (10.1)	-8.9 (8.1)	-5.6 (4.6)	-4.9 (3.4)	-4.6 (3.9)
Optic nerve mean area affected eye	15.8 (3.5)	14.0 (1.7)	13.0 (1.5)	12.4 (2.6)	10.9 (1.9)
Optic nerve mean area fellow eye	13.4 (2.4)	13.3 (1.3)	13.1 (1.7)	13.2 (1.5)	12.8 (1.8)
Baseline gadolinium length	24.0 (11.8)	-	-	-	-
T2 brain lesion load	26.4 (0-988.1)	-	-	-	42.6 (0-767.3)
Optic radiation lesion load	0.0 (0-312.9)	-	-	-	0.0 (0-318.2)
VEP whole field amplitude affected eye	1.9 (0-18.1)	5.3 (0-18.3)	4.9 (0-27.2	-	8.4 (1.5-35.9)
VEP whole field amplitude fellow eye	10.9 (3.4-28.2)	12.4 (2.8-31.5)	9.8 (2.0-32.0)	-	9.6 (3.7-41.2)
VEP whole field latency affected eye	115.5 (99.6-150.7)	123.9 (99.0-168.2)	126.4 (97.2-166.2)	-	117.9 (96.7-160.0)
VEP whole field latency fellow eye	98.0 (94.3-114.2)	99.6 (91.9-116.2)	97.5 (91.9-118.1)	-	97.5 (88.9-134.1)

Table 3.5. Characteristics of patients chosen from table 1 to enter into the correlation analyses. Columns denote the chosen time points and rows show the number of patients, mean days from symptom onset (SD) and then mean logMAR acuity (SD), mean Humphrey mean deviation score in dB (SD), mean optic nerve area in mm2 (SD) and mean baseline gadolinium lesion length in mm (SD), median T2-weighted brain lesion load in mm2 (range), median T2-weighted optic radiation lesion load in mm2 (range), median VEP amplitudes in μV and latencies in msec (range).

3.4.3.1 Direct correlations

For visual function, significant correlations were found only at baseline within the occipital cortex (table 3.6, figures 3.6-8). The directions of the correlations indicated that better visual function was associated with a stronger fMRI response in the visual cortices. Interestingly, a significant effect was found for the fMRI response of the fellow eye at baseline which was positively correlated with the HMD score for the affected eye.

	Affected eye		Region	MNI coordinate			k	Z	p	Fig
				x	y	z				
Acuity (LogMAR)	Baseline	Aff	R Occ -ve	26	-54	16	442	4.44	0.0000242	3.6
		Fell	-	-	-	-	-	-	-	-
	1 m	Aff	-	-	-	-	-	-	-	-
		Fell	-	-	-	-	-	-	-	-
	3 m	Aff	-	-	-	-	-	-	-	-
		Fell	-	-	-	-	-	-	-	-
	6 m	Aff	-	-	-	-	-	-	-	-
		Fell	-	-	-	-	-	-	-	-
	1 y	Aff	-	-	-	-	-	-	-	-
		Fell	-	-	-	-	-	-	-	-
Field (Humph)	Baseline	Aff	VC +ve	14	-82	2	1402	4.54	9.27×10^{-12}	3.7
		Fell	VC +ve	-12	-78	8	304	4.37	0.002	3.8
	1 m	Aff	-	-	-	-	-	-	-	-
		Fell	-	-	-	-	-	-	-	-
	3 m	Aff	-	-	-	-	-	-	-	-
		Fell	-	-	-	-	-	-	-	-
	6 m	Aff	-	-	-	-	-	-	-	-
		Fell	-	-	-	-	-	-	-	-
	1 y	Aff	-	-	-	-	-	-	-	-
		Fell	-	-	-	-	-	-	-	-

Table 3.6. The direct correlation results for fMRI affected/fellow eye vs visual function. Significant correlations were found only at baseline and in the occipital cortex. The direction of the correlations are shown as well as MNI co-ordinates (x,y,z), cluster size in voxels (k), peak Z score and the cluster P values. More negative logMAR scores and more negative HMD scores represent better visual function. Occ = Occipital lobe. VC = Visual cortex. The corresponding figures demonstrating the significant clusters are shown below and listed in the last column (Fig).

For optic nerve structure (table 3.7), baseline gadolinium-enhanced lesion length, at baseline and at one month, was associated with reduced fMRI activity in the visual cortex when either the affected

or fellow eyes were stimulated. By three months this relationship had reversed for the lateral temporal cortex and right hippocampus/fusiform region such that the greater the initial lesion length, the greater the fMRI response within these regions. By one year there were significant results again in the right lateral temporal cortex and left fusiform region. The only significant relationship for optic nerve mean area was at one year, when greater optic atrophy was associated with greater fMRI activation for the fellow eye within the left orbitofrontal cortex.

No significant correlations were found at baseline and one year for the brain T2-weighted lesion loads or optic radiation lesion loads.

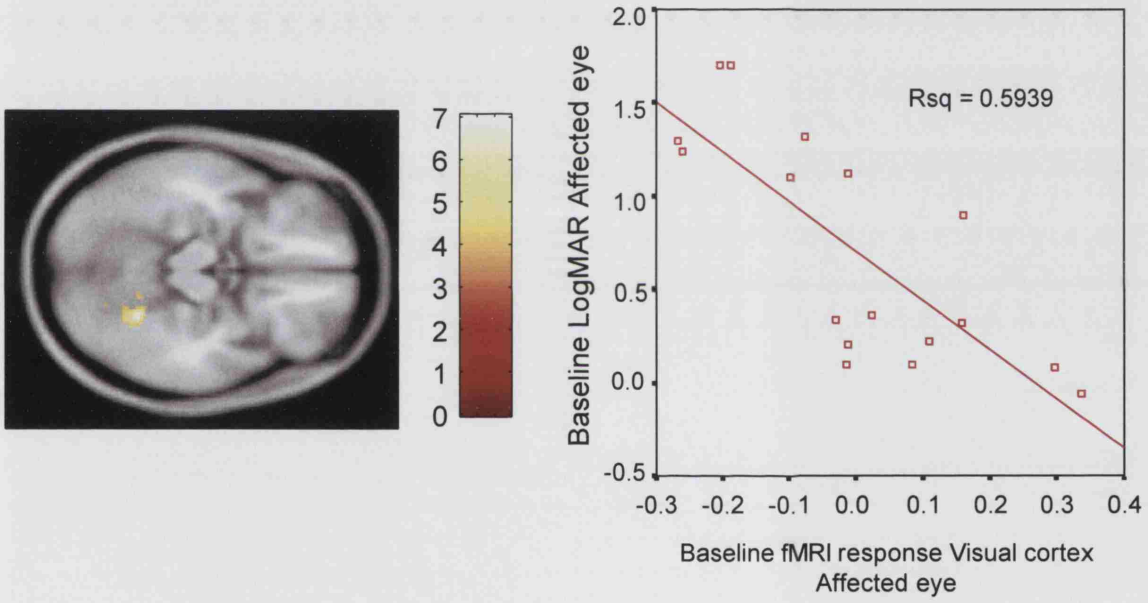

Figure 3.6. The logMAR of the affected eye was inversely correlated with the fMRI response in the right occipital cortex (i.e. a greater fMRI response is associated with better visual function). The displayed cluster is at MNI 26,-54,16.

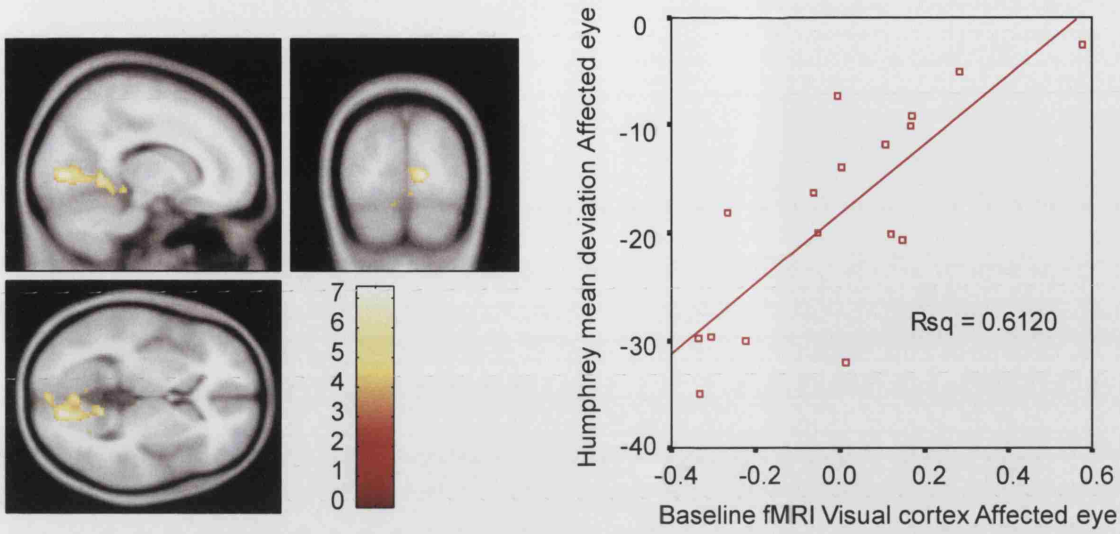

Figure 3.7. The baseline affected eye fMRI response in the visual cortex was positively correlated with the Humphrey mean deviation of the affected eye. The displayed cluster is at MNI 14,-82, 2.

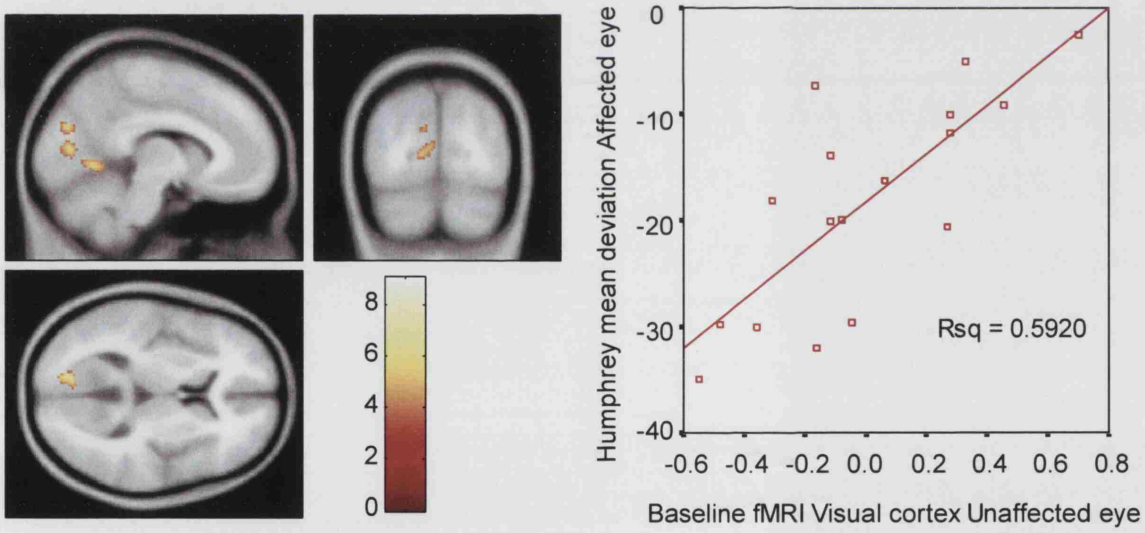

Figure 3.8. The baseline fellow eye fMRI response in the visual cortex was also positively correlated with the Humphrey mean deviation of the affected eye. The displayed cluster is at MNI -12,-78, 8.

Affected optic nerve structure			Region	MNI coordinates			k	Z	p	Fig
				x	y	z				
Area (FLAIR)	Baseline	Aff	-	-	-	-	-	-	-	-
		Fell	-	-	-	-	-	-	-	-
	1 m	Aff	-	-	-	-	-	-	-	-
		Fell	-	-	-	-	-	-	-	-
	3 m	Aff	-	-	-	-	-	-	-	-
		Fell	-	-	-	-	-	-	-	-
	6 m	Aff	-	-	-	-	-	-	-	-
		Fell	-	-	-	-	-	-	-	-
	1 y	Aff	-	-	-	-	-	-	-	-
		Fell	L OFC-ve	-14	52	-2	186	4.49	0.002	3.9
Baseline Gad lesion	Baseline	Aff	R VC –ve	22	-50	0	306	3.63	0.0003	3.10
		Fell	L VC –ve	-10	-80	24	413	4.08	0.00003	3.11
			R VC –ve	12	-66	10	251	4.36	0.001	3.11
	1 m	Aff	L VC –ve	-26	-94	-8	158	5.53	0.0025	3.12
		Fell	(L VC –ve	-40	-76	-8	108	3.95	0.024)	3.13
	3 m	Aff	L Lat Temp +ve	-60	-22	6	1116	5.11	8.9×10^{-12}	3.14
			R Lat Temp +ve	50	-28	12	394	4.09	0.00001	3.14
			R Hippo/Fus +ve	36	-32	-14	140	4.10	0.0099	3.14
		Fell	-	-	-	-	-	-	-	-
	6 m	Aff	-	-	-	-	-	-	-	-
		Fell	-	-	-	-	-	-	-	-
	1 y	Aff	R Lat Temp -ve	46	-24	-10	171	4.08	0.0012	3.15
		Fell	L Fusif/Cerebellum +ve	-24	-44	-26	119	4.25	0.0045	3.16

Table 3.7. The direct correlation results for fMRI affected/fellow eye vs affected optic nerve structure. The direction of the correlations are shown as well as the MNI co-ordinates (x,y,z), cluster size in voxels (k), peak Z score and cluster level P (p) values. Larger optic nerve areas were considered to represent greater swelling early on, but by one year smaller areas were felt to represent atrophy. Higher lesion lengths represented reduced optic nerve integrity. OFC = Orbitofrontal cortex. VC = Visual cortex. Lat Temp = Lateral temporal cortex. Hippo/Fus = hippocampal gyrus/fusiform gyrus. Fusif/Cerebellum represented a cluster that straddled the fusiform gyrus and cerebellum. The corresponding figures for the significant clusters are shown below and are listed in the last column.

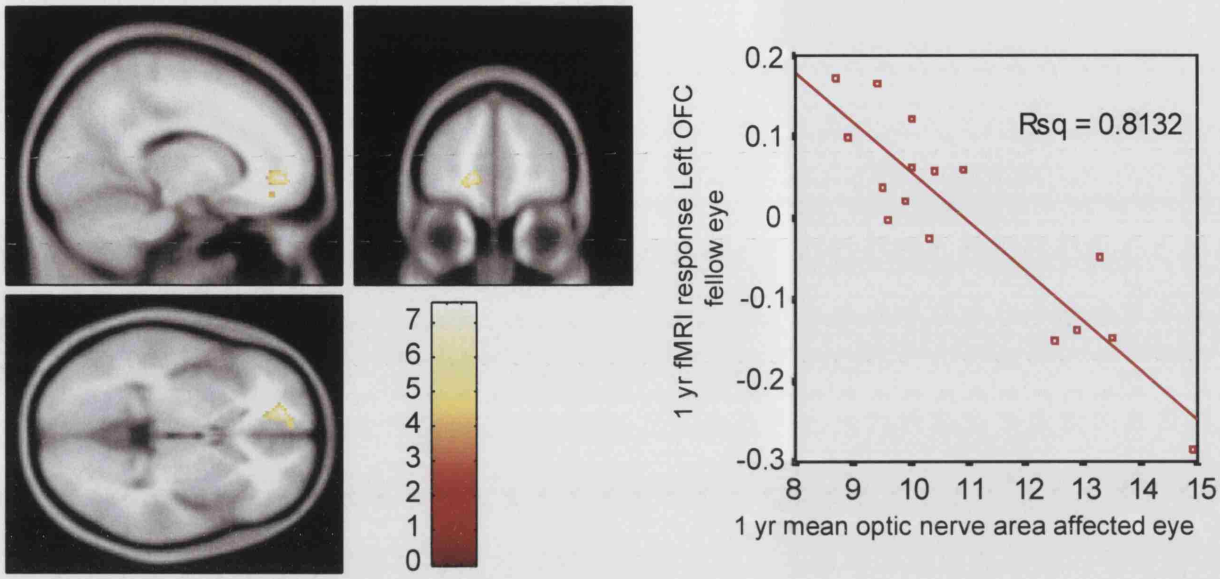

Figure 3.9. The fMRI response for the fellow eye at one year was inversely correlated with the one year mean affected optic nerve area. The displayed cluster is at MNI -14, 52, -2.

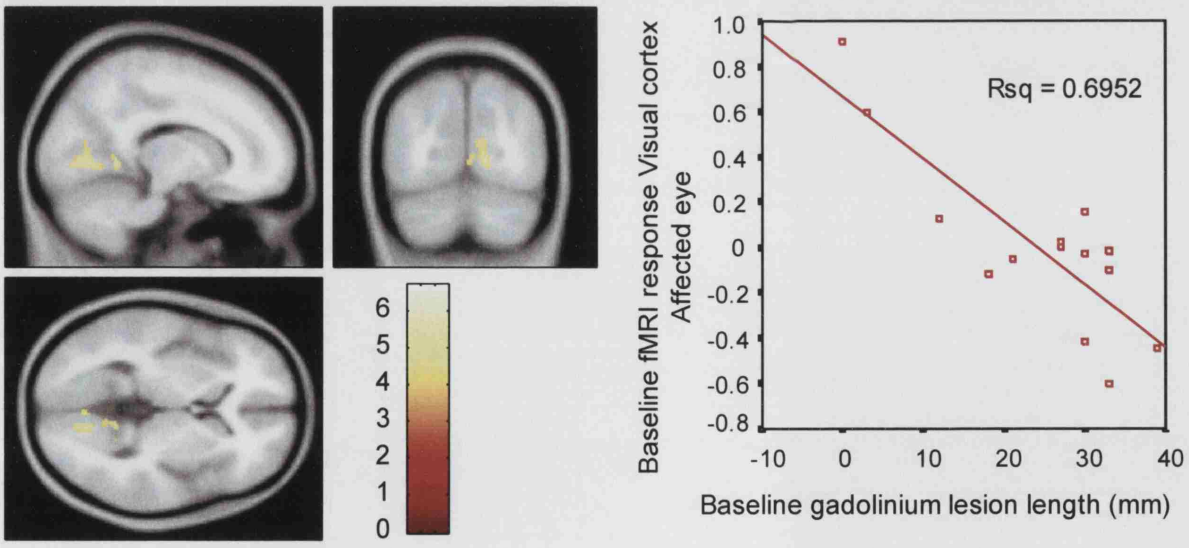

Figure 3.10. The fMRI response for the affected eye at baseline was inversely correlated with the baseline gadolinium enhanced lesion length. The displayed cluster is at MNI 14, -72, 2.

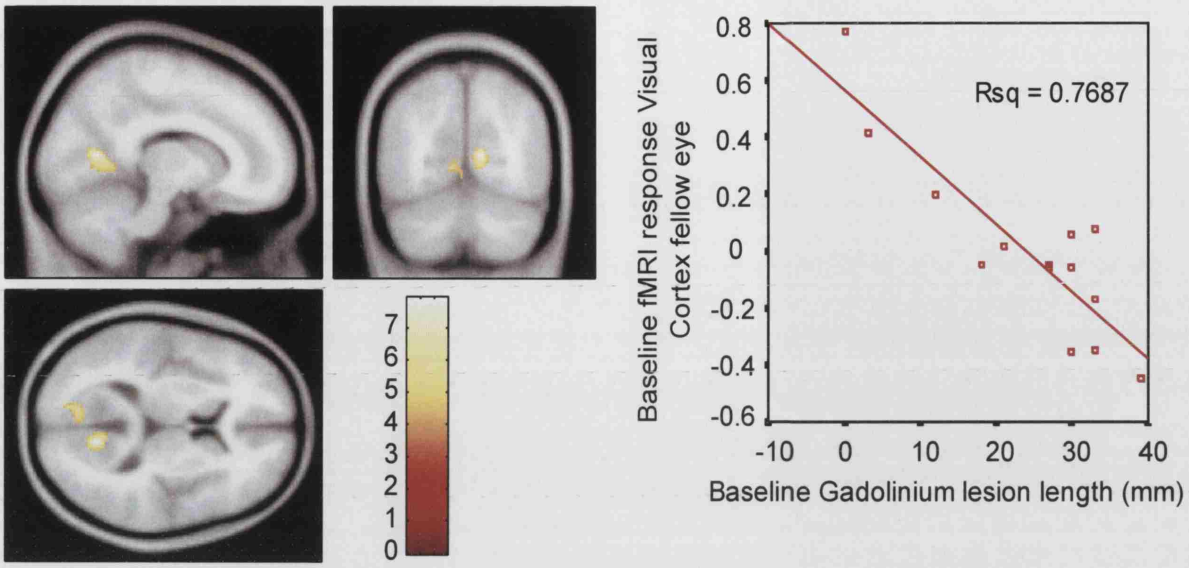

Figure 3.11. The fMRI response for the fellow eye at baseline was inversely correlated with the baseline gadolinium enhanced lesion length. The displayed cluster is at MNI 12, -66, 10.

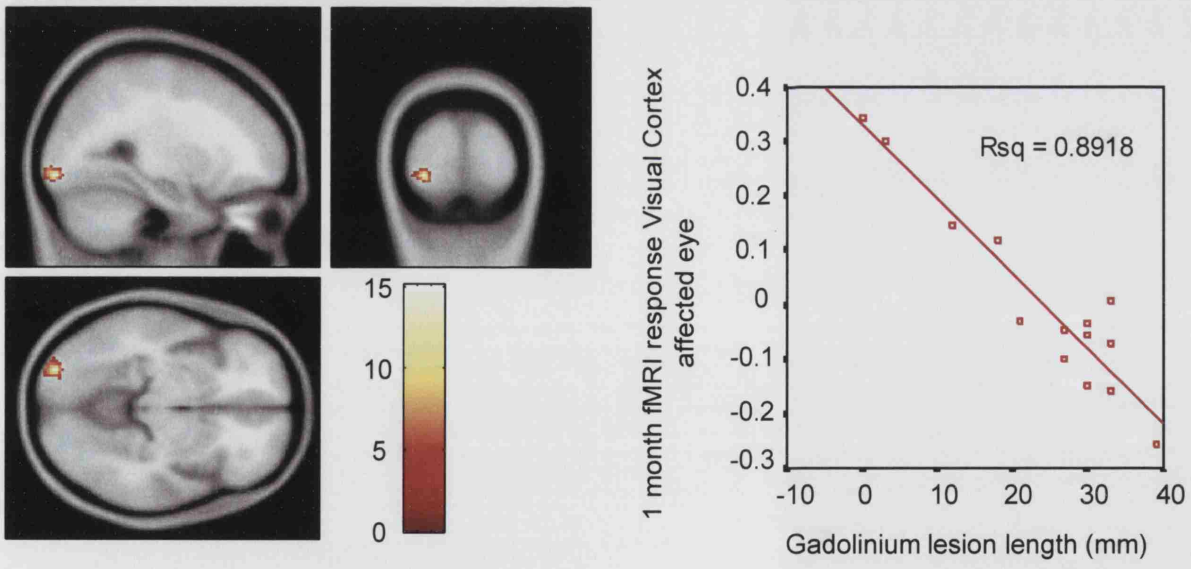

Figure 3.12. The fMRI response for the affected eye at one month was inversely correlated with the baseline gadolinium enhanced lesion length. The displayed cluster is at MNI -26, -94, -8.

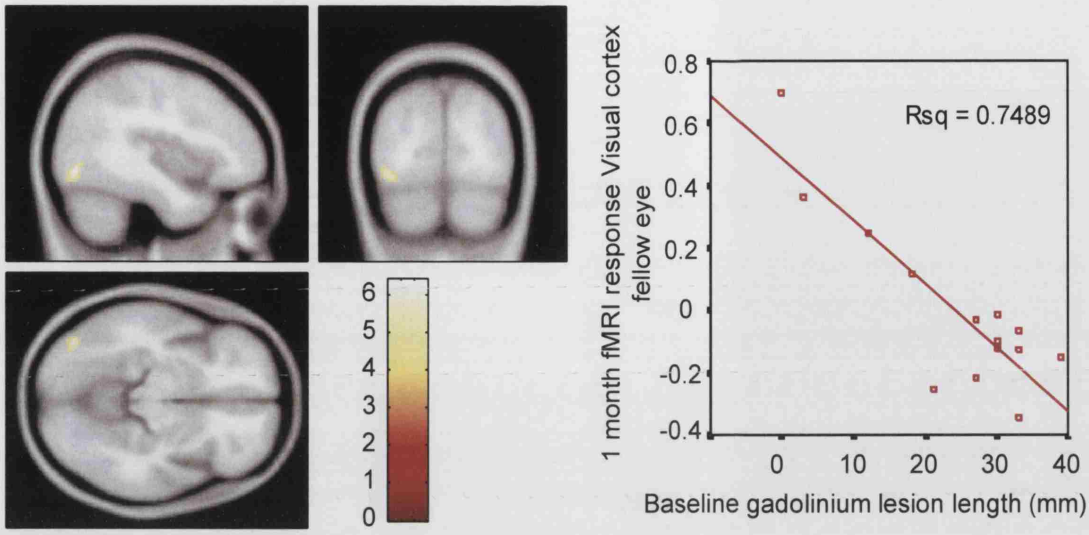

Figure 3.13. The fMRI response for the fellow eye at one month was inversely correlated with the baseline gadolinium enhanced lesion length. The displayed cluster is at MNI -40, -80, -11.

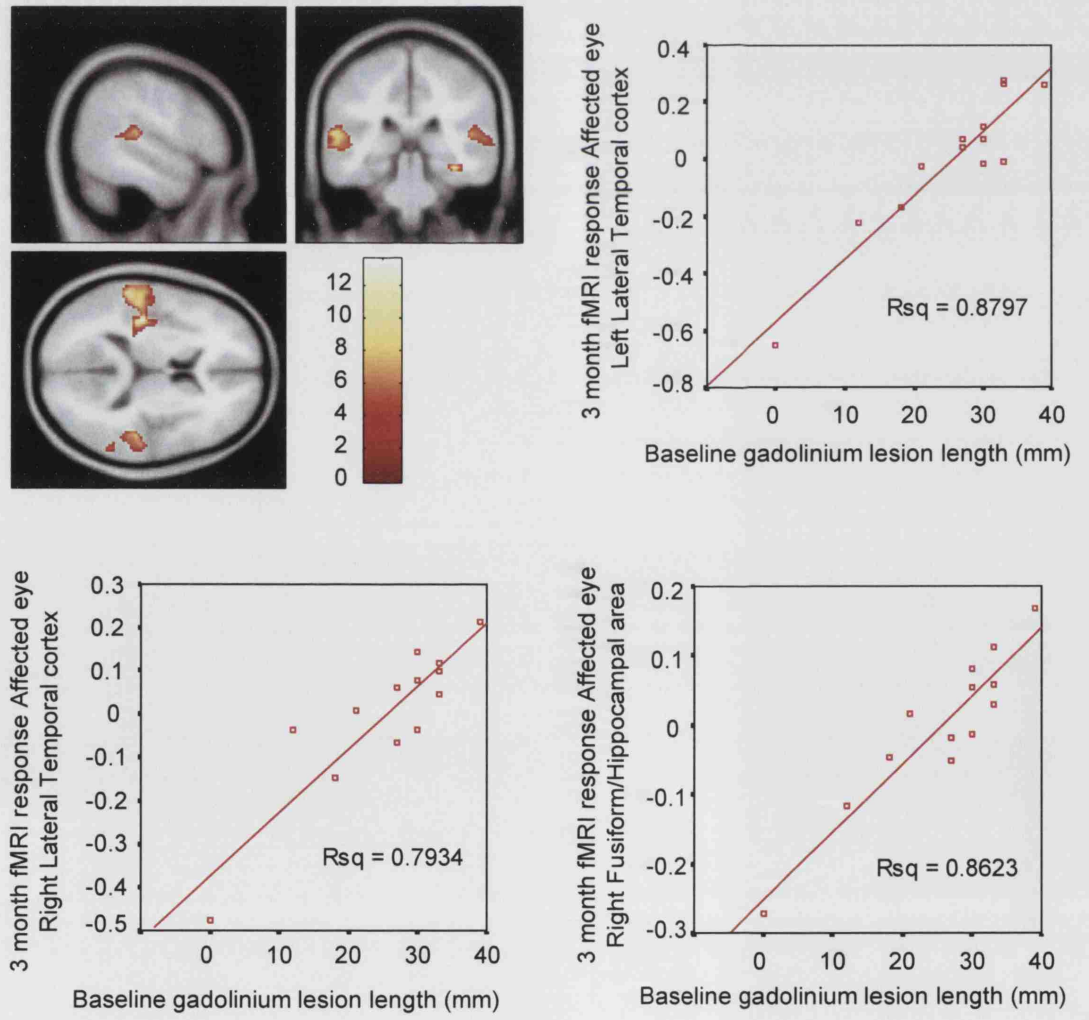

Figure 3.14. The fMRI response for the fellow eye at three months was positively correlated with the baseline gadolinium enhanced lesion length. The clusters are displayed at MNI 52, -32, 12.

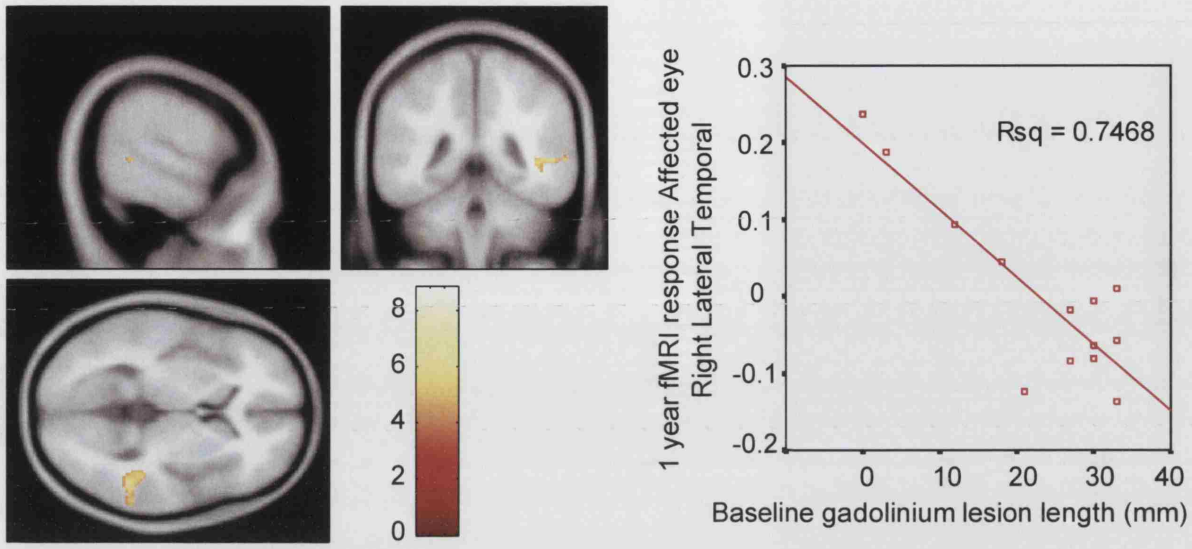

Figure 3.15. The fMRI response for the affected eye at one year was negatively correlated with the baseline gadolinium enhanced lesion length. The cluster is displayed at MNI 60, -43, 3.

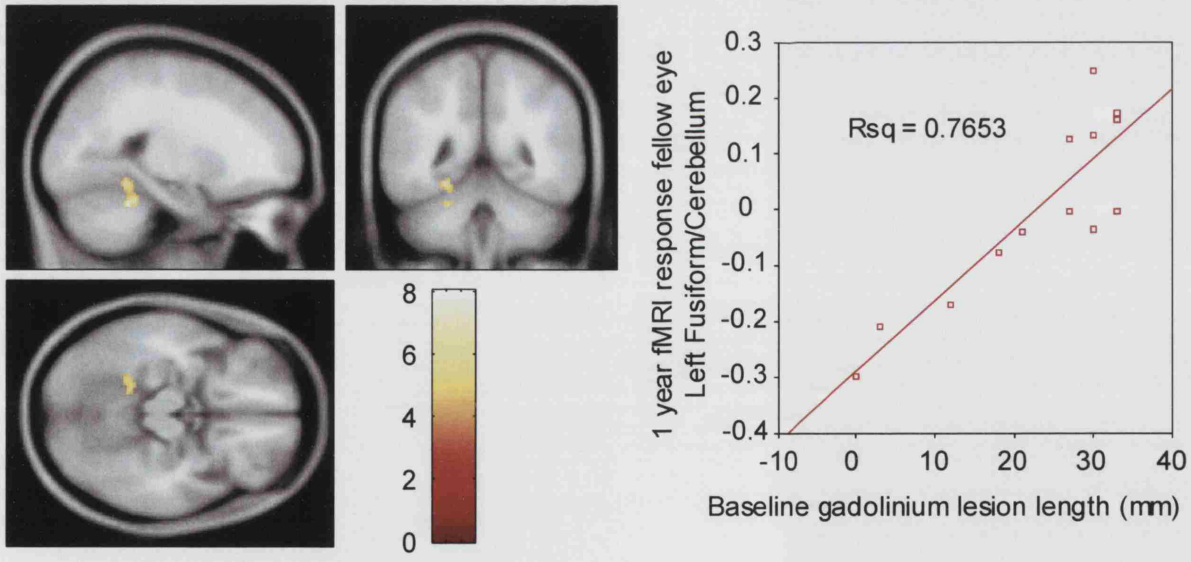

Figure 3.16. The fMRI response for the fellow eye at one year was positively correlated with the baseline gadolinium enhanced lesion length. The cluster is displayed at MNI -23, -47, -16.

3.4.3.2 *Indirect correlations*

Significant clusters were found at baseline only for the affected eye fMRI response. *ResY* was positively correlated with fMRI activation in the bilateral infero-lateral occipital cortices and right peristriate cortex (table 3.8 and figure 3.17). The bilateral regions (figure 3.18) were identified as overlapping the inferior occipital and fusiform gyri (Rorden and Brett 2000; Tzourio-Mazoyer et al, 2002) and were felt to functionally represent the lateral occipital complexes. These are higher order extra-striate regions along the ventral visual processing stream. To test this we compared the locations of our regions with the stereotaxic coordinates described in the literature for the lateral occipital complexes (LOCs) (Goebel et al, 2001; Grill-Spector et al, 1999; Grill-Spector et al, 2000; Grill-Spector 2003; Lerner et al, 2001; Malach et al, 1995). We also looked at the location of V5/MT (Berman and Colby 2002; Buchel et al, 1998; Dumoulin et al, 2000; Friston and Buchel 2000; Goebel et al, 1998; Goebel et al, 2001; Rees et al, 2000; Taylor et al, 2000; Tootell et al, 1995; Watson et al, 1993) - a higher order region along the dorsal stream which is located just supero-anteriorly to the LOCs. The results are illustrated in figure 3.19 and show that the functional locations of the bilateral occipital regions identified in this study are consistent with the LOCs.

Region	MNI coordinates			k	Z score	Cluster p value
	x	y	z			
L inferolateral occipital cortex	-40	-66	-16	125	3.84	0.008
R inferolateral occipital cortex	46	-74	-10	77	4.24	0.062
R peristriate cortex	24	-86	2	115	5.26	0.013

Table 3.8. Significant effects are shown within the occipital lobe for the indirect correlations. They can be visualized in figure 3.17. The regions are listed with the peak MNI coordinates (x,y,z), cluster size (k), Z score and p value (cluster level). The R inferolateral occipital region is mentioned even though the p value is 0.062 because of its symmetrical location with the left sided region. Also, we felt it to be of relevance because its p value became significant with more lenient peak thresholds (i.e. at $p<0.01$ rather than $p<0.001$).

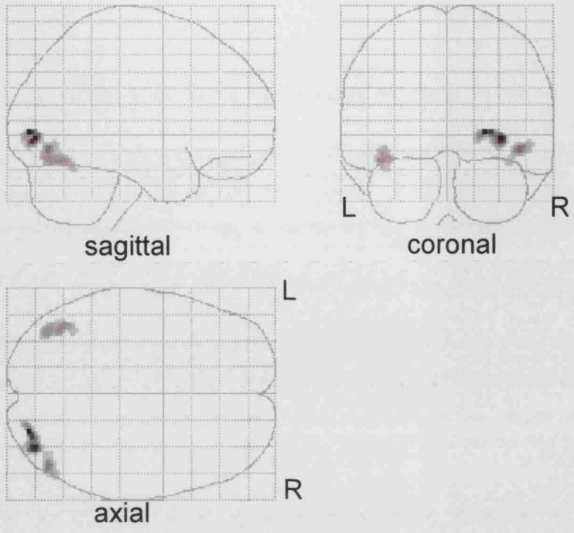

Figure 3.17. SPM(T) glass brain representations for the indirect correlations. Significant effects were found at the baseline time point for the fMRI response of the affected eye. The regions seen are in the bilateral inferolateral occipital cortices and right peristriate area (see table 5). Maps are thresholded with peak $p<0.001$ (uncorrected) and spatial extent of 50 voxels for visual display.

Model confirmation – The indirect correlations model (i.e. $Y=F+S$) assumed normal residual error distribution and no interaction term between *F* and *S*. Having discovered significant effects within the LOCs and right peristriate cortex we retrospectively validated the analysis by first extracting the averaged parameter estimates from these regions. We then applied SPSS 11.0 to construct general linear models which tested for interaction terms between the fMRI response (parameter estimates) and optic nerve structure by applying the model $Y = F + S + (F*S) + side + protocol$. Side of stimulation and fMRI protocol were entered as fixed factors of no interest. This model was estimated separately for each of the three regions. Significant effects for *F* were confirmed in the left ($p=0.00036$) and right ($p=0.00016$) LOCs and right peristriate cortex ($p=2.1\times10^{-5}$). There was no evidence for any interaction between *F* and *S* in the left ($p=0.673$) or right ($p=0.305$) LOCs nor right peristriate cortex ($p=0.339$). In addition the residual errors for each fitted model were observed to be random.

3.4.3.3 Recovery Rates

No significant relationships were found between the baseline fMRI response and estimated recovery rate.

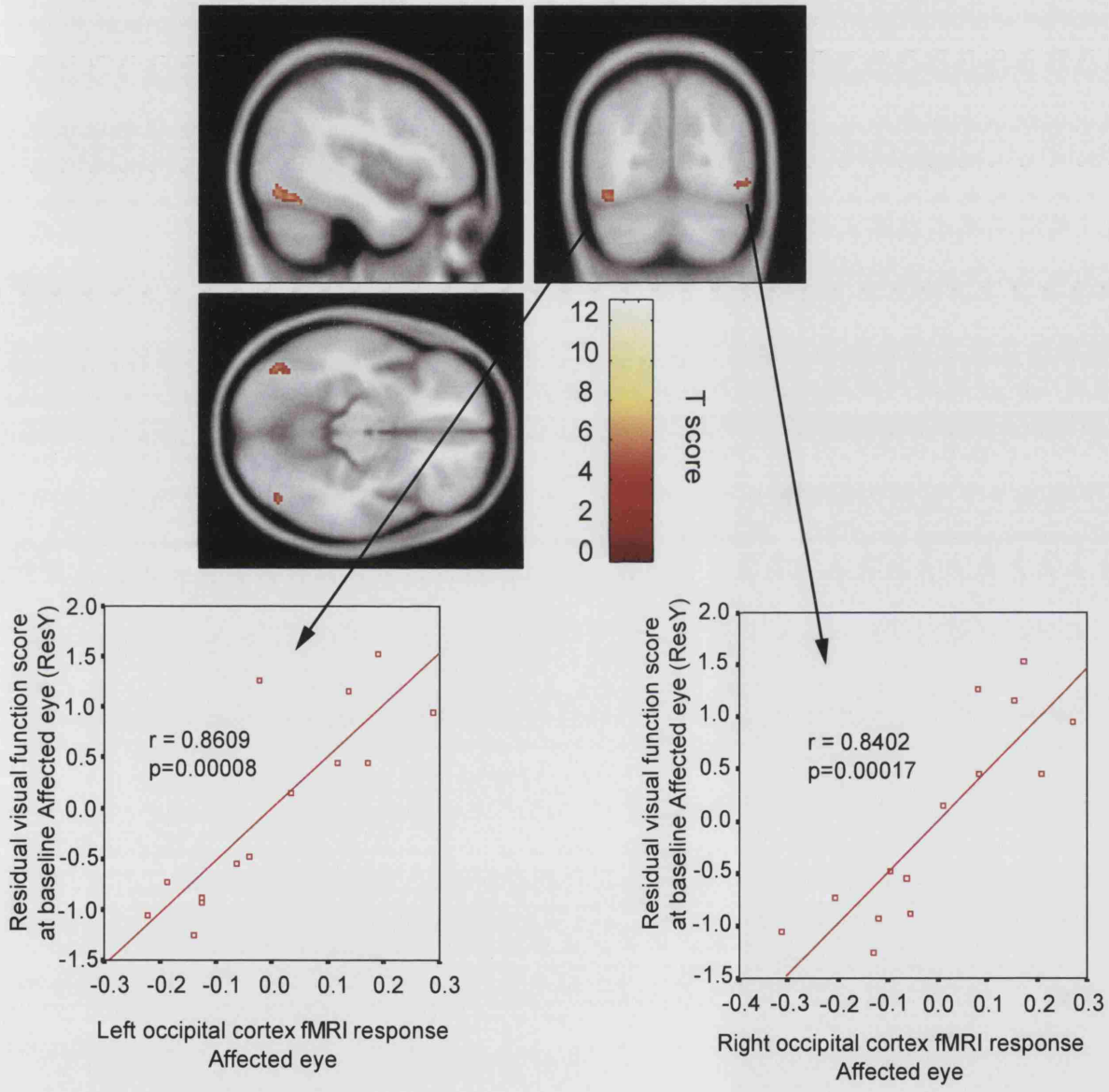

Figure 3.18. The bilateral inferolateral occipital regions are highlighted with plots of mean corrected *ResY* (dimensionless units) against the mean corrected fMRI response (approximate % BOLD signal change) at the peak voxels within each cluster. The slice orientations are the same as in figure 2. The slices are at MNI coordinates [-42,-71,-12]. Maps are thresholded with peak $p<0.001$ (uncorrected) and spatial extent of 50 voxels for visual display purposes.

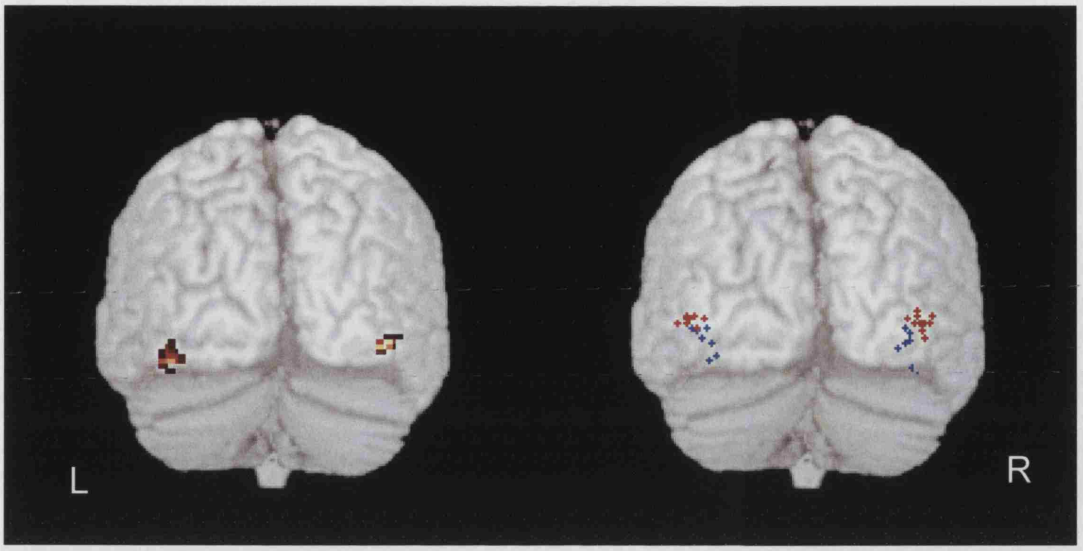

Figure 3.19. The bilateral inferolateral occipital regions are compared with literature based coordinates for the lateral occipital complexes and human V5/MT. The views are of the back of the brain. The left hand figure localizes the inferolateral occipital regions detected in this study. The red crosses in the right hand figure show the locations of human V5/MT whereas the blue crosses show the LOC. The regions from our study appear to be more closely related to the LOCs than V5/MT. MRIcro (www.mricro.com) was used for this figure.

3.5 Discussion

3.5.1 Serial comparisons – differential deactivations between ON patients and controls

We demonstrated dynamic differences in visual task related fMRI activation between patients and controls following acute ON. These differences varied in both space and time and were found within the visual cortices for affected eye stimulation and in extra-occipital areas for both the affected and fellow eyes. The extra-occipital differences were most prominent early after the onset of ON and subsided by 6 months. The extra-occipital regions that we focused on were the insula, lateral temporal cortex, corpus striatum, orbitofrontal cortex and inferior parietal areas and have been observed in past fMRI studies of ON (Toosy et al, 2002b; Werring et al, 2000). Interestingly, the extra-occipital differences themselves arose as a result of differential deactivations between patients

and controls, with controls exhibiting greater deactivation magnitudes. The probable contributions towards control deactivation behaviour will be discussed below.

3.5.1.1 Control deactivation behaviour

The normal subjects in this study exhibited fMRI activation within the visual cortical areas related to visual stimulation but also fMRI deactivation outside the occipital cortex (i.e. the fitted BOLD signal was more positive during the resting baseline than during the visual stimulation epochs). Of note, the deactivation effect sizes (parameter estimates) were of a lower magnitude to the activation effect sizes. Possible causes for control deactivation were postulated and then investigated. These investigations are detailed in appendix A for the interested reader. They are summarized below.

We ruled out hardware associated periodic signal drift and spatial registration issues as causes for the observed deactivations. We also considered whether eye movements occurring during baseline (darkness) could lead to the observation of deactivations. In order to produce the observed differences between ON patients and controls however, these putative eye movements would need to be systematically more pronounced in controls than in the ON patients. We felt that differential eye movements did not contribute to our findings for several reasons. Firstly, it is known that three main bilateral cortical areas or 'eye fields' are involved in the generation of simple saccades. These comprise the frontal eye fields, the supplementary eye fields and the eye movement related region within the intraparietal sulci (Anderson et al, 1994; Pierrot-Deseilligny et al, 1995; Tehovnik et al, 2000). These regions are distinct from the extra-occipital areas of interest that were investigated in our study. Secondly, the deactivations seen in the controls (figure A.10B, appendix A) do not prominently involve these eye movement areas (note that the intraparietal sulci are classically involved and not the interparietal sulcus). Thirdly, we conducted *post-hoc* eye movement experiments on five healthy subjects to determine whether the control deactivation pattern could be replicated. Each experiment comprised a paradigm of 20 second photic stimulation epochs that alternated with 20 second epochs of pre-planned self paced (approximately 1-2 Hz) saccadic eye movement cycles

(during darkness). A fixed effects conjunction analysis of the five subjects (Friston *et al.*, 1999) was performed to show the common activations associated with eye movements (relative to photic stimulation). A significance threshold of $p<0.05$ (corrected across the whole brain) revealed activation within the intraparietal sulci and lingual gyri (figure A.9, appendix A). At lower thresholds ($P<0.0001$ uncorrected) regions corresponding to the frontal eye fields were also shown. The activation patterns were dissimilar to the deactivations seen with the controls in the main study. From the evidence above, it is most likely that eye movements did not contribute to the deactivation patterns seen in the control group especially in extra-occipital areas of interest investigated in the longitudinal study.

It is very likely that the extra-occipital deactivations can be explained by recently described physiological mechanisms that relate to the relative suppression of task related brain processes during the baseline of the visual fMRI experiments. There are two main sources of references to support this proposition. The mechanisms that they describe may be interrelated. The first relates to task independent BOLD decreases and the second to task dependent decreases.

3.5.1.1.1 Task independent BOLD decreases (default mode or baseline state of brain function)

Task-related BOLD signal decreases (deactivations) have been frequently observed at sites distant from the sites of increases (Shulman et al, 1997b), making a vascular steal explanation untenable. Some deactivations appear to be *task dependent* (see 3.5.1.1.2 below) i.e. vary in location depending upon the nature of the task. Some however are *task independent* – varying little in locations across a wide range of tasks. It has been proposed that these represent an organized mode of brain function that is attenuated during the goal-directed behavioural task (Raichle 1998a; Raichle 1998b; Raichle et al, 2001). These regions include posterior medial cortices (posterior cingulate, precuneus, retrosplenial), posterior lateral cortices (mainly association areas BA 39,40 (parietal lobe), BA 22 (temporal lobe), BA 19 (occipital lobe)), ventral and dorsal prefrontal cortices (e.g. orbitofrontal) (figure 3.20) (Gusnard and Raichle 2001).

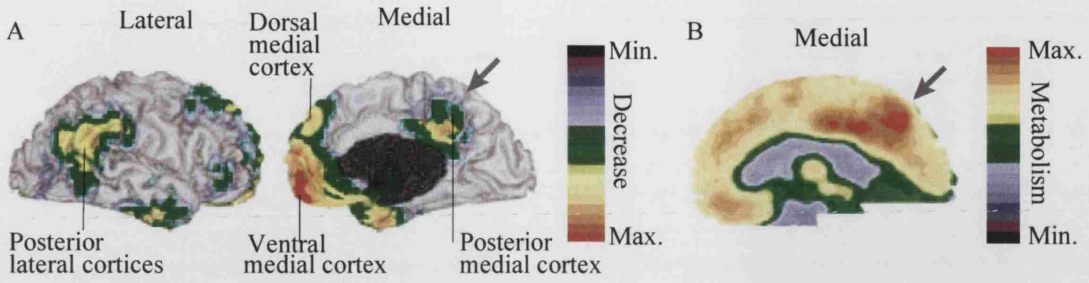

Figure 3.20. Adapted from Gusnard et al (2001). (A) Regional decreases seen after a meta-analysis of nine PET studies involving 132 normal subjects (Shulman et al, 1997b). The tasks involved the processing of various visual stimuli. These decreases were noted for their task independence. Areas showing task independent decreases especially within medial parietal (precuneus) and posterior cingulate cortex, show higher resting metabolic rates in (B). This data came from a PET study in 22 normal subjects which measured the resting glucose metabolism (Gusnard and Raichle 2001).

Raichle et al (2001) hypothesized that the OEF (oxygen extraction fraction) at rest in the normal brain can be used to define a functional baseline of brain activity[4] and in support of this, demonstrated a spatial uniformity of the OEF pattern more or less independent of whether the subjects had their eyes open or closed (some decreases from baseline OEF were noted in the extrastriate cortex when subjects had their eyes closed – suggesting that the true baseline state of these areas occurs when the eyes are open) (Raichle et al, 2001). As a result, the OEF pattern in resting, awake subjects has been proposed to represent a baseline level of brain function (Gusnard and Raichle 2001). Localized task related decreases in OEF would signify 'activations' and conversely, increases in OEF would imply 'deactivations'. In this thesis, although the OEF could not be measured, the baseline state of the fMRI paradigm involved resting, awake subjects. Therefore, the negative BOLD responses in this thesis could be reasonably thought to reflect real deactivations.

In another study, a meta-analysis of 9 PET studies was conducted by Shulman et al (1997) (involving 132 subjects) across various visual tasks and noted common regions of decreases between the

[4] Note that OEF *decreases* with increasing brain activity because blood flow increases outweigh oxygen consumption. Brain regions with reduced OEFs relative to the mean OEF of the brain are activated and local increases in OEF from the brain mean are deactivations.

studies (figure 3.20), indicating the presence of processes that were attenuated during the goal-directed task (Shulman et al, 1997b). A further study compared the resting baseline state (using PET) with various tasks (language, motor, visual, auditory and other cognitive) in 63 patients in a meta-analysis (Mazoyer et al, 2001). It found consistent activations in very similar areas to Shulman et al during the baseline (i.e. deactivations relative to the task).

Binder et al (1999) provide an interesting perspective on the resting brain state (Binder et al, 1999). Cognitive fMRI experiments were conducted with a rest condition, a tone monitoring task, a semantic decision task and a phonetic monitoring task. A network of polymodal cortical regions showed signal increases (similar to Shulman et al (1997)) during the resting state compared with the perceptual task (tone monitoring) but equal values during the resting and semantic conditions. They suggest firstly that the resting baseline activation is involved in subconscious computational information processing (as opposed to non-computational such as random background or intrinsic activity) and secondly that it represents a conceptual processing network that operates on internal sources of information (as opposed to perceptual networks that rely upon information sources outside to the brain). This could manifest as spontaneous thinking in conscious resting subjects during the baseline. These processes would be interrupted during the behavioural task condition.

3.5.1.1.2 Task dependent BOLD decreases (cross-modal suppression)

Task dependent deactivations have also been reported in the literature and describe the phenomenon of multi-modal sensory interactions. It is thought that, decreases in regions remote from the activations may reflect the suppression or 'gating' of information processing in those areas (which presumably are not directly engaged in the task performance) or the filtering of unattended sensory input. Functionally, this is thought to facilitate information processing in regions involved with the behavioural task and is also known as cross-modal suppression or inhibition (Haxby et al, 1994; Kawashima et al, 1995; Kawashima et al, 1999; Laurienti et al, 2002; Lewis et al, 2000; Shulman et al, 1997a).

Laurienti et al (2002) performed passive visual-only, auditory-only and visual-auditory experiments in a group of 13 subjects and discovered cross-modal deactivations with the visual-only and auditory-only experiments but not with the combined sensory experiments (Laurienti et al, 2002), e.g. lateral temporal cortex deactivation was noted with visual-only stimulation and visual cortex deactivation was seen with auditory-only stimulation. This is consistent with our finding that the lateral temporal cortices were particularly deactivated in the control subjects studied for this thesis. In fact, cross modal BOLD suppression within auditory areas (especially lateral temporal cortex) has been reported in several other studies including the meta-analysis by Shulman of nine PET studies (Shulman et al, 1997a).

Other sensory modalities have been implicated. In another study, Kawashima et al (1995) noted visual cortex deactivation in PET studies during somatosensory tasks regardless of whether their eyes were open or closed (Kawashima et al, 1995). The authors suggested that cross-modal decreases in cortical activity in areas not directly required in performing a given task may be a consequence of the regulation of attention.

Cross-modal interactions may also be facilitatory i.e. there may be enhancement of the task related fMRI response. Several studies have investigated this possibility (Bushara et al, 2003; Calvert et al, 1999; Calvert et al, 2000; Macaluso et al, 2000). Facilitation and inhibition is only one way of classifying cross-modal interactions. An alternative classification subdivides cross-modal interactions into (i) cross-modal matching – which determines whether previously associated features of some shared parameter such as shape or size are matched across two distinct objects, and (ii) cross-modal integration – in which two or more sensory cues are perceived as emanating from the same object and which can be subdivided itself into cross-modal identification, localization and learning (for full review see (Calvert 2001)). There is accumulating evidence from neurophysiological animal studies and human imaging studies that the heteromodal areas involved in cross-modal processing constitute

networks of cortical regions that may include superior temporal gyrus, parieto-preoccipital cortex, posterior insula, frontal regions (including motor, prefrontal and anterior cingulated regions) and subcortical regions that may include claustrum, superior colliculus, thalamus and the amygdaloid complex (Calvert 2001). These networks appear to be involved in the matching and integration of cross-modal inputs. Components of these networks, however, appear to be differentially specialized for synthesizing different types of cross-modal information. It is interesting to note that some of these putative regions were detected by Werring et al (2000) in an fMRI investigation of ON patients (Werring et al, 2000) and were also detected in the longitudinal study reported in this thesis.

3.5.1.1.3 Control deactivation conclusions

The main conclusion from the literature on deactivation behaviour is that there exists a set of brain areas whose activities are attenuated during the performance of goal-directed behavioural tasks. The baseline activity implies the presence of sustained information processing. This processing may have different functions depending upon the particular area involved and upon the experimental context. We feel it is likely that the control deactivations represent a mixture of task-dependent and task independent deactivations as previously described in the literature. Our findings of dynamic extra-occipital differences between ON patients and controls can now be appraised in the context of this realization.

3.5.1.2 ON patient extra-occipital behaviour

We found that the extra-occipital differences between patients and controls were caused by the ON group being unable to mount a deactivation response of the same magnitude as that found in controls. What are the possible explanations for this finding?

One could be that in the patient group, the damaged optic nerve allows fewer afferent neural signals to reach the visual cortex which subsequently results, though polysynaptic pathways, in a reduced

level of deactivation. The reduced deactivation levels would then be a simple function of the reduced quality and quantity of afferent signal. However, a similar pattern of difference between patients and controls was noted for the fellow eye. This is important because the fellow eye is clinically intact and allows the same afferent signals to reach the visual cortex as the control group (because there are no significant differences between patients and controls in the visual cortex).

This implies, for the fellow eye at least (and probably for both eyes), that the differences may be attributed to an interruption of the higher order processing pathways that would normally produce deactivations in the control group with the experimental paradigm. Another perspective is to view the regions as being tonically active in the patient group and therefore not influenced or only minimally affected by the experimental design. The roles of extra-occipital regions may be adaptive (i.e. contribute to clinical recovery) or non-adaptive. Both possibilities are compatible with the observation of early extra-occipital differences, after the onset of ON, which subside as patients recover.

By one year, a few extra-occipital differences begin to re-emerge between patients and controls (figure 3.4) although the spatial extent of these differences is not as prominent as was observed at the earlier time points. We have demonstrated, in an affiliated study of this patient cohort, that optic atrophy also develops by this time (Hickman et al, 2004b) It is possible therefore, that these fMRI differences may be related to ongoing structural changes within the optic nerve.

Deactivations tend not to be reported in brain imaging studies unless they are specifically looked for. This may be because for single sensory/motor task fMRI experiments, there is a strong tendency to search for activations related to the experimental paradigm in areas that are known to be associated with the behavioural task. Other regions are consequently considered uninteresting. In addition, there is little evidence for monosynaptic projections between modality specific brain areas and task independent areas associated with deactivation (Laurienti et al, 2002) This discourages the active

pursuit of remotely located deactivations. However, it does not preclude the existence of polysynaptic connections between brain regions which almost certainly exist. Alternatively activity in certain areas (e.g. sensory specific) may be modulated via pathways from multisensory areas that interconnect different cortical regions (Calvert et al, 2000; Calvert 2001).

3.5.1.3 Study limitiations

It was not feasible to determine whether differences in attentional processes between patients and controls could have accounted for the fMRI differences reported in this study. The patients did not report excess fatigue compared with the controls as a result of the fMRI paradigm, making this possibility less likely. If attentional differences were significant then one may have expected to see differences in visual cortex activation at least with the comparisons of the fellow eyes between patients and controls. However, no differences were noted at any time point. Nevertheless, attentional effects are important features to control for and should be addressed in future studies.

The analysis of the fMRI data was also limited in that the field of view was restricted to that of the partial brain fMRI acquisition, in order to make valid comparisons across every subject. This precluded the investigation of more superior and inferior regions especially the interparietal sulcus, implicated in the default network of brain function. This again will be addressed in future studies in which whole brain fMRI acquisition protocols will be utilized.

3.5.1.4 Conclusions

We demonstrated dynamic longitudinal differences between subjects with acute ON and healthy controls. A particularly interesting finding relates to the differential extra-occipital deactivation behaviour of the two groups, this being attenuated in patients. These differences appear to be most prominent early during ON recovery before receding to some degree. Changes in deactivation patterns have been reported in other populations such as Alzheimer's disease (Lustig et al, 2003),

schizophrenia (Fletcher et al, 1998; Spence et al, 2000) and fragile X syndrome (Tamm et al, 2002). The role of deactivations will therefore become increasingly important as studies continue to investigate cortical reorganization in disease.

3.5.2 Correlation analyses – Evidence for adaptive cortical plasticity in higher visual processing areas after acute ON

We used MR markers of optic nerve integrity and measures of clinical function to investigate their relationships with fMRI activation in response to photic stimulation in patients after ON. Related studies have published structural and clinical data from the same recruited patient cohort as this one, and have shown that reduced optic nerve integrity (indicated by greater triple-dose gadolinium-enhanced lesion length and higher affected optic nerve mean area at baseline) is associated with worse visual function (measured by logMAR visual acuity and HMD) (Hickman et al, 2004a; Hickman et al, 2004b). These structural and clinical measures were therefore appropriate to use in this study.

3.5.2.1 Direct correlations

Our findings demonstrated dynamic relationships between structure, clinical function and functional activation. The early direct correlations within the visual cortices can be appreciated by understanding how input stimuli are normally processed. Reduced optic nerve integrity limits the afferent stimulus transmitted to the visual cortex. This is consistent with the early findings that greater optic nerve inflammation, as determined by the MR markers of optic nerve structure, was associated with lower functional activation within the visual cortex and, consequently, worse vision.

Surprisingly, the fellow eye fMRI response was also related in a similar manner to optic nerve structure and visual function (tables 3.6 and 3.7) i.e a greater fMRI response at baseline for the fellow eye was related to better visual function for the affected side. This cannot be explained by subclinical sympathetic fellow optic nerve swelling (or demyelination) which would theoretically also limit the

transmission of visual input stimulus. An affiliated study to this one demonstrated no evidence for sympathetic swelling of the fellow optic nerve and no change in its mean area over one year(Hickman et al, 2004a) (also optic nerve mean areas in table 3.5). In addition, measures of visual function were not correlated (r^2=0.208, p=0.066 for HMD and r^2=0.058, p=0.352 for logMAR acuity) between affected and fellow eyes. Finally, sympathetic fellow eye demyelination might be detectable electrophysiologically. However, table 3.5 shows stable and generally normal fellow eye VEP whole field amplitudes and latencies over the year. We hypothesize that this finding represents a remodulation of the visual fMRI response that affects primary visual processing holistically i.e. affected optic nerve damage influences the visual cortex fMRI response irrespective of which eye is stimulated.

At three months, direct correlations were found outside the visual cortex such as the bilateral temporal cortices. A greater fMRI response was associated with greater structural damage (table 3.7). At one year the right lateral temporal cortex correlation reversed. We feel these results reflect the complexity and dynamic behaviour of the brain especially after neurological insult. The same regions may play different roles at different times during recovery. The nature of the correlation is difficult to elucidate although the absence of significant findings after baseline for the indirect correlations may make a non-adaptive role seem more likely. The left orbitofrontal fMRI correlation at one year (table 3.7) is interesting. Greater optic nerve atrophy was associated with a larger fellow eye fMRI response. The reason for this cannot be determined from our study. However, both orbitofrontal and particularly lateral temporal cortices have been implicated in cortical reorganization after ON (Toosy et al, 2002a; Werring et al, 2000). They have also been suggested as sites of multimodal sensory processing (Mesulam 1998) as part of extensive cortical and subcortical networks that are involved in the matching and integration of cross-modal inputs (Calvert 2001).

3.5.2.2 *Indirect correlations*

The indirect correlations provide the most striking results (figures 3.17 and 3.18, table 3.8). They support adaptive cortical plasticity during early recovery within the peristriate cortex and LOCs, regions known to be involved in higher order visual processing. Higher order visual processing itself has been divided into two major streams: the ventral stream that projects from V1 to the infero-temporal cortex, and the dorsal stream which projects from V1 to the posterior parietal cortex (Ungerleider and Mishkin 1982). The ventral stream is thought to mediate the perceptual construction of the visual world involving cognitive processes such as recognition and identification whereas the dorsal stream is felt to oversee the visual control of actions directed at objects within this world (Goodale and Milner 1992; Goodale and Westwood 2004). The LOC lies in the ventral stream and has been implicated in object shape recognition in healthy subjects (Grill-Spector et al, 1999; Grill-Spector et al, 2000; Grill-Spector 2003; Malach et al, 1995). It is largely non-retinotopic and shows selectivity to objects and object fragments (Grill-Spector et al, 1998). Within the LOC itself, anatomical subdivisions into dorsal-caudal (LO or lateral occipital) and ventral-anterior regions (termed pFs for posterior fusiform) have been suggested (Grill-Spector et al, 2001). Our findings should allow future fMRI studies to target plasticity in these areas with specifically designed paradigms.

Interestingly, indirect correlations were not found after the baseline time point. This could indicate that adaptive functional plasticity has no significant role after the acute stage of ON recovery. Alternatively it could be explained by type II error. For example, as patients recover, their structural and clinical markers will show less variation. This will weaken any subsequent correlations especially in the second stage of the indirect correlations. In addition, it is known that the pathophysiological mechanisms contributing to clinical deficit in ON are not fully understood. They comprise a mixture of inflammation, oedema and demyelination (Smith and McDonald 1999). Inflammation and vasogenic oedema are felt to contribute to the degree of clinical deficit (Youl et al, 1991) and, by implication, optic nerve integrity. Inflammation is characterized by the secretion of pro-inflammatory cytokines

with cell infiltration and oedema. The MRI markers of optic nerve structure used were relatively crude (degree of swelling and enhanced lesion length) and may not be as useful after baseline at predicting optic nerve integrity. In the future more sophisticated measures that evaluate optic nerve integrity at different times during recovery, e.g. the measurement of inflammatory cell infiltration, may become important.

3.5.2.3 Conclusions

In summary, we used measures of optic nerve structure, clinical function and functional MRI to investigate cortical reorganization of the fMRI response following ON. Our results demonstrated dynamic processes at work within the brain during clinical recovery. In particular there is evidence for adaptive cortical plasticity within the occipital cortex early after ON onset. Future work should be aimed at developing appropriate fMRI experimental paradigms to investigate the roles of these regions as well as investigating non-invasive methods to characterize the structural integrities of the anterior and posterior visual pathways.

3.6 References

The clinical profile of optic neuritis. Experience of the Optic Neuritis Treatment Trial. Optic Neuritis Study Group. *Arch Ophthalmol.* 1991. **109**(12), 1673-8.

Anderson, TJ, Jenkins, IH, Brooks, DJ, Hawken, MB, Frackowiak, RS, and Kennard, C. Cortical control of saccades and fixation in man. A PET study. *Brain.* 1994. **117 (Pt 5)**, 1073-84.

Berman, RA and Colby, CL. Auditory and visual attention modulate motion processing in area MT+. *Brain Res.Cogn Brain Res.* 2002. **14**(1), 64-74.

Binder, JR, Frost, JA, Hammeke, TA, Bellgowan, PS, Rao, SM, and Cox, RW. Conceptual processing during the conscious resting state. A functional MRI study. *J.Cogn Neurosci.* 1999. **11**(1), 80-95.

Brusa, A, Jones, SJ, and Plant, GT. Long-term remyelination after optic neuritis: A 2-year visual evoked potential and psychophysical serial study. *Brain.* 2001. **124**(Pt 3), 468-79.

Buchel, C, Josephs, O, Rees, G, Turner, R, Frith, CD, and Friston, KJ. The functional anatomy of attention to visual motion. A functional MRI study. *Brain.* 1998. **121 (Pt 7)**, 1281-94.

Bushara, KO, Hanakawa, T, Immisch, I, Toma, K, Kansaku, K, and Hallett, M. Neural correlates of cross-modal binding. *Nat.Neurosci.* 2003. **6**(2), 190-5.

Calvert, GA. Crossmodal processing in the human brain: insights from functional neuroimaging studies. *Cereb.Cortex.* 2001. **11**(12), 1110-23.

Calvert, GA, Brammer, MJ, Bullmore, ET, Campbell, R, Iversen, SD, and David, AS. Response amplification in sensory-specific cortices during crossmodal binding. *Neuroreport.* 1999. **10**(12), 2619-23.

Calvert, GA, Campbell, R, and Brammer, MJ. Evidence from functional magnetic resonance imaging of crossmodal binding in the human heteromodal cortex. *Curr.Biol.* 2000. **10**(11), 649-57.

Catalan, MJ, Honda, M, Weeks, RA, Cohen, LG, and Hallett, M. The functional neuroanatomy of simple and complex sequential finger movements: a PET study. *Brain.* 1998. **121 (Pt 2)**, 253-64.

Dumoulin, SO, Bittar, RG, Kabani, NJ, Baker, CL, Jr., Le Goualher, G, Bruce, PG, and Evans, AC. A new anatomical landmark for reliable identification of human area V5/MT: a quantitative analysis of sulcal patterning. *Cereb.Cortex.* 2000. **10**(5), 454-63.

Ferris, FL, III, Kassoff, A, Bresnick, GH, and Bailey, I. New visual acuity charts for clinical research. *Am.J.Ophthalmol.* 1982. **94**(1), 91-6.

Filippi, M and Comi, G. Primary progressive multiple sclerosis. Milan; Springer-Verlag, 2002.

Filippi, M, Rocca, MA, Falini, A, Caputo, D, Ghezzi, A, Colombo, B, Scotti, G, and Comi, G. Correlations between structural CNS damage and functional MRI changes in primary progressive MS. *Neuroimage.* 2002. **15**(3), 537-46.

Fletcher, PC, McKenna, PJ, Frith, CD, Grasby, PM, Friston, KJ, and Dolan, RJ. Brain activations in schizophrenia during a graded memory task studied with functional neuroimaging. *Arch Gen.Psychiatry.* 1998. **55**(11), 1001-8.

Frackowiak, RS. The Cerebral Basis of Functional Recovery. In: Frackowiak, RS, Friston, KJ, Frith, CD, Dolan, RJ, and Mazziotta, JC. Human Brain Function. San Diego; Academic Press, 1997: 275-99.

Friston, KJ and Buchel, C. Attentional modulation of effective connectivity from V2 to V5/MT in humans. *Proc.Natl.Acad.Sci.U.S.A.* 2000. **97**(13), 7591-6.

Friston, KJ, Holmes, A, Poline, JB, Price, CJ, and Frith, CD. Detecting activations in PET and fMRI: levels of inference and power. *Neuroimage.* 1996. **4**(3 Pt 1), 223-35.

Friston, KJ, Holmes, AP, Worsley, KJ, Poline, JB, Frith, CD, and Frackowiak, RSJ. Statistical parametric maps in functional imaging: A general linear approach. *Hum.Brain Mapp.* 1995. **2**, 189-210.

Friston, KJ, Worsley, KJ, Frackowiak, RSJ, Mazziotta, JC, and Evans, AC. Assessing the significance of focal activations using their spatial extent. *Hum.Brain Mapp.* 1994. **1**, 214-20.

Goebel, R, Khorram-Sefat, D, Muckli, L, Hacker, H, and Singer, W. The constructive nature of vision: direct evidence from functional magnetic resonance imaging studies of apparent motion and motion imagery. *Eur.J.Neurosci.* 1998. **10**(5), 1563-73.

Goebel, R, Muckli, L, Zanella, FE, Singer, W, and Stoerig, P. Sustained extrastriate cortical activation without visual awareness revealed by fMRI studies of hemianopic patients. *Vision Res.* 2001. **41**(10-11), 1459-74.

Goodale, MA and Milner, AD. Separate visual pathways for perception and action. *Trends Neurosci.* 1992. **15**(1), 20-5.

Goodale, MA and Westwood, DA. An evolving view of duplex vision: separate but interacting cortical pathways for perception and action. *Curr.Opin.Neurobiol.* 2004. **14**(2), 203-11.

Grafman, J and Litvan, I. Evidence for four forms of neuroplasticity. In: Grafman, J and Christen, Y. Neuronal Plasticity: Building a bridge from the laboratory to the clinic (research and perspectives in neurosciences). Berlin Heidelberg; Springer-Verlag, 1999: 131-9.

Grill-Spector, K. The neural basis of object perception. *Curr.Opin.Neurobiol.* 2003. **13**(2), 159-66.

Grill-Spector, K, Kourtzi, Z, and Kanwisher, N. The lateral occipital complex and its role in object recognition. *Vision Res.* 2001. **41**(10-11), 1409-22.

Grill-Spector, K, Kushnir, T, Edelman, S, Avidan, G, Itzchak, Y, and Malach, R. Differential processing of objects under various viewing conditions in the human lateral occipital complex. *Neuron.* 1999. **24**(1), 187-203.

Grill-Spector, K, Kushnir, T, Hendler, T, Edelman, S, Itzchak, Y, and Malach, R. A sequence of object-processing stages revealed by fMRI in the human occipital lobe. *Hum.Brain Mapp.* 1998. **6**(4), 316-28.

Grill-Spector, K, Kushnir, T, Hendler, T, and Malach, R. The dynamics of object-selective activation correlate with recognition performance in humans. *Nat.Neurosci.* 2000. **3**(8), 837-43.

Gusnard, DA and Raichle, ME. Searching for a baseline: functional imaging and the resting human brain. *Nat.Rev.Neurosci.* 2001. **2**(10), 685-94.

Haxby, JV, Horwitz, B, Ungerleider, LG, Maisog, JM, Pietrini, P, and Grady, CL. The functional organization of human extrastriate cortex: a PET-rCBF study of selective attention to faces and locations. *J Neurosci.* 1994. **14**(11 Pt 1), 6336-53.

Hickman, SJ, Brex, PA, Brierley, CM, Silver, NC, Barker, GJ, Scolding, NJ, Compston, DA, Moseley, IF, Plant, GT, and Miller, DH. Detection of optic nerve atrophy following a single episode of unilateral

optic neuritis by MRI using a fat-saturated short-echo fast FLAIR sequence. *Neuroradiology*. 2001. **43**(2), 123-8.

Hickman, SJ, Brierley, CM, Brex, PA, MacManus, DG, Scolding, NJ, Compston, DA, and Miller, DH. Continuing optic nerve atrophy following optic neuritis: a serial MRI study. *Mult.Scler.* 2002. **8**(4), 339-42.

Hickman, SJ, Toosy, AT, Jones, SJ, Altmann, DR, Miszkiel, KA, MacManus, DG, Barker, GJ, Plant, GT, Thompson, AJ, and Miller, DH. A serial MRI study following optic nerve mean area in acute optic neuritis. *Brain*. 2004a. **127**(Pt 11), 2498-505.

Hickman, SJ, Toosy, AT, Miszkiel, KA, Jones, SJ, Altmann, DR, MacManus, DG, Plant, GT, Thompson, AJ, and Miller, DH. Visual recovery following acute optic neuritis: A clinical, electrophysiological and magnetic resonance imaging study. *J Neurol*. 2004b. **251**(8), 996-1005.

Jacobs, KM and Donoghue, JP. Reshaping the cortical motor map by unmasking latent intracortical connections. *Science*. 1991. **251**(4996), 944-7.

Jones, TA and Schallert, T. Overgrowth and pruning of dendrites in adult rats recovering from neocortical damage. *Brain Res.* 1992. **581**(1), 156-60.

Kawashima, R, Imaizumi, S, Mori, K, Okada, K, Goto, R, Kiritani, S, Ogawa, A, and Fukuda, H. Selective visual and auditory attention toward utterances-a PET study. *Neuroimage*. 1999. **10**(2), 209-15.

Kawashima, R, O'Sullivan, BT, and Roland, PE. Positron-emission tomography studies of cross-modality inhibition in selective attentional tasks: closing the "mind's eye". *Proc Natl Acad Sci U S A*. 1995. **92**(13), 5969-72.

Kupersmith, MJ, Alban, T, Zeiffer, B, and Lefton, D. Contrast-enhanced MRI in acute optic neuritis: relationship to visual performance. *Brain*. 2002. **125**(Pt 4), 812-22.

Laurienti, PJ, Burdette, JH, Wallace, MT, Yen, YF, Field, AS, and Stein, BE. Deactivation of sensory-specific cortex by cross-modal stimuli. *J Cogn Neurosci*. 2002. **14**(3), 420-9.

Lee, MA, Blamire, AM, Pendlebury, S, Ho, KH, Mills, KR, Styles, P, Palace, J, and Matthews, PM. Axonal injury or loss in the internal capsule and motor impairment in multiple sclerosis. *Arch Neurol*. 2000. **57**(1), 65-70.

Lerner, Y, Hendler, T, Ben Bashat, D, Harel, M, and Malach, R. A hierarchical axis of object processing stages in the human visual cortex. *Cereb.Cortex*. 2001. **11**(4), 287-97.

Lewis, JW, Beauchamp, MS, and DeYoe, EA. A comparison of visual and auditory motion processing in human cerebral cortex. *Cereb.Cortex*. 2000. **10**(9), 873-88.

Liepert, J, Dettmers, C, Terborg, C, and Weiller, C. Inhibition of ipsilateral motor cortex during phasic generation of low force. *Clin.Neurophysiol*. 2001. **112**(1), 114-21.

Lotze, M, Flor, H, Grodd, W, Larbig, W, and Birbaumer, N. Phantom movements and pain. An fMRI study in upper limb amputees. *Brain*. 2001. **124**(Pt 11), 2268-77.

Lustig, C, Snyder, AZ, Bhakta, M, O'Brien, KC, McAvoy, M, Raichle, ME, Morris, JC, and Buckner, RL. Functional deactivations: Change with age and dementia of the Alzheimer type. *Proc Natl Acad Sci U S A*. 2003.

Macaluso, E, Frith, CD, and Driver, J. Modulation of human visual cortex by crossmodal spatial attention. *Science*. 2000. **289**(5482), 1206-8.

Malach, R, Reppas, JB, Benson, RR, Kwong, KK, Jiang, H, Kennedy, WA, Ledden, PJ, Brady, TJ, Rosen, BR, and Tootell, RB. Object-related activity revealed by functional magnetic resonance imaging in human occipital cortex. *Proc.Natl.Acad.Sci.U.S.A.* 1995. **92**(18), 8135-9.

Mazoyer, B, Zago, L, Mellet, E, Bricogne, S, Etard, O, Houde, O, Crivello, F, Joliot, M, Petit, L, and Tzourio-Mazoyer, N. Cortical networks for working memory and executive functions sustain the conscious resting state in man. *Brain Res.Bull.* 2001. **54**(3), 287-98.

Mesulam, MM. From sensation to cognition. *Brain.* 1998. **121 (Pt 6)**, 1013-52.

Pantano, P, Iannetti, GD, Caramia, F, Mainero, C, Di Legge, S, Bozzao, L, Pozzilli, C, and Lenzi, GL. Cortical motor reorganization after a single clinical attack of multiple sclerosis. *Brain.* 2002a. **125**(Pt 7), 1607-15.

Pantano, P, Mainero, C, Iannetti, GD, Caramia, F, Di Legge, S, Piattella, MC, Pozzilli, C, Bozzao, L, and Lenzi, GL. Contribution of corticospinal tract damage to cortical motor reorganization after a single clinical attack of multiple sclerosis. *Neuroimage.* 2002b. **17**(4), 1837-43.

Pierrot-Deseilligny, C, Rivaud, S, Gaymard, B, Muri, R, and Vermersch, AI. Cortical control of saccades. *Ann.Neurol.* 1995. **37**(5), 557-67.

Plummer, DL. Dispimage: a display and analysis tool for medical images. *Riv Neuroradiol.* 1992. **5**(489), 495.

Poline, JB, Worsley, KJ, Evans, AC, and Friston, KJ. Combining spatial extent and peak intensity to test for activations in functional imaging. *Neuroimage.* 1997. **5**(2), 83-96.

Raichle, ME. Behind the scenes of functional brain imaging: a historical and physiological perspective. *Proc Natl Acad Sci U S A.* 1998a. **95**(3), 765-72.

Raichle, ME. The neural correlates of consciousness: an analysis of cognitive skill learning. *Philos.Trans R.Soc Lond B Biol.Sci.* 1998b. **353**(1377), 1889-901.

Raichle, ME, MacLeod, AM, Snyder, AZ, Powers, WJ, Gusnard, DA, and Shulman, GL. A default mode of brain function. *Proc.Natl.Acad.Sci.U.S.A.* 2001. **98**(2), 676-82.

Reddy, H, Narayanan, S, Arnoutelis, R, Jenkinson, M, Antel, J, Matthews, PM, and Arnold, DL. Evidence for adaptive functional changes in the cerebral cortex with axonal injury from multiple sclerosis. *Brain.* 2000a. **123 (Pt 11)**, 2314-20.

Reddy, H, Narayanan, S, Matthews, PM, Hoge, RD, Pike, GB, Duquette, P, Antel, J, and Arnold, DL. Relating axonal injury to functional recovery in MS. *Neurology.* 2000b. **54**(1), 236-9.

Reddy, H, Narayanan, S, Woolrich, M, Mitsumori, T, Lapierre, Y, Arnold, DL, and Matthews, PM. Functional brain reorganization for hand movement in patients with multiple sclerosis: defining distinct effects of injury and disability. *Brain.* 2002. **125**(Pt 12), 2646-57.

Rees, G, Friston, K, and Koch, C. A direct quantitative relationship between the functional properties of human and macaque V5. *Nat.Neurosci.* 2000. **3**(7), 716-23.

Rocca, MA, Falini, A, Colombo, B, Scotti, G, Comi, G, and Filippi, M. Adaptive functional changes in the cerebral cortex of patients with nondisabling multiple sclerosis correlate with the extent of brain structural damage. *Ann.Neurol.* 2002. **51**(3), 330-9.

Rocca, MA, Gavazzi, C, Mezzapesa, DM, Falini, A, Colombo, B, Mascalchi, M, Scotti, G, Comi, G, and Filippi, M. A functional magnetic resonance imaging study of patients with secondary progressive multiple sclerosis. *Neuroimage*. 2003a. **19**(4), 1770-7.

Rocca, MA, Mezzapesa, DM, Falini, A, Ghezzi, A, Martinelli, V, Scotti, G, Comi, G, and Filippi, M. Evidence for axonal pathology and adaptive cortical reorganization in patients at presentation with clinically isolated syndromes suggestive of multiple sclerosis. *Neuroimage*. 2003b. **18**(4), 847-55.

Rocca, MA, Mezzapesa, DM, Ghezzi, A, Falini, A, Agosta, F, Martinelli, V, Scotti, G, Comi, G, and Filippi, M. Cord damage elicits brain functional reorganization after a single episode of myelitis. *Neurology*. 2003c. **61**(8), 1078-85.

Rocca, MA, Pagani, E, Ghezzi, A, Falini, A, Zaffaroni, M, Colombo, B, Scotti, G, Comi, G, and Filippi, M. Functional cortical changes in patients with multiple sclerosis and nonspecific findings on conventional magnetic resonance imaging scans of the brain. *Neuroimage*. 2003d. **19**(3), 826-36.

Rombouts, SA, Lazeron, RH, Scheltens, P, Uitdehaag, BM, Sprenger, M, Valk, J, and Barkhof, F. Visual activation patterns in patients with optic neuritis: an fMRI pilot study. *Neurology*. 1998. **50**(6), 1896-9.

Rorden, C and Brett, M. Stereotaxic display of brain lesions. *Behav.Neurol.* 2000. **12**(4), 191-200.

Russ, MO, Cleff, U, Lanfermann, H, Schalnus, R, Enzensberger, W, and Kleinschmidt, A. Functional magnetic resonance imaging in acute unilateral optic neuritis. *J Neuroimaging*. 2002. **12**(4), 339-50.

Shulman, GL, Corbetta, M, Buckner, RL, Raichle, ME, Fiez, JA, Miezin, FM, and Petersen, SE. Top-down modulation of early sensory cortex. *Cereb.Cortex*. 1997a. **7**(3), 193-206.

Shulman, GL, Fiez, JA, Corbetta, M, Buckner, RL, Miezin, FM, Raichle, ME, and Petersen, SE. Common blood flow changes across visual tasks. 2. Decreases in cerebral cortex. *J Cogn Neurosci.* 1997b. **9**, 648-63.

Smith, KJ and McDonald, WI. The pathophysiology of multiple sclerosis: the mechanisms underlying the production of symptoms and the natural history of the disease. *Philos.Trans.R.Soc.Lond B Biol.Sci.* 1999. **354**(1390), 1649-73.

Spence, SA, Liddle, PF, Stefan, MD, Hellewell, JS, Sharma, T, Friston, KJ, Hirsch, SR, Frith, CD, Murray, RM, Deakin, JF, and Grasby, PM. Functional anatomy of verbal fluency in people with schizophrenia and those at genetic risk. Focal dysfunction and distributed disconnectivity reappraised. *Br.J Psychiatry.* 2000. **176**, 52-60.

Staffen, W, Mair, A, Zauner, H, Unterrainer, J, Niederhofer, H, Kutzelnigg, A, Ritter, S, Golaszewski, S, Iglseder, B, and Ladurner, G. Cognitive function and fMRI in patients with multiple sclerosis: evidence for compensatory cortical activation during an attention task. *Brain.* 2002. **125**(Pt 6), 1275-82.

Tamm, L, Menon, V, Johnston, CK, Hessl, DR, and Reiss, AL. fMRI study of cognitive interference processing in females with fragile X syndrome. *J Cogn Neurosci.* 2002. **14**(2), 160-71.

Taylor, JG, Schmitz, N, Ziemons, K, Grosse-Ruyken, ML, Gruber, O, Mueller-Gaertner, HW, and Shah, NJ. The network of brain areas involved in the motion aftereffect. *Neuroimage.* 2000. **11**(4), 257-70.

Tehovnik, EJ, Sommer, MA, Chou, IH, Slocum, WM, and Schiller, PH. Eye fields in the frontal lobes of primates. *Brain Res.Brain Res.Rev.* 2000. **32**(2-3), 413-48.

Toosy, A, Werring, D, Bullmore, E, Plant, G, Barker, G, Miller, D, and Thompson, A. Functional magnetic resonance imaging of the cortical response to photic stimulation in humans following optic neuritis recovery. *Neurosci.Lett.* 2002a. **330**(3), 255.

Toosy, AT, Werring, DJ, Bullmore, ET, Plant, GT, Barker, GJ, Miller, DH, and Thompson, AJ. Functional magnetic resonance imaging of the cortical response to photic stimulation in humans following optic neuritis recovery. *Neurosci.Lett.* 2002b. **330**(3), 255-9.

Tootell, RB, Reppas, JB, Kwong, KK, Malach, R, Born, RT, Brady, TJ, Rosen, BR, and Belliveau, JW. Functional analysis of human MT and related visual cortical areas using magnetic resonance imaging. *J.Neurosci.* 1995. **15**(4), 3215-30.

Tzourio-Mazoyer, N, Landeau, B, Papathanassiou, D, Crivello, F, Etard, O, Delcroix, N, Mazoyer, B, and Joliot, M. Automated anatomical labeling of activations in SPM using a macroscopic anatomical parcellation of the MNI MRI single-subject brain. *Neuroimage.* 2002. **15**(1), 273-89.

Ungerleider, LG and Mishkin, M. Two cortical visual systems. In: Ingle, DJ, Goodale, MA, and Mansfield, RJ. Analysis of visual behavior. Cambridge (MA); MIT Press, 1982: 549-86.

Ward, NS and Frackowiak, RS. Age-related changes in the neural correlates of motor performance. *Brain.* 2003. **126**(Pt 4), 873-88.

Watson, JD, Myers, R, Frackowiak, RS, Hajnal, JV, Woods, RP, Mazziotta, JC, Shipp, S, and Zeki, S. Area V5 of the human brain: evidence from a combined study using positron emission tomography and magnetic resonance imaging. *Cereb.Cortex.* 1993. **3**(2), 79-94.

Waxman, SG. Acquired channelopathies in nerve injury and MS. *Neurology.* 2001. **56**(12), 1621-7.

Werring, DJ, Bullmore, ET, Toosy, AT, Miller, DH, Barker, GJ, MacManus, DG, Brammer, MJ, Giampietro, VP, Brusa, A, Brex, PA, Moseley, IF, Plant, GT, McDonald, WI, and Thompson, AJ. Recovery from optic neuritis is associated with a change in the distribution of cerebral response to visual stimulation: a functional magnetic resonance imaging study. *J.Neurol.Neurosurg.Psychiatry*. 2000. **68**(4), 441-9.

Wexler, BE, Fulbright, RK, Lacadie, CM, Skudlarski, P, Kelz, MB, Constable, RT, and Gore, JC. An fMRI study of the human cortical motor system response to increasing functional demands. *Magn Reson.Imaging*. 1997. **15**(4), 385-96.

Worsley, KJ. Developments in Random Field Theory. In: Frackowiak, RSJ, Friston, KJ, Frith, CD, Dolan, RJ, Price, CJ, Zeki, S, Ashburner, J, and Penny, W. Human Brain Function. London; Elsevier Science, 2004: 881-6.

Youl, BD, Turano, G, Miller, DH, Towell, AD, MacManus, DG, Moore, SG, Jones, SJ, Barrett, G, Kendall, BE, and Moseley, IF. The pathophysiology of acute optic neuritis. An association of gadolinium leakage with clinical and electrophysiological deficits. *Brain*. 1991. **114 (Pt 6)**, 2437-50.

CHAPTER 4

THE USE OF DIFFUSION TENSOR IMAGING TO DETECT CORTICOSPINAL TRACT PATHOLOGY IN AMYOTROPHIC LATERAL SCLEROSIS

4.1 Introduction

This chapter introduces DTI as a viable tool with which to study white matter tract structure. It was applied to the corticospinal tracts, easily identifiable structures, in the disease model of amyotrophic lateral sclerosis (ALS). Although not directly related to the main subject matter in this thesis, it was important to clinically validate its use before more novel applications were developed from it (to be described in chapter 5).

ALS is a neurodegenerative condition of complex pathology that targets the corticospinal tracts, brainstem and lower motor neurons (Charcot and Joffroy 1869; Holmes 1909; Swash 2000). It results in progressive weakness of the bulbar, limb, thoracic and abdominal musculature usually with a mixture of upper and lower motor neurological signs. Phenotypic variants include progressive bulbar palsy, progressive muscular atrophy (lower motor syndrome) and primary lateral sclerosis (upper motor syndrome). The main histological changes include loss of motor neurons and associated astrocytosis (Lowe et al, 1997).

Magnetic resonance imaging has investigated the involvement of the corticospinal tracts in ALS with variable success. Changes in signal intensity along the internal capsule have been described using T2-weighted (Hofmann et al, 1998; Thorpe et al, 1996), proton density (Cheung et al, 1995; Hofmann et

al, 1998) and FLAIR (Hecht et al, 2001) sequences. Magnetization transfer (MT) imaging has demonstrated quantitative evidence for a reduced MT ratio in the internal capsule (Kato et al, 1997) and MR spectroscopy has shown changes in the primary motor cortex (Pioro et al, 1994; Rooney et al, 1998; Suhy et al, 2002).

The quantitative assessment of water diffusion using DTI allows the investigation of white matter architecture affected by different pathologies. This has been performed for chronic conditions that exhibit Wallerian (anterograde) degeneration such as stroke (Pierpaoli et al, 2001; Werring et al, 2000), tumour (Wieshmann et al, 1999a) and trauma (Werring et al, 1998; Wieshmann et al, 1999b). These studies consistently show reduced anisotropy in the affected white matter tracts and, less consistently, increased diffusivity.

Diffusion Tensor imaging (DTI) has also been used to quantitatively assess involvement of the corticospinal tracts in ALS at the level of the internal capsule (Ellis et al, 1999). ALS pathology affects both white and grey matter but its hallmark is corticospinal tract degeneration (as well as lower motor neuron degeneration). Ellis et al (1999) found evidence for reduced FA and increased MD at the level of the internal capsules in ALS patients when compared to controls although other levels of the corticospinal tracts were not sampled. We acquired wholebrain DTI in patients with ALS. This enabled us to investigate the intracranial course of the corticospinal tract from the internal capsules down to the pyramids.

4.2 Methods

4.2.1 Subject recruitment

21 patients (median age 58 years; range 28-71 years; 16 men, 5 women) with probable or definite ALS (Brooks et al, 2000) were recruited from the Motor Neuron Disease clinic at The National Hospital for Neurology and Neurosurgery, London. 14 controls (median age 51.5; range 37-71 years;

9 men, 5 women) were also recruited. All subjects gave written informed consent to participate in the study. The study was approved by the Joint Ethics Committee of the Institute of Neurology and The National Hospital for Neurology and Neurosurgery.

Each patient was examined and a questionnaire for the ALS functional rating scale (ALSFRS) was used to assess disease severity (The ALS CNTF treatment study, 1996). This provided a bulbar and spinal score that were added together to give a total ALS severity score out of 40. A greater disability was indicated by a lower score. The disease progression rate was estimated by the following formula (Ellis et al, 1999):

$$\text{Disease Rate} = \frac{(40 - \text{ALS severity score})}{\text{Disease Duration}}$$

4.2.2 Image Acquisition

Imaging was performed on a 1.5 T GE Signa Horizon Echospeed system (General Electric, Milwaukee, WI, USA) with a standard quadrature head coil and gradient coils (0-22 mT/m). Head motion was restricted by placing pads on both sides of the subject's head. A single-shot spin echo EPI (echo planar imaging) diffusion-weighted sequence was performed for DTI acquisition. Three sets of seven 5 mm slices were collected, with a 10 mm slice gap, giving a total of 21 contiguous 5 mm axial slices which covered most of the brain (TE 78 msec, TR approx 2.25 sec, acquired image matrix 96x96 reconstructed as 128x128 giving pixel dimensions 1.88 mm x 1.88 mm, 4 diffusion b values increasing from 0 to 700 smm^{-2}, Δ=35 ms, δ=28 ms, maximum gradient 22 mT/m in each of 7 non-collinear directions). Five acquisitions for each set of diffusion data were performed and averaged after magnitude reconstruction to improve the signal to noise ratio. Cardiac gating was used to avoid pulsatile artefacts; image acquisition was triggered from every second R wave monitored using pulse

oximetry (trigger delay 10% of the expected RR interval, i.e. approximately 200ms, 3 or 4 shots per RR interval).

Structural images were also acquired, including axial dual echo FSE images (28 contiguous axial slices, dimensions 0.94x0.94 mm, matrix 256x256, slice thickness 5 mm, TR 3 s, TE 15/90 ms) and high resolution multishot inversion-recovery prepared EPI images matched in position and geometric distortion to the corresponding diffusion-weighted images (28 contiguous axial slices, dimensions 0.94x0.94 mm, matrix 256x256, slice thickness 5mm, TR 5.5 s, TE 78 ms, TI 200 ms).

Correction of eddy-current distortions in DW-EPI was performed using a two-dimensional image registration technique (Symms et al, 1997). The diffusion tensor, mean diffusivity and fractional anisotropy were calculated on a pixel by pixel basis (Basser et al, 1994; Pierpaoli and Basser 1996).

4.2.3 Region of interest (ROI) analysis

On the FA and MD maps (both derived from the diffusion tensor and therefore in the same space), regions-of-interest (ROIs) were manually applied to the left and right corticospinal tracts on all axial slices extending from the pyramids to the top of the internal capsule (*DispImage* (Plummer 1992)). The high resolution EPI images and co-registered z-weighted ADC (apparent diffusion coefficient) map were also displayed during ROI positioning. The z-weighted ADC map displayed voxels in which signal intensity was proportional to diffusion magnitude in the vertical direction allowing more precise positioning of the ROIs along the corticospinal tracts. The datasets under analysis were observer blinded. All ROIs were the same size (28 mm^2) and the pyramidal tracts were localized based on *a priori* anatomical knowledge and reference to relevant literature (Hirayama et al, 1962; Ross 1980). The cross-sectional area and length of the corticospinal tracts varied between individuals. We therefore chose to vary the number of ROIs that were applied per side on each axial slice so that the corticospinal tract area was sufficiently covered (figure 4.1). In practice we applied 2-3 ROIs per side on each axial slice except for the pyramids where 1 ROI was applied per side per

axial slice (because the cross-sectional areas of the pyramids were smaller). The ROI measurements were then divided into four groups corresponding to four locations along the corticospinal tract – internal capsule, cerebral peduncles, pons and pyramids. The average value of the ROIs for each location was then entered into the statistical analysis (which was performed by Martin King).

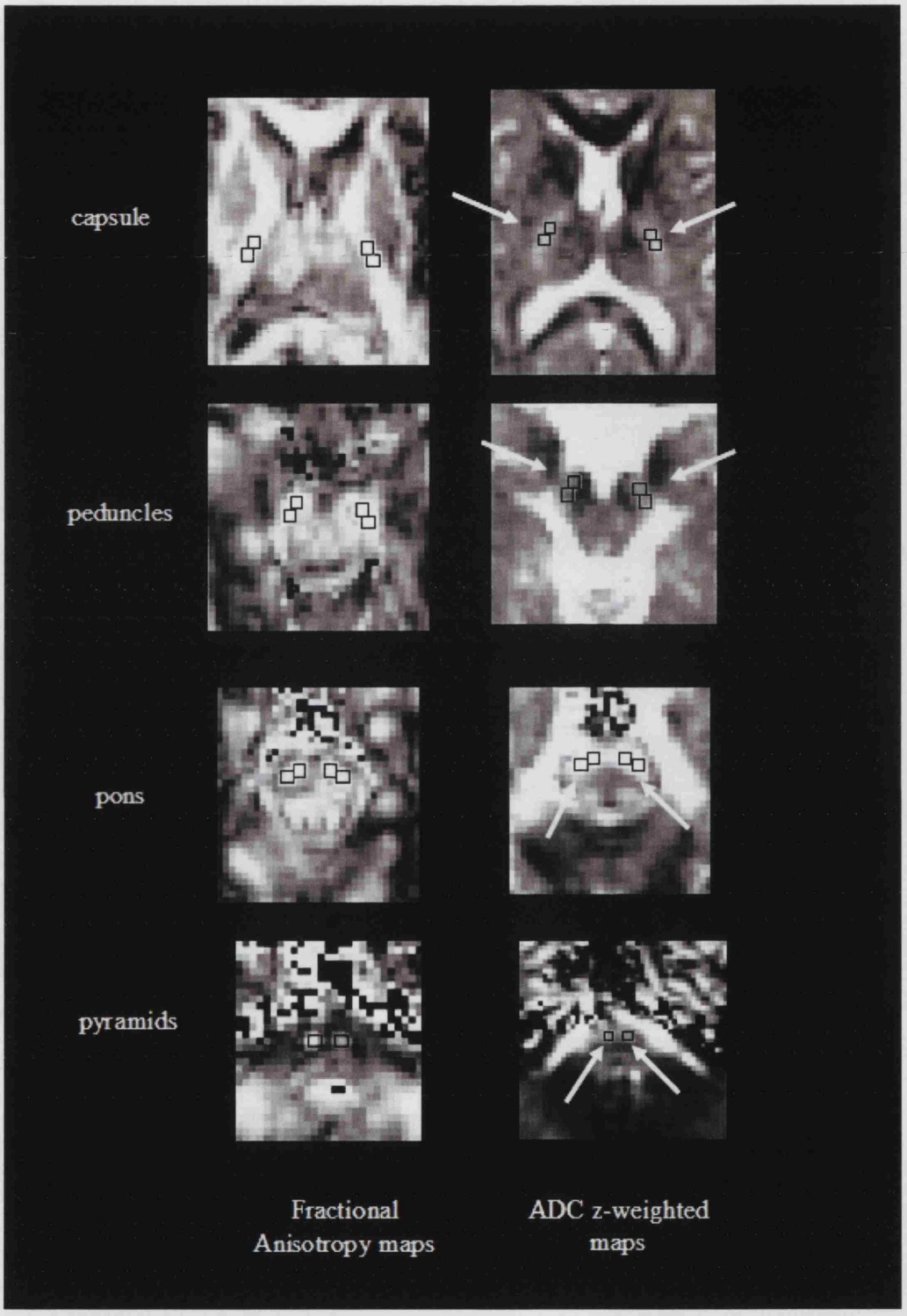

Figure 4.1. Axial images through the internal capsules, cerebral peduncles, pons and pyramids on FA and z-weighted ADC maps for a representative control subject. Regions of interest have been positioned along the left and right corticospinal tracts.

4.2.4 Statistical analysis

4.2.4.1 Fractional anisotropy

A mixed model regression analysis was performed with age and sex as covariates and side and location as within subject fixed effect factors (Hand et al, 1996; Sullivan et al, 1999). A random coefficients model was adopted. Fixed effects terms were selected using the likelihood ratio test to compare various nested models. Akaikes Information Criterion (Sullivan et al, 1999) was used to determine which random effects should be included in the model. The covariance structure was modeled using separate covariance matrices for the two groups to account for the greater between-subject variability within the patient group. Probability values were obtained subsequent to a conversion of the restricted maximum likelihood (REML) Wald statistics to F ratios, using denominator degrees of freedom (ddf) equal to the difference between the number of observations and the rank of the fixed effects design matrix. Inferences were not altered by adopting alternative specifications for the ddf. The calculations were performed using SAS Version 6.12 PROC MIXED (SAS Institute Inc. 1996). In the results, two sided probability values are given throughout, although many of the statements are expressed in a one sided form.

4.2.4.2 Mean diffusivity

The same procedure was used with the exception of the regression model which included quadratic terms in corticospinal location, together with linear and quadratic random coefficient location terms. The latter were required to capture the progressive increase in between-subject variability associated with the caudal corticospinal locations.

4.2.4.3 *Assessment of gradient calibration changes over time*

The plots for predicted FA versus location showed a random intercept effect i.e. an apparently constant offset for a given subject. To determine if this could be caused by changes in scanner gradient calibration over time, serial data for three controls were analyzed. These controls belonged to the original control group and had been rescanned at 12 months. For each of these six scans (three at baseline and three at 1 year), another control dataset was selected that had been acquired within 1 month of each scan. This gave six 'date-matched' pairs of datasets. The first member of each pair was either a baseline scan or a 1 year rescan of the three selected controls. Examination of the resulting FA data demonstrated that the observed between-subject random intercept effect was not caused by changes in gradient calibration i.e. real intersubject differences make a major contribution to the observed differences.

4.3 Results

4.3.1 Subject characteristics

The subject characteristics are shown in table 4.1. Gender was found to be unimportant and was removed from the model. Age was incorporated into the model as a covariate during statistical analysis because some dependence of FA and MD on age was found that differed between ALS and control groups. This, however, did not alter the major findings that are discussed for MD and FA and the qualitative results are maintained across the age range. Thus, for simplicity, the estimated differences between sides and subject groups will be quoted only for a representative midpoint age of 55 years.

Subject	Age, years	Sex	Disease Duration (mths)	ALS Functional Rating Scale	Disease Rate (ALS units/mth)	Predominant Clinical Signs
	65	male	36	31	0.25	umn
	51	male	84	34	0.07	umn
	66	female	14	30	0.71	mixed
	58	male	36			mixed
	60	female	15	26	0.93	mixed
	71	male	42	22	0.43	mixed
	55	female	22	25	0.68	mixed
	42	male	12	32	0.67	umn
	53	male	48	32	0.17	mixed
	67	female	27	23	0.63	lmn
Patients	56	male	17	32	0.47	mixed
	51	male	11	28	1.09	mixed
	63	male	60	28	0.20	umn
	70	female	12	31	0.75	mixed
	46	male	7	18	3.14	mixed
	63	male	24	27	0.54	lmn
	59	male	24	37	0.13	mixed
	28	male	14	23	1.21	mixed
	59	male	18	30	0.56	mixed
	57	male	54	31	0.17	mixed
	54	male	23	27	0.57	mixed
Patient group	58.0 (28-71)	16M:5F	23 (7-84)	28 (11-37)	0.55 (0.07-1.21) excludes outlier	4 umn 15 mixed 2 lmn
Control group	51.5 (37-71)	9M:5F				

Table 4.1. Patient characteristics for age, gender, disease duration, ALS functional rating scale and disease rate. Clinical examination findings divided patients into those with predominantly upper motor neuron (umn), lower motor neuron (lmn) and mixed signs. One patient with some missing clinical data was not entered into the correlation analyses between FA, MD and clinical markers. Median values with ranges (in brackets) are shown at the bottom of the table.

4.3.2 Fractional anisotropy

The estimated population means for control and ALS groups were plotted against location from internal capsule caudally to pyramids (figure 4.2). These estimates were obtained using a regression model in which a linear dependence on location was adopted between the pyramids and peduncles, while an unconstrained mean value was adopted for the internal capsule. A dependence on side was found at the internal capsule ($p=0.0004$) with the FA higher on the right, which was not group specific ($p=0.68$). Therefore left (LHS) and right (RHS) estimated means are plotted separately for better visualization. There is a significant linear downward trend in FA ($p=0.0001$) descending caudally from the peduncles to the pyramids. The gradient does not differ significantly between group ($p=0.48$) or side ($p=0.54$). Mean FA is lower in patients compared to controls at the internal capsule ($p=0.036$), and at the peduncles, pons and pyramids ($p=0.038$). These differences were quantified. For age 55 years, at the internal capsule, the estimated FA difference between groups for the LHS is 48.8×10^{-3} (Standard Error [SE]$=22.6\times10^{-3}$, $t=2.16$, $p=0.032$) and for the RHS is 58.0×10^{-3} (SE$=22.6\times10^{-3}$, $t=2.56$,$p=0.011$). Below the internal capsule the estimated difference in FA for the LHS is 52.2×10^{-3} (SE$=16.1\times10^{-3}$, $t=3.25$, $p=0.0013$) and for the RHS is 41.8×10^{-3} (SE$=16.1\times10^{-3}$, $t=2.60$, $p=0.01$).

FA observations were plotted against location, showing variability of FA raw data (Figure 4.3). Greater FA variance is demonstrated in the ALS group relative to the control group, which is consistent with the assumption that disease pathology increases between-subject variability.

Correlation between FA and clinical markers – No significant correlations were found between FA and ALS rating scale or between FA and disease progression rate (Spearman's rho), at each location on both sides.

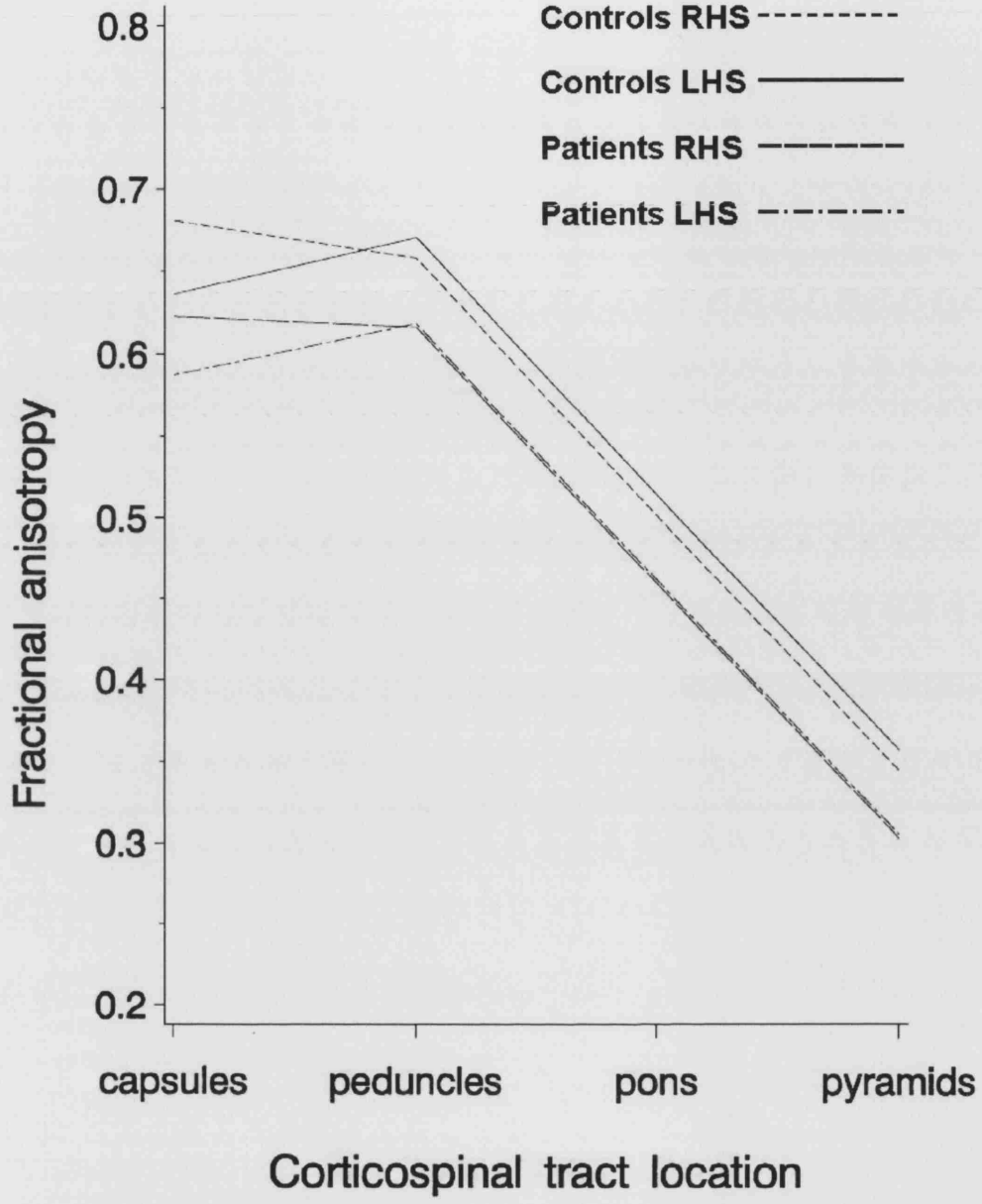

Figure 4.2. The predicted population FA means for age 55 years are plotted against corticospinal tract location for the controls (left and right hand sides) and patients (left and right hand sides). FA values theoretically range from 0 to 1, where 0 indicates completely isotropic diffusion and 1 indicates perfectly coherent (anisotropic) diffusion. Note that there is some side dependence of FA at the internal capsules. ALS demonstrates significantly lower FA at all levels. Controls LHS (solid line), RHS (short dashed line), patients LHS (long and short alternating dashed line), RHS (long dashed line).

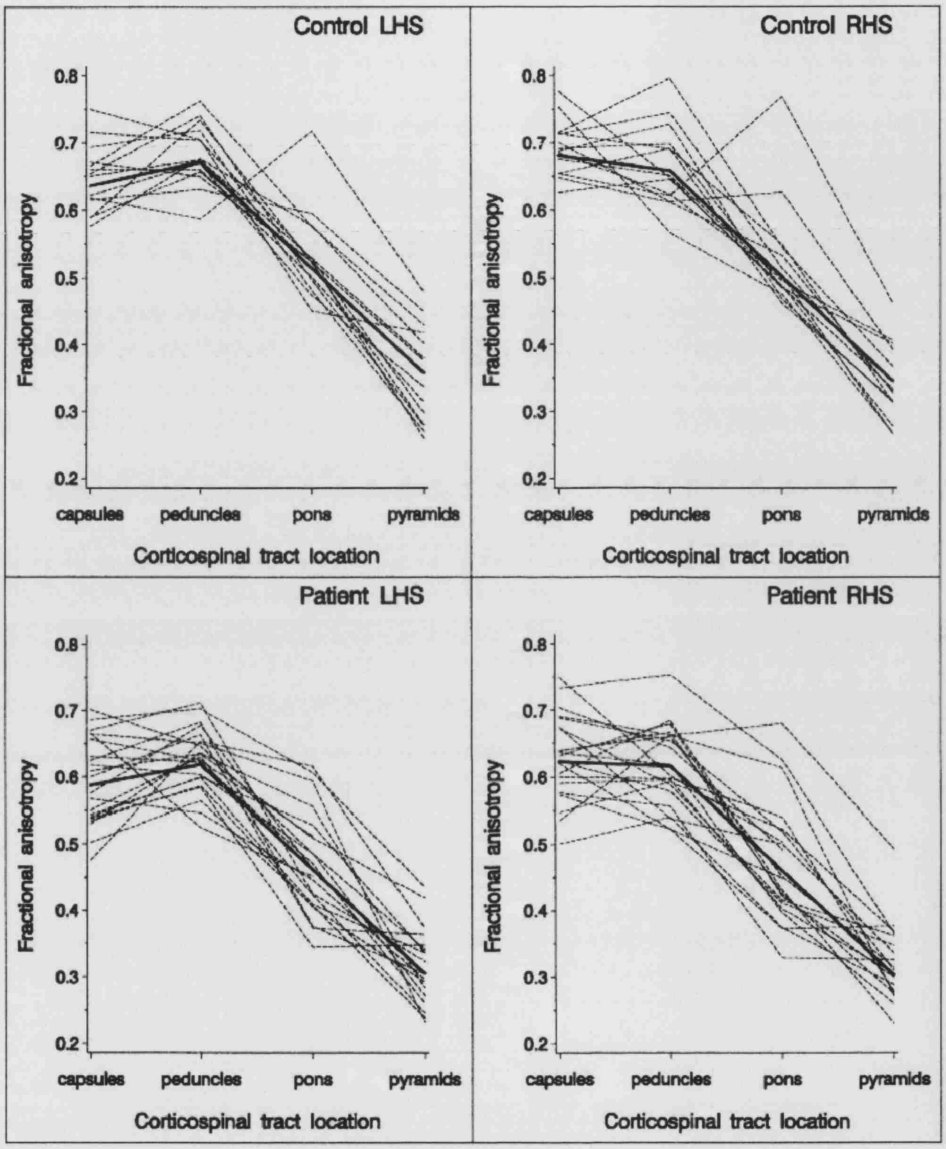

Figure 4.3. FA raw data measurements in ALS patients and controls for left and right sides are plotted against location demonstrating the variability in observed FA. The predicted (fitted) population means are overlaid for each group.

4.3.3 Mean diffusivity

The estimated population means were plotted against location for LHS and RHS (figure 4). There is borderline significance for a difference in sides which is group dependent (p=0.05). For example, at age 55 years, mean diffusivity at the internal capsule, is higher on the left than the right in patients although this does not reach significance (p=0.08) and not significantly different between left and right sides in controls (p=0.68). Overall there is weak evidence for a group difference that is dependent on location (p=0.09). This is reflected by the different gradients of the regression slopes for the ALS and control group (figure 4.4). MD is significantly higher in patients than controls at the level of the internal capsule on the LHS (e.g. for age 55 years, estimated MD difference 87.4×10^{-6} mm^2s^{-1}, SE 33.9×10^{-6}, t -2.58, p=0.01) although on the RHS it does not reach significance (e.g. for age 55, estimated MD difference 52.3×10^{-6} mm^2s^{-1}, SE 33.9×10^{-3}, t -1.54, p=0.12). Descending caudally along the corticospinal tract, the predicted means for the ALS group cross over and dip below the control group. At the level of the pyramids the MD predicted means for the ALS group (for LHS and RHS) are lower than for the control group but these differences are not significant (for LHS at age 55, estimated MD difference 49.0×10^{-6} mm^2s^{-1}, SE 79.6×10^{-3}, t 0.62, p=0.54; for RHS, estimated MD difference 84.1×10^{-6} mm^2s^{-1}, SE 79.6×10^{-3}, t 1.06, p=0.29).

MD was plotted against location for LHS and RHS (Figure 4.5). As well as showing the upward trend in MD as one ascends the corticospinal tracts, greater MD variance is demonstrated caudally in the corticospinal tracts especially at the pyramids.

Correlation between MD and clinical markers – Correlations between MD with disease progression rate and MD with ALS rating scale were examined using Spearman's rho for each location on each side. No correlations were found between MD and the ALS rating scale. For the disease progression rate, borderline significance was found for MD in the right pyramid (p=0.05) after performing the correlations without correcting for multiple comparisons. We considered that this could be due to the influence of the excessive disease rate in one patient which was 3.14 units/mth (see table 4.1). All

other patients had disease rates of less than 1.30. When this particular patient was excluded, no significant correlations were found.

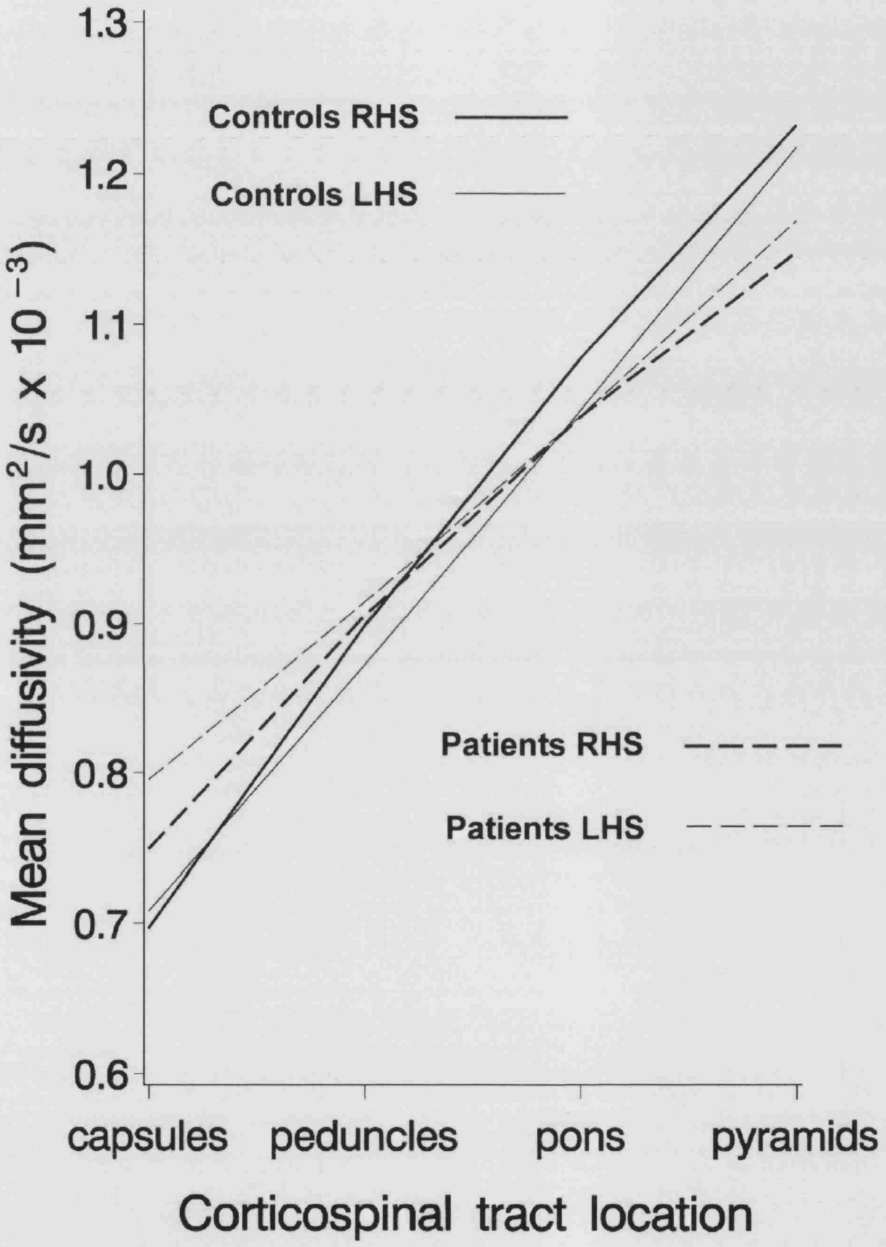

Figure 4.4. The predicted population MD means for age 55 years are plotted against corticospinal tract location for controls and patients. Control lines are solid, patient lines are dashed. Right hand side lines are bold, left hand side lines are thin. Note that the gradients of the regression slopes for the patient and control groups show some differences over all ages (p=0.09). MD in the ALS group is lower than in the control group at the internal capsules. The MD for both groups increases as one descends caudally. However, towards the pyramids, the patient lines crossover and dip below the control lines. There are also some differences in side which vary according to location and group.

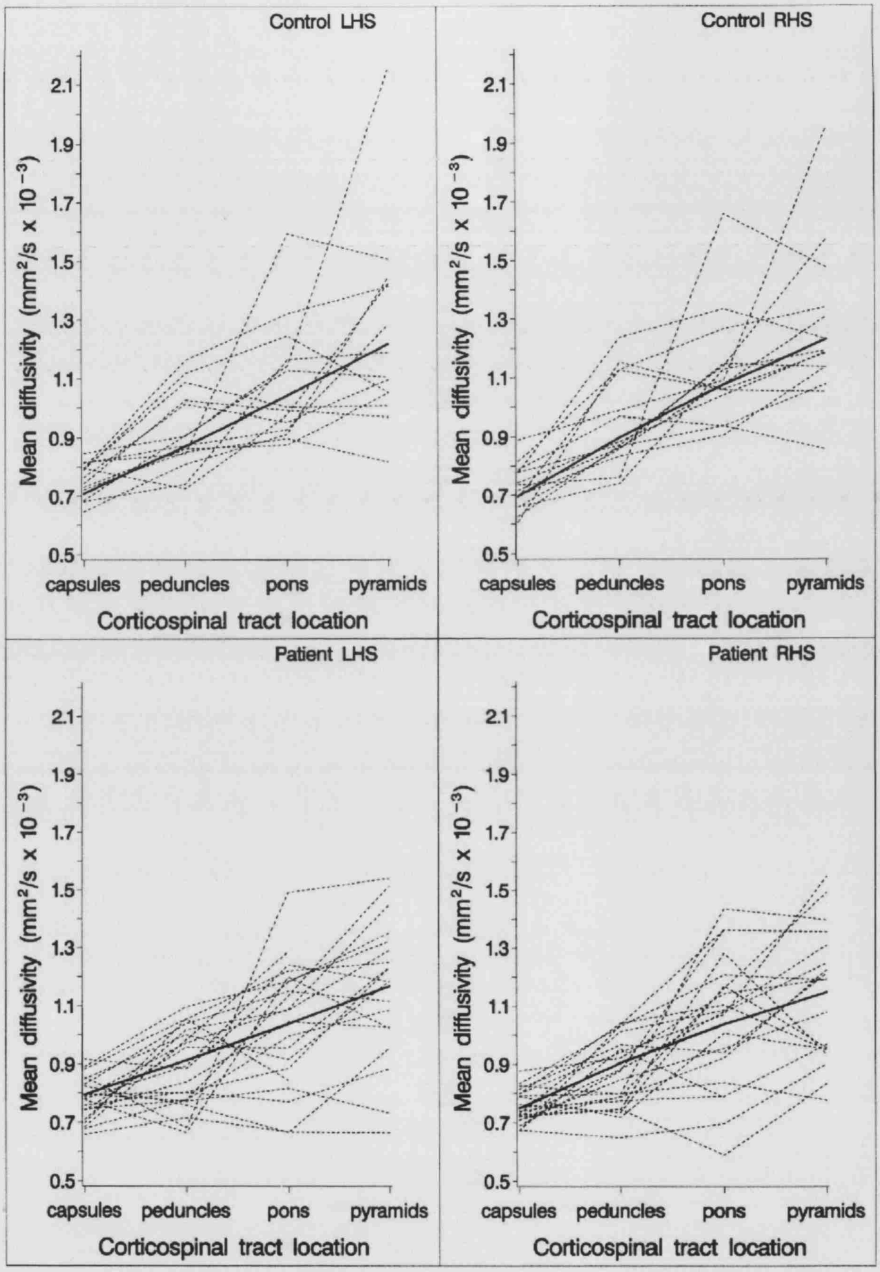

Figure 4.5. MD raw data are plotted against location to demonstrate the variability in MD measurements at different levels of the corticospinal tracts. Greater variability is observed lower down in the corticospinal tracts and in the patient group. The predicted (fitted) population means are overlaid for each group.

4.4 Discussion

This study quantifies the water diffusion characteristics along the corticospinal tracts in ALS and provides insight into the underlying *in vivo* pathology. MD and FA form the basis for this characterization, and regression analysis has been used to examine the spatial dependence in these parameters. Thus, the main focus is on the spatial trends in MD and FA along the corticospinal tracts, although we also give statistics for the individual regions. We emphasize, however, that the region specific statistics arise from the simultaneous modeling of the behaviour of all four regions. It is also important to note that a smooth dependence on location is not imposed on the statistical model at the outset. In fact, an adequate modeling of the FA data was obtained only after allowing for the presence of a discontinuity between the capsules and peduncles (see figure 4.3). The main result arising from the regression analysis is that the corticospinal tract FA is lower in ALS compared to controls, this difference being maintained from the capsules to the pyramids. In addition, there is weak evidence that the MD is higher in ALS at the level of the internal capsules but caudally in the corticospinal tracts this difference is lost and there is an associated larger between-subject variance in observed MD (figures 4.4 and 4.5).

To interpret findings in relation to ALS pathology, it is first necessary to explain the changes in FA and MD along the corticospinal tract in normal controls. Progressing caudally along the corticospinal tract, we found that FA generally decreases and MD increases. Other studies have investigated measures of anisotropy and/or diffusivity at different levels of the corticospinal tracts (Pierpaoli et al, 2001; Stieltjes et al, 2001; Virta et al, 1999). Virta et al (1999) measured water diffusion changes at the peduncles, pons and medulla; Stieltjies et al (2001) at the midbrain, pons and medulla; and Pierpaoli et al (2001) at the capsules, peduncles and pons. They all reported trends in water diffusion characteristics similar to the observations of this study.

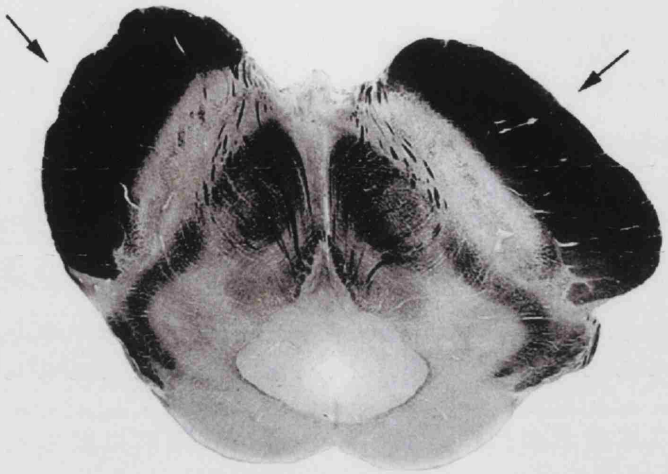

Cerebral Peduncles

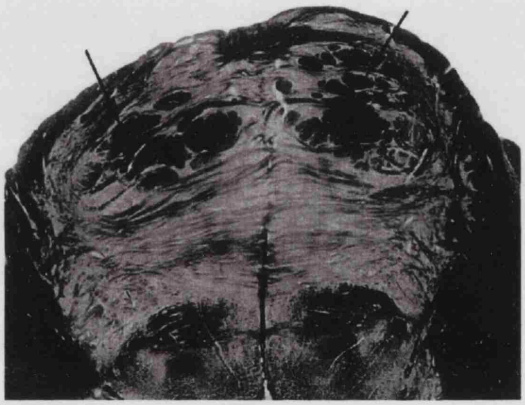

Pons

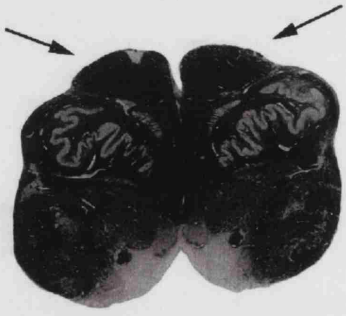

Rostral Pyramids

Figure 4.6. Histological sections of the brainstem taken at the cerebral peduncles, pons and rostral medulla to indicate the relative fibre packing and local architecture at each level. Black arrows indicate the corticospinal tracts. At the peduncles, pyramidal fibres are relatively tightly packed. At the pons, the tracts split into multiple bundles resulting in some loss of fibre coherence. The rostral medulla illustrates the smaller size of the pyramids and the complexity of multidirectional fibres connecting other nuclei and pathways. The photographs are adapted from The Human Brain, Nolte J and Angevine JB, pp 23, 25, 27, © (1995), from Elsevier Science.

Anatomically, the tract fibres are very coherent and tightly packed in the internal capsule and more so in the peduncle (figure 4.6). Thus, diffusivity is relatively low and FA is relatively high. We observed a higher FA on the right than the left at the internal capsules. FA asymmetry of the anterior limbs of the internal capsules has been reported previously (Peled et al, 1998) and was found not to be associated with handedness. At the pons the corticospinal tract fibres split into multiple bundles, which run through interdigitating transverse pontine fibres. Fibre packing is less tight than higher up, leading to a reduction in FA and an increase in MD (because there is more extracellular matrix to allow greater water diffusion) within each ROI resulting from partial volume effects. Progressing from the peduncles to the pyramids, many fibres leave the corticospinal tracts. In the pons and pyramids, collateral fibres leave to various brainstem nuclei, and the peduncles consist of 20 million fibres per side, whereas the pyramids contain only 1 million fibres per side (Brodal 1981) At the pyramids, therefore, although the motor tracts may be relatively coherent, small pyramid size and limitations of ROI analysis mean that there will be contributing influences on disruption of fibre coherence from adjacent multidirectional tracts to other brain stem nuclei, adjacent CSF and the decussation of the pyramids. These factors collectively decrease FA and increase MD.

In the ALS group, the findings at the internal capsule are compatible with a previous study which used DTI to quantify water diffusion changes in ALS (Ellis et al, 1999) and found evidence for lower FA and higher MD. These changes were interpreted as being secondary to axonal degeneration accompanied by increased extracellular volume. In our study, which addresses water diffusion changes at additional levels from the internal capsules down to the pyramids a more complex relationship emerges. The relationship to ALS pathology and the underlying tissue architecture is of interest. Most histopathological studies have been performed on end-stage or near end-stage disease and little is known about *in vivo* pathology or its temporal evolution (Martin and Swash 1995). The main features are: loss of large motor neurons with focal astrogliosis, "senescent changes" with lipofuscin pigment atrophy, various cytoplasmic inclusions with chromatolysis, proximal and distal axonopathy with axonal spheroids, tract degeneration, lower motor fibre degeneration and muscle atrophy (Chou

1995; Ince 2000; Lowe et al, 1997). Post mortem studies have described histologically uneven involvement of the corticospinal tracts showing variable patterns of degeneration (Bertrand and Van Bogaert 1925; Brownell et al, 1970; Davison 1941). The changes in ALS are thus more complex than those seen in classical Wallerian degeneration – the anterograde degeneration of axons and their myelin sheaths after proximal axonal or cell body injury. The main histological changes seen in the corticospinal system include the loss of cortical pyramidal motor neurons and the degeneration of corticospinal tract axons with associated astrocytosis, which can be very variable (Chou 1995; Lowe et al, 1997). Disorders of axonal transport are thought to play important roles in the development of the resulting axonopathy and a "dying back" model of axon degeneration has been proposed as part of the natural history of motor neuron degeneration (Cavanagh 1979). Surviving motor neurons tend to be smaller and are histologically abnormal. They contain various inclusion bodies (within the cell body) and abnormalities of the neurofilament and microtubule structures that will disrupt intra-axonal flow (Griffin and Watson 1988). Further evidence of abnormalities within the surviving motor tracts comes from observations of the accumulation of axonal spheroids (swellings of the axons thought to result from impaired axonal transport), particularly at the level of the internal capsules (Chou and Huang 1988; Leigh et al, 1989). These may affect intracellular water diffusion and contribute to the changes in measured diffusivity. The relationship between water diffusion and neurodegeneration has been previously investigated in both the peripheral (Beaulieu et al, 1996) and central (Pierpaoli et al, 2001) nervous systems. Diffusion changes have been explained in terms of contributions from degenerated fibre tracts, extracellular matrix, glial cell proliferation and residual cell debris.

The finding of lower FA in the ALS group, at multiple levels, reflects tract degeneration, which results in loss of fibre coherence. The space between surviving fibres may be occupied by partially degenerated tracts, extracellular matrix or glial cells. Abnormalities of the surviving axons and reduced anisotropy of intracellular diffusion contribute to the reduced FA.

Changes in MD as a result of ALS pathology also depend on a balance between the competing influences of similar factors including extracellular matrix expansion which will encourage water diffusion and increase MD, astrocytosis within the inter-axonal spaces which will hinder free water diffusion and lower MD, and cell debris resulting from partially degenerated or disintegrated nerve fibres along the corticospinal tracts that should restrict diffusion between the surviving axons and lower MD. In support of this, neuronophagia, shrinkage, pyknosis and vacuolation have been described in the brainstem in post mortem studies (Chou 1979; Hirano and Iwata 1979). In the ALS group, the changes in MD, progressing caudally down the corticospinal tracts, suggest differing relative contributions of these factors, restricting or encouraging water diffusion. Thus, the group effect of ALS pathology at the internal capsules elevates MD, whereas at lower levels, this is counterbalanced by factors that restrict diffusion. The interpretation of MD differences at the lowest levels, where the corticospinal tract is smallest, is limited by partial volume effects that may obscure subtle changes in MD due to disease and contribute to the greater variance of MD measurements (figure 4.5). The differences in MD between ALS and controls at the internal capsule were asymmetrical, and this is supported by descriptions of asymmetry in ALS pathology of the corticospinal tracts (Swash et al, 1988).

Clinicopathological correlations in ALS are heterogeneous. Prominent clinical disability during life may occur in the absence of corticospinal tract involvement at post-mortem, the reverse has also been observed reported (Brownell et al, 1970; Lawyer and Netsky 1953). In addition, the ALS functional rating scale used may not monitor clinical involvement of the upper motor neurons sensitively. It is therefore not surprising that we did not detect any convincing correlations between markers of clinical disability and indices of water diffusion. It was not feasible in our study to compare the DTI findings between patients with upper and lower motor neuron signs because most possessed a mixed clinical picture, as is typical in ALS (see table 4.1). A future approach will be to compare larger numbers of patients with predominantly upper motor neuron signs against mixed and lower motor neuron signs to determine whether DTI distinguishes corticospinal tract degeneration more

readily. It may be, however, that further technological advances in MRI or a greater understanding of the molecular pathology of ALS are required to develop more reliable clinical or prognostic indicators.

In the quantitative image analysis, we used an ROI approach, which has several limitations. Determining the boundaries of the structure of interest and avoiding partial volume contamination from CSF or grey matter are universal problems. In our experience the pyramidal tract is anatomically well defined and readily identified on the FA maps. In addition we displayed co-registered z-directional ADC maps where signal intensity is proportional to high diffusivity in the z direction, helping to exclude non-pyramidal fibres tracking in orthogonal directions. This approach was satisfactory higher up in the corticospinal tracts. At the level of the pyramids, however, limitations of ROI analysis were more apparent. The pyramids are small and there is partial volume contamination from surrounding CSF (at higher levels of the corticospinal tracts CSF does not contaminate ROI placement). In addition, the medulla is anatomically complex with many crossing fibres. These factors will reduce FA, increase MD and increase the variability of ROI measurements, especially for MD, which is partial to CSF contamination. This was reflected in the greater variance of the measurements at the pyramids compared with higher levels.

The advantage of ROI analysis is that specific parts of the brain may be accurately localized, allowing comparison between individuals, provided the areas of interest (e.g. pyramidal tract) are anatomically well defined and there is no operator dependent bias. An alternative method is to co-register the FA and MD maps of interest into a standard space and cross-reference the measurements with a known co-ordinate system or perform voxel based morphometry (Ashburner and Friston 2000). However, the registration process may not be error free. It assumes that each part of an individual's pyramidal tract will map precisely to the standard map, but there is probably some natural inter-individual variation for pyramidal tract location and structure. A better method may be to use the recently developed technique of tractography (Parker et al, 2002) to map the pyramidal tract location, and

use this as an unbiased guide to placing ROIs. Formal assessments of these alternative techniques will establish which will provide the best quantitative assessment of ALS pathology. However, neither of these alternative methods fully overcomes partial volume effects with ROI analysis. This requires DTI to be developed to acquire higher resolution images. Advances in newer techniques related to DTI, such as diffusion spectrum imaging (DSI) or conductivity tensor mapping (Tuch et al, 2001; Wiegell et al, 2001) may provide important insights into brain tissue microstructure in the future, although the effectiveness of clinical DSI may be determined by gradient strength limitations (Basser 2002; King et al, 1994).

In conclusion, by sampling the corticospinal tracts from the internal capsule down to the pyramids using DTI, and performing a rigorous statistical analysis to detect differences between the ALS and the control group, we found evidence for altered microstructural organization at multiple levels, which we attribute to neuronal degeneration in ALS. Further development of these techniques and direct comparisons with other MR imaging modalities (e.g. MT imaging, MR spectroscopy) may be important for the sequential quantification of neuronal degeneration, understanding the progress of disease pathology, and assessing the effects of therapeutic intervention, in patients with ALS.

4.5 References

The Amyotrophic Lateral Sclerosis Functional Rating Scale. Assessment of activities of daily living in patients with amyotrophic lateral sclerosis. The ALS CNTF treatment study (ACTS) phase I-II Study Group. *Arch Neurol.* 1996. **53**(2), 141-7.

Ashburner, J and Friston, KJ. Voxel-based morphometry--the methods. *Neuroimage.* 2000. **11**(6 Pt 1), 805-21.

Basser, PJ. Relationships between diffusion tensor and q-space MRI. *Magn Reson.Med.* 2002. **47**(2), 392-7.

Basser, PJ, Mattiello, J, and LeBihan, D. Estimation of the effective self-diffusion tensor from the NMR spin echo. *J.Magn Reson.B.* 1994. **103**(3), 247-54.

Beaulieu, C, Does, MD, Snyder, RE, and Allen, PS. Changes in water diffusion due to Wallerian degeneration in peripheral nerve. *Magn Reson.Med.* 1996. **36**(4), 627-31.

Bertrand, I and Van Bogaert, L. La sclerose laterale amyotrophique (anatomie pathologique). *Rev Neurol.* 1925. **25**, 779-806.

Brodal, A. Descending Supraspinal Pathways. In: Brodal, A. Neurological Anatomy in relation to Clinical Medicine. Oxford; Oxford University Press, 1981: 180-293.

Brooks, BR, Miller, RG, Swash, M, and Munsat, TL. El Escorial revisited: revised criteria for the diagnosis of amyotrophic lateral sclerosis. *Amyotroph.Lateral.Scler.Other Motor Neuron Disord.* 2000. **1**(5), 293-9.

Brownell, B, Oppenheimer, DR, and Hughes, JT. The central nervous system in motor neurone disease. *J.Neurol Neurosurg.Psychiatry*. 1970. **33**(3), 338-57.

Cavanagh, JB. The 'dying back' process. A common denominator in many naturally occurring and toxic neuropathies. *Arch.Pathol.Lab Med.* 1979. **103**(13), 659-64.

Charcot, JM and Joffroy, A. Deux cas d'atrophie musculaire progressive avec lesions de la substence grise et de faiscaux anterolateraux di la moelle epiniere. *Arch Physicol Norm Pathol Paris*. 1869. **2**, 744-60.

Cheung, G, Gawel, MJ, Cooper, PW, Farb, RI, Ang, LC, and Gawal MJ [corrected to Gawel MJ]. Amyotrophic lateral sclerosis: correlation of clinical and MR imaging findings. *Radiology*. 1995. **194**(1), 263-70.

Chou, SM. Pathognomy of intraneuronal inclusions in ALS. In: Tsubaki, T and Toyokura, Y. Amyotrophic Lateral Sclerosis. Tokyo; University of Tokyo Press, 1979: 135-76.

Chou, SM. Pathology of Motor System Disorder. In: Leigh, PN and Swash, M. Motor Neuron Disease: Biology and Management. London; Springer-Verlag, 1995: 53-92.

Chou, SM and Huang, TE. Giant axonal spheroids in internal capsules of amyotrophic lateral sclerosis brains revisited. *Ann Neurol.* 1988. **24**, 168.

Davison, C. Amyotrophic lateral sclerosis: origin and extent of upper motor neuron lesion. *Neurol Psychiatr.* 1941. **46**, 1039-56.

Ellis, CM, Simmons, A, Jones, DK, Bland, J, Dawson, JM, Horsfield, MA, Williams, SC, and Leigh, PN. Diffusion tensor MRI assesses corticospinal tract damage in ALS. *Neurology*. 1999. **53**(5), 1051-8.

Griffin, JW and Watson, DF. Axonal transport in neurological disease. *Ann Neurol.* 1988. **23**(1), 3-13.

Hand, D, Crowder, MJ, and Crowder, DJ. Practical longitudinal data analysis. 1st ed. London; 1996.

Hecht, MJ, Fellner, F, Fellner, C, Hilz, MJ, Heuss, D, and Neundorfer, B. MRI-FLAIR images of the head show corticospinal tract alterations in ALS patients more frequently than T2-, T1- and proton-density-weighted images. *J.Neurol.Sci.* 2001. **186**(1-2), 37-44.

Hirano, A and Iwata, M. Pathology of motor neurons with special reference to amyotrophic lateral sclerosis and related diseases. In: Tsubaki, T and Toyokura, Y. Amyotrophic Lateral Sclerosis. Tokyo; University of Tokyo Press, 1979: 107-33.

Hirayama, K, Tsubaki, T, Toyokura, Y, and Okinaka, S. The representation of the pyramidal tract in the internal capsule and basis pedunculi. *Neurology.* 1962. **12**(5), 337-42.

Hofmann, E, Ochs, G, Pelzl, A, and Warmuth-Metz, M. The corticospinal tract in amyotrophic lateral sclerosis: an MRI study. *Neuroradiology.* 1998. **40**(2), 71-5.

Holmes, G. The pathology of amytrophic lateral sclerosis. *Rev Neurol Psychiatry.* 1909. **7**, 693-725.

Ince, PG. Neuropathology. In: Brown, RH, Meininger, V, and Swash, M. Amytrophic Lateral Sclerosis. London; Martin Dunitz Ltd, 2000: 83-112.

Kato, Y, Matsumura, K, Kinosada, Y, Narita, Y, Kuzuhara, S, and Nakagawa, T. Detection of pyramidal tract lesions in amyotrophic lateral sclerosis with magnetization-transfer measurements. *AJNR Am.J.Neuroradiol.* 1997. **18**(8), 1541-7.

King, MD, Houseman, J, Roussel, SA, van Bruggen, N, Williams, SR, and Gadian, DG. q-Space imaging of the brain. *Magn Reson.Med.* 1994. **32**(6), 707-13.

Lawyer, TJr and Netsky, MG. Amyotrophic lateral sclerosis: a clinico-anatomic study of 53 cases. *Arch Neurol.* 1953. **69**, 171-92.

Leigh, PN, Dodson, A, Swash, M, Brion, JP, and Anderton, BH. Cytoskeletal abnormalities in motor neuron disease. An immunocytochemical study. *Brain.* 1989. **112 (Pt 2)**, 521-35.

Lowe, J, Lennox, G, and Leigh, PN. Disorders of movement and system degenerations. In: Graham, DJ and Lantos, PL. Greenfield's Neuropathology vol 2. London; Arnold, 1997: 281-366.

Martin, JE and Swash, M. The Pathology of Motor Neuron Disease. In: Leigh, PN and Swash, M. Motor Neuron Disease: Biology and Management. London; Springer-Verlag, 1995: 93-118.

Parker, GJ, Klaas, SE, Barker, GJ, Rowe, JB, MacManus, DG, Wheeler-Kingshott, CA, Ciccarelli, O, Passingham, RE, Lemon, RN, and Turner, R. Initial demonstration of in vivo tracing of axonal projections in the Macaque brain and comparison with the human brain using diffusion tensor imaging and fast marching tractography. *Neuroimage.* 2002.

Peled, S, Gudbjartsson, H, Westin, CF, Kikinis, R, and Jolesz, FA. Magnetic resonance imaging shows orientation and asymmetry of white matter fiber tracts. *Brain Res.* 1998. **780**(1), 27-33.

Pierpaoli, C, Barnett, A, Pajevic, S, Chen, R, Penix, LR, Virta, A, and Basser, P. Water diffusion changes in Wallerian degeneration and their dependence on white matter architecture. *Neuroimage.* 2001. **13**(6 Pt 1), 1174-85.

Pierpaoli, C and Basser, PJ. Toward a quantitative assessment of diffusion anisotropy. *Magn Reson.Med.* 1996. **36**(6), 893-906.

Pioro, EP, Antel, JP, Cashman, NR, and Arnold, DL. Detection of cortical neuron loss in motor neuron disease by proton magnetic resonance spectroscopic imaging in vivo. *Neurology.* 1994. **44**(10), 1933-8.

Plummer, DL. Dispimage: a display and analysis tool for medical images. *Riv Neuroradiol.* 1992. **5**(489), 495.

Rooney, WD, Miller, RG, Gelinas, D, Schuff, N, Maudsley, AA, and Weiner, MW. Decreased N-acetylaspartate in motor cortex and corticospinal tract in ALS. *Neurology.* 1998. **50**(6), 1800-5.

Ross, ED. Localization of the pyramidal tract in the internal capsule by whole brain dissection. *Neurology.* 1980. **30**(1), 59-64.

SAS Institute Inc. SAS/STAT software: Changes and Enhancements through Release 6.11. 1996.

Stieltjes, B, Kaufmann, WE, van Zijl, PC, Fredericksen, K, Pearlson, GD, Solaiyappan, M, and Mori, S. Diffusion tensor imaging and axonal tracking in the human brainstem. *Neuroimage.* 2001. **14**(3), 723-35.

Suhy, J, Miller, RG, Rule, R, Schuff, N, Licht, J, Dronsky, V, Gelinas, D, Maudsley, AA, and Weiner, MW. Early detection and longitudinal changes in amyotrophic lateral sclerosis by (1)H MRSI. *Neurology.* 2002. **58**(5), 773-9.

Sullivan, LM, Dukes, KA, and Losina, E. Tutorial in biostatistics. An introduction to hierarchical linear modelling. *Stat.Med.* 1999. **18**(7), 855-88.

Swash, M. Clinical features and diagnosis of amyotrophic lateral sclerosis. In: Brown, RH, Meininger, V, and Swash, M. Amyotrophic Lateral Sclerosis. London; Martin Dunitz Ltd, 2000: 3-30.

Swash, M, Scholtz, CL, Vowles, G, and Ingram, DA. Selective and asymmetric vulnerability of corticospinal and spinocerebellar tracts in motor neuron disease. *J.Neurol Neurosurg.Psychiatry*. 1988. **51**(6), 785-9.

Symms, MR, Barker, GJ, Franconi, F, and Clark, CA. Correction of eddy-current distortions in diffusion-weighted echo-planar images with a two-dimensional registration technique. *Proceedings of the International Society for Magnetic Resonance in Medicine*. 1997. 1723.

Thorpe, JW, Moseley, IF, Hawkes, CH, MacManus, DG, McDonald, WI, and Miller, DH. Brain and spinal cord MRI in motor neuron disease. *J.Neurol.Neurosurg.Psychiatry*. 1996. **61**(3), 314-7.

Tuch, DS, Wedeen, VJ, Dale, AM, George, JS, and Belliveau, JW. Conductivity tensor mapping of the human brain using diffusion tensor MRI. *Proc.Natl.Acad.Sci.U.S.A.* 2001. **98**(20), 11697-701.

Virta, A, Barnett, A, and Pierpaoli, C. Visualizing and characterizing white matter fiber structure and architecture in the human pyramidal tract using diffusion tensor MRI. *Magn Reson.Imaging*. 1999. **17**(8), 1121-33.

Werring, DJ, Clark, CA, Barker, GJ, Miller, DH, Parker, GJ, Brammer, MJ, Bullmore, ET, Giampietro, VP, and Thompson, AJ. The structural and functional mechanisms of motor recovery: complementary use of diffusion tensor and functional magnetic resonance imaging in a traumatic injury of the internal capsule. *J.Neurol.Neurosurg.Psychiatry*. 1998. **65**(6), 863-9.

Werring, DJ, Toosy, AT, Clark, CA, Parker, GJ, Barker, GJ, Miller, DH, and Thompson, AJ. Diffusion tensor imaging can detect and quantify corticospinal tract degeneration after stroke. *J.Neurol.Neurosurg.Psychiatry*. 2000. **69**(2), 269-72.

Wiegell, MR, Reese, T, Tuch, DS, Sorensen, AG, and Wedeen, VJ. Diffusion Spectrum Imaging of Fiber White Matter Degeneration. *Proceedings of the 9th International Society of Magnetic Resonance in Medicine*. 2001. **1**, 504.

Wieshmann, UC, Clark, CA, Symms, MR, Franconi, F, Barker, GJ, and Shorvon, SD. Reduced anisotropy of water diffusion in structural cerebral abnormalities demonstrated with diffusion tensor imaging. *Magn Reson.Imaging*. 1999a. **17**(9), 1269-74.

Wieshmann, UC, Symms, MR, Clark, CA, Lemieux, L, Franconi, F, Parker, GJ, Barker, GJ, and Shorvon, SD. Wallerian degeneration in the optic radiation after temporal lobectomy demonstrated in vivo with diffusion tensor imaging. *Epilepsia*. 1999b. **40**(8), 1155-8.

CHAPTER 5

COMBINING FUNCTIONAL MRI AND DIFFUSION TENSOR IMAGING

This chapter deals with techniques that were developed to combine measures of function and structure from MR imaging using fMRI and DTI respectively. This was applied in a group of normal subjects and then in a small group of optic neuritis patients. Before this, a preliminary methodology is described that allowed us to combine white matter tractography results from different individuals to allow group level inferences. This methodology has useful applications for investigating white matter pathology. The registration techniques described in this particular study were used as the basis for spatially transforming the estimated white matter tracts in the DTI-fMRI studies.

5.1 Diffusion tractography based group mapping of major white-matter pathways in the human brain

5.1.1 Introduction

Investigating structural connections within the brain is fundamental to our understanding of the effects pathology may have on neural plasticity, development and function. Until recently, studies of white matter pathways have been limited to post-mortem and animal brains, using histological tracer techniques (Jones 1999). However diffusion tensor imaging (DTI) (Basser et al, 1994) has allowed the *in vivo* investigation of brain microarchitecture and more recently, inter-regional fibre tracking (Basser et al, 2000; Conturo et al, 1999; Xue et al, 1999). Several tractography methods (discussed in chapter 2) have been developed in order to infer continuity of fibre orientation from voxel to voxel and to

reconstruct connections between brain regions (Basser et al, 2000; Behrens et al, 2003; Conturo et al, 1999; Jones et al, 1999b; Mori et al, 1999; Mori et al, 2000; Poupon et al, 2000).

Fast Marching Tractography (FMT) (Parker et al, 2002b; Parker et al, 2002a) is a tractography technique that generates Voxel Scale Connectivity[5] (VSC) maps *in vivo* within the brain using the information provided by DTI. These maps provide, at each voxel in the brain, a scalar index that estimates the degree of connection to a particular starting voxel. The FMT method has received some validation by application to animal data (Parker et al, 2002a) and by comparison with standard atlases (Parker et al, 2002b). A recent study has been performed using FMT to investigate the reproducibility of quantitative tract measurements (Ciccarelli et al, 2003b), and the maps generated by FMT corresponded well with known anatomy (Burgel et al, 1999; Rademacher et al, 2001).

This work describes the evaluation of estimated white matter tract variability between normal subjects, as determined using FMT. This step is essential in order to move on to the investigation of neurological and psychiatric diseases, in which the white matter pathways are known to be disrupted (Foong et al, 2000; Mori et al, 2002; Pierpaoli et al, 2001; Steel et al, 2001). The methods of creating group maps of white matter tracts, and therefore, compensating for normal inter-subject variability, may ultimately allow the construction of 'brain atlases' that represent *in vivo* white matter tracts. These would be invaluable for investigating how white matter is affected by pathological conditions of the central nervous system (Steel et al, 2001).

As a step towards this goal, we have generated group maps of white matter pathways in a group of 21 healthy subjects using FMT. Three clinically relevant white matter pathways were chosen: the left and right pyramidal tracts, the left and right optic radiations, and the anterior callosal fibres. We

[5] The term 'connectivity' is used in this section to indicate bulk inter-regional anatomical connectivity that may be derived from Fast Marching Tractography. Whilst this does not permit an analysis of point-to-point connectivity it does shed light upon macroscopic routes of white matter fibre bundles.

applied three different group mapping techniques for each pathway and investigated the contribution of each technique to understanding the behaviour of the estimated pathways between subjects. The first technique simply averaged the individual VSC maps generated by FMT; the second produced maps that demonstrated inter-subject tract variability and degree of overlap; the third employed SPM (Ashburner and Friston 2000) to construct a statistical image that represented the group effect. With the last technique we were also able to investigate any asymmetry between left and right sides for the estimated optic radiation and pyramidal tracts.

5.1.2 Methods

5.1.2.1 Subjects

Twenty-one healthy volunteers were studied (11 females and 10 males). The mean age was 33 ± 9.7 years. Informed consent was obtained from all subjects before entering into the study.

5.1.2.2 MRI protocol

All scans were performed on a 1.5-T Signa Echospeed MRI system (GE Medical Systems, Milwaukee, WI). The following data sets were acquired: 1) Conventional proton density- and T_2-weighted spin echo imaging [TR 2000, TE 30/120ms, FOV 240 mm, matrix 256 × 256; 28 contiguous axial slices; 5 mm slice thickness]; 2) Single-shot peripherally gated diffusion-weighted echo-planar imaging (DW-EPI) [TE 95 ms; TR 5-6 s; acquisition matrix 96 × 96 reconstructed as 128 × 128; FOV 240 mm; 3 $b \approx 0$ smm^{-2} images; 60 diffusion weighted images, with diffusion gradients applied along 60 optimised diffusion directions (Jones et al, 1999a), diffusion times of Δ = 32ms and δ = 40ms, and max gradient amplitude of 22x10^{-3} T m^{-1}, giving a maximum b-factor b = 1000 smm^{-2}; 42 contiguous axial slices; 2.5 mm slice thickness; diffusion data acquisition time = 20-30 minutes, dependent upon heart rate. Peripheral gating was used to reduce motion artefacts due to pulsation of blood and CSF. Correction of eddy-current distortions in DW-EPI was performed using a two-dimensional image registration

technique (Symms et al, 1997). The data were then processed to determine the diffusion tensor on a pixel-by-pixel basis (Basser et al, 1994) using in-house software. Fractional anisotropy (FA), eigenvector and eigenvalue maps were calculated (Basser and Pierpaoli 1996; Pierpaoli and Basser 1996).

5.1.2.3 FMT method

The information contained in the FA, eigenvector and eigenvalue maps was used by FMT (Parker et al, 2002b; Parker et al, 2002a) to trace the three white matter pathways. For each tract, a single voxel was chosen (on the FA map) as seed point using the following anatomical guidelines (Ciccarelli et al, 2003a):

1. Pyramidal tract: on the first axial slice below the most inferior slice where both optic tracts were fully visible, a voxel in the middle third of the cerebral peduncle was selected.
2. Optic radiation: on the axial slice where the transition from the posterior limb of the internal capsule to the cerebral peduncle was visible, a voxel within the optic radiation at the apex of the arc (Meyer's loop) around the lateral ventricle was chosen.
3. Anterior callosal fibres: on the lowest axial slice where both the genu and the splenium of corpus callosum were fully visible, a midline voxel in the anterior genu was selected.

Each seed voxel had a FA value > 0.5, which ensured that it was located within white matter. Visual guidance from the corresponding slices of the dual echo images was used for the placement of the starting voxel.

The degree of connection between each starting voxel and other brain regions was estimated using the FMT algorithm, which employed a lower FA threshold of 0.1 and an upper diffusivity threshold of 2.0×10^{-3} mm^2s^{-1} to prevent pathways from being traced erroneously into cerebrospinal fluid. A restricted brain volume was used in the analysis in order to speed up the FMT analysis and focus only

on the tracts under investigation. The FMT algorithm uses the spatial and orientational arrangement of the diffusion tensor principal eigenvector between the seed voxel and every other voxel in the restricted brain volume to generate a VSC map. This map provides a scalar value at each voxel that estimates the degree of connection to the particular seed voxel. A histogram of each map generated by FMT was created, and a threshold defining a group of voxels with the highest VSC values to the seed voxel was identified.

It is important to note that this thresholding technique was objective and determined *a priori*. Every histogram possessed a significant peak that contained the greatest number of voxels with the highest VSC values. The threshold for each histogram was defined by selecting the value that isolated this peak (Ciccarelli et al, 2003a). The threshold varied between subjects, but was specific for each white-matter tract. The means (with standard deviations) for histogram thresholds of each white matter tract were as follows (n=21): Anterior callosal fibres 455 (SD 12), left optic radiation 456 (SD 39), right optic radiation 464 (SD 20), left pyramidal tract 434 (SD 48), right pyramidal tract 422 (SD 65). This threshold was then applied to the VSC map to define regions of interest (ROIs) identifying the areas with the highest VSC values, and subsequent "thresholded" maps were obtained (Ciccarelli et al, 2003a). These were simply binary images that indicated where the tracts were likely to be located with highest certainty.

Thus, for each of the five white matter pathways that were examined (left and right pyramidal tracts, left and right optic radiations, anterior callosal fibres), two types of VSC maps were generated for each subject: unthresholded maps that preserved the estimated degree of connection at each voxel within the restricted brain volume and thresholded maps that provided spatial information purely about tract location and extent.

5.1.2.4 Spatial Normalisation

The thresholded and unthresholded maps were normalized into a standardized space (as defined by the Montreal Neurological Institute (MNI)) using SPM99 (Wellcome Department of Cognitive Neurology, London, UK). This was performed by initially normalizing each b0 image to the default EPI template, which shares similar T_2-weighted contrast. The normalization parameters were estimated with the following settings: 12 parameter affine transformation followed by non-linear warping with 7x8x7 basis function sets, 12 non-linear iterations, medium regularization and default brain mask. The default (asymmetrical) EPI template was used in all cases except for the left-right comparisons (see later) when the original unthresholded maps were normalized again using a symmetrical template. The b0 normalization parameters were then applied to all the VSC maps (which were in the same stereotactic space as the original b=0 images). The resampled voxel size was 2x2x2mm for normalization. Nearest neighbour interpolation of the VSC maps was used to maintain the VSC values derived using FMT. The resulting normalized thresholded and unthresholded maps were entered into the next stage of analysis.

5.1.2.5 Group mapping of white matter pathways

We calculated group maps for each of the five pathways under investigation. Three different group mapping techniques were employed using SPM99. Each has merits and limitations that will be discussed later:

1) Average Group Maps - The normalized unthresholded maps were averaged at each point in standard space across the whole group of subjects for each of the five white matter tracts. The mean images were overlaid onto a structural template.

2) Variability Group Maps - The normalized, thresholded maps were averaged at each point in standard space and the resulting images were overlaid onto a structural template. As the individual maps were binary and defined where the tracts were likely to be, mathematical averaging had the effect of indicating the degree of spatial variability and overlap of the tracts between subjects.

3) SPM Analysis of Unthresholded Maps - The normalized, unthresholded maps were initially smoothed. Smoothing results in the voxel values approximating a parametric distribution and, through the central limit theorem, allows the use of standard parametric statistics to make inferences about differences and similarities between VSC distributions (Ashburner and Friston 2000). The unthresholded images were chosen in order to preserve as much spatial information about the particular white matter tract under investigation as possible. The size of Gaussian filter was chosen according to white matter tract: 10 mm was used for the anterior callosal fibres, 7 mm for the optic radiations and 5 mm for the pyramidal tracts. These values were chosen because, between subjects, the spatial variability in tract position was greatest for the anterior callosal fibres and least for the pyramidal tracts, as discussed in the results. The individual smoothed images were then entered into a design matrix for a one sample t-test. Significance was assigned to the resulting t fields using the theory of Gaussian random fields (Worsley et al, 1996). The resulting statistical maps were corrected for multiple comparisons across the volume under analysis.

5.1.2.6 Tract volumes and asymmetry

Tract volume assessment - The ROIs derived from the histogram thresholds that defined the individual thresholded maps (before normalization) were used to calculate the tract volumes for each subject. For the pyramidal tract and optic radiation, the Wilcoxon test was used to compare the tract volumes, between left and right sides.

SPM analysis - An SPM analysis was also conducted to assess regional interhemispheric asymmetry for the pyramidal tract and optic radiation. To do this, the individual unthresholded maps were first normalized using a symmetrical EPI template and then smoothed as before. The resulting smoothed, normalized right sided tracts were then flipped across the midline and the 'mirror images' were subsequently compared, using SPM, to the left sided tracts with paired t-tests.

5.1.2.7 *Assessment of seed voxel placement in normalized space.*

The consistency of seed voxel location within the standard stereotactic reference frame (MNI space) was assessed for each tract across the 21 subjects. Each seed voxel co-ordinate (defined in native space) was normalized with the same spatial transformation parameters as the maps (see spatial normalization above).

5.1.3 Results

5.1.3.1 *Average Group Maps*

The average group maps across the whole group of subjects for the white matter pathways under investigation were created and then overlaid onto a T_1-weighted template image (figure 5.1). On visual inspection they qualitatively conform to the known anatomy of the tracts. The colour intensity of these maps reflects the average connectivity value of each voxel to the seed point across all subjects.

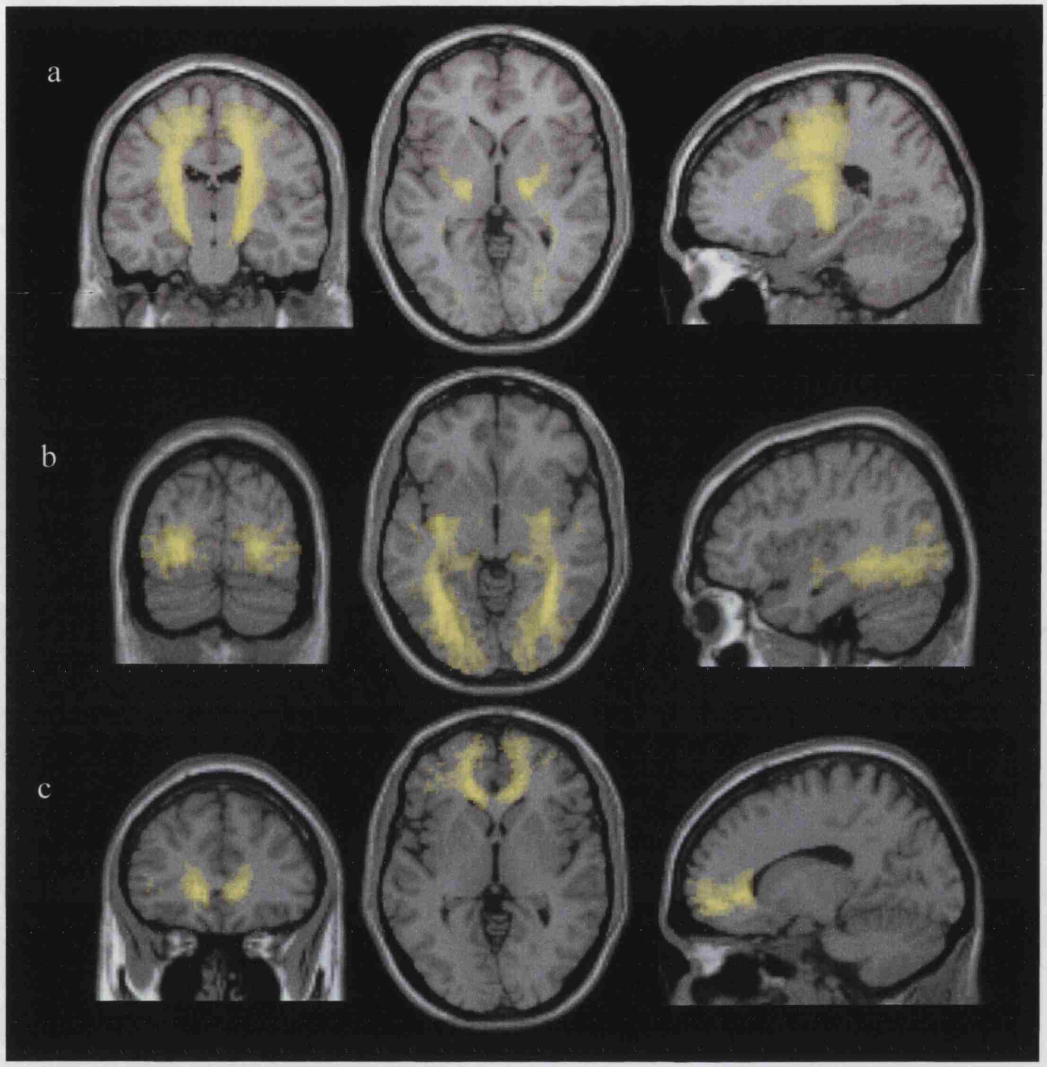

Figure 5.1. Average group maps are shown for the a) pyramidal tracts (MNI co-ordinates x=-20 mm, y=-16 mm, z=0.4 mm), b) optic radiations (MNI co-ordinates x=38 mm, y=-75.6 mm, z=2.7 mm) and c) anterior callosal fibres (MNI co-ordinates x=-14.5 mm, y=33.3 mm, z=0 mm). The locations of the tracts conform to the known anatomy. The colour intensity indicates the average connectivity metric value across the whole group of subjects. The maps have been thresholded (at a value of 100) to exclude very low average values and highlight the tracts of interest. Note that in b) some erroneous tracts are traced (centre image) anteriorly from the loop of Meyer; this may result from other white matter tracts in close proximity with Meyer's loop, for example inferior longitudinal fasciculus and uncinate fascicle. In a) some finely traced tracts of low connectivity along the optic radiations are seen in the centre image.

5.1.3.2 Variability Group Maps

The variability group maps were constructed using the thresholded maps and then were overlaid onto a structural template (figure 5.2). They represent the degree of spatial variability between subjects, and are visually consistent with data derived from post-mortem human brains (Burgel et al, 1999; Rademacher et al, 2001). The 'hot' colour scale indicates the proportional degree of overlap of

the tracts between subjects; for example, the number 1 represents 100% subject overlap (i.e. the voxel in question is within the identified tract in all subjects), 0.5 represents 50% overlap, and 0.05 represents data from only 1 out of the 21 subjects. The inter-subject spatial variability was greatest for the anterior callosal fibres (range: 0.05 - 0.49) and smallest for the pyramidal tracts (maximum overlap was 1 for the left and 0.95 for the right). The optic radiations demonstrate intermediate variability (maximum overlap 0.72 for the right and 0.62 for the left). The greatest overlap, for each tract, is found centrally as indicated by the brighter colours. Greater inter-subject variability is consistently found around the terminal projections of the tracts adjacent to cerebral cortex, indicated by darker colours.

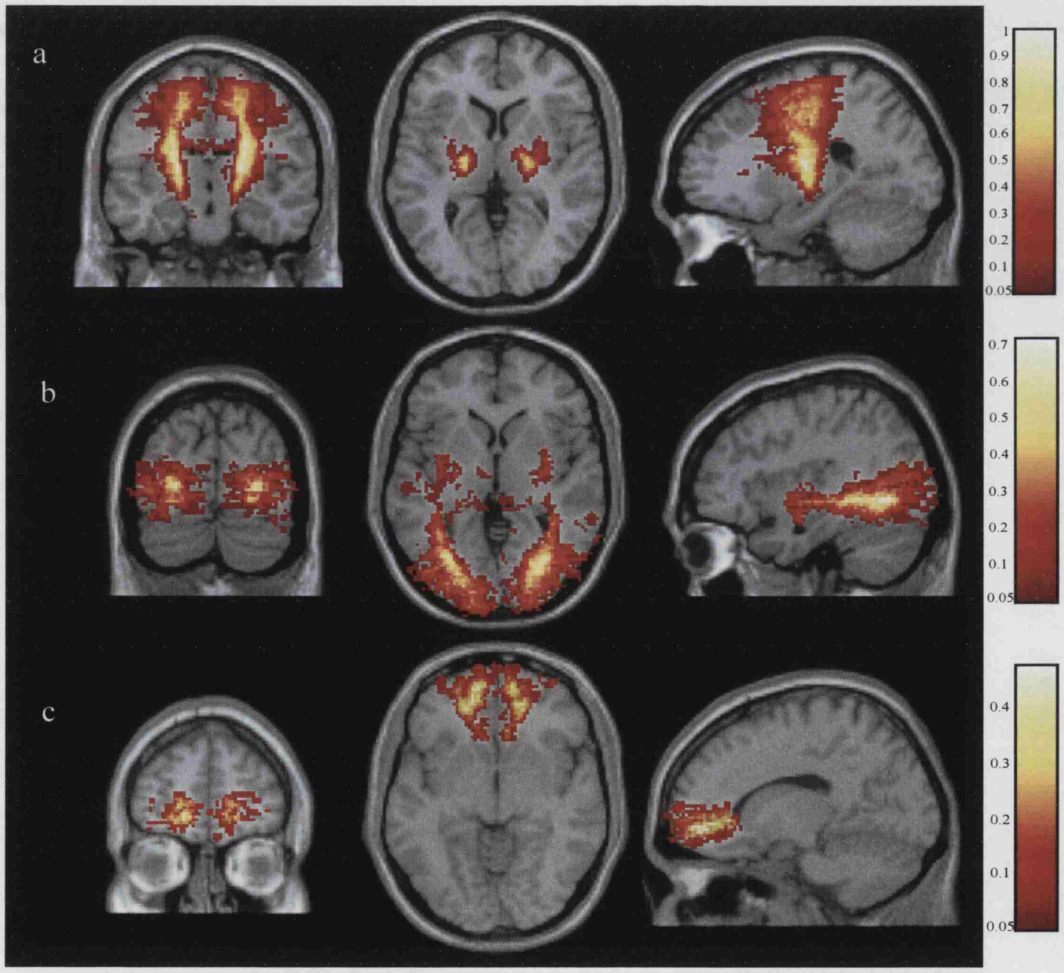

Figure 5.2. Variability maps for the a) pyramidal tracts (MNI co-ordinates x=-20.8 mm, y=-12.9 mm, z=4.3 mm), b) optic radiations (MNI co-ordinates x=37.2 mm, y=-77.9 mm, z=1.2 mm) and c) anterior callosal fibres (MNI co-ordinates x=-14.5 mm, y=52.1 mm, z=-5.1 mm). A 'hot' colour scale indicates the degree of overlap amongst subjects. 0.05 indicates that data is present in only 1 out of 21 subjects and 1 indicates 100% overlap. The peripheral distribution of each of the tracts demonstrates the greatest interindividual variability. Note that in a) a few tracts extend across the corpus callosum (left image), which would conform to collaterals of cortico-spinal fibres. In b) note few anteriorly projecting erroneous tracts from Meyer's loop (centre image).

5.1.3.3 SPM analysis of Unthresholded Maps

Statistical parametric maps (SPMs) were derived from one sample t-tests for each of the five tracts in order to determine where the unthresholded maps were significantly different from zero. Statistical inference was performed with correction for multiple comparisons ($p<0.001$). Representative SPMs for the pyramidal tracts, optic radiations and anterior callosal fibres are overlaid onto standard template (figure 5.3).

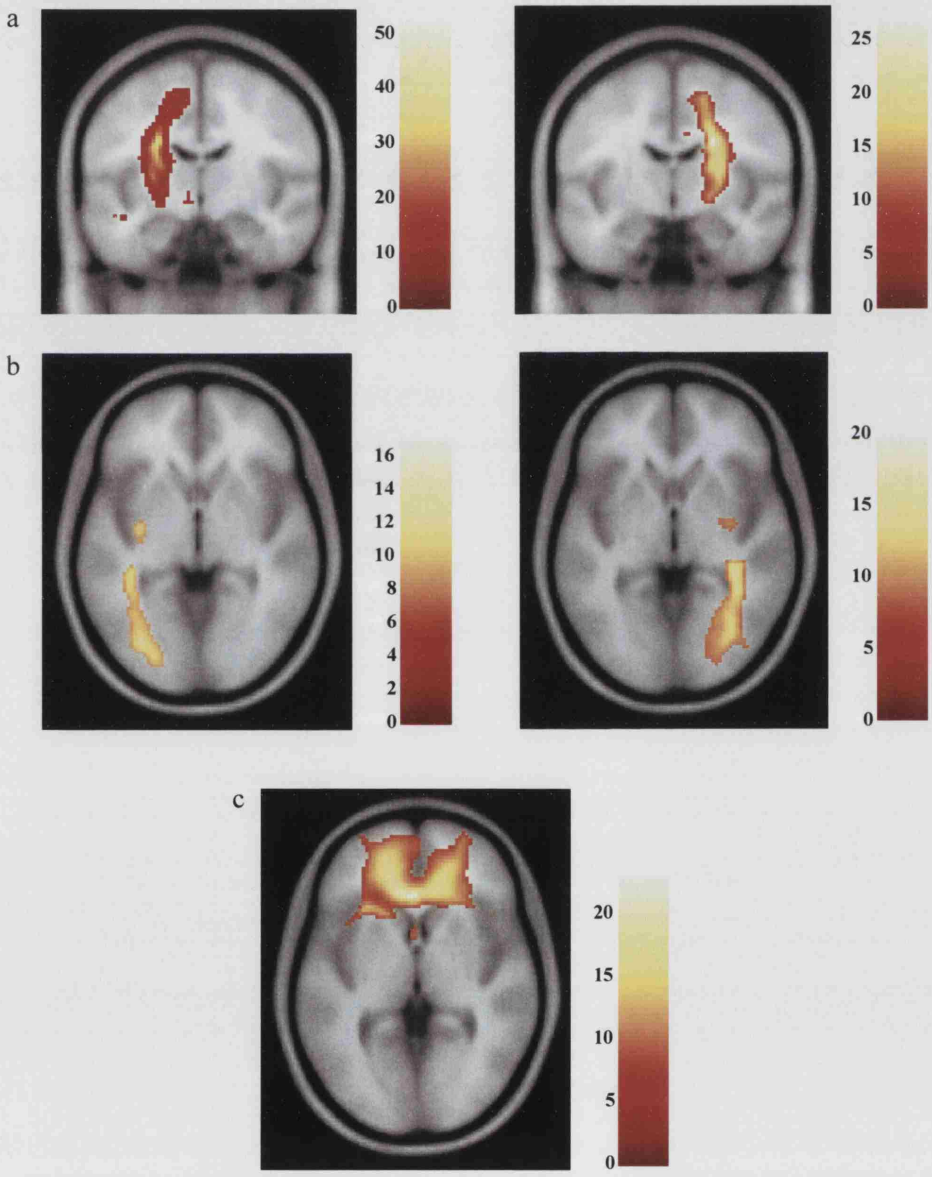

Figure 5.3. An example of the techniques to construct group effects using SPM is shown for the a) left and right right pyramidal tracts (y=-9 mm in MNI coordinates b) left and right optic radiation (z=-3 mm in MNI coordinates) and c) anterior callosal fibres (z=0.6 mm in MNI coordinates) (all maps corrected $p<0.001$). No asymmetry was detectable between left and right sides using SPM analysis. The colour scales indicate the t-scores.

5.1.3.4 *Tract volumes and asymmetry*

Tract volume assessment - The anterior callosal fibres showed the smallest tract volume, while the pyramidal tracts showed the highest. There were no significant differences in tract volume between the left and right pyramidal tracts and optic radiations (table 5.1). The tract volumes obtained for the pyramidal tracts and optic radiations are comparable to those that have been derived from myelo-architectonic studies on post mortem brains (Burgel et al, 1999; Rademacher et al, 2001). It should be noted that the tract volumes in our study were calculated before normalization i.e. they were not corrected for head size. The post-mortem tract volumes that are compared with our tract volumes are also uncorrected for head size.

White matter pathways	Total volume (cm^3) (Mean±SD)
Callosal fibres	3.33 (±0.72)
Left optic radiation	5.51 (±1.75)
Right optic radiation	5.16 (±1.44)
Left pyramidal tract	10.28 (±2.18)
Right pyramidal tract	11.49 (±3.57)

Table 5.1. Total volumes of the major white matter pathways in 21 normal subjects.

SPM analysis - No significant group effect differences were detectable between left and right sides using SPM99 for the pyramidal tracts and optic radiations. This is consistent with the comparison that we performed, between left and right sides, of tract volumes.

5.1.3.5 *Assessment of seed voxel placement in normalized space.*

The means and standard deviations of the x, y and z co-ordinates for the normalized seed voxels of each white matter tract are displayed in table 5.2. The greatest variability in seed point placement

occurs with the y direction for the optic radiations (standard deviation 7 mm for the left and 6.18 mm for the right). The lowest variability in seed point location was found in the x direction for the anterior callosal fibres (standard deviation 1.1 mm).

	Mean (SD) stereotactic seed voxel co-ordinates.		
	X	Y	Z
Anterior Corpus Callosum	-2 (1.1)	-66.6 (3.24)	1.2 (3.12)
Left Optic Radiation	-38.8 (2.68)	-9.6 (7)	-5.6 (3.18)
Right Optic Radiation	34.4 (2.24)	-13.4 (6.18)	-6.0 (2.96)
Left Cerebral Peduncle	-14.4 (1.78)	-20.8 (2.14)	-16 (2.42)
Right Cerebral Peduncle	12 (2.04)	-20.6 (2.12)	-15.8 (2.16)

Table 5.2. Table demonstrating the mean x, y and z voxel-coordinates (in mm) across the 21 subjects in MNI (Montreal Neurological Institute) space for each of the white matter tracts that were investigated. Standard deviations (SDs) are in brackets. The normalized voxel size was 2x2x2 mm.

5.1.4 Discussion

We have used mapping methods with FMT to investigate how the pyramidal tracts, the optic radiations and the anterior callosal fibres are represented in a group of 21 normal volunteers. We have constructed group maps in a standard reference frame that show the interindividual variability of tract location and shape and have generated statistical images that represent the group effect for each tract. A few other studies have recently addressed the issue of making group specific inferences with diffusion tractography. For example, recent work reported a method to create probabilistic maps of callosal fibres in a group of 10 subjects by combining methodologies for fibre tracking and spatial normalization (Xu et al, 2002), although the tractography algorithm and the normalization procedures were substantially different from those applied in this study. An alternative approach to

tracking the fibres prior to creating group maps is to average the tensor data sets before tracking fasciculi (Jones et al, 2002), in order to generate a generic map of brain connectivity.

In this study SPM was used to investigate asymmetry between left and right sides for the pyramidal tracts and optic radiations. Similar methods of assessing asymmetry of cerebral grey and white matter using voxel-wise statistical analysis have been previously reported (Good et al, 2001; Watkins et al, 2001). Discussion will initially focus on the results for each of the three white matter tracts and then move on to issues regarding DTI, tractography and FMT.

5.1.4.1 Pyramidal Tracts

The average group map of the pyramidal tracts (figure 5.1), on inspection, qualitatively compares well with known pyramidal tract anatomy (Brodal 1981; Ross 1980). The variability maps (figure 5.2) show a central core along the tracts of common overlap among 95% of subjects for the right side and 100% for the left. This indicates that relative tract location between individuals is generally constant. Outside this core there appears to be considerable variability in tract overlap. We believe this reflects variation in tract volume between individuals, which is also reflected in the calculated tract volumes and their standard deviations (table 5.1). The pyramidal tract volumes are approximately in the same range of volumes reported by Rademacher et al. (Rademacher et al, 2001), who performed a cytoarchitectonic and myeloarchitectonic study of the human motor system in 11 post-mortem brains. Our volumes are slightly higher on both sides (table 5.1) than the volumes reported in their study (left mean PRPT (precentral portion of the pyramidal tract) volume=9.32 cm^3 (± 2.58 cm^3) and right mean PRPT volume=7.94 cm^3 (± 2.34 cm^3)). In our variability maps (defined by averaging the thresholded maps) (figure 5.2), the pyramidal tracts mainly extend towards the motor cortex, but also show contributions from the premotor cortex. This may account for the slightly larger volumes reported in our study. Pyramidal tract fibres are known to take their origin mainly from the motor and caudal premotor cortex (Jane et al, 1967) and the appearance of our variability maps may reflect this. In addition, the differences could also be explained by sample selection differences between the

two studies. For example, the relatively low sample sizes for the post-mortem study and our study may contribute to slightly different estimates of population parameters for the pyramidal tracts and so good agreement between the two studies should not necessarily be expected. In support of this, we find no differences between left and right pyramidal tract volumes, whereas the other authors report greater left sided tract volumes. Future studies with larger sample sizes should allow better estimates of normal population variability. Finally, methodological differences in tract volume calculations could also contribute to the observed differences between the two studies.

5.1.4.2 Optic Radiations

The appearance of the optic radiations on the average (figure 5.1) and variability group maps (figure 5.2) again conform closely to their known anatomy. On the variability maps the maximum overlap was 62% (15 out 21 subjects) on the left and 72% (17 out of 21 subjects) on the right. This probably reflects relative differences in FMT-derived tract position between individuals and may be attributed to inter-individual anatomical differences in tract morphology. Also, the fact that the calculated optic radiation volumes are smaller than the pyramidal tract volumes (table 5.1) may make overlap between individual tracts less likely. The calculated tract volumes are only slightly lower than the volumes reported by Burgel's myeloarchitectonic study (Burgel et al, 1999) of 11 post-mortem human brains (mean left optic radiation volume=6.81 cm^3 (±1.71 cm^3); mean right optic radiation=6.69 cm^3 (±1.69 cm^3)). These differences could be explained by the fact that they identified optic radiation fibres that originated from the lateral geniculate body, whereas we positioned our seed point within Meyer's loop, which would tend to produce lower FMT-derived tract volumes. As in our study, they found significant interindividual variability. They also found significant asymmetry of tract volumes (left being greater than right), which we did not reproduce *in vivo* either by statistical comparison between left and right optic radiation volumes or by SPM analysis. This is probably due to random differences in the population samples that were studied and methodological differences between DTI based tractography and myeloarchitectonic based histological studies.

5.1.4.3 Anterior callosal tracts

The anterior callosal fibres demonstrate the smallest overlap in tract position (figure 5.2) with a maximum of 49% sharing the same voxel space. This may be because the tract volumes are the smallest of all three pathways examined in this study (mean 3.33 cm^3), which probably makes significant overlap unlikely. Also, it is known that the cortico-cortical connections through the corpus callosum are topographically organised (de Lacoste et al, 1985); those connections through the genu (anterior region) of the corpus callosum span out to serve a large area of the frontal cortex. The high variability in the position of FMT-derived callosal fibres may thus reflect natural anatomical differences, between individuals, in the topographical organisation of callosal projections. Moreover, the frontal regions can be highly affected by EPI geometric distortions (Farzaneh et al, 1990). These distortions may vary between individuals and limit the ability of FMT to trace tracts in these regions, and affect the registration methods used.

5.1.4.4 Benefits of FMT in mapping white matter pathways

An advantage of FMT is that the algorithm permits the determined pathways of connection to divide, thus allowing for branching pathways (Parker et al, 2002a). This is useful for tracing the pyramidal tracts and optic radiations. A consequence of this, however, is that erroneous false positive branches that do not conform to known neuroanatomy may be traced (figures 1 and 2). These tend to have lower VSC values and can be explained by the way the tract is locally traced through the particular orientations of a group of eigenvectors, which may be affected by crossing or "kissing" fibres. It is also clear from the examination of the variability maps in figure 5.2 that the false positive pathways have inherently higher positional variability than the true paths.

A second advantage of FMT is the ability to quantify the degree of connection at every voxel in the brain for any given seed point. The resulting VSC maps can be compared across individuals to assess inter-subject group effects and variability.

5.1.4.5 Limitations of FMT Tractography

General limitations of DTI tractography are discussed in detail chapter 6. Specifically, FMT relies upon the placement of seed voxels or regions of interest from which the resulting white matter pathways are mapped. Spatial normalization occurs after the tractography algorithm is run in native space. Differences between subjects in the resulting normalized tracts may arise from real anatomical differences in tract anatomy, errors during spatial transformation or differences in the relative locations of the seed voxels. In our study, seed voxel placement was fairly consistent in normalized space (table 5.2) with standard deviations in each direction of about 2 to 3 mm. The seed voxel y co-ordinates for the optic radiations demonstrated greater variability (standard deviation of 6.18 and 7 mm), possibly resulting from differences in axial tilt of the head between datasets. It is uncertain to what degree this variability influenced the observed differences for the optic radiation group maps and volumes. In an attempt to overcome seed point placement variability, registration algorithms that allow the transformation of the diffusion tensor into normalised space before applying tractography, have been developed (Alexander et al, 2001). The normalized individual tensor datasets can then be mapped into a standardized reference frame and a predefined co-ordinate system used to place the seed point. However, as before, spatial transformation will not be error free. In addition, the resulting 'normalized' datasets will possess some natural inter-individual variation of white matter tracts. A seed voxel placed at the same co-ordinate may therefore be located at relatively slightly different points, along the same white matter tract, in different subjects. Nevertheless, it would be useful to assess this method in future group mapping studies.

A quantitative evaluation of the errors that may occur with spatial normalization techniques will be helpful, in the future, to assess the robustness of DTI and tractography normalization procedures. In particular, it would be interesting to compare the errors produced by spatial transformations of the tensor (before applying tractography) with spatial transformations of tractography derived maps (after tensor normalization). SPM intersubject registration has been recently evaluated for structural

MRI anatomical data and the mean error for registering cortical sulci was about 8mm which compares favourably with other methods (Hellier et al, 2002).

5.1.4.6 Average Group Maps

The average group maps used the unthresholded maps from each subject. This allows quantitative information for a group effect to be calculated at each voxel and potentially has the ability to detect novel branching pathways. However, they do not provide information about inter-subject variability and also can be sensitive to the effects of outliers. For example, voxels with very high VSC values may skew the resulting means of the corresponding voxels in the average map.

5.1.4.7 Variability Group Maps

The variability maps are very informative at assessing inter-subject overlap. In addition, their appearance and their individual volumetric quantification compares favourably with white matter tract volumes reported in histological studies (Burgel et al, 1999; Rademacher et al, 2001). However, as they purely provide spatial information about tract location and morphology, they do not allow VSC quantification.

5.1.4.8 SPM analysis of Unthresholded Maps

SPM can be used to assess the group effect of the individual unthresholded maps. It can also be used to demonstrate variability between subjects (by displaying the residual variability map after model estimation). Caution should be taken, however, when making inferences from one sample t-tests because the assumption that residual errors are distributed normally about zero may not be valid. In this study the figures depicting the results from one sample t-tests are displayed primarily as a visual aid. A more useful application would be in its ability to compare, at each voxel, VSC values between

different groups (with the assumption that the residual errors behave similarly between them) and may be an important application in investigating white matter pathology in the future.

5.1.4.9 Future applications

We have applied three group mapping techniques, which are complementary to each other and explore different aspects of the behaviour of estimated white matter pathways across individuals. Three specific white matter tracts were chosen because: 1) They have well-known structural connections; 2) They are large, which makes their identification more convenient than other fibre tracts of finer or more intricate structure; 3) They are clinically relevant pathways in pathological conditions; 4) They have been qualitatively compared between human and macaque brains using FMT algorithm (Parker et al, 2002a).

The ability to combine white matter tractography maps across individuals is an essential step in understanding how white matter pathways are organized and how they vary *in vivo* within populations. By constructing 'white matter atlases' it should be possible to investigate diseases of white matter or conditions in which neural trajectories have altered. Our study should be considered as an early step towards this goal.

A further exciting prospect for DTI tractography is to elucidate neuronal connections between regions of cortical grey matter. This will help to address how structural substrates influence and are influenced by functionally segregated neuronal circuits and how functionally integrated networks of high complexity interact. The next study makes initial steps towards these goals by quantitatively investigating the relationship between function and structure in a group of normal controls.

5.2 Characterising function-structure relationships in the human visual system.

5.2.1 Introduction

The relationship between the function of the brain and its structure is a fundamental issue in neuroscience research. Function-structure relationships may be intrinsic or extrinsic to cortical regions. The latter description encompasses how cortico-cortical and cortico-subcortical white matter structural connections relate to regional gray matter activity. Recent developments in magnetic resonance imaging (MRI) have allowed the indirect investigation of both cortical function and white matter structure *in vivo*. Blood oxygenation level dependent (BOLD) functional MRI (fMRI) has been used to measure regional cerebral activity (Kwong et al, 1992; Logothetis et al, 2001; Ogawa et al, 1990; Ogawa et al, 1992) and diffusion tensor imaging (DTI) to quantitatively probe the microscopic and macroscopic architectural properties of the brain (Basser et al, 1994; Pierpaoli et al, 1996).

In this study, we employed fMRI and DTI with tractography to investigate the relationship between functional and structural properties of the posterior visual pathways. The visual system was chosen because, as well as being anatomically well defined, fMRI paradigms using photic stimulation are known to robustly activate the visual cortex (Rombouts et al, 1996; Werring et al, 2000a). In addition, recent work has successfully utilized diffusion tractography to demarcate the optic radiations in humans (Ciccarelli et al, 2003b; Ciccarelli et al, 2003a) from which the mean diffusion, anisotropy and volumes were calculated. By assuming that the anisotropy measurements of the optic radiations reflect their structural integrity, we hypothesized that the mean optic radiation anisotropy would correlate with the degree of fMRI activity in the visual cortex.

5.2.2 Methods

We aimed to derive two fMRI measures of visual cortex activity (corresponding to degree and spatial extent of fMRI response) and two DTI based measures for the optic radiations (mean fractional anisotropy (Pierpaoli and Basser 1996) (FA) and normalized connected volume).

5.2.2.1 Subjects

Twenty-two healthy volunteers were studied (7 women and 15 men). The mean age was 29.6 ± 6.3 (s.d.) years. Informed consent was obtained from all subjects before entering into the study.

5.2.2.2 MRI Protocol

All scans were performed on a 1.5T Signa Echospeed MRI system (GE Medical Systems, Milwaukee, WI). Each subject underwent the following scans.

Conventional MRI - Proton density- and T2-weighted fast spin echo imaging [TR 2000, TE 30/120ms, FOV 240 mm, matrix 256 × 256; 28 contiguous axial slices; 5 mm slice thickness] was performed.

Functional MRI - 150 T2* weighted images sensitive to BOLD contrast were acquired in each fMRI experiment, which lasted 10 minutes and covered the whole brain with 27 near-axial slices [TE 40 ms, TR 4000 ms, field of view 38 cm x 19 cm; matrix size 128 × 64; voxel size 3x3x3.6 mm^3, interslice gap 0.4 mm]. Lightproof goggles (Grass Instruments, Quincy, MA, USA Model S10VSB) with flashing LED displays in each eyepiece were used to provide photic stimulation. Each subject underwent two monocular fMRI experiments, one for each eye, rather than binocular stimulation, in order to avoid the possibility of binocular rivalry influencing the fMRI response (Blake and Logothetis 2002). During each experiment subjects passively viewed a visual display which alternated periodically between 20 second epochs of two contrasting conditions: (A) red 8 Hz photic stimulation to the

whole visual field was presented to one eye whereas the other eye received no visual stimulation; (B) no visual stimulation (darkness) was presented to both eyes; condition B (no stimulation) was always presented first. The order of experiments was randomly decided.

Diffusion tensor imaging - Single-shot diffusion-weighted echo-planar imaging (DW-EPI) was used [TE 95 ms; TR 5RR intervals ≅ 5-6 s; acquisition matrix 96 × 96 reconstructed to 128 × 128; FOV 240 mm; 3 b ≈ 0 smm^{-2} images; 60 diffusion weighted images, with diffusion gradients applied along 60 optimized diffusion directions (Jones *et al.*, 1999a); diffusion times of Δ = 32 ms and δ = 40 ms, and max gradient amplitude of 22x 10^{-3} Tm^{-1}, giving a maximum b-factor b = 1000 smm^{-2}; 42 contiguous axial slices; acquired voxel size 2.5x2.5x2.5 mm^3, reconstructed to 1.9x1.9x2.5 mm^3; diffusion data acquisition time = 20-30 minutes, dependent upon heart rate]. Cardiac gating was used to reduce motion artefacts due to pulsation of blood and CSF.

5.2.2.3 FMRI analysis

Statistical parametric mapping software (SPM99, Wellcome Department of Cognitive Neurology, London, UK) was used. Each fMRI time series was realigned, normalized to a standard stereotactic space (defined by the Montreal Neurological Institute (MNI)) and smoothed (8mm isotropic Gaussian kernel). The general linear model (Friston et al, 1995) was implemented to determine the main effect of the photic stimulation paradigm, with realignment parameters entered as covariates of no interest. For every subject a fixed effects analysis was performed, comprising the two fMRI time series (for left and right eyes) entered as separate sessions. Three contrasts were derived from the fitted model that represented the fMRI response of the left and right eyes and the average response from both eyes. For each contrast image the degree of fMRI activity in the visual cortex was estimated by extracting and averaging the parameter estimates within a predefined spherical volume (20mm radius) centered at the MNI co-ordinate [0,-86,0]. The spatial extent of fMRI activity was estimated by counting the suprathreshold voxels (within a predefined box in the occipital cortex) in the subsequently derived SPM(T) maps thresholded at $p<0.05$ (corrected across whole search volume).

Thus two scalar values were derived for each contrast image that estimated the degree (called *fMRIPE* which abbreviates fMRI parameter estimate) and spatial extent (called *fMRIvox* which abbreviates fMRI voxel number) of fMRI activity in the visual cortex. The fMRI contrast images and scalar values for the average response from both eyes were used in the main analysis. This was because anatomically each optic radiation shares its input stimuli between both eyes.

5.2.2.4 DTI and DTI tractography analysis

The DTI data were processed to determine the diffusion tensor on a pixel-by-pixel basis (Basser et al, 1994), using locally written software. Fractional anisotropy (FA) maps were then calculated (Basser and Pierpaoli 1996; Hasan et al, 2001; Pierpaoli and Basser 1996). An FA template was generated in MNI space from all the subjects to be used later (figure 5.4).

After this, the PICo (Probabilistic Index of Connectivity) algorithm (Parker et al, 2003) was used to track the optic radiations. This works by first generating a probability distribution function (PDF) from the diffusion tensor for each voxel, which provides voxelwise estimates of confidence in the fibre tract orientation. A streamline based tracking propagation is then performed using the derived PDFs from a chosen seed voxel. This process is repeated in a Monte Carlo fashion to allow adequate sampling of the PDFs and produces maps that estimate the confidence of connection from the seed voxel to a distributed area.

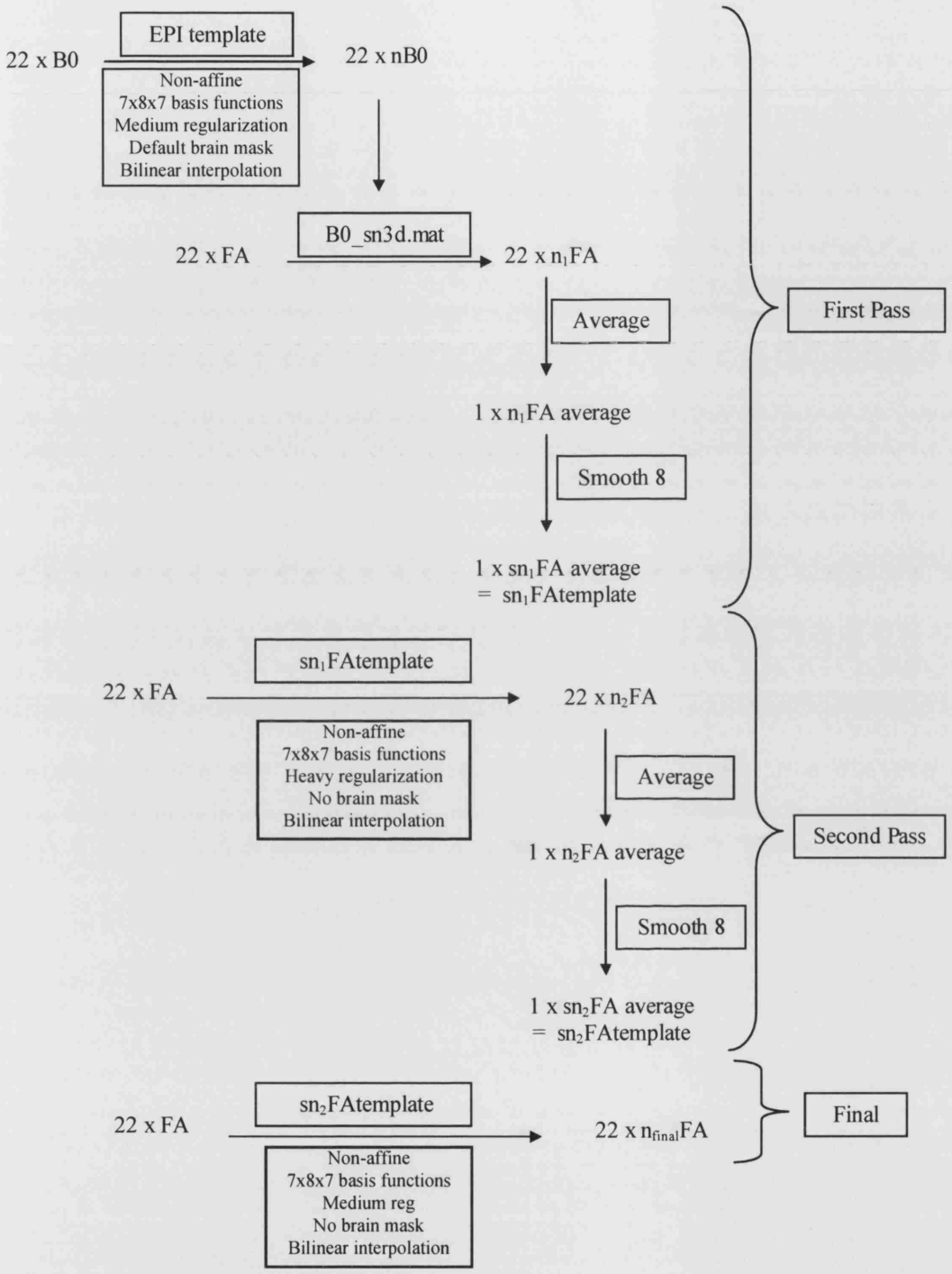

Figure 5.4. An FA template was constructed using SPM99 in a two stage process using all 22 subjects. B0=B0 image. FA=FA image. The prefix 'n' signifies normalized. The template construction used two registration passes. The final registration process refers to the final spatial normalization procedure used in the study.

Seed voxel placement – A robust, new method was designed for seed voxel placement, with the aim of reducing intersubject variability. It was performed in two stages. For each side, a single observer initially chose a seed voxel (with FA > 0.4) on every subject's FA map within the optic radiation apex

around the lateral ventricle, using previously described anatomical guidelines (first stage) (Ciccarelli et al, 2003a). The native seed coordinates were transformed into normalized FA space (normalized first stage) and then averaged across the subjects to provide two coordinates, one for each side. These two averaged, normalized seed coordinates were then reverse normalized for every subject to obtain a second list of native seed coordinates. This second list was used to direct the placement of the seed voxels that would be finally used by PICo on the native images (second stage). This methodology minimized the amount of intersubject variability of the traced optic radiations that could be attributed to intersubject differences in seed voxel placement. The final chosen native seed coordinates were transformed into normalized FA space (normalized second stage) to generate a further list that was used to assess intersubject variability as described below. A second observer also chose seed voxels directly on the native FA images which subsequently were normalized to the FA template to assess the inter-rater differences in seed voxel placement (this was only a single stage process).

Since seed voxel placement was the only operator dependent input in the process of parcellating the optic radiations, it was important to assess its intersubject variability in MNI space. This was done by calculating the distance of each normalized second stage seed voxel from the averaged normalized second stage seed coordinate (called residual deviation). Pearson correlation analyses were then performed for left and right sides between the residual seed deviations and the respective measures of tract FA and normalized volume but no associations were found (data not shown). This indicated that the intersubject variability of the tract measures could not be explained by the intersubject variability of the normalized seed coordinates and therefore probably reflected genuine structural intersubject variability of the optic radiations. We also averaged the left and right residual seed deviations for each subject and used these as covariates in the general linear modeling for mean FA and normalized volume.

PICo analysis – The PICo (Parker et al, 2003) analysis consisted of 10,000 Monte Carlo probabilistic streamline-based tracking iterations for each chosen seed voxel. The number of iterations was chosen *a priori* and was based on results from PICo experiments performed on a single subject unrelated to this study which demonstrated adequate convergence of the Monte Carlo method at this number of iterations (figure 5.5). The algorithm employed information derived from the diffusion tensor and used an FA threshold of 0.01 (effectively unthresholded, except for residual CSF contamination) above which the voxelwise connectivity analysis was performed. The maps had previously been CSF segmented using locally written software (Hadjiprocopis et al, 2003). A restricted brain volume was used in the analysis in order to speed up the PICo analysis and to focus upon the tracts under investigation.

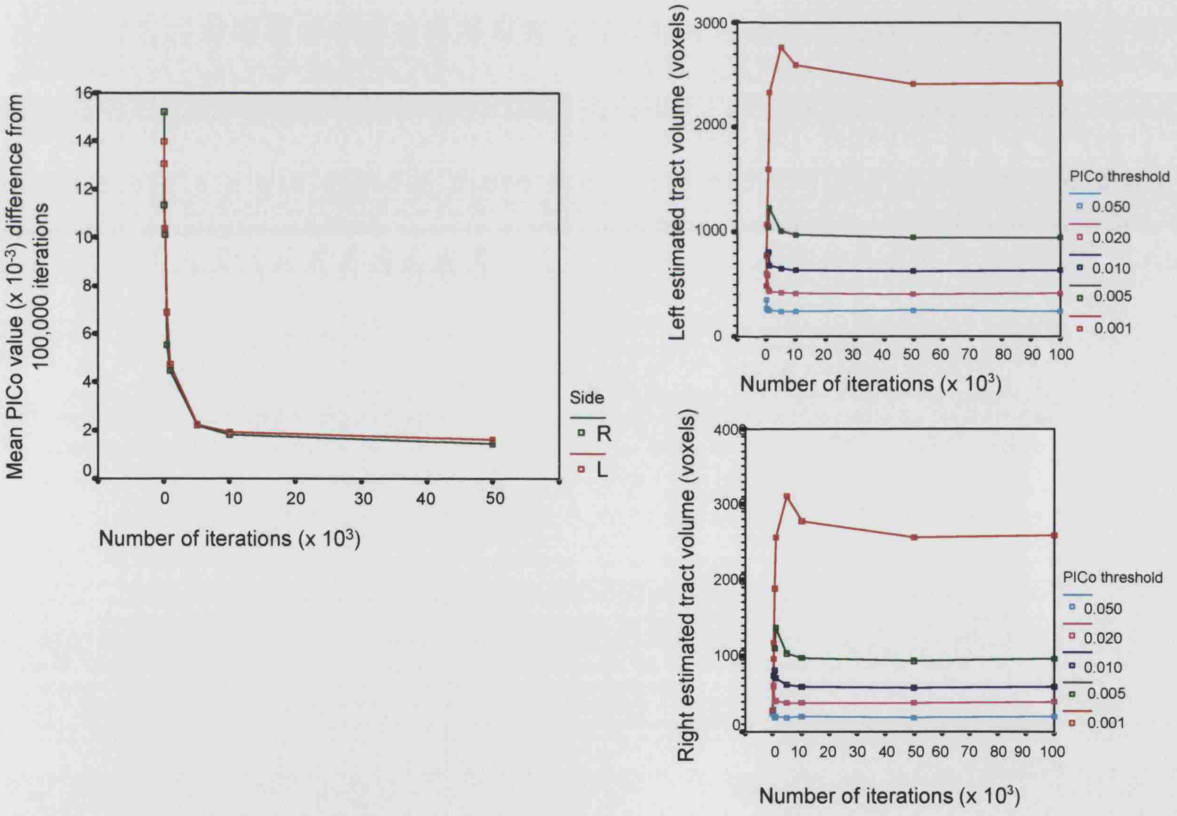

Figure 5.5. Choice of iteration number. A single subject experiment was performed using multiple iterations up to 100,000 with the same seed voxel. The top graph quantifies the mean absolute differences in voxel intensity (x 10^{-3}) across the whole image between a particular iteration number and 100,000 (chosen to represent a gold standard). Iterations greater than 10,000 differ very little from 100,000 iterations in the mean absolute voxel intensity. The right hand graphs demonstrate the calculated tract volumes at five PICo thresholds for different iterations numbers. Again very little change is noted above 10,000 iterations.

The voxel values of the PICo output maps for the optic radiations ranged from 0 to 1 with an intensity resolution step of 0.001. They represented the probability values of connection for each voxel to the seed voxel. Each PICo map was thresholded at five probability values ranging from 0.001 (the lowest recorded probability value) to 0.05 to generate five objective binary masks. These thresholds allowed us to progressively interrogate with increasing degrees of certainty the cores of the tracts where the fibre alignment should be greatest. The threshold range was chosen because it accounted for over 90% of the variance of estimated tract volumes derived from the binary masks on an unrelated healthy subject (figure 5.6).

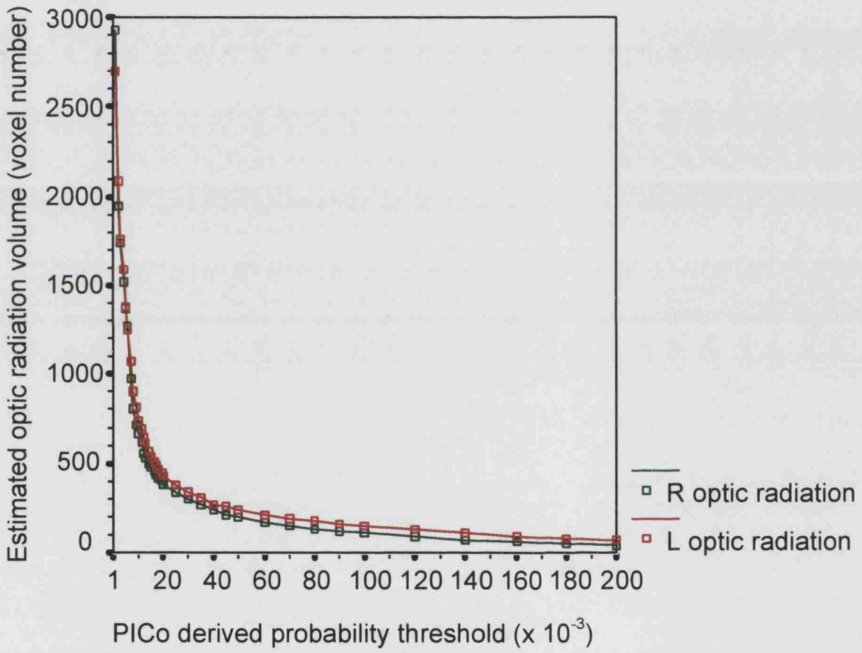

Figure 5.6. Choice of PICo thresholds. A single subject experiment using 10,000 iterations. Estimated optic radiation volumes are calculated using different PICo thresholds ranging from 0.001 to 0.2. About 90% of the variability in calculated tract volume can be captured by choosing PICo thresholds between 0.001 and 0.05.

For each threshold, the mean FA of the connected volume in native space (representing the estimated optic radiation) was calculated. The five thresholded binary masks for each subject were then spatially transformed to an FA template reference space and the normalized volumes for left and right optic radiations subsequently derived. Spatial normalization also allowed the construction of spatial variability maps to examine the intersubject variation of the estimated optic radiations

(Ciccarelli et al, 2003b) and contour maps to visualize the effect of thresholding on the spatial characteristics of the estimated optic radiations.

5.2.2.5 General linear modeling with fMRI and DTI derived scalars

The DTI scalar measures (mean FA and normalized volumes) were explored for each of the PICo thresholds (0.001, 0.005, 0.010, 0.020 and 0.050). Some evidence was found for unequal variances between thresholds (figure 5.7A) for the normalized connected volumes, with the variance approximately scaling with mean volume. The left and right sides were also compared in paired t-tests for each threshold, but no significant differences were found for either mean FA or normalized volume. It was therefore decided to analyze each threshold independently and collapse the left and right sides into an average measurement per subject for mean FA and normalized volume. This would also avoid any issue of repeated measurements in the statistical modeling. The fMRI scalar data were also explored. High correlations were found between left, right and the average fMRI measures for both degree of BOLD activity (fMRIPE) and spatial extent (fMRIvox) (figure 5.8). The fMRI measures averaged over both eyes (bfMRIPE and bfMRIvox) were consequently entered in the main statistical analysis.

A general linear model approach was adopted in SPSS 11.0 (SPSS Inc., Chicago, IL, USA). For each PICo threshold, either the normalized volume or mean FA was entered as the dependent variable. Subjects were treated as random factors. Initial modeling entered sex as a fixed factor and age, residual seed point variation, bfMRIvox and bfMRIPE as covariates. Unimportant effects that were not significant ($p \geq 0.05$) were discarded. Interactions were tested and kept only if the ANOVA global F test showed a significant effect ($p < 0.05$). The interactions tested were bfMRIvox*sex, bfMRIPE*sex, bfMRIPE*bfMRIvox. The final model included only significant main effects or interactions and also bfMRIvox and bfMRIPE as covariates.

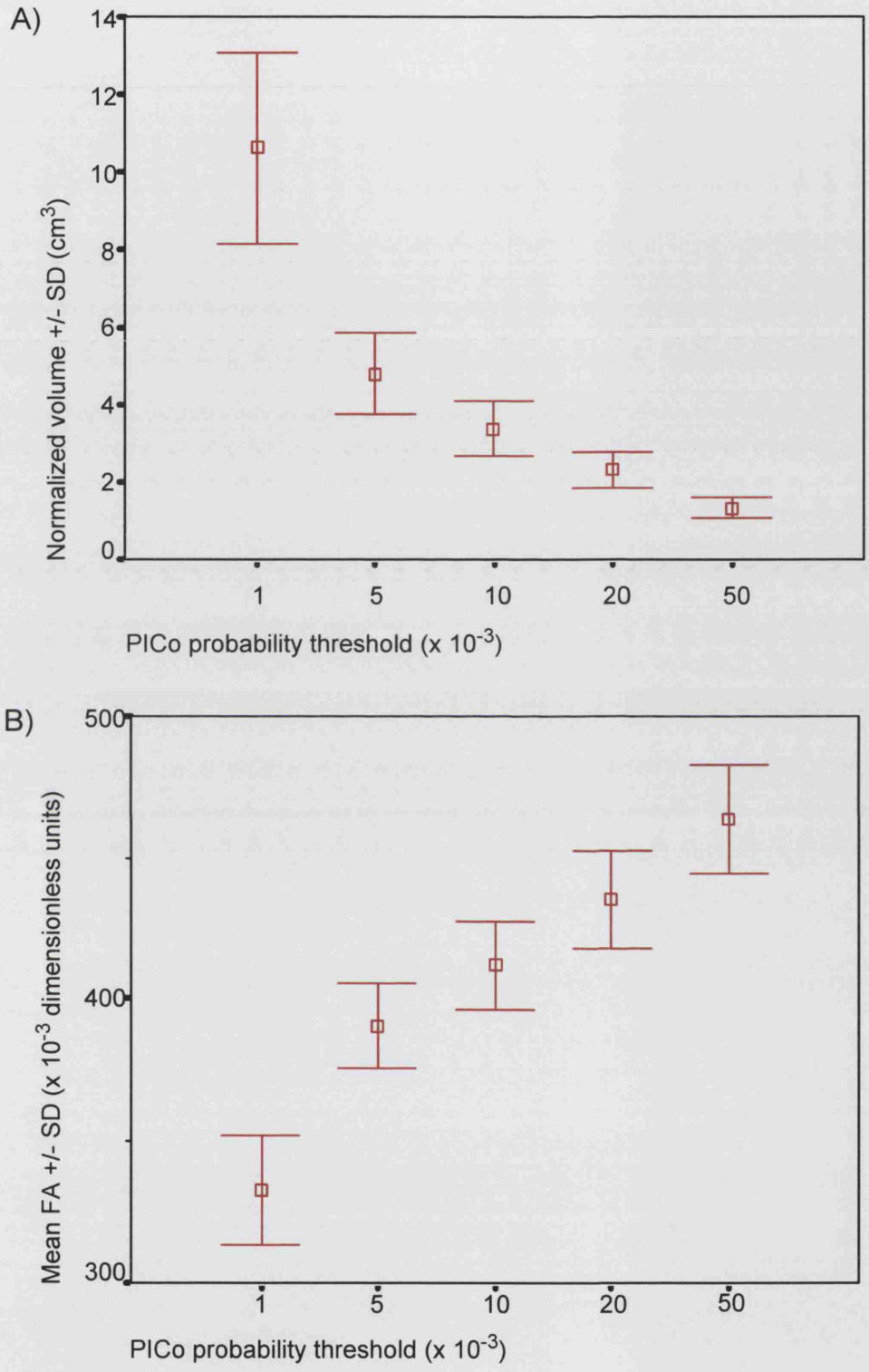

Figure 5.7. Calculated normalized volumes (A) and mean FA (B) for the 22 subjects are summarized for the estimated optic radiations derived from different PICo thresholds ranging from 0.001 to 0.050. Error bars show mean ± standard deviations. As the PICo thresholds increase, the estimated tract volumes decrease and the FA increases. This is because higher PICo thresholds increasingly isolate the tract core where the greatest fibre coherence is expected and partial volume effects are reduced.

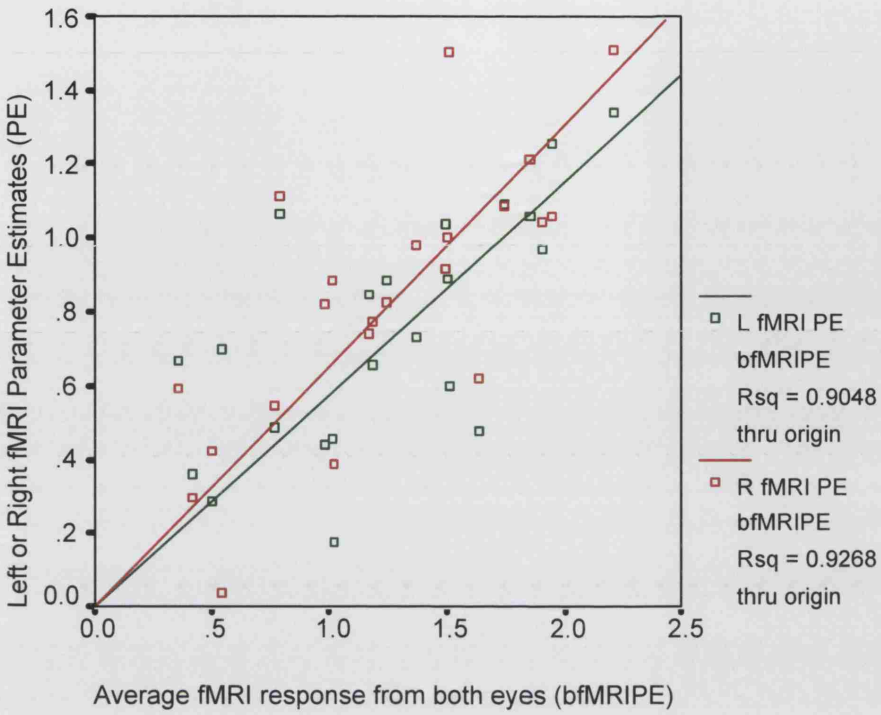

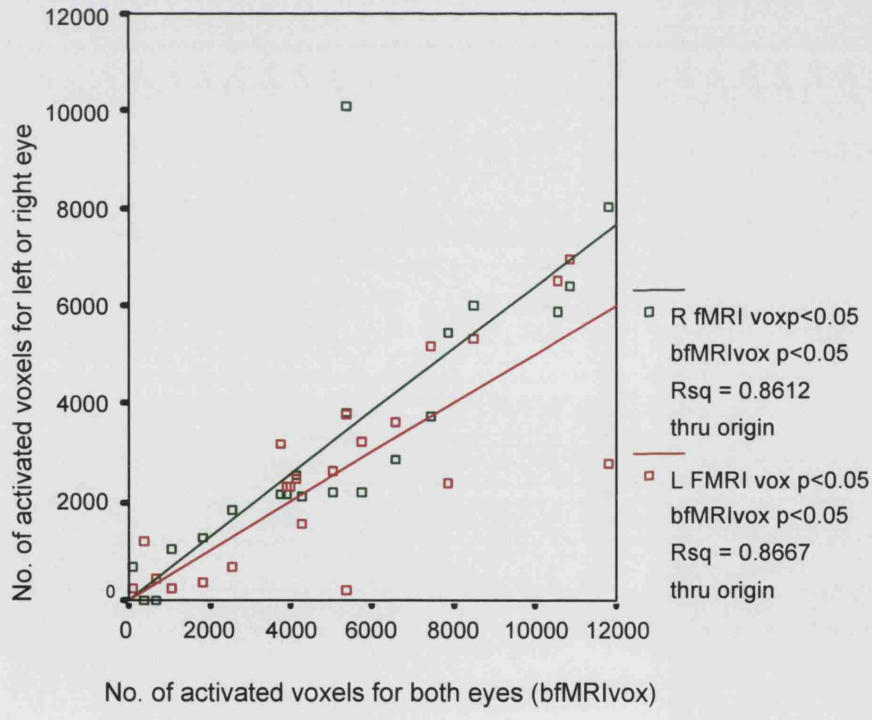

Figure 5.8. Top graph shows the Left/Right fMRI response vs the fMRI response from both eyes (bfMRIPE) in parameter estimate units (approximately %BOLD signal change). Bottom graph shows Left/Right fMRI vox vs bfMRIvox.

5.2.2.6 *SPM post-hoc regression analysis*

The subject specific contrast images for the average fMRI response across both eyes were entered into a SPM99 covariate model with the mean FA (for the estimated optic radiations) as a regressor column. Each PICo threshold was analysed in a separate design matrix. This allowed us to investigate any voxel-specific relationships between fMRI activity and mean FA for the estimated optic radiations. Statistical inferences employed a peak threshold of $p<0.001$ (uncorrected) with a spatial extent of 10 voxels on the SPM(T) maps.

5.2.2.7 *Group display*

The spatial variability optic radiation maps were overlaid with the SPM(T) maps that represented the group effect of the fMRI response from both eyes for the subjects onto an MNI structural template.

5.2.3 Results

5.2.3.1 *Seed voxel assessment*

Table 5.3 and figure 5.9 show the intersubject seed coordinate variability in normalized space. Residual deviations are displayed for three groups: the normalized coordinates from the first and second stages for the first observer and the normalized coordinates for the second observer. Formal one way ANOVAs between the three groups showed no significant differences in the seed coordinate means.

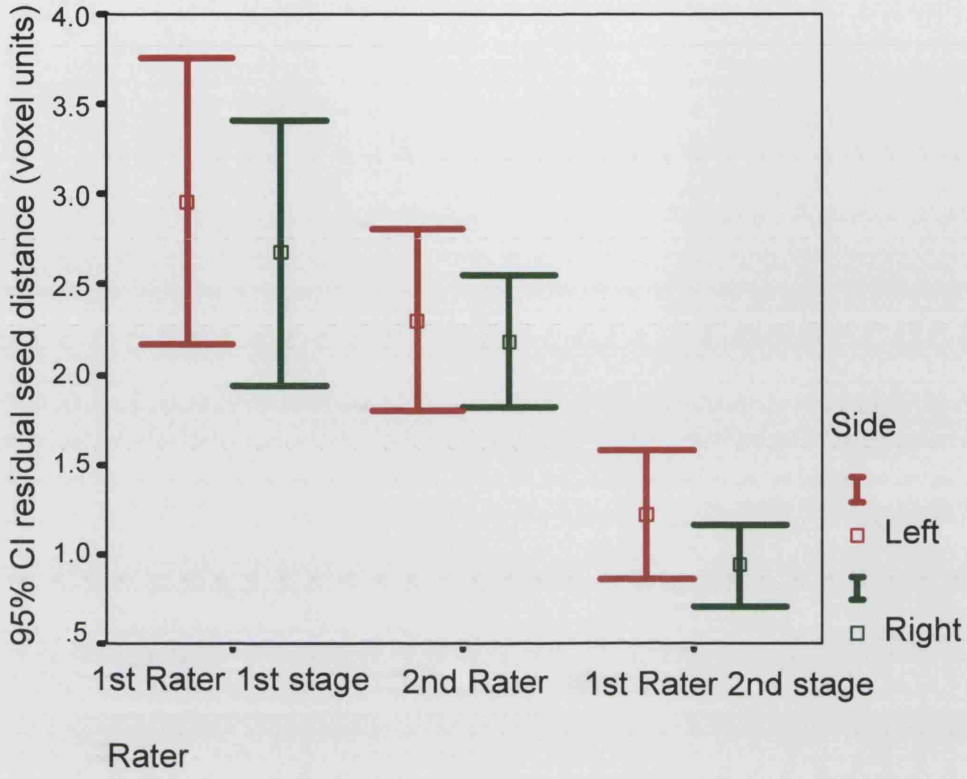

Figure 5.9. Seed placement variability for the first rater (first and second stages) and the second rater. The error bars indicate the residual seed coordinate variability after mean correction in normalized space. The two stage process is much better at reducing the intersubject seed coordinate variability (first rater second stage) than just applying the seed coordinates in native space (first rater first stage and second rater). The second rater chooses the seed coordinates slightly more consistently than the first rater because of greater experience although the actual mean coordinates chosen by both are the same (table 5.3). The error bars represent the 95% confidence intervals for the residual seed variation.

The two stage process reduces the variability of the intersubject seed coordinates in normalized space (figure 5.9 and table 5.3 – compare first rater first stage with first rater second stage) and reduces nearly all standard deviations to under one voxel. The residual deviations (a measure of seed coordinate variability in MNI space) are also smaller with a mean of around 1 voxel after the two stage process (table 5.3). The second rater chose seed coordinates with similar means to the first rater (compare first rater first stage with second rater) indicating that the anatomical guidelines were accurate and followed by both raters in a compatible manner.

		Left Optic Radiation				Right Optic Radiation			
		x	y	z	Residual deviation	x	y	z	Residual deviation
First rater 1st stage	Mean	20.25	42.49	21.94	2.96	59.05	43.64	22.25	2.67
	SD	0.94	2.75	1.98	1.79	0.72	2.61	1.70	1.66
Second rater	Mean	20.13	42.22	21.80	2.30	59.10	43.34	22.30	2.18
	SD	0.78	2.01	1.48	1.14	0.91	1.71	1.39	0.82
First rater 2nd stage	Mean	19.92	42.74	21.48	1.22	59.20	43.75	22.16	0.93
	SD	0.54	0.92	1.04	0.81	0.55	0.61	0.71	0.52

Table 5.3. Table demonstrating the effectiveness of the two stage process for minimizing the intersubject seed coordinate variability in normalized space (by comparing 1st and 2nd stage for first rater). Normalized seed coordinates (x, y and z) are shown in MNI (Montreal Neurological Institute) voxel units. The last column of each optic radiation summarizes the stereotactic residual distances of each normalized seed coordinate from the average, normalized seed coordinate in each group (mean deviations) in voxel units and indicate seed coordinate intersubject variability. A second rater independently chose the seed coordinates in native space using the same anatomical guidelines to check whether the mean seed coordinates were similar between raters. SD = standard deviation. Each voxel is 2x2x2 mm.

5.2.3.2 General linear modeling with fMRI and DTI derived scalars

Normalized connected volume – The standard deviation bars of the normalized volumes for each PICo threshold are indicated in figure 5.7A. The variability can be seen to tighten as the PICo threshold value is increased. The effect of the different PICo thresholds can be visualized on contour maps which show how the effect of increasing the PICo threshold allows one to probabilistically target the tract core (figure 5.10). Variation in seed voxel placement had no significant effects on normalized volume. There were no significant associations between the normalized volume and the number of activated voxels (bfMRIvox) or the degree of fMRI activity (bfMRIPE) (table 5.4). A significant effect for gender was noted however with females having consistently larger normalized

tracts than males (table 5.4). This was shown by all the PICo thresholds except 0.050 where the evidence was weak (p=0.056).

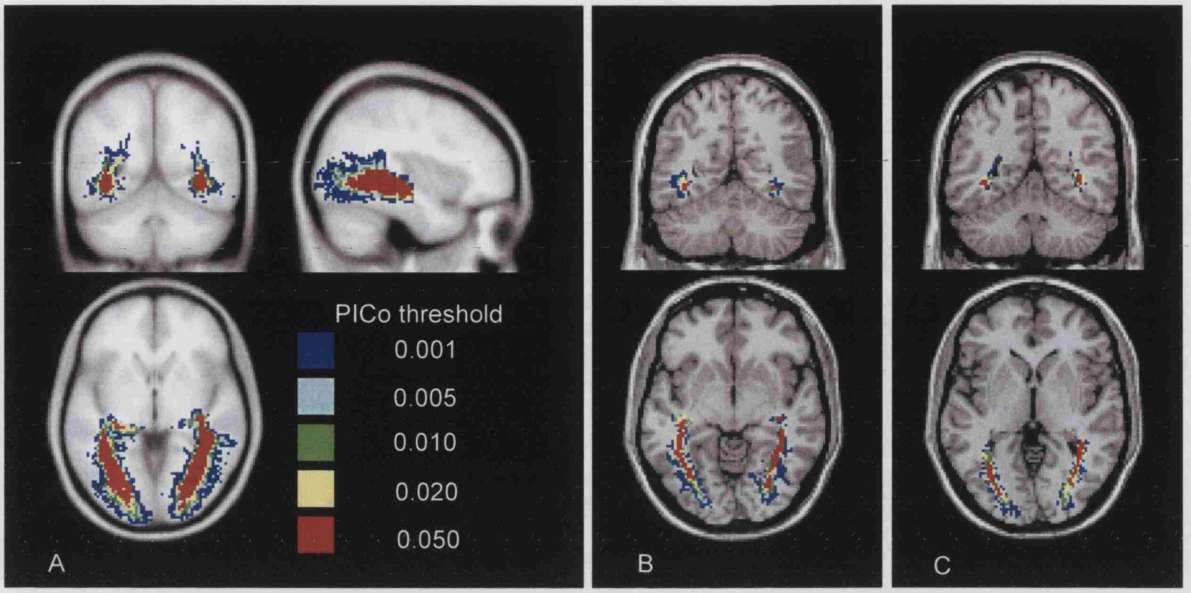

Figure 5.10. Contour maps illustrating the effects of applying different PICo thresholds. A) A group map for 22 subjects that demonstrates the general population effect of increasing the PICo threshold. For each threshold a spatial variability map was first constructed for the 22 subjects that indicated the degree of overlap between subjects for the thresholded tracts. A separate mask was then created from each of the five spatial variability maps and the five masks were combined to produce the contour map. The image is overlaid on to a T1 weighted template constructed from 152 volunteers available in SPM99. B) and C) demonstrate contour maps from representative individuals overlaid on to a single subject T1 weighted template in SPM99.

Mean FA – The standard deviation bars for mean FA are shown in figure 5.3B. The variability remains approximately constant as the PICo threshold increases. We found significant associations between the degree of fMRI activity (bfMRIPE) and the mean FA at all thresholds (table 5.4 and figure 5.11). The threshold which showed the strongest association was 0.020, whilst threshold 0.001 showed weak evidence for an association (p=0.06). The number of suprathreshold voxels (bfMRIvox) was not significantly related to the mean FA. There were no significant gender, age or seed voxel variation effects.

	Normalized Volume				Mean FA		
Probability threshold	**bfMRIvox**	**bfMRIPE**	**Gender**	**Estimated mean NV (SE)**	**bfMRIvox**	**bfMRIPE**	**Estimated mean FA $x10^{-3}$ (SE)**
0.001	p=0.333	p=0.111	p=0.017*	M 9.78 (0.54) F 12.38 (0.80)	p=0.408	p=0.06	332.63 (3.86)
0.005	p=0.608	p=0.586	p=0.002*	M 4.35 (0.22) F 5.75 (0.33)	p=0.257	p=0.044*	390.26 (2.99)
0.010	p=0.755	p=0.734	p=0.002*	M 3.01 (0.15) F 4.04 (0.22)	p=0.262	p=0.040*	411.82 (3.09)
0.020	p=0.789	p=0.792	p=0.004*	M 2.14 (0.10) F 2.75 (0.15)	p=0.089	p=0.005*	435.04 (3.07)
0.050	p=0.842	p=0.817	p=0.056	M 1.26 (0.07) F 1.51 (0.10)	p=0.139	p=0.019*	463.46 (3.68)

Table 5.4. Univariate general linear modeling results for the dependent variables – normalized volume and mean FA. PICo probability thresholds (from 0.001 to 0.050) are listed down the left hand column. For normalized volume note the significant effects for gender (females demonstrating larger optic radiations after normalization). For the optic radiation mean FA there are significant associations with the degreed of fMRI activity in the visual cortex (bfMRIPE). FMRIvox = no. of suprathresholded voxels occipital cortex. NV = normalized volume in cm^3. SE = standard error of the estimated mean. The estimated means are provided for the average bfMRIvox and bfMRIPE values.

5.2.3.3 SPM post-hoc regression analysis and group display

Significantly activated clusters were found confined to the visual cortices at all thresholds (figure 5.12) and localized where associations between the estimated tract mean FA and the fMRI voxelwise activity were strongest.

A qualitative combination of the optic radiations and visual activity is shown in figure 5.13, in which the spatial variability maps for the optic radiations at PICo threshold 0.001 are overlaid with the

SPM(T) maps for fMRI activity. The maps indicate that most intersubject overlap is found in the core of the optic radiations and conversely high intersubject spatial variability occurs in the peripheries.

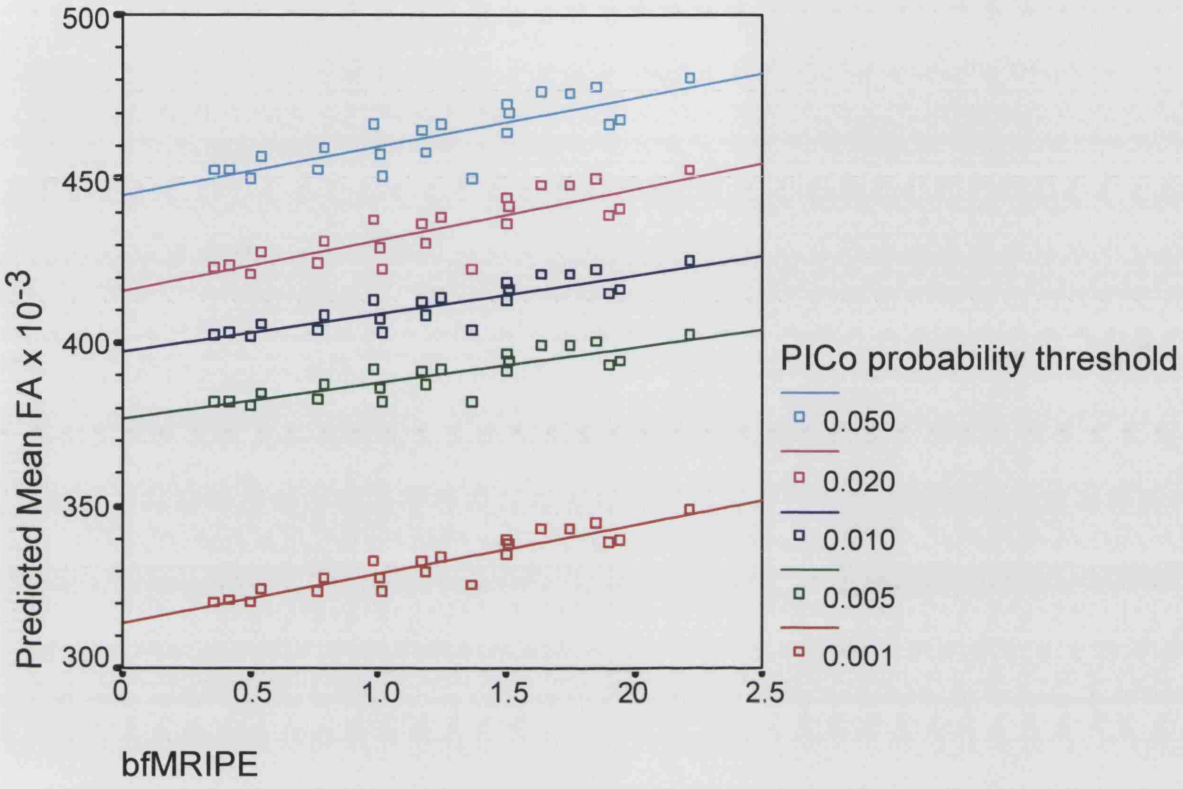

Figure 5.11. Plots of the predicted mean FA against the average fMRI response from both eyes (bfMRIPE) are displayed for each PICo threshold. There is a positive relationship between increasing FA and increasing fMRI response noticeable at all thresholds. There does not appear to be any difference in the regression gradients between thresholds.

5.2.4 Discussion

We have demonstrated a relationship between markers of neural activity within the visual cortex and markers of neural structure within the subserving optic radiations. The mean FA values of the estimated tracts correlate well with the degree of fMRI activity. The number of suprathreshold voxels and the normalized tract volumes (both markers of spatial extent of function/structure) make no significant contributions. Structure-function relationships exist at many spatial scales across different levels of brain organization that range from synapses to neuronal populations. A detailed

knowledge of these relationships is not possible because of the brain's complexity but certain aspects can be investigated with fMRI and DTI.

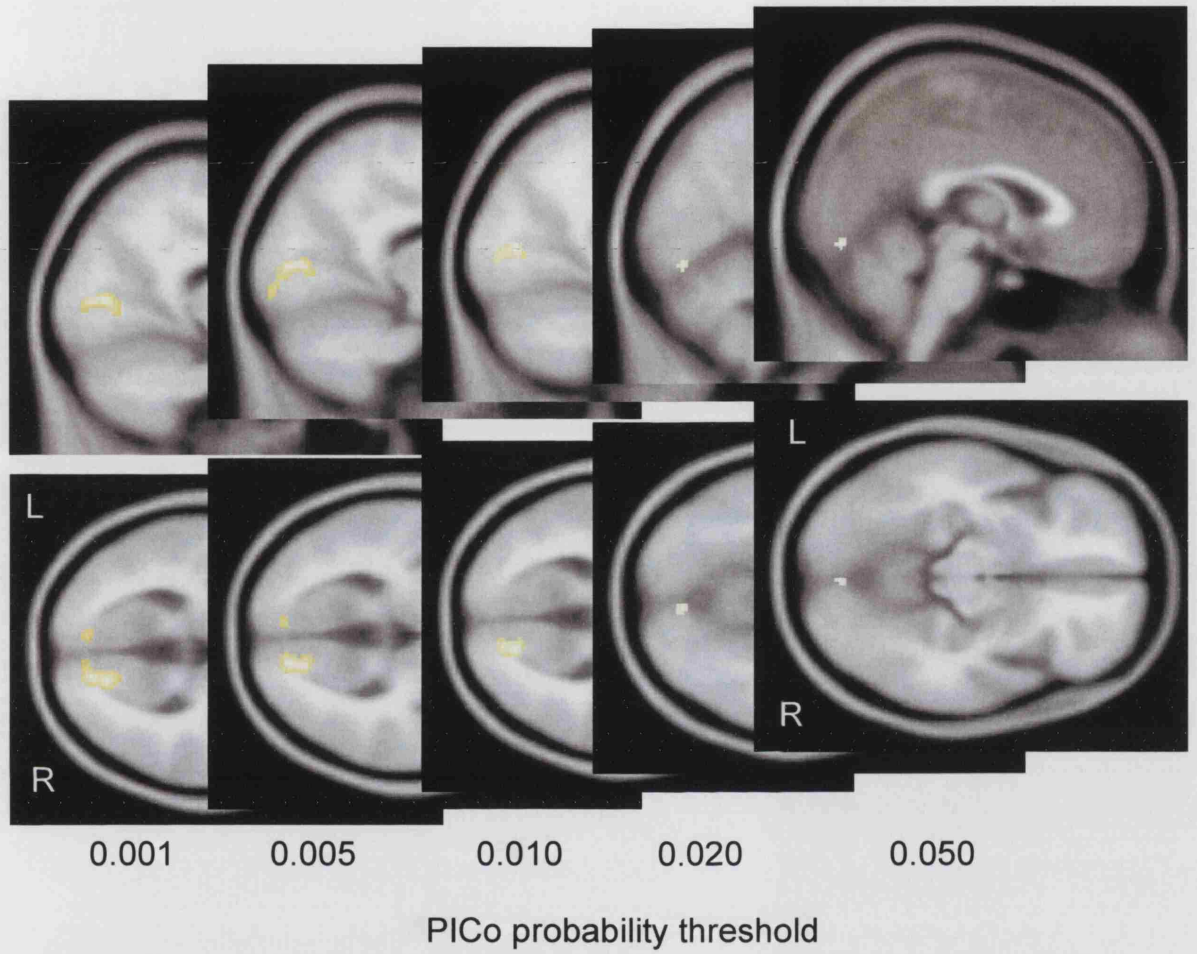

Figure 5.12. SPM99 results for a voxelwise regression analysis between the fMRI contrasts averaged across both eyes and the mean FA for the estimated optic radiations. Significant clusters are seen at all thresholds confined to the visual cortical areas. The peak T scores for each PICo threshold were: 6.25 for 1 at MNI coordinates 16, -80, 8; 4.58 for 5 at coordinates 16, -86, 4; 5.01 for 10 at 18, -80, 6; 4.03 for 20 at 6, -82, -12; 3.84 for 50 at 2, -84, -12. Significance was thresholded at $P<0.001$ and a spatial extent of >10 contiguous suprathreshold voxels.

Knowledge about the precise structural correlates for FA is still incomplete. The major determinants of anisotropy in neural tissue are felt to be axonal membranes (Beaulieu 2002). Myelin might modulate the degree of anisotropy although its role is minor (Beaulieu and Allen 1994; Gulani et al, 2001). Fast axonal transport, the axonal skeleton of neurofilaments and microtubules and local susceptibility-difference-induced gradients are not thought to be important (Beaulieu 2002). In addition, pathological models of axonal degeneration in animals and humans offer some insights and have shown reductions in FA for the affected white matter tracts (Ford et al, 1994; Fraidakis et al,

1998; Pierpaoli et al, 2001; Werring et al, 2000b). Overall the evidence suggests that anisotropic measures of water diffusion in neural tissue are "due to the dense packing of axons and their inherent axonal membranes that hinder water diffusion significantly perpendicular to the long axis of the fibers" (Beaulieu 2002). It was in this context that we applied FA as a measure of white matter architecture.

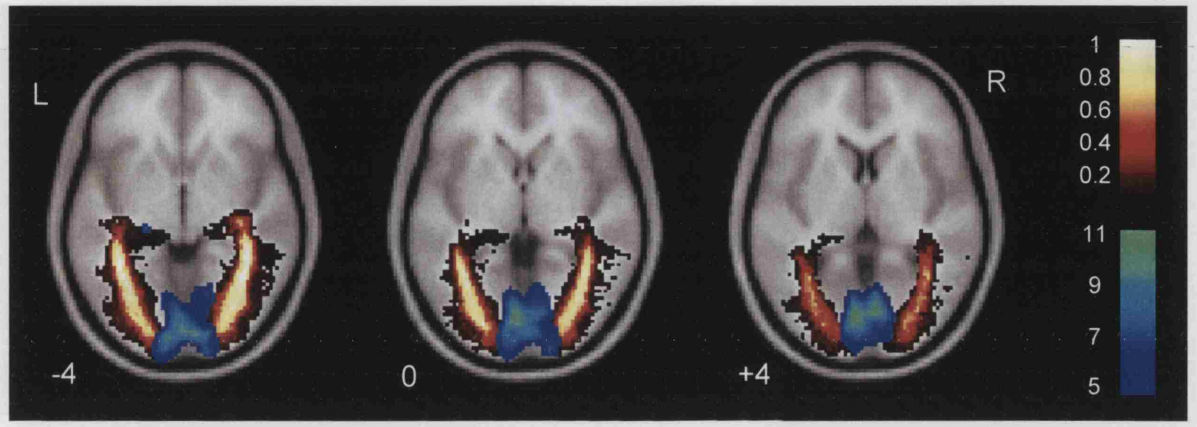

Figure 5.13. Group effects for functional activation and estimated optic radiations (for PICo threshold 0.001) are overlaid onto a structural template. The fMRI activity was derived from a one sample t test for the 22 subjects of the fMRI contrasts averaged for both eyes. The winter (blue) colour scale shows the T scores. Note that there is some left sided lateral geniculate activity detectable. The optic radiations are displayed as spatial variability maps which demonstrate the degree of overlap (shown by the hot colour scale) between subjects for the estimated optic radiations when the PICo threshold was 0.001. A value of 0.8 indicates 80% overlap between subjects. Greater intersubject overlap is noted towards the cores of the estimated optic radiations.

Function-structure relationships within the brain can be investigated partly because parallel distributed processing occurs in a hierarchical fashion. Thus, at the macroscopic level this can manifest as functional segregation that refers to the existence of specialized cortical areas capable of responding to specific input features. Functional integration also occurs and describes the interactions between cortical areas usually mediated by reciprocal cortico-cortical connections (Sporns et al, 2002). The functional dynamics within functionally segregated cortical areas are believed to be constrained by both intrinsic (intracortical) and extrinsic (cortico-cortical) anatomical connections (Passingham et al, 2002). This formed the basis of our study which utilized fMRI and DTI to make population level inferences, both macroscopically and quantitatively, about the relationship between visual cortex function and its extrinsic anatomical connections with the optic radiations.

Our study used PICo to probabilistically demarcate the optic radiations. As with FMT, used in the previous study, this technique relies upon the placement of seed voxels which may influence the nature of the resulting PICo maps. Intersubject variability may be influenced by seed coordinate variability in normalized space. To minimize this, we adopted a new two stage process which reduced the residual mean seed coordinate deviation to around one voxel (figure 5.9). It is unlikely that the final seed coordinate variability influenced the tract derived measures because no statistical relationships were found between them. Therefore true intersubject variability probably contributed to the estimated optic radiation measures.

The derived tract measures (normalized volume and mean FA) provided different types of information depending upon the PICo threshold. It is likely that low PICo thresholds allowed the inclusion of connected voxels with greater partial volume effects from gray matter contributions or from white matter pathways with different orientations. This is consistent with the observation of reduced mean FA with lower thresholds and may also explain why the fMRI response (bfMRIPE) showed weak associations with mean FA at the lowest PICo threshold (table 5.2). Conversely higher PICo thresholds may exclude interesting FA information that would otherwise contribute to fMRI correlations, possibly the case with PICo threshold 0.050 (table 5.3).

Interestingly, we found larger normalized tract volumes in females compared with males (after correcting for head size). Few studies investigating anatomical gender differences within the optic radiations have been performed. Good *et al.* however, used voxel based morphometry to investigate regional differences in brain structure (from high resolution T1 weighted MRI) in 465 people (Good et al, 2001). They reported evidence for greater white matter volume and concentration within the optic radiations in females which is consistent with our findings.

By averaging left and right sides for both the optic radiation measures and the SPM derived fMRI contrasts we maximized our ability to detect a function-structure relationship. This was because the

visual pathways from each eye are shared between left and right optic radiations as well as visual cortices. Therefore focusing upon one side only (e.g. left optic radiation versus left eye stimulation) would introduce contralateral functional or structural confounds. A future approach could be to perform hemi-field visual stimulation to target the contralateral optic radiation and corresponding visual cortex.

In summary, we have demonstrated a macroscopic relationship between MR markers of function and structure for the posterior visual pathways. Higher FA within the optic radiations is associated with a greater BOLD response within the visual cortex following visual stimulation. Although this is a novel finding, it is nevertheless consistent with the idea that the dynamics of functionally segregated cortical areas are constrained by the anatomical characteristics of the underlying subserving white matter tracts. Future developments could aim to investigate anatomical and effective connectivities between cortical regions and also determine the effects of pathological models of visual, sensorimotor and cognitive systems on function-structure relationships. With this in mind we performed a pilot study, with a small group of seven patients who were scanned one year after optic neuritis and compared their posterior visual function-structure relationships with seven controls.

5.3 Function-structure relationships of the posterior visual pathways following optic neuritis

5.3.1 Introduction

The previous study reports novel correlations between measures of function and structure in the visual pathways of normal controls. In an exploratory follow up study, described in this section, the techniques developed during the previous study were applied to a small group of patients who were studied one year after acute optic neuritis. This was felt to be of interest partly because previous work has demonstrated some evidence for reduced anatomical connectivity within the optic

radiations, one year after optic neuritis (Ciccarelli et al, 2005). These patients were therefore investigated to determine how the function-structure relationships of their posterior visual pathways differed from those of normal controls.

5.3.2 Methods

5.3.2.1 Subjects

Seven patients (mean age 37.3 years, SD 9.4, all women, 3 left and 4 right affected side) 1 year after isolated optic neuritis and 7 controls (mean age 27.6 SD 4.3, all women) were recruited.

5.3.2.2 MRI Protocol

All subjects underwent fMRI and DTI scanning as described in section 5.2.2.2.

5.3.2.3 FMRI Analysis

SPM99 (Wellcome Department of Cognitive Neurology, London, UK) was used. Each fMRI time series was realigned, normalized to a standard stereotactic space (defined by the Montreal Neurological Institute (MNI)) and smoothed (8mm isotropic Gaussian kernel). The general linear model (Friston et al, 1995) was implemented to determine the main effect of the photic stimulation paradigm, with realignment parameters entered as covariates of no interest. For each time series a fixed effects analysis was performed to derive the contrast image that represented the fMRI response to photic stimulation. The control contrast images were regrouped to match the affected and fellow sides in the patient group (i.e. 3 left sided and 4 right sided stimulation control derived contrasts were chosen to match the affected eyes in the patient group).

5.3.2.4 DTI and DTI Tractography Analysis

This was performed with similar principles to those described in 5.2.2.4. The aims were to derive two structural measures for each optic radiation – the volume and average FA – by using the PICo algorithm.

Seed voxel placement - This was conducted again using a two stage process. Before this, every subject's b0 images had been normalized to the SPM99 default EPI template in MNI space to generate a b0_sn3d.mat (individual normalization parameter estimate) files (see 5.1.2.4). During the first stage, seed voxels for left and right optic radiations were chosen by a rater on the native FA images of the control subjects using the anatomical guidelines described in 5.1.2.3 (Ciccarelli et al, 2003a). These native seed coordinates were transformed into normalized b0 space (normalized first stage) and then averaged across the controls to provide two coordinates, one for each side. The reason for using b0 normalization rather than FA normalization as in the previous study will be discussed later. These two averaged, normalized seed coordinates were then reverse normalized for every subject (patients and controls) to obtain a second list of native seed coordinates. This second list was used to direct the placement of the seed voxels that would be finally used by PICo on the native images (second stage). Seed voxel placement was assessed by comparing the final normalized seed coordinates between ON patients and controls for each side. Correlation analyses were also performed between the x, y and z coordinates and the structural optic radiation measures (their derivation is described below) to determine whether the variability in seed coordinates contributed to the variability of tract FA or volume.

PICo Analysis – 10,000 PICo iterations were performed (Parker et al, 2003) for each chosen seed voxel on CSF segmented maps (Hadjiprocopis et al, 2003) with an FA threshold of 0.01, as described in the previous study (5.2.2.4). Each resulting PICo map was thresholded at 0.02 (chosen because it seemed to give the strongest function-structure correlations in the previous study) to generate a binary mask from which the mean FA and the connected volume of the estimated tract were

calculated. Paired t-tests showed no differences between left and right sides, which were therefore averaged to produce one tract measure per subject for FA and volume. Independent sample t-tests were conducted between patients and controls for estimated mean tract FA and tract volumes.

5.3.2.5 SPM regression analysis of fMRI results for tract FA

Effect of Group - Two-sample t-tests were conducted in SPM99 for both the affected and fellow eyes versus side matched controls to determine whether controls and ON patients differed in the fMRI response within the visual cortex.

Effect of Age - As the ON patient and control groups were not age matched, preliminary SPM regression models were run to determine whether age was required as a nuisance covariate in the main analysis below. However no effect of age was found for the fMRI response of the stimulation of either eye in patients or controls.

Effect of FA – Two SPM based GLM models were fitted. The first regressed the fMRI derived contrast images for the affected eye with the mean tract FA for ON patients and controls who were entered as fixed factors. Age was not entered as a covariate. The analysis allowed us to compare the function-stucture gradients of the posterior visual pathways between ON patients and controls, by specifying the appropriate contrasts. The second model examined the function-structure relationships of the fellow eyes of ON patients and the side matched controls. Statistical inferences were performed on the resulting SPM(T) maps by correcting for multiple comparisons within a predefined spherical volume (10mm radius) centered in the visual cortex. The data from the most significant suprathresholded voxels were extracted and plotted for affected and fellow eyes.

5.3.3 Results

5.3.3.1 Patients' characteristics

The patients' characteristics are listed below (table 5.5). Six out of seven patients had made excellent visual recoveries.

Patient	1	2	3	4	5	6	7
Affected side	R	L	R	L	R	L	R
Age	30	39	36	54	34	43	25
Sex	F	F	F	F	F	F	F
Visual acuity at one year	6/4	6/5	6/5	6/24	6/5	6/5	6/5

Table 5.5. Patient characteristics. Most patients make a good clinical recovery. All patients are female.

5.3.3.2 Seed voxel placement

Table 5.6 shows the normalized seed coordinates for ON patients and controls. Figure 5.14 demonstrates the residual mean deviations in voxel units for left and right sides within each group. Interestingly, there were significant differences between patients and controls in the seed coordinates for the right optic radiation. We went on to perform correlation analyses (Spearman's rho) between the left or right seed coordinates and the corresponding tract measures (left or right FA or volume) within each subject group and found only one statistically significant correlation. This was between the left y seed coordinate and left optic radiation FA for normal controls ($p=0.039$) but may have been a type I error resulting from multiple comparisons as, in total, 24 correlations were performed. The mean residual deviations themselves are within 1-2 voxels.

		Left Optic Radiation			Right Optic Radiation		
		x	y	z	x	y	z
ON patients	Mean	20.64	42.64	22.00	58.29	42.57	23.07
	SD	0.48	0.48	0.58	0.76	0.53	0.61
Controls	Mean	20.36	43.14	22.14	59.14	44.52	22.17
	SD	0.94	0.85	0.85	0.38	0.77	0.71
T Test	P value	0.489	0.200	0.720	0.020*	0.001*	0.025*

Table 5.6. Normalized seed coordinates for ON patients and controls in MNI voxel coordinate space. SD = standard deviation. There were 7 patients and 7 controls. Although the seed voxels for the right optic radiations were significantly different between the two groups, this did not affect the subsequently derived FA tract measures (discussed in paragraph above). Voxel size is 2x2x2 mm.

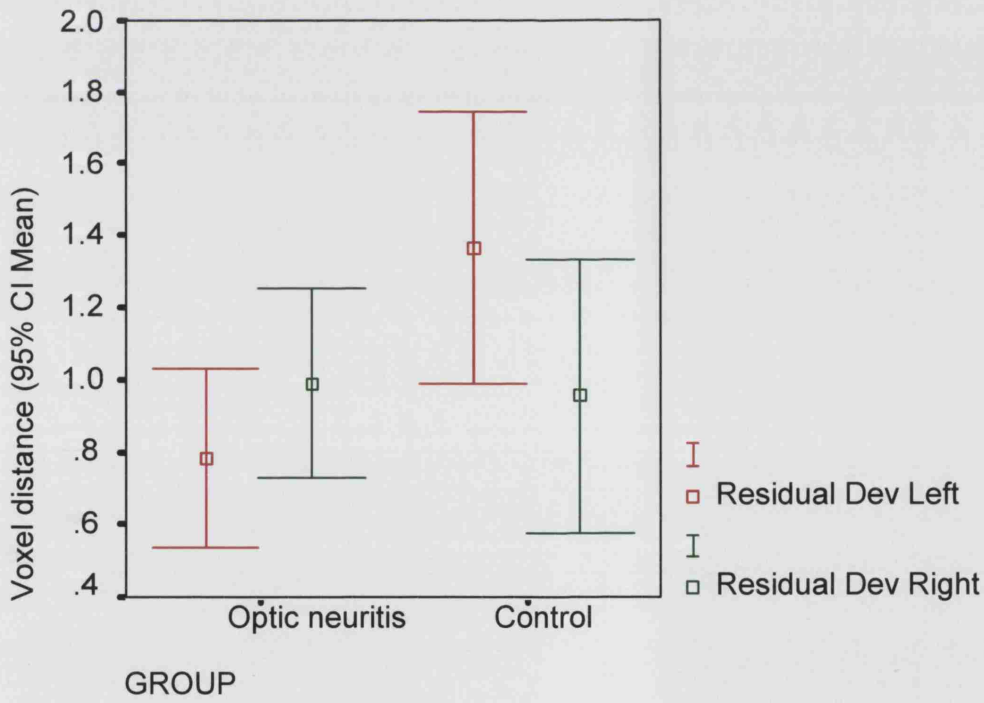

Figure 5.14. Residual mean deviations for seed voxel coordinates are kept between one and two voxel units for each sub group.

5.3.3.3 Estimated tract measures (FA and volume)

		Mean FA (of left and right ORs) x 10^{-3}	Mean volume (of left and right ORs) cm^{-3}
ON Patients	Mean	406.02	1.40
	SE	8.85	0.13
Controls	Mean	435.93	1.90
	SE	8.97	0.10
P value (Patients vs Controls)		p=0.035*	p=0.01*

Table 5.7. The mean FA and volumes (averaged between left and right sides) are shown for ON patients and controls. There were no significant differences between left and right measures of FA and volume in patients and in controls. Controls are shown to have higher FA and larger optic radiation volumes than the ON patients. The OR volumes have been estimated at a PICo threshold of 0.020 (see previous study). SE = standard error of the mean. OR = optic radiation.

The table above demonstrates that controls tend to have higher mean FA values and volumes for their optic radiations than the ON patients. These results support previous work that has investigated anatomical connectivity within the optic radiations following optic neuritis (Ciccarelli et al, 2002). The volumes calculated for the current study are in native space i.e. are unnormalized.

5.3.3.4 SPM regression analysis of fMRI data for tract FA

There were no differences between ON patients and controls in the overall fMRI response within the visual cortex.

5.3.3.4.1 Affected eye (ON patients vs controls)

There was a tendency towards a relationship between tract FA and fMRI response within the visual cortex in both patients (p=0.078) and in controls (p=0.059) after correcting for multiple

comparisons. A higher fMRI response was weakly associated with greater tract FA. There was no difference in the function-structure gradients between ON patients and controls. These results are illustrated in figure 5.15.

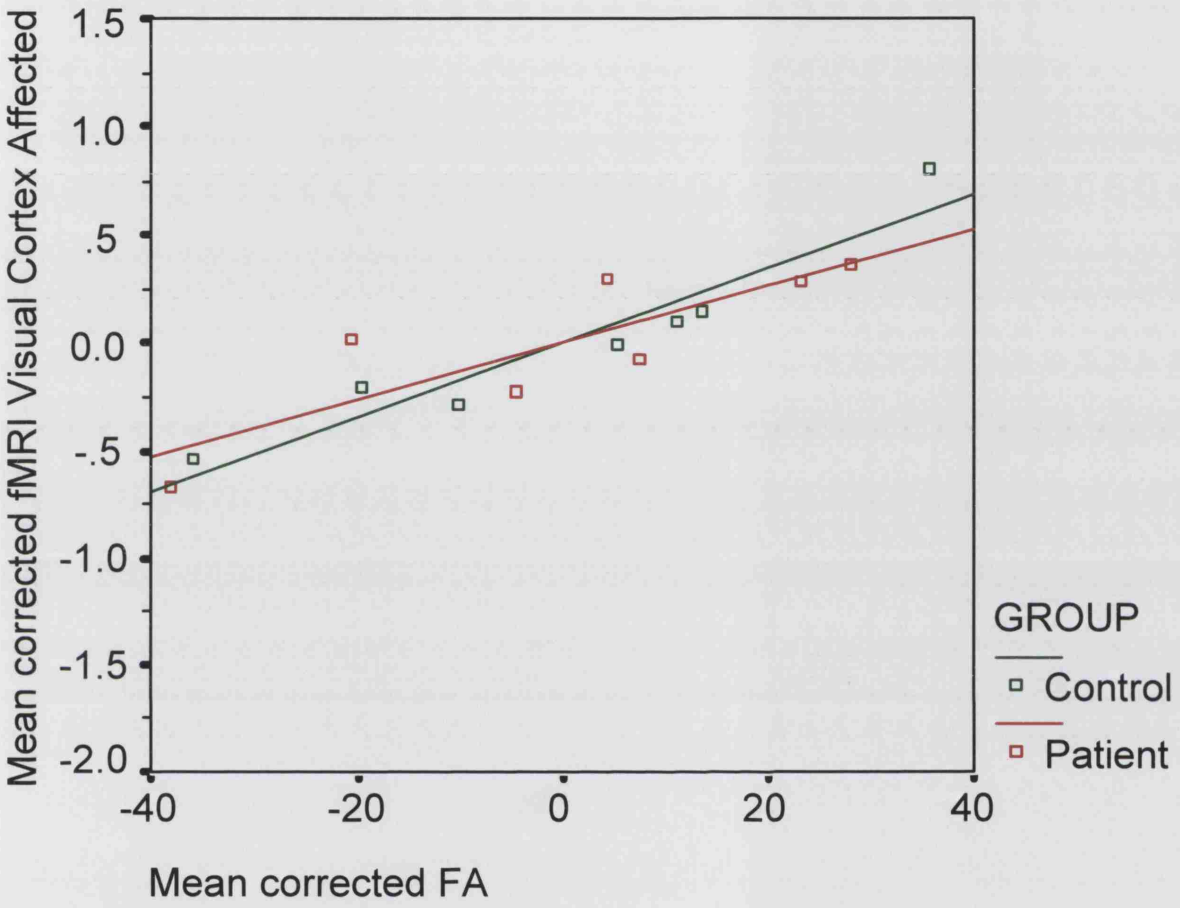

Figure 5.15. The fMRI response of the affected eye (raw adjusted fMRI parameter estimate) at MNI coordinate [0,-78,-10] within the visual cortex is plotted against optic radiation FA ($x10^{-3}$) for patients and side matched controls. There is weak evidence for a function-structure gradient in patients (P=0.078) and in controls (P=0.059) but no difference between the two.

5.3.3.4.2 Fellow eye (ON patients vs controls)

There was a significant positive correlation between mean tract FA and the fMRI response of the fellow eye for both ON patients (p=0.002) and controls (p=0.02) after correction for multiple comparisons. There was weak evidence (p=0.073) for a difference in the function-structure relationship between patients and controls (see figure 5.16).

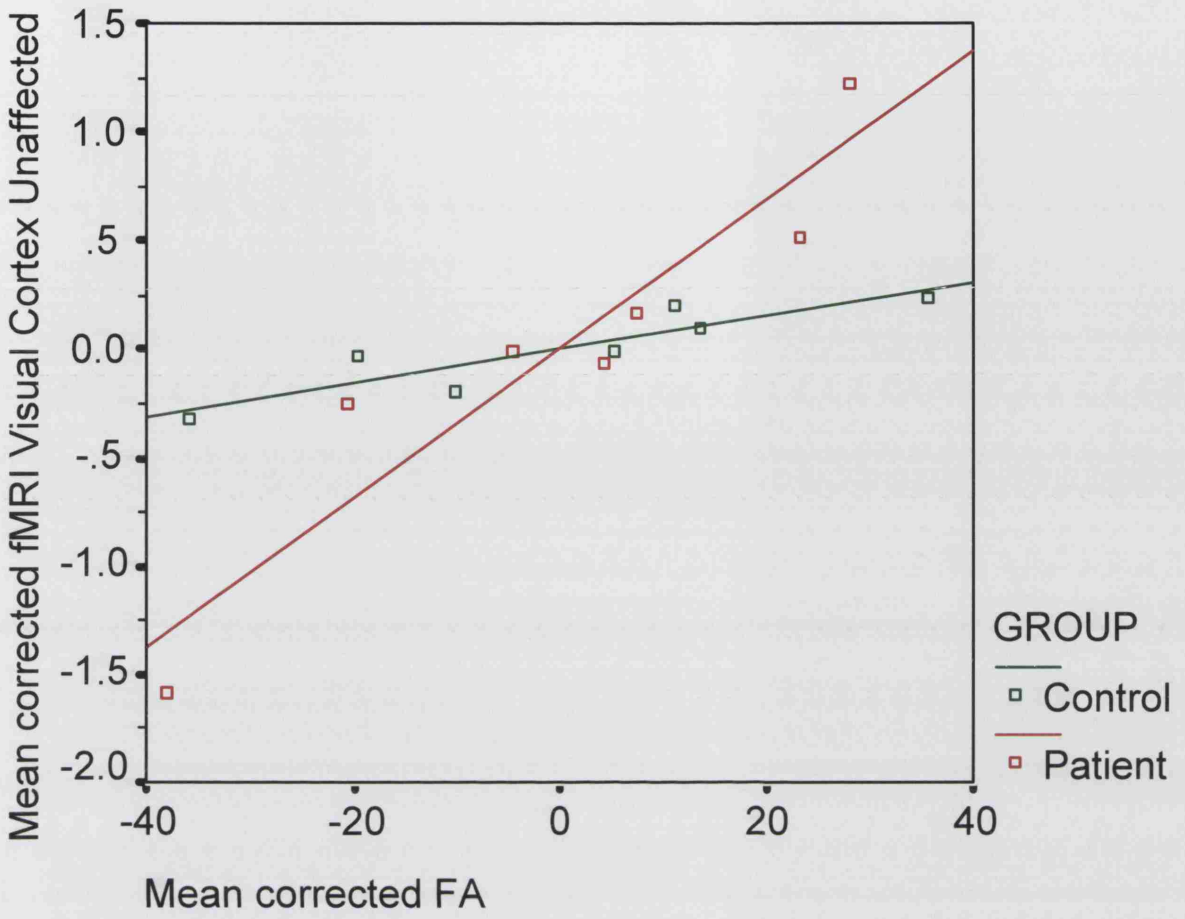

Figure 5.16. The fMRI response of the fellow eye (raw adjusted fMRI parameter estimate) at MNI coordinate [0,-78,0] within the visual cortex is plotted against optic radiation FA ($x10^{-3}$) for patients and side matched controls. There are significant function-structure gradients for both ON patients (p=0.002) and controls (p=0.02) and weak evidence for a difference between the two subject groups (p=0.073). The relationship between function and structure in the posterior visual pathways of patients appears to be steeper than the relationship for controls.

For illustration, the SPM(T) maps are shown for the analysis of the fellow eye in figure 5.17.

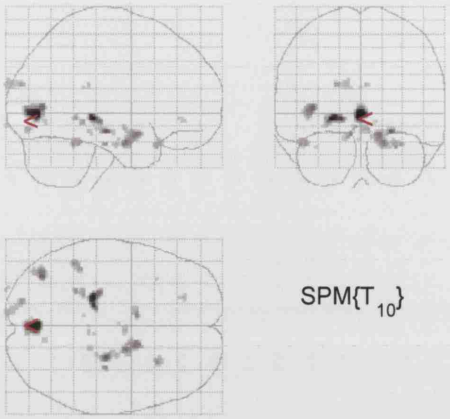

A) Fellow eye fMRI response vs FA for patients

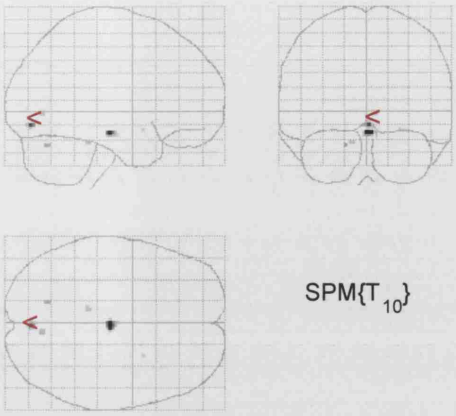

B) Fellow eye fMRI response vs FA for controls

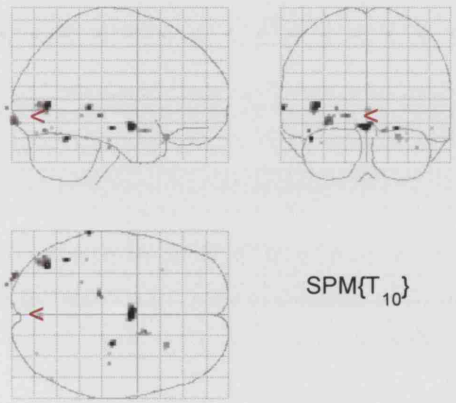

C) Fellow eye fMRI response vs tract FA – patients > controls

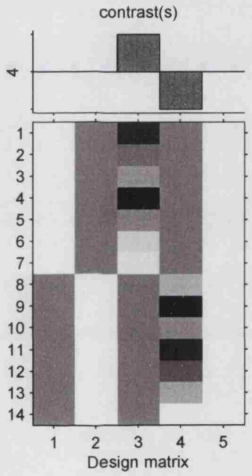

D) Design matrix for SPM regression analysis – fMRI response vs FA.

Figure 5.17. SPM(T) maps were derived for the analysis of the fellow eye thresholded at p<0.001 (uncorrected). Maps are shown for (A) patients, (B) controls and (C) patients>controls. Small volume correction was applied within the visual cortex. The regions outside the visual cortex were not part of the *a priori* hypothesis. (D) shows the design matrix used for the regression analysis and the contrast to demonstrate patients>controls.

5.3.4 Discussion

The results of this study appear to corroborate the findings of the previous work (5.2) by demonstrating function-structure gradients in controls and in patients after optic neuritis. This relationship is most striking when the fellow eye of the patient group is stimulated. Although possible

explanations for these findings will be discussed, it should be noted that this was a small exploratory study which will limit the definitive conclusions that can be made. Before discussing these main findings, other points arising from the study will be highlighted.

We used b0 normalization rather than FA normalization for the registration of the DTI derived maps. In the previous study (5.2), although the FA normalization technique was described, we actually performed b0 normalization, as well, for the PICo maps (results not shown). We found that although there were minor visual differences in the appearances of the normalized tracts, there were no significant differences between b0 and FA normalization for the resulting tract measures of volume and FA. The main visual difference noticed was that FA normalization appeared to result in slightly narrower tracts. This could be explained if FA is considered a surrogate marker for white matter coherence (as an approximate assumption). FA registration techniques would therefore allow closer alignment of white matter structure than b0 registration, although, in practice, this appears to be insignificant.

The optic neuritis group has evidence for lower optic radiation FA and volumes compared with normal controls. This suggests there may have been trans-synaptic axonal degeneration (Evangelou et al, 2001) of the optic radiations following the acute demyelinating episode. This phenomenon has been investigated before by performing SPM analysis of FMT derived VSC (voxel scale connectivity) maps (Ciccarelli et al, 2005) in patients with optic neuritis resulting in similar findings. However in our group, 3 out of the 7 patients possessed lesions within each optic radiation whilst one patient had only one optic radiation that was affected by lesions. This raises the possibility of local neuronal transection causing the presumed optic radiation degeneration. To investigate this, we conducted a repeated measures ANOVA analysis (for the patient group with side as the repeated measure) to examine the presence or absence of lesions using SPSS 11.0 (SPSS Inc., Chicago, IL, USA). We found no significant effect for the presence of lesions on the FA of the left ($p=0.120$) or right ($p=0.189$) optic radiations. This makes it more likely that the lower tract FA in the patient group results from

trans-synaptic degenerative changes rather than local, lesion related degeneration. However, the latter possibility cannot be completely excluded because (i) this study was cross-sectional at one year after the acute episode, (ii) the non-significant result described above may have arisen from a type II error due to the low degrees of freedom employed.

The main finding of this study relates to the steep function-structure gradient in the ON group with stimulation of the fellow eye (figure 5.16) compared with controls. One potential explanation for this results from the hypothesis propounded in the previous paragraph. If trans-synaptic degeneration occurs after optic neuritis, then the involved axonal fibres will originate from the visual pathways of the affected eye. This should result in lower FA of both optic radiations (both are involved because the affected eye pathways decussate) as is observed. However, as a further consequence, the structural integrity of remaining optic radiation fibres, which originate from the fellow eye, will now contribute to the estimated FA of the tract. This phenomenon would result in a stronger quantitative function-structure relationship when the fMRI response of the fellow eye is measured. In essence, the true function-structure gradient of the posterior visual pathways for the fellow eye has been 'unmasked' by the degeneration of the axons that constituted the affected eye's visual pathways.

A further corollary of trans-synaptic degeneration is that fMRI plasticity within the visual cortex may account for the function-structure gradient of the affected eye being similar between patients and controls. Contingent upon the previous paragraph's hypothesis, one may expect a shallower function-structure gradient for the affected eye of optic neuritis patients compared with controls. However, figure 5.15 shows that the patient and control estimated function-structure gradients are very similar, although visually the patient line is slightly less steep than the control line. This similarity could be explained by an adaptive reorganization of the fMRI response strength within the visual cortex for the patient group which may be stimulated by the presence of degenerating optic radiation axons from the affected eye in an attempt to maintain visual function.

It should be noted that the explanation posited above is hypothetical and based upon the available results in this exploratory study. The low subject numbers and cross-sectional nature of this study naturally indicate that more comprehensive investigations are required in the future to explore the ideas that have been discussed. Nevertheless, we hope that the potential usefulness of combining structural and functional information has been demonstrated in helping to understand brain dynamics in both normal health and pathology.

5.4 References

Alexander, DC, Pierpaoli, C, Basser, PJ, and Gee, JC. Spatial transformations of diffusion tensor magnetic resonance images. *IEEE Trans.Med.Imaging.* 2001. **20**(11), 1131-9.

Ashburner, J and Friston, KJ. Voxel-based morphometry--the methods. *Neuroimage.* 2000. **11**(6 Pt 1), 805-21.

Basser, PJ, Mattiello, J, and LeBihan, D. Estimation of the effective self-diffusion tensor from the NMR spin echo. *J.Magn Reson.B.* 1994. **103**(3), 247-54.

Basser, PJ, Pajevic, S, Pierpaoli, C, Duda, J, and Aldroubi, A. In vivo fiber tractography using DT-MRI data. *Magn Reson.Med.* 2000. **44**(4), 625-32.

Basser, PJ and Pierpaoli, C. Microstructural and physiological features of tissues elucidated by quantitative-diffusion-tensor MRI. *J.Magn Reson.B.* 1996. **111**(3), 209-19.

Beaulieu, C. The basis of anisotropic water diffusion in the nervous system - a technical review. *NMR Biomed.* 2002. **15**(7-8), 435-55.

Beaulieu, C and Allen, PS. Determinants of anisotropic water diffusion in nerves. *Magn Reson.Med.* 1994. **31**(4), 394-400.

Behrens, TE, Johansen-Berg, H, Woolrich, MW, Smith, SM, Wheeler-Kingshott, CA, Boulby, PA, Barker, GJ, Sillery, EL, Sheehan, K, Ciccarelli, O, Thompson, AJ, Brady, JM, and Matthews, PM. Non-invasive mapping of connections between human thalamus and cortex using diffusion imaging. *Nat.Neurosci.* 2003. **6**(7), 750-7.

Blake, R and Logothetis, NK. Visual competition. *Nat.Rev.Neurosci.* 2002. **3**(1), 13-21.

Brodal, A. Descending Supraspinal Pathways. In: Brodal, A. Neurological Anatomy in relation to Clinical Medicine. Oxford; Oxford University Press, 1981: 180-293.

Burgel, U, Schormann, T, Schleicher, A, and Zilles, K. Mapping of histologically identified long fiber tracts in human cerebral hemispheres to the MRI volume of a reference brain: position and spatial variability of the optic radiation. *Neuroimage.* 1999. **10**(5), 489-99.

Ciccarelli, O, Hickman, SJ, Toosy, AT, Parker, GJM, Wheeler-Kingshott, CA, Barker, GJ, Miller, DH, and Thompson, AJ. Group connectivity maps of optic radiations after isolated optic neuritis. *7th Annual Meeting ACTRIMS, 18th Congress ECTRIMS. Multiple Sclerosis* 2002. **8 (Suppl 1),** S2.

Ciccarelli, O, Parker, GJ, Toosy, AT, Wheeler-Kingshott, CA, Barker, GJ, Boulby, PA, Miller, DH, and Thompson, AJ. From diffusion tractography to quantitative white matter tract measures: a reproducibility study. *Neuroimage.* 2003a. **18**(2), 348-59.

Ciccarelli, O, Toosy, AT, Hickman, SJ, Parker, GJ, Wheeler-Kingshott, CA, Miller, DH, and Thompson, AJ. Optic radiation changes after optic neuritis detected by tractography-based group mapping. *Hum Brain Mapp.* 2005.

Ciccarelli, O, Toosy, AT, Parker, GJ, Wheeler-Kingshott, CA, Barker, GJ, Miller, DH, and Thompson, AJ. Diffusion tractography based group mapping of major white-matter pathways in the human brain. *Neuroimage.* 2003b.

Conturo, TE, Lori, NF, Cull, TS, Akbudak, E, Snyder, AZ, Shimony, JS, McKinstry, RC, Burton, H, and Raichle, ME. Tracking neuronal fiber pathways in the living human brain. *Proc.Natl.Acad.Sci.U.S.A.* 1999. **96**(18), 10422-7.

de Lacoste, MC, Kirkpatrick, JB, and Ross, ED. Topography of the human corpus callosum. *J Neuropathol.Exp.Neurol.* 1985. **44**(6), 578-91.

Evangelou, N, Konz, D, Esiri, MM, Smith, S, Palace, J, and Matthews, PM. Size-selective neuronal changes in the anterior optic pathways suggest a differential susceptibility to injury in multiple sclerosis. *Brain.* 2001. **124**(Pt 9), 1813-20.

Farzaneh, F, Riederer, SJ, and Pelc, NJ. Analysis of T2 limitations and off-resonance effects on spatial resolution and artifacts in echo-planar imaging. *Magn Reson.Med.* 1990. **14**(1), 123-39.

Foong, J, Maier, M, Clark, CA, Barker, GJ, Miller, DH, and Ron, MA. Neuropathological abnormalities of the corpus callosum in schizophrenia: a diffusion tensor imaging study. *J.Neurol.Neurosurg.Psychiatry.* 2000. **68**(2), 242-4.

Ford, JC, Hackney, DB, Alsop, DC, Jara, H, Joseph, PM, Hand, CM, and Black, P. MRI characterization of diffusion coefficients in a rat spinal cord injury model. *Magn Reson.Med.* 1994. **31**(5), 488-94.

Fraidakis, M, Klason, T, Cheng, H, Olson, L, and Spenger, C. High-resolution MRI of intact and transected rat spinal cord. *Exp.Neurol.* 1998. **153**(2), 299-312.

Friston, KJ, Holmes, AP, Worsley, KJ, Poline, JB, Frith, CD, and Frackowiak, RSJ. Statistical parametric maps in functional imaging: A general linear approach. *Hum.Brain Mapp.* 1995. **2**, 189-210.

Good, CD, Johnsrude, I, Ashburner, J, Henson, RN, Friston, KJ, and Frackowiak, RS. Cerebral asymmetry and the effects of sex and handedness on brain structure: a voxel-based morphometric analysis of 465 normal adult human brains. *Neuroimage.* 2001. **14**(3), 685-700.

Gulani, V, Webb, AG, Duncan, ID, and Lauterbur, PC. Apparent diffusion tensor measurements in myelin-deficient rat spinal cords. *Magn Reson.Med.* 2001. **45**(2), 191-5.

Hadjiprocopis, A, Rashid, W, and Tofts, PS. Segmentation of T2-weighted MRI using an ensemble of neural network and clustering experts. *Proc Intl Soc Mag Reson Med.* 2003. **11**, 3504.

Hasan, KM, Basser, PJ, Parker, DL, and Alexander, AL. Analytical computation of the eigenvalues and eigenvectors in dt-mri. *J.Magn Reson.* 2001. **152**(1), 41-7.

Hellier, P, Ashburner, J, Corouge, I, Barillot, C, and Friston, KJ. Intersubject registration of functional and anatomical data using SPM. *Proceedings of the 5th International Conference for Medical Image Computing and Computer-Assisted Intervention.* 2002. **2,** 590-597.

Jane, JA, Yashon, D, DeMyer, W, and Bucy, PC. The contribution of the precentral gyrus to the pyramidal tract of man. *J Neurosurg.* 1967. **26**(2), 244-8.

Jones, DK, Griffin, LD, Alexander, DC, Catani, M, Horsfield, MA, Howard, R, and Williams, SC. Spatial normalization and averaging of diffusion tensor MRI data sets. *Neuroimage.* 2002. **17**(2), 592-617.

Jones, DK, Horsfield, MA, and Simmons, A. Optimal strategies for measuring diffusion in anisotropic systems by magnetic resonance imaging. *Magn Reson.Med.* 1999a. **42**(3), 515-25.

Jones, DK, Lythgoe, D, Horsfield, MA, Simmons, A, Williams, SC, and Markus, HS. Characterization of white matter damage in ischemic leukoaraiosis with diffusion tensor MRI. *Stroke.* 1999b. **30**(2), 393-7.

Jones, EG. Making brain connections: neuroanatomy and the work of TPS Powell, 1923-1996. *Annu.Rev.Neurosci.* 1999. **22**, 49-103.

Kwong, KK, Belliveau, JW, Chesler, DA, Goldberg, IE, Weisskoff, RM, Poncelet, BP, Kennedy, DN, Hoppel, BE, Cohen, MS, Turner, R, and . Dynamic magnetic resonance imaging of human brain activity during primary sensory stimulation. *Proc.Natl.Acad.Sci.U.S.A.* 1992. **89**(12), 5675-9.

Logothetis, NK, Pauls, J, Augath, M, Trinath, T, and Oeltermann, A. Neurophysiological investigation of the basis of the fMRI signal. *Nature.* 2001. **412**(6843), 150-7.

Mori, S, Crain, BJ, Chacko, VP, and van Zijl, PC. Three-dimensional tracking of axonal projections in the brain by magnetic resonance imaging. *Ann.Neurol.* 1999. **45**(2), 265-9.

Mori, S, Kaufmann, WE, Davatzikos, C, Stieltjes, B, Amodei, L, Fredericksen, K, Pearlson, GD, Melhem, ER, Solaiyappan, M, Raymond, GV, Moser, HW, and van Zijl, PC. Imaging cortical association tracts in the human brain using diffusion-tensor-based axonal tracking. *Magn Reson.Med.* 2002. **47**(2), 215-23.

Mori, S, Kaufmann, WE, Pearlson, GD, Crain, BJ, Stieltjes, B, Solaiyappan, M, and van Zijl, PC. In vivo visualization of human neural pathways by magnetic resonance imaging. *Ann.Neurol.* 2000. **47**(3), 412-4.

Ogawa, S, Lee, TM, Kay, AR, and Tank, DW. Brain magnetic resonance imaging with contrast dependent on blood oxygenation. *Proc.Natl.Acad.Sci.U.S.A.* 1990. **87**(24), 9868-72.

Ogawa, S, Tank, DW, Menon, R, Ellermann, JM, Kim, SG, Merkle, H, and Ugurbil, K. Intrinsic signal changes accompanying sensory stimulation: functional brain mapping with magnetic resonance imaging. *Proc Natl Acad Sci U S A.* 1992. **89**(13), 5951-5.

Parker, GJ, Haroon, HA, and Wheeler-Kingshott, CA. A framework for a streamline-based probabilistic index of connectivity (PICo) using a structural interpretation of MRI diffusion measurements. *J Magn Reson Imaging*. 2003. **18**(2), 242-54.

Parker, GJ, Stephan, KE, Barker, GJ, Rowe, JB, MacManus, DG, Wheeler-Kingshott, CA, Ciccarelli, O, Passingham, RE, Spinks, RL, Lemon, RN, and Turner, R. Initial demonstration of in vivo tracing of axonal projections in the macaque brain and comparison with the human brain using diffusion tensor imaging and fast marching tractography. *Neuroimage*. 2002a. **15**(4), 797-809.

Parker, GJ, Wheeler-Kingshott, CA, and Barker, GJ. Estimating distributed anatomical connectivity using fast marching methods and diffusion tensor imaging. *IEEE Trans Med.Imaging*. 2002b. **21**(5), 505-12.

Passingham, RE, Stephan, KE, and Kotter, R. The anatomical basis of functional localization in the cortex. *Nat.Rev.Neurosci.* 2002. **3**(8), 606-16.

Pierpaoli, C, Barnett, A, Pajevic, S, Chen, R, Penix, LR, Virta, A, and Basser, P. Water diffusion changes in Wallerian degeneration and their dependence on white matter architecture. *Neuroimage*. 2001. **13**(6 Pt 1), 1174-85.

Pierpaoli, C and Basser, PJ. Toward a quantitative assessment of diffusion anisotropy. *Magn Reson.Med.* 1996. **36**(6), 893-906.

Pierpaoli, C, Jezzard, P, Basser, PJ, Barnett, A, and Di Chiro, G. Diffusion tensor MR imaging of the human brain. *Radiology*. 1996. **201**(3), 637-48.

Poupon, C, Clark, CA, Frouin, V, Regis, J, Bloch, I, Le Bihan, D, and Mangin, J. Regularization of diffusion-based direction maps for the tracking of brain white matter fascicles. *Neuroimage.* 2000. **12**(2), 184-95.

Rademacher, J, Burgel, U, Geyer, S, Schormann, T, Schleicher, A, Freund, HJ, and Zilles, K. Variability and asymmetry in the human precentral motor system. A cytoarchitectonic and myeloarchitectonic brain mapping study. *Brain.* 2001. **124**(Pt 11), 2232-58.

Rombouts, SA, Barkhof, F, Sprenger, M, Valk, J, and Scheltens, P. The functional basis of ocular dominance: functional MRI (fMRI) findings. *Neurosci.Lett.* 1996. **221**(1), 1-4.

Ross, ED. Localization of the pyramidal tract in the internal capsule by whole brain dissection. *Neurology.* 1980. **30**(1), 59-64.

Sporns, O, Tononi, G, and Edelman, G. Theoretical neuroanatomy and the connectivity of the cerebral cortex. *Behav.Brain Res.* 2002. **135**(1-2), 69.

Steel, RM, Bastin, ME, McConnell, S, Marshall, I, Cunningham-Owens, DG, Lawrie, SM, Johnstone, EC, and Best, JJ. Diffusion tensor imaging (DTI) and proton magnetic resonance spectroscopy (1H MRS) in schizophrenic subjects and normal controls. *Psychiatry Res.* 2001. **106**(3), 161-70.

Symms, MR, Barker, GJ, Franconi, F, and Clark, CA. Correction of eddy-current distortions in diffusion-weighted echo-planar images with a two-dimensional registration technique. *Proceedings of the International Society for Magnetic Resonance in Medicine.* 1997. 1723.

Watkins, KE, Paus, T, Lerch, JP, Zijdenbos, A, Collins, DL, Neelin, P, Taylor, J, Worsley, KJ, and Evans, AC. Structural asymmetries in the human brain: a voxel-based statistical analysis of 142 MRI scans. *Cereb.Cortex.* 2001. **11**(9), 868-77.

Werring, DJ, Bullmore, ET, Toosy, AT, Miller, DH, Barker, GJ, MacManus, DG, Brammer, MJ, Giampietro, VP, Brusa, A, Brex, PA, Moseley, IF, Plant, GT, McDonald, WI, and Thompson, AJ. Recovery from optic neuritis is associated with a change in the distribution of cerebral response to visual stimulation: a functional magnetic resonance imaging study. *J.Neurol.Neurosurg.Psychiatry*. 2000a. **68**(4), 441-9.

Werring, DJ, Toosy, AT, Clark, CA, Parker, GJ, Barker, GJ, Miller, DH, and Thompson, AJ. Diffusion tensor imaging can detect and quantify corticospinal tract degeneration after stroke. *J.Neurol.Neurosurg.Psychiatry*. 2000b. **69**(2), 269-72.

Worsley, KJ, Marrett, S, Neelin, P, Vandal, AC, Friston, KJ, and Evans, AC. A unified statistical approach for determining significant signals in images of cerebral activation. *Hum.Brain Mapp.* 1996. **4**, 58-73.

Xu, D, Mori, S, Solaiyappan, M, van Zijl, PC, and Davatzikos, C. A framework for callosal fiber distribution analysis. *Neuroimage*. 2002. **17**(3), 1131-43.

Xue, R, van Zijl, PC, Crain, BJ, Solaiyappan, M, and Mori, S. In vivo three-dimensional reconstruction of rat brain axonal projections by diffusion tensor imaging. *Magn Reson.Med.* 1999. **42**(6), 1123-7.

CHAPTER 6

CONCLUSIONS

This chapter will first summarize the main results and themes of this thesis. It will then outline potential follow up studies to address issues raised in previous chapters. Following this it will discuss the long term importance of exploring both anatomical and functional CNS connectivity.

6.1 Summary of results

The overall aim of this thesis was to apply MR imaging techniques to study structural and functional aspects of CNS damage and recovery. Chapter 3 presented analysis from a longitudinal fMRI study of optic neuritis (ON) patients. This analysis was in fact part of a larger study using several MR modalities on the same recruited patient cohort, for which several analyses have been published (Hickman et al, 2004a; Hickman et al, 2004b; Hickman et al, 2004c). FMRI analysis in this thesis demonstrated differential deactivation behaviour between ON patients and controls and also significant correlations with structural and clinical data especially early after ON insult. By integrating structural optic nerve information with the fMRI data, significant regions were then discovered in higher visual areas at baseline, very likely to contribute to clinical function. It was only by modelling aspects of both CNS structure and function that we were able to conclude this. Chapter 4 introduced DTI as a useful MR technique to investigate CNS structure. A clinical DTI study of ALS patients reported differences along the pyramidal tracts between ALS patients and healthy controls for FA and MD, using an ROI based approach.

Evolving applications of DTI were initially explored in chapter 5 with the introduction of DTI tractography. A group mapping technique was developed for three major white matter tracts – the

anterior callosal fibres, the pyramidal tracts and the optic radiations. Average group maps and spatial variability maps were generated for the three tracts, which had been segmented probabilistically, for each individual, using the FMT tractography algorithm. The next study then integrated DTI with fMRI to characterize function-structure relationships within the posterior visual pathways in 22 healthy volunteers. A correlation was found between visual cortex fMRI activation and the FA of the subserving optic radiations. The final study then compared function-structure gradients between healthy volunteers and ON patients, in a small study, to illustrate a potential application of combining DTI and fMRI data in pathological models.

6.2 Future work

This will first concentrate on technical developments and then possible clinical applications to follow up the work in this thesis.

6.2.1 Technical developments

For fMRI, further work on the whole brain acquisition parameters should improve SNR without compromising image resolution. Stimulus presentation paradigms could be developed whereby the presentation system would synchronize with MR acquisition. Biofeedback systems to monitor and control subject performance and attention could also be applied. Event related fMRI paradigms can be used in studies to characterize the haemodynamic response e.g. within the visual cortex after optic neuritis. These would complement epoch based fMRI paradigms which possess greater sensitivity at detecting experimental effects.

For DTI, specialized optic nerve and spinal cord sequences could be developed. Whole brain DTI can also be optimized taking into account multiple tensor fitting and high b-factor diffusion measurements. DTI tractography algorithms can be advanced to tackle intravoxel multiple fibre tract crossing and to provide better estimates of intervoxel connectivity.

6.2.2 Clinical studies

These could focus on the visual system with optic neuritis as a model of functional recovery. Both the anterior and posterior visual pathways can be structurally characterized using DTI and correlated with visual fMRI and clinical function. Statistical modelling could be used to identify the structural contributions from the optic nerve and optic radiations and fMRI contributions to clinical function. The structural contributions may vary in time, with optic nerve structure hypothetically demonstrating greater influence early after optic neuritis onset and optic radiation structure perhaps contributing more later on.

The lateral occipital complexes could be investigated in greater detail with specific paradigms designed to activate them. Other higher order visual processing areas could also be explored and event-related designs would determine morphological differences from controls for the haemodynamic response in these areas after optic neuritis.

Longer term directions could focus on brain connectivity and determine how different cortical and subcortical areas functionally interact and how this is related to their structural connections. The next section will outline how and why a greater understanding of brain connectivity is considered important.

6.3 Understanding brain connectivity

The concepts of functional segregation and integration were introduced in chapter 1. These two organizational principles exhibit an apparent dichotomy. Functional neuroimaging studies generally contribute to functional segregation. To achieve a better appreciation of brain function, however, principles of functional integration need to be incorporated. This will provide greater insight into brain function in terms of information flow within neuronal networks between dynamically

interacting regions. There has been increasing interest in this field, boosted by recent advances in understanding how various cortical regions are anatomically and functionally connected. The following sections will discuss our present understanding of brain connectivity. The interested reader may refer to several recent reviews which form the basis of this discussion (Bullmore et al, 2004; Lee et al, 2003; Ramnani et al, 2004; Sporns et al, 2004)

Three types of connectivity have been described. *Anatomical connectivity* relates to the physical nature of inter-regional connections. The other two, *functional* and *effective connectivity,* are related to information transmission and integration within brain networks and are predicated on the premise of correlated patterns of brain activity between functionally interacting regions.

6.3.1 Anatomical connectivity

Anatomical connectivity has been defined as the set of physical or structural connections linking neuronal units within a network at a given time (Sporns 2002). It refers to the connection strengths between different locations within the brain and its nature changes with the spatial scale experimentally investigated. Analyses at the microscopic level focus on axonal architecture, dendritic arborization and synaptic distribution. Analyses of intra-areal patterns of connections involve "connection bundles" linking local neuronal populations (neuronal groups or columns). Macroscopic analyses of large-scale connection patterns focus on pathways linking segregated areas of the brain (i.e. extrinsic cortico-cortical connections) (Sporns 2002).

Anatomical connectivity is generally influenced by: 1) *Structural plasticity* – which alludes to interactions between gene expression, cell migration and neurogenesis in the developing brain, and 2) *Synaptic plasticity* – the activity-dependent modelling of the pattern and strength of synaptic connections. This plasticity endures through life (Friston 2004).

The cat's visual cortices serve as an example. They are organized hierarchically with reciprocal (forward and backward) extrinsic cortico-cortical connections that exhibit microstructural asymmetry. Forward connections (from low to high levels) tend to be topographically organized, sparsely collateralize and terminate in cortical layer IV. Backward connections show diffuse topography, frequently bifurcate and terminate in supragranular layers. They also terminate across more hierarchical levels than forward connections and are more abundant. Macroscopically, backward connections are more divergent (Friston 2004; Salin and Bullier 1995).

6.3.1.1 Graph theory and network analysis

Various mathematical disciplines have provided valuable insights into the structural organization of cortical networks. Studies have investigated large-scale connection patterns in the rat (Burns and Young 2000), cat (Scannell et al, 1995; Scannell et al, 1999) and monkey (Felleman and Van Essen 1991; Passingham et al, 2002), but little data have been available for humans (Crick and Jones 1993). Mathematical techniques, used to model connection topology, include multivariate methods and graph theoretical approaches. The latter will be discussed below as it is quite promising at describing large-scale (macroscopic) connectivity.

Graph theory considers networks as sets of *nodes* (also called hubs or vertices) linked by *edges* (also called connections). The *degree* of a node is its total number of afferent and efferent edges. A *path* is an ordered sequence of edges and nodes, linking a source node to a target node. The *path length* is the number of distinct edges in the path. The shortest path length between source and target node is the *distance*. The *characteristic path length (L)* is the global mean of all distances in a network. Shorter characteristic path lengths indicate "closer" nodes within a network, on average. The *clustering coefficient* (or *cluster index*, *C*) is the number of connections divided by the number of possible connections for each node's neighbours averaged for the whole graph. It ranges between 0 and 1 and captures the degree to which a node's neighbours connect to each other, forming a local cluster or "clique".

Certain topological classes exist for graphs (figure 6.1). For *n* nodes and *k* connections, a *random graph* is generated by assigning uniform probability to each connection (figure 6.1a). This is considered a poor approximation to most complex systems. *Small-world networks*, on the other hand, possess very short distances between nodes resulting in high degrees of local clustering (figure 6.1b). They emerge from the combination of ordered lattice-like connections with a small admixture of random links (Watts and Strogatz 1998). Finally there are *scale-free networks*. Nodes within random graphs have similar degrees. However, this homogeneity (single scale) of degree distribution is not followed in nature. Many natural networks follow a power law degree distribution (Barabasi and Albert 1999) possessing many nodes that have a few connections and a few nodes (hubs) that have many connections (figure 6.1c). These scale-free networks are robust to the random deletion of nodes but can be destroyed by targeted attacks on heavily connected hubs.

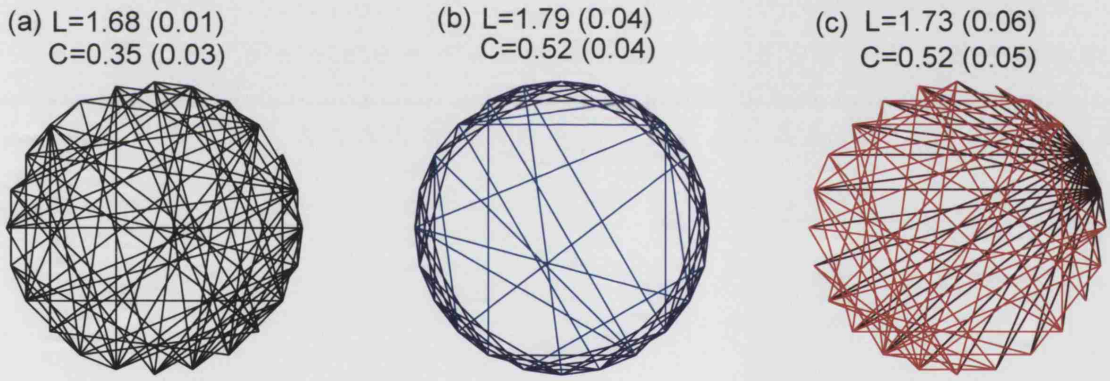

Figure 6.1. Graphs of (a) Random network, (b) Small-world network – most connections are among neighbouring nodes on the dark blue circle, some connections short-cut (light blue) to distant nodes. (c) Scale-free network – most nodes have few connections (red) to other nodes, but some are linked to more than 12 other nodes (black). All networks have 24 nodes and 86 connections. L is the characteristic path length and C is the clustering coefficient. Reprinted from Sporns et al 2004 with permission from Elsevier.

Large-scale connectivity analyses using graph theory have been applied to neuroanatomical data from the cat and monkey. The reported connection patterns have favoured small-world properties with short path lengths and high clustering coefficients (Hilgetag et al, 2000; Sporns et al, 2000b; Sporns and Zwi 2004). These findings do not preclude the existence of scale-free networks with low maximum degrees, which would also prevent the emergence of highly connected hubs. This

possibility is supported by the observed vulnerability of cat and monkey cortical networks to the damage of a few highly connected nodes (Martin et al, 2001).

6.3.1.2 *The use of DTI tractography to investigate structural connectivity*

DTI tractography is considered an exciting and potentially valuable tool for the *in vivo* study of large-scale neural architecture in humans for whom structural connectivity data is lacking (Crick and Jones 1993). Potential uses of DTI tractography were exploited in chapter 5. For example, the DTI tractography algorithms generated *connectivity metrics* which expressed levels of confidence between seed voxels and the resulting projections. These were used to probabilistically segment major white matter pathways. Other studies have utilized similar features to probabilistically map thalamo-cortical projections (Behrens et al, 2003a).

In spite of its potential value DTI tractography does rely upon certain assumptions and, as a result, has some limitations with its interpretation. Firstly, it assumes that the intravoxel microstructural fibre architecture is well approximated by the principle eigenvector. Consequently, conventional DTI data acquisition and processing may not be able to distinguish more than one population of axonal tracts that are in different orientations within the same voxel. Secondly, it is assumed that intrinsic noise has a negligible effect on the measured principle eigenvector. This has been tackled by quantifying the uncertainty in the principle eigenvector field and determining that it is low within white matter fibres and high within complex fibre structures (e.g. crossing fibres or near grey matter) (Jones 2003). Some linear propagation algorithms (such as PICo) also account for this uncertainty by incorporating it in the generation of PDFs (probability density or distribution functions), that are used to estimate the fibre orientations (Behrens et al, 2003b; Parker et al, 2003). Thirdly, it cannot provide information about cellular level axonal connectivity because this information is averaged within each voxel. Fourthly, afferent and efferent axonal pathways cannot be distinguished.

6.3.1.2.1 *Future diffusion imaging research*

Much DTI research is focussed upon the first assumption and aims to model, with greater accuracy, the complex intravoxel diffusion behaviour of water molecules, especially in situations where multivariate Gaussian model assumptions may break down. There are several potential areas of research.

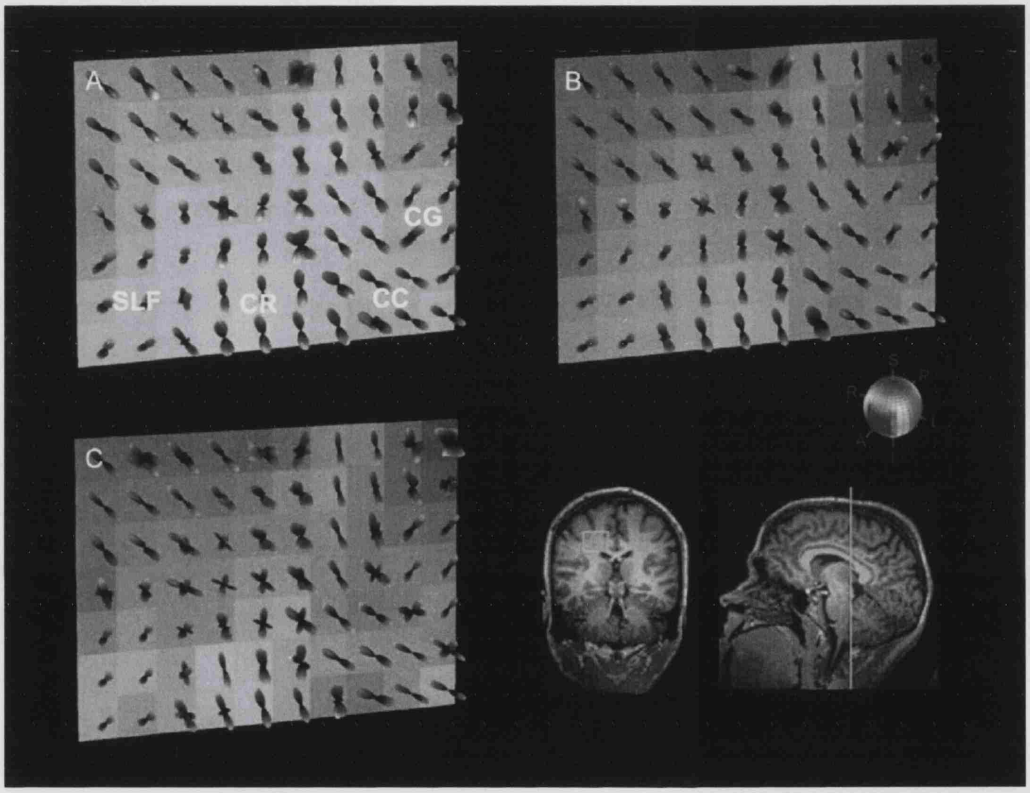

Figure 6.2. Diffusion Q-ball imaging showing three way fibre crossing at the corpus callosum. The region of interest and anteroposterior level are shown in the structural images at bottom right. The region includes the intersection of the corona radiate (CR in blue) with the projections from corpus callsoum (CC in red). Voxels containing intersecting fibers such as between the callosal projections and the corona radiata exhibit multimodal diffusion. Other abbreviations: CG, cingulate gyrus; SLF, superior longitudinal fasciculus. Reprinted from Tuch et al 2004 with permission from Elsevier.

1) Q-space diffusion imaging – Q-space imaging measures the microscopic diffusion function directly without making any assumptions about the nature of the underlying diffusion function. This model-free approach provides a more direct description of the underlying intravoxel microscopic tissue environment. It has been applied to biological tissue *in vitro* (Assaf et al, 2000; Assaf and Cohen 1999) and small animals *in vivo* (King et al, 1994; King et al, 1997). A particular disadvantage is a requirement of the diffusion time, δ to approach zero. This is unfeasible on whole body scanners. Diffusion

spectrum imaging (DSI) is a derivative of q-space imaging and compromises on gradient requirements by using finite but small diffusion times. It samples the three dimensional diffusion function and can resolve complex intravoxel tissue structure (Wiegell et al, 2001). However, its use is hindered by very long acquisition times. More recently, a novel approach with reduced acquisition times, called q-ball imaging (QBI), has been introduced (Tuch et al, 2003; Tuch 2004). This samples the diffusion signal only on a spherical shell, rather than the complete three dimensional Cartesian grid. This also reduces gradient requirements (because only a single spatial frequency is sampled – the radius of the sampling sphere) whilst is able to resolve the angular structure of the diffusion function and, by inference, multi-oriented fibre directions (figure 6.2).

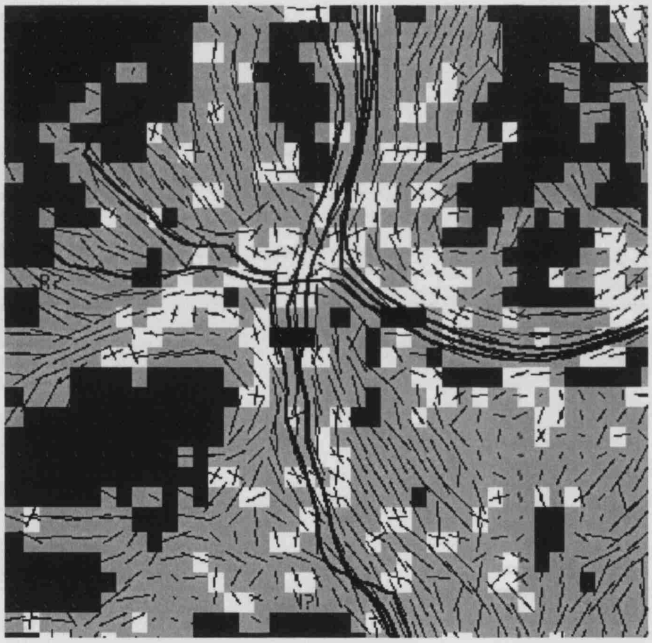

Figure 6.3. A coronal display of the right corpus callosum is shown. Dark grey voxels show single isotropic voxels. Mid grey voxels show single anisotropic voxels and white voxels show two tensors. Two streamline propagations are shown through the crossing fibres (black lines) with the corresponding seed voxels in black. Adapted from Parker and Alexander, 2003.

2) Advances in diffusion tensor modelling – More elaborate models of the diffusion tensor have attempted to resolve intravoxel fibre-crossing confounds. When diffusion behaviour within a voxel is non-Gaussian, it cannot be sufficiently described by a single tensor. Such deviations can be detected by modelling the diffusion behaviour using a set of even numbered *spherical harmonics*. These are an orthogonal set of solutions represented in a spherical co-ordinate system to Laplace's equation, which itself has found importance in many fields of science including electromagnetism, astronomy

and fluid dynamics. Recent work has demonstrated deviations from the standard tensor model using this approach (Alexander et al, 2002; Frank 2002). Further work has used the algorithm developed by Alexander et al to identify voxels in which the single tensor model is poor. BiGaussian models were then fitted to these voxels to model assumed crossing fibres (figure 6.3). PDFs were subsequently estimated and streamline propagation, based on the PICo algorithm, could then generate maps of voxel level connectivity (from particular seed voxels) (Parker and Alexander 2003).

3) Compartmentalized water – A study with varying b-factors has reported fast and slow diffusion components (biexponential) (Clark and Le Bihan 2000). Attempts have been made to model the extra- and intra-cellular components of water molecule diffusion. Water transport across cell membranes is assumed to be negligible. Low b-factors would theoretically be dominated by fast diffusion (extracellular) and higher b-factors by slow diffusion (intracellular). However, the estimated extra- and intra-cellular volume fractions are not consistent with known values. This is an area of continuing research.

6.3.1.2.2 DTI tractography validation

As previously mentioned, a central assumption of DTI based tractography is that the measured diffusion characteristics of tissue water and how they are related across adjacent voxels are faithful representations of the underlying axonal microstructure. The extent of the validity of this assumption is unknown because there is no gold standard to authenticate the anatomical inferences of DTI tractography. Indirect comparisons with post-mortem studies may provide some partial validation. Qualitative validation was reported in the macaque monkey when DTI tractography-derived fibre projections were found to be consistent with known monkey connectional pathways (Parker et al, 2002). An alternative technique would compare DTI and histological findings on the same post-mortem brain tissue. This has been performed for myocardium (Holmes et al, 2000) but inferences are limited by the fact that histological preparation may alter tissue microstructure and water diffusion properties. A further technique has been developed by directly comparing manganese-based

with DTI-derived tractography (Lin et al, 2001; Pautler et al, 1998; Saleem et al, 2002). It has also been performed for diffusion spectrum imaging (Lin et al, 2003). This is a promising strategy although it is really restricted to animal models, relies upon assumptions of the characteristics of manganese tracing, and is suitable only for certain types of white matter fascicles.

6.3.2 Dynamic (functional and effective) connectivity

Aspects of dynamic interactions between neural units are described in terms of functional or effective connectivity.

6.3.2.1 Functional connectivity

Functional connectivity refers to temporal correlations (or deviations from statistical independence) between spatially remote neurophysiological events (Friston et al, 1993). Such correlations often arise from neuronal interactions along structural connections, but may sometimes be caused by a common input from an external neuronal or stimulus source (Sporns 2002). Deviations from statistical independence are commonly captured in a covariance (or correlation) matrix, representing the systems functional connectivity (under certain statistical assumptions). Functional connectivity is time-dependent and model-free, measuring statistical interdependence (mutual information) without explicit reference to causal effects (Sporns et al, 2004).

Studies of functional connectivity apply statistical techniques such as principal or independent component analysis (PCA/ICA). These data-driven methods make no assumptions about the underlying biology and are therefore best applied when the structural connections within networks associated with certain tasks are unknown. Clustering methods have also been implemented on fMRI data to produce temporal correlation matrices whose elements signify how functionally connected voxels are to each other. These have discovered both scale-free and small-world attributes within functional architecture (Eguiluz et al, 2005; Sporns et al, 2004).

6.3.2.2 *Effective connectivity*

Effective connectivity is defined as the influence that one neural system exerts over another (Friston 2004). It describes the set of causal effects between neural systems within a network (Sporns et al, 2004). It is time-dependent, as is functional connectivity, but unlike the latter requires the specification of a causal model founded on anatomically based assumptions i.e. it is hypothesis rather than data driven. Inferences are restricted to networks of these preselected regions.

Causal inference can be achieved by the principle of "temporal precedence" whereby regions activating later in a model have been driven by earlier activating regions that are connected to them. In fMRI, however, this principle may be masked by the temporal smoothing inherent in the coupling between neuronal and haemodynamic changes. Another way to determine causality is perturbation via experimental manipulation. This is the conventional approach in fMRI which tends to use stimulus driven protocols. Evolving techniques, such as transcranial magnetic stimulation (TMS), can selectively alter neural activity independently of behavioural confounds, an important advantage when assessing the interactions between perturbed and non-perturbed regions.

Several modelling techniques have been used to investigate effective connectivity with fMRI data.

1) Structural equation models (SEM) – These describe sets of regions with directed connections, which are causally defined *a priori*. Particular connection strengths indicate particular inter-regional correlations, presumed to be instantaneous. The modelled connection strengths can be statistically fitted to the observed data by minimizing the differences. Disadvantages include the limited number of specified connections for the networks, which might result in inaccurate models. Also, structural equation modelling does not make use of temporal information e.g. randomly permuting the data points in time would give the same results (Ramnani et al, 2004).

2) Multivariate autoregressive (MAR) modelling – This overcomes the limitation in SEM of the inability to model temporal information. Autoregressive modelling is able to characterize structure within a time series. Time values are modelled as weighted sums of previous values. Multivariate autoregressive modelling extends this to multiple time series from different regions such that the vector of current values of all regions is modelled as a linear sum of previous vector values (Harrison et al, 2003).

3) Dynamic causal modelling (DCM) – This attempts to construct a realistic neuronal model of interacting cortical regions. A supplemental forward model then transforms the neuronal activity into the haemodynamic response by using the Balloon model (Friston et al, 2003). Parameters of the neuronal model (i.e. effective connectivity) can then be estimated from observed data. Mathematically, bilinear differential equations model the neuronal activity whereby external inputs initiate transient responses within the network. This approach intuitively regards an experiment as a designed perturbation of neuronal dynamics that are propagated within a network to change region-specific neuronal activity. Changes in connectivity can be attributed to experimental manipulation. The model fitting algorithm is computationally demanding, which restricts the number of specifiable regions for the causal model. A further limitation is that only single state variables can be used to characterize region-specific neurodynamics. This prevents the modelling of excitatory and inhibitory subpopulations in each region which require multiple state variables (Ramnani et al, 2004). The main advantage of DCM over the previous two techniques is that it models neuronal connectivity whereas SEM and MAR model correlations at the level of the observed fMRI response.

6.3.3 Relationships between structural connectivity and functional dynamics

Anatomical, functional and effective connectivity are interrelated. Within the neuroanatomical substrate (anatomical connectivity), the non-linear dynamics of neuronal populations result in patterned statistical dependencies or correlations (functional connectivity) and causal interactions (effective connectivity). In particular, structural connections impose constraints on the types of

functional/effective connectivity patterns within a network. Structural afferents and efferents for a particular cortical region (or its connectional fingerprint (Passingham et al, 2002)) will strongly influence its functional properties. Conversely, functional interactions can help to mould the underlying anatomical architecture, either directly via synaptic plasticity or over longer time periods by affecting the brain's perceptual, cognitive or behavioural capabilities and consequently its survival (Sporns et al, 2004).

6.3.3.1 Computational modelling techniques

Certain insights into the inter-relationships between anatomical and dynamic connectivity have been gained from graph based computations using *motif analysis*. Motifs are small network building blocks that are repeated within larger networks. A particular motif consists of *M* nodes and a variable set of edges. For each M, there is a limited set of motif classes.

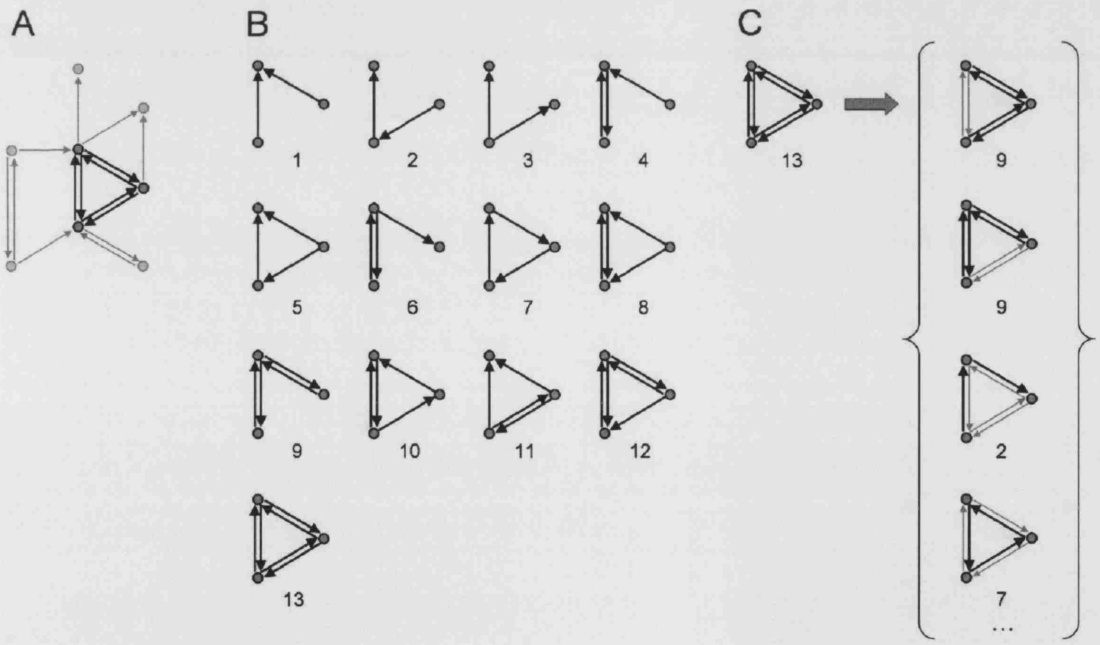

Figure 6.4. Structural and functional motifs. (A) Three nodes and their structural connections are selected as a candidate structural motif from a network (M = 3). (B) The thirteen motif classes are shown for the generic motif M=3. The candidate motif is detected as motif class = 13. In detecting structural motifs, only exact matches of candidate motif and motif class are counted. (C) A single instance of a structural motif contains many instances of functional motifs. Here, structural motif M = 3, class = 13 is shown to contain, for example, two distinct instances of the functional motif ID = 9, one motif ID = 2, and one motif ID = 7. Many other distinct instances of functional motifs are present that are not shown. Note that, in order to be counted as a functional motif of size M = 3, all three vertices of the original structural motif must participate. Adapted from Sporns and Kotter 2004.

Figure 6.4 portrays the set of 13 motif classes for M=3. These motifs are *structural motifs* because they provide the anatomical substrate for functional interactions between nodes. However, not all structural connections will always participate in functional interactions. The recruitment of different combinations of nodes and edges during dynamic neural processing results in different *functional motifs* emerging from the same structural motif at different times. Computational motif analyses have compared large-scale connectional data from animals (macaque monkey, cat, worm) with random and lattice networks. The results have shown high functional motif numbers in animals compared with control networks whilst the corresponding structural motif numbers were low. The large variety of functional motifs in animals is thought to facilitate flexible and dynamic processing, while the small structural repertoire promotes efficient assembly with short wiring length requirements. Both of these have obvious evolutionary advantages. In addition, certain motifs were frequently observed (especially M=3 and M=4) with topology supporting the combination of functional segregation and integration. Finally, evolutionary algorithms optimizing functional (but not structural) motif number, when applied to random networks, led to the emergence of networks with small-world attributes (high clustering, short path lengths), which are frequently observed in real brain networks (Sporns and Kotter 2004). These networks invariably possessed low structural motif numbers, in concordance with the results mentioned above.

Small-world properties are also found when simulation algorithms are optimized to select for complexity (Sporns et al, 2000a; Sporns et al, 2000b), which can be regarded as the amount of "interesting" (non-repeating) structure present within a system's dynamics. Complexity is low for systems whose elements are completely independent and random and for systems that are completely ordered. In such systems, there is little "interesting" information necessary to describe their dynamics. Neuronal dynamics of high complexity however, have mixtures of locally dense (highly clustered) connections with some long range connections (i.e. they possess high cluster indices with relatively short characteristic path lengths). These properties also combine segregated

information processing (specialization) with global integration to generate high integration of specialized information (Tononi et al, 1998) whereby different parts of the system engage in different activity patterns whilst remaining highly interdependent. The co-expression of functional segregation and integration is also associated with *metastability*, providing the ability to switch between different dynamic regimes (or attractor subregions). This flexibility allows the transient coupling between distributed cortical regions in response to changing sensorimotor and cognitive demands. Cognitive architecture is consequently adaptive and responsive to change, whilst maintaining some inertia to external perturbation.

6.3.3.2 MR imaging techniques

As previously, mentioned there is a dearth of knowledge about human brain connectivity (Crick and Jones 1993). As a consequence, whole brain connectivity computational analyses are not yet possible in humans. It is hoped that future MR research will help to overcome this by exploring the relationships between anatomical and functional connectivity.

From the 1990s neuroimaging studies have combined functional with structural MR and DTI measures. Several have made qualitative inferences on single subjects (Kim et al, 2003; Walters et al, 2003; Werring et al, 1998; Werring et al, 1999) or have been primarily methodological (Nakada 1997; Teo et al, 1997; Viergever et al, 1997). Werring et al (Werring et al, 1999) for example, overlaid fMRI visual activation maps onto the corresponding DTI derived FA maps in single subjects and raised the possibility of performing future group studies. Walters et al (Walters et al, 2003) specifically confined their investigation to intracortical function-structure relationships for human V5/MT using high resolution structural MRI with fMRI. Kim et al presented *in vivo* fMRI and DTI tractography mapping in cats at high field MRI (9.4T) with the potential of future post-mortem validation (Kim et al, 2003).

Another potential method of combining functional with structural MR data is to use fMRI activation foci to drive DTI tractography analyses and generate probabilistic connectivity maps related to particular functional systems. This was adopted in a study of the structural connections to the human primary motor cortex in 8 subjects (Guye et al, 2003) in which more extensive structural connections were inferred for the dominant, compared with non-dominant, hemisphere. Methods have also been developed to co-localize structural and functional profiles within certain cortical and subcortical regions using fMRI and DTI tractography. These have applied to the medial frontal cortex (Johansen-Berg et al, 2004) and thalamus with its projections (Johansen-Berg et al, 2005).

Finally, quantitative methods have estimated the probability of two functionally correlated voxels being anatomically connected between adjacent gyri within the human cortex using fMRI and DTI tractography. The findings support the notion that regions with direct white matter links should show high functional connectivity, but the converse need not be true, in that high functional connectivity may be mediated via distant grey matter regions, displaying low anatomical connectivity (Koch et al, 2002).

6.4 Conclusions

This thesis has used MRI to investigate disease models of the motor and visual system. Its main themes were (i) The use of multi-modal MRI techniques with the development of specific statistical analysis to integrate structural and functional information in optic neuritis. (ii) The initial application of DTI in MND. (iii) The development of DTI tractography to provide a framework for multi-subject group mapping. (iv) The integration of DTI tractography with fMRI data to explore function-structure relationships in normal controls. (v) The preliminary application of this technique to investigate function-structure gradients in pathology (optic neuritis).

In the immediate future the themes introduced by the work in this thesis will be expanded. For example, multi-modal MRI techniques will be able to structurally investigate both anterior and posterior visual pathways in optic neuritis and the information correlated with fMRI and clinical data using appropriate statistical modelling (see earlier section on future work). Over the next few years, as fMRI and DTI based techniques increase in sophistication, quantitative relationships between anatomical connectivity and functional dynamics will be characterized in greater detail. This knowledge may help to model large scale connectional networks of the human brain and provide us with a greater understanding of how it works in health and disease.

6.5 References

Alexander, DC, Barker, GJ, and Arridge, SR. Detection and modeling of non-Gaussian apparent diffusion coefficient profiles in human brain data. *Magn Reson.Med.* 2002. **48**(2), 331-40.

Assaf, Y and Cohen, Y. Structural information in neuronal tissue as revealed by q-space diffusion NMR spectroscopy of metabolites in bovine optic nerve. *NMR Biomed.* 1999. **12**(6), 335-44.

Assaf, Y, Mayk, A, and Cohen, Y. Displacement imaging of spinal cord using q-space diffusion-weighted MRI. *Magn Reson.Med.* 2000. **44**(5), 713-22.

Barabasi, AL and Albert, R. Emergence of scaling in random networks. *Science.* 1999. **286**(5439), 509-12.

Behrens, TE, Johansen-Berg, H, Woolrich, MW, Smith, SM, Wheeler-Kingshott, CA, Boulby, PA, Barker, GJ, Sillery, EL, Sheehan, K, Ciccarelli, O, Thompson, AJ, Brady, JM, and Matthews, PM. Non-invasive mapping of connections between human thalamus and cortex using diffusion imaging. *Nat.Neurosci.* 2003a. **6**(7), 750-7.

Behrens, TE, Woolrich, MW, Jenkinson, M, Johansen-Berg, H, Nunes, RG, Clare, S, Matthews, PM, Brady, JM, and Smith, SM. Characterization and propagation of uncertainty in diffusion-weighted MR imaging. *Magn Reson.Med.* 2003b. **50**(5), 1077-88.

Bullmore, E, Harrison, L, Lee, L, Mechelli, A, and Friston, K. Brain Connectivity Workshop, Cambridge UK, May 2003. *Neuroinformatics.* 2004. **2**(2), 123-5.

Burns, GA and Young, MP. Analysis of the connectional organization of neural systems associated with the hippocampus in rats. *Philos.Trans.R.Soc.Lond B Biol.Sci.* 2000. **355**(1393), 55-70.

Clark, CA and Le Bihan, D. Water diffusion compartmentation and anisotropy at high b values in the human brain. *Magn Reson.Med.* 2000. **44**(6), 852-9.

Crick, F and Jones, E. Backwardness of human neuroanatomy. *Nature.* 1993. **361**(6408), 109-10.

Eguiluz, VM, Chialvo, DR, Cecchi, GA, Baliki, M, and Apkarian, AV. Scale-free brain functional networks. *Phys Rev.Lett.* 2005. **94**(1), 018102.

Felleman, DJ and Van Essen, DC. Distributed hierarchical processing in the primate cerebral cortex. *Cereb.Cortex.* 1991. **1**(1), 1-47.

Frank, LR. Characterization of anisotropy in high angular resolution diffusion-weighted MRI. *Magn Reson.Med.* 2002. **47**(6), 1083-99.

Friston, KJ. Functional Integration in the Brain. In: Frackowiak, RSJ, Friston, KJ, Frith, CD, Dolan, RJ, Price, CJ, Zeki, S, Ashburner, J, and Penny, W. Human Brain Function. London; Elsevier Science, 2004: 971-97.

Friston, KJ, Frith, CD, Liddle, PF, and Frackowiak, RS. Functional connectivity: the principal-component analysis of large (PET) data sets. *J.Cereb.Blood Flow Metab.* 1993. **13**(1), 5-14.

Friston, KJ, Harrison, L, and Penny, W. Dynamic causal modelling. *Neuroimage.* 2003. **19**(4), 1273-302.

Guye, M, Parker, GJ, Symms, M, Boulby, P, Wheeler-Kingshott, CA, Salek-Haddadi, A, Barker, GJ, and Duncan, JS. Combined functional MRI and tractography to demonstrate the connectivity of the human primary motor cortex in vivo. *Neuroimage.* 2003. **19**(4), 1349-60.

Harrison, L, Penny, WD, and Friston, K. Multivariate autoregressive modeling of fMRI time series. *Neuroimage.* 2003. **19**(4), 1477-91.

Hickman, SJ, Toosy, AT, Jones, SJ, Altmann, DR, Miszkiel, KA, MacManus, DG, Barker, GJ, Plant, GT, Thompson, AJ, and Miller, DH. A serial MRI study following optic nerve mean area in acute optic neuritis. *Brain.* 2004a. **127**(Pt 11), 2498-505.

Hickman, SJ, Toosy, AT, Jones, SJ, Altmann, DR, Miszkiel, KA, MacManus, DG, Barker, GJ, Plant, GT, Thompson, AJ, and Miller, DH. Serial magnetization transfer imaging in acute optic neuritis. *Brain.* 2004b. **127**(Pt 3), 692-700.

Hickman, SJ, Toosy, AT, Miszkiel, KA, Jones, SJ, Altmann, DR, MacManus, DG, Plant, GT, Thompson, AJ, and Miller, DH. Visual recovery following acute optic neuritis: A clinical, electrophysiological and magnetic resonance imaging study. *J Neurol.* 2004c. **251**(8), 996-1005.

Hilgetag, CC, Burns, GA, O'Neill, MA, Scannell, JW, and Young, MP. Anatomical connectivity defines the organization of clusters of cortical areas in the macaque monkey and the cat. *Philos.Trans.R.Soc.Lond B Biol.Sci.* 2000. **355**(1393), 91-110.

Holmes, AA, Scollan, DF, and Winslow, RL. Direct histological validation of diffusion tensor MRI in formaldehyde- fixed myocardium. *Magn Reson.Med.* 2000. **44**(1), 157-61.

Johansen-Berg, H, Behrens, TE, Robson, MD, Drobnjak, I, Rushworth, MF, Brady, JM, Smith, SM, Higham, DJ, and Matthews, PM. Changes in connectivity profiles define functionally distinct regions in human medial frontal cortex. *Proc.Natl.Acad.Sci.U.S.A.* 2004. **101**(36), 13335-40.

Johansen-Berg, H, Behrens, TE, Sillery, E, Ciccarelli, O, Thompson, AJ, Smith, SM, and Matthews, PM. Functional-anatomical validation and individual variation of diffusion tractography-based segmentation of the human thalamus. *Cereb.Cortex.* 2005. **15**(1), 31-9.

Jones, DK. Determining and visualizing uncertainty in estimates of fiber orientation from diffusion tensor MRI. *Magn Reson.Med.* 2003. **49**(1), 7-12.

Kim, DS, Kim, M, Ronen, I, Formisano, E, Kim, KH, Ugurbil, K, Mori, S, and Goebel, R. In vivo mapping of functional domains and axonal connectivity in cat visual cortex using magnetic resonance imaging. *Magn Reson.Imaging.* 2003. **21**(10), 1131-40.

King, MD, Houseman, J, Gadian, DG, and Connelly, A. Localized q-space imaging of the mouse brain. *Magn Reson.Med.* 1997. **38**(6), 930-7.

King, MD, Houseman, J, Roussel, SA, van Bruggen, N, Williams, SR, and Gadian, DG. q-Space imaging of the brain. *Magn Reson.Med.* 1994. **32**(6), 707-13.

Koch, MA, Norris, DG, and Hund-Georgiadis, M. An investigation of functional and anatomical connectivity using magnetic resonance imaging. *Neuroimage.* 2002. **16**(1), 241-50.

Lee, L, Harrison, LM, and Mechelli, A. A report of the functional connectivity workshop, Dusseldorf 2002. *Neuroimage.* 2003. **19**(2 Pt 1), 457-65.

Lin, CP, Tseng, WY, Cheng, HC, and Chen, JH. Validation of diffusion tensor magnetic resonance axonal fiber imaging with registered manganese-enhanced optic tracts. *Neuroimage.* 2001. **14**(5), 1035-47.

Lin, CP, Wedeen, VJ, Chen, JH, Yao, C, and Tseng, WY. Validation of diffusion spectrum magnetic resonance imaging with manganese-enhanced rat optic tracts and ex vivo phantoms. *Neuroimage.* 2003. **19**(3), 482-95.

Martin, R, Kaiser, M, Andras, P, and Young, MP. Is the brain a scale-free network? *Soc.Neurosci.Abstracts.* 2001. **27**, 814-6.

Nakada, T. [Functionality and connectivity analysis by magnetic resonance imaging]. *Rinsho Shinkeigaku.* 1997. **37**(12), 1155-7.

Parker, GJ and Alexander, DC. Probabilistic Monte Carlo based mapping of cerebral connections utilising whole-brain crossing fibre information. *Inf.Process Med.Imaging.* 2003. **18**, 684-95.

Parker, GJ, Haroon, HA, and Wheeler-Kingshott, CA. A framework for a streamline-based probabilistic index of connectivity (PICo) using a structural interpretation of MRI diffusion measurements. *J Magn Reson Imaging.* 2003. **18**(2), 242-54.

Parker, GJ, Stephan, KE, Barker, GJ, Rowe, JB, MacManus, DG, Wheeler-Kingshott, CA, Ciccarelli, O, Passingham, RE, Spinks, RL, Lemon, RN, and Turner, R. Initial demonstration of in vivo tracing of axonal projections in the macaque brain and comparison with the human brain using diffusion tensor imaging and fast marching tractography. *Neuroimage.* 2002. **15**(4), 797-809.

Passingham, RE, Stephan, KE, and Kotter, R. The anatomical basis of functional localization in the cortex. *Nat.Rev.Neurosci.* 2002. **3**(8), 606-16.

Pautler, RG, Silva, AC, and Koretsky, AP. In vivo neuronal tract tracing using manganese-enhanced magnetic resonance imaging. *Magn Reson.Med.* 1998. **40**(5), 740-8.

Ramnani, N, Behrens, TE, Penny, W, and Matthews, PM. New approaches for exploring anatomical and functional connectivity in the human brain. *Biol.Psychiatry*. 2004. **56**(9), 613-9.

Saleem, KS, Pauls, JM, Augath, M, Trinath, T, Prause, BA, Hashikawa, T, and Logothetis, NK. Magnetic resonance imaging of neuronal connections in the macaque monkey. *Neuron*. 2002. **34**(5), 685-700.

Salin, PA and Bullier, J. Corticocortical connections in the visual system: structure and function. *Physiol Rev*. 1995. **75**(1), 107-54.

Scannell, JW, Blakemore, C, and Young, MP. Analysis of connectivity in the cat cerebral cortex. *J.Neurosci*. 1995. **15**(2), 1463-83.

Scannell, JW, Burns, GA, Hilgetag, CC, O'Neil, MA, and Young, MP. The connectional organization of the cortico-thalamic system of the cat. *Cereb.Cortex*. 1999. **9**(3), 277-99.

Sporns, O. Network analysis, complexity and brain function. *Complexity*. 2002. **8**(1), 56-60.

Sporns, O, Chialvo, DR, Kaiser, M, and Hilgetag, CC. Organization, development and function of complex brain networks. *Trends Cogn Sci*. 2004. **8**(9), 418-25.

Sporns, O and Kotter, R. Motifs in brain networks. *PLoS.Biol*. 2004. **2**(11), e369.

Sporns, O, Tononi, G, and Edelman, GM. Connectivity and complexity: the relationship between neuroanatomy and brain dynamics. *Neural Netw*. 2000a. **13**(8-9), 909-22.

Sporns, O, Tononi, G, and Edelman, GM. Theoretical neuroanatomy: relating anatomical and functional connectivity in graphs and cortical connection matrices. *Cereb.Cortex*. 2000b. **10**(2), 127-41.

Sporns, O and Zwi, JD. The small world of the cerebral cortex. *Neuroinformatics*. 2004. **2**(2), 145-62.

Teo, PC, Sapiro, G, and Wandell, BA. Creating connected representations of cortical gray matter for functional MRI visualization. *IEEE Trans.Med.Imaging*. 1997. **16**(6), 852-63.

Tononi, G, McIntosh, AR, Russell, DP, and Edelman, GM. Functional clustering: identifying strongly interactive brain regions in neuroimaging data. *Neuroimage*. 1998. **7**(2), 133-49.

Tuch, DS. Q-ball imaging. *Magn Reson.Med.* 2004. **52**(6), 1358-72.

Tuch, DS, Reese, TG, Wiegell, MR, and Wedeen, VJ. Diffusion MRI of complex neural architecture. *Neuron*. 2003. **40**(5), 885-95.

Viergever, MA, Maintz, JB, and Stokking, R. Integration of functional and anatomical brain images. *Biophys.Chem.* 1997. **68**(1-3), 207-19.

Walters, NB, Egan, GF, Kril, JJ, Kean, M, Waley, P, Jenkinson, M, and Watson, JD. In vivo identification of human cortical areas using high-resolution MRI: an approach to cerebral structure-function correlation. *Proc Natl.Acad.Sci.U.S.A.* 2003. **100**(5), 2981-6.

Watts, DJ and Strogatz, SH. Collective dynamics of 'small-world' networks. *Nature*. 1998. **393**(6684), 440-2.

Werring, DJ, Clark, CA, Barker, GJ, Miller, DH, Parker, GJ, Brammer, MJ, Bullmore, ET, Giampietro, VP, and Thompson, AJ. The structural and functional mechanisms of motor recovery: complementary use of diffusion tensor and functional magnetic resonance imaging in a traumatic injury of the internal capsule. *J.Neurol.Neurosurg.Psychiatry*. 1998. **65**(6), 863-9.

Werring, DJ, Clark, CA, Parker, GJ, Miller, DH, Thompson, AJ, and Barker, GJ. A direct demonstration of both structure and function in the visual system: combining diffusion tensor imaging with functional magnetic resonance imaging. *Neuroimage.* 1999. **9**(3), 352-61.

Wiegell, MR, Reese, T, Tuch, DS, Sorensen, AG, and Wedeen, VJ. Diffusion Spectrum Imaging of Fiber White Matter Degeneration. *Proceedings of the 9th International Society of Magnetic Resonance in Medicine.* 2001. **1**, 504.

APPENDIX A

Investigations into control deactivation

Several possible causes were postulated and then tested to explain why controls deactivated as they did in chapter 3:

1) Periodic signal drift during fMRI acquisition.

2) Spatial registration issues.

3) Saccadic eye movements during baseline.

The investigations effectively excluded these three possibilities to leave physiological mechanisms as most likely to explain the control related deactivation behaviour. The investigations will be summarized in turn.

A.1 Periodic signal drift

Hypothesis - A periodic drift in signal intensity (related to hardware issues) at the frequency of the experimental paradigm could account for deactivations.

Test - Subject data was acquired for one fMRI session in the scanner with no photic stimulation. The subject asked to lie still and relaxed with the eyes closed. The data were examined as if a normal fMRI experiment was conducted.

Results – No BOLD intensity correlations were seen (either negative or positive) at the experimental paradigm frequency after statistical analysis, implying that periodic signal variations were unlikely to account for deactivations.

A.2 Spatial registration issues

Hypothesis – Some systematic normalization error may misregister brains to the EPI template and induce false deactivations.

Test – Visual fMRI data from two normal subjects were analysed. For each subject two analyses were conducted - one with and the other without normalization to the EPI template. Realignment and smoothing performed for each analysis as usual. Fixed effects analyses were performed to qualitatively compare the activations and deactivations between normalized and un-normalized data.

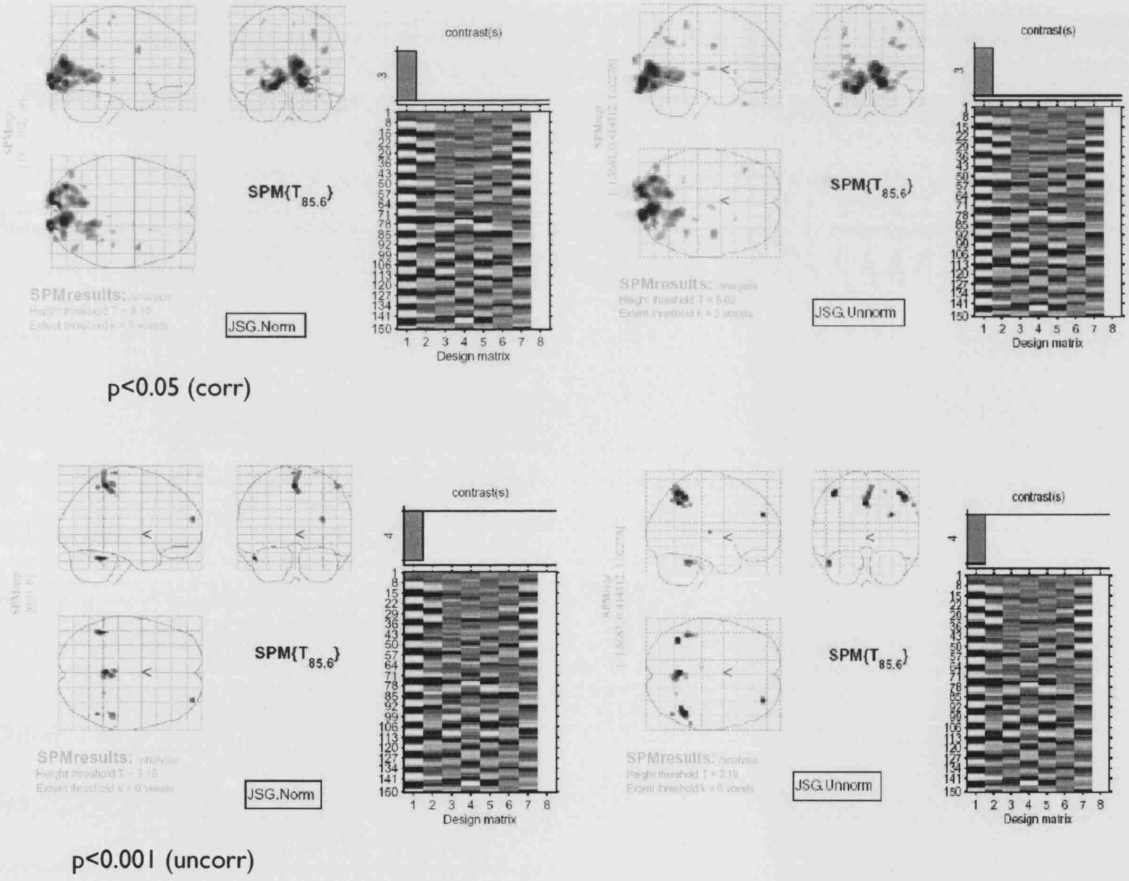

Figure A.1. Activations (top figure) and deactivations (bottom figure) are shown for one subject after normalization (left side) and in native space (right side). The effect of normalization does not qualitatively alter the activation or deactivation pattern.

Results – Normalized and un-normalized analyses gave qualitatively very similar results. There was no evidence therefore, for a mis-registration effect in contributing to deactivations. Some of the results are shown below for one of the subjects (figure A.1).

A.3 The effects of saccadic eye movements

Hypothesis – Eye movements occur during darkness (baseline) and result in deactivations in the brain regions of interest (especially those defined by the *a priori* hypothesis). A corollary is that these putative eye movements need to be more systematically more pronounced in the control group than in the patient group for differences to be observed.

Tests – Several approaches were taken.

A.3.1 Literature review

Several regions are involved in saccades (voluntary and involuntary) – Frontal eye fields (FEFs), Supplementary eye fields (SEFs), Intraparietal sulcus (IPS) and also lateral occipital cortex (LO) (Anderson et al, 1994; Mort et al, 2003; Pierrot-Deseilligny et al, 1995; Tehovnik et al, 2000). In addition the precuneus, cerebellum and superior colliculi have been described. None of these regions form part of our *a priori* hypothesis.

Other regions, which do sometimes overlap with the areas used in the *a priori* hypothesis, have been described less consistently but have resulted from contrasts of complex saccadic paradigms. For instance the superior temporal gyrus has been reported when remembered saccades were compared with reflexive saccades (Anderson et al, 1994) and also when eye movements were compared with fixation in attentional related tasks (Corbetta et al, 1998). Areas within the basal ganglia areas have also been noted with comparisons between predictable and unpredictable saccades (in the globus pallidus and caudate) (Gagnon et al, 2002) and also when comparing new versus familiar saccade

sequences (in the left caudate) (Grosbras et al, 2001). Anderson et al (Anderson et al, 1994) additionally described changes in the insula, cingulated cortex, thalamus, midbrain, cerebellum as well as right superior temporal gyrus (see above) when remembered saccades were compared with reflexive saccades.

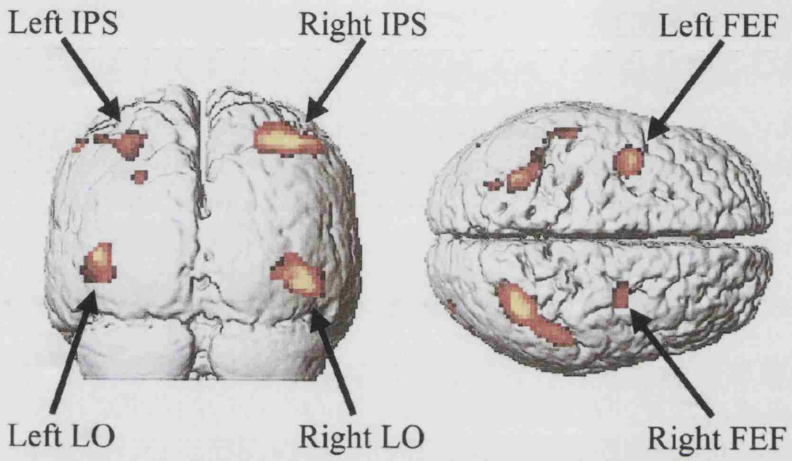

Figure A.2. Surface rendered activations are shown for illustrative purposes for the locations of the IPS, FEF and LO cortex. Adapted from Mort et al, 2003.

In conclusion, it appears that most literature commonly describes saccadic movements associated with brain regions unrelated to the regions of our study.

A.3.2 FMRI single subject experiments

Three classes of experiments were performed on a single control subject (AT) to investigate whether eye movements activated the extra-occipital regions that differed between patients and controls.

A.3.2.1 Eye movement effects (interesessional)

Four visual fMRI sessions were conducted for the left eye. Wholebrain fMRI images were acquired. Two fMRI sessions (10 minutes) comprised a paradigm of 20 second photic stimulation epochs that

alternated with 20 second epochs of preplanned self paced (approximately 1-2 Hz) saccadic eye movement cycles (during darkness). The eye movement cycle was upgaze, right lateral gaze, left lateral gaze, downgaze followed by upgaze again etc. For the other two fMRI sessions the 20 second photic stimulation epochs were alternated with darkness only, during which the subject looked straight ahead. An additional factor of fixation was also investigated whereby a silver marker was stuck to the inside of the centre of the goggles. Although the subject could not accommodate to focus the marker, visualization was still possible, allowing crude fixation to help keep the eye still. Fixation was applied during two of the four fMRI sessions to maximize the ability to detect eye movement related BOLD changes:

		Eye movements	
		YES	NO
Crude Fixation	YES	1	2
	NO	3	4

Where the numbers represent the fMRI sessions entered (in order) into the design matrix. Thus a fixed effects analysis was performed by entering all four sessions for a 2x2 factorial design using SPM99.

(i) Overall effect – the SPM below (figure A.3) shows the overall effect of eye movement when contrasted with the paradigms without eye movement.

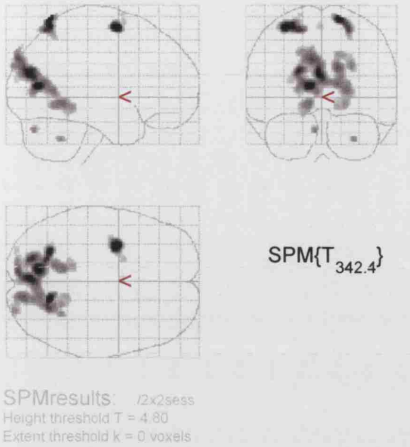

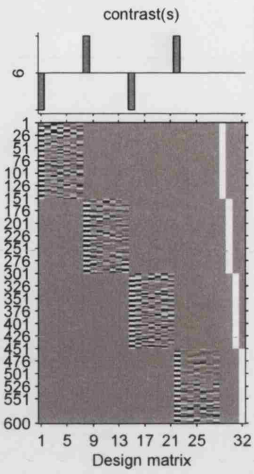

x,y,z mm	label	%
-32 -2 62	Precentral_L	51.11
	Frontal_Sup_L	33.33
	Frontal_Mid_L	12.78
	OUTSIDE	2.78
16 -62 70	Parietal_Sup_R	88.24
	Precuneus_R	8.50
	Postcentral_R	1.96
	Parietal_Inf_R	1.31
-12 -72 10	Calcarine_L	22.80
	Cuneus_L	19.53
	Calcarine_R	17.41
	Occipital_Sup_L	10.31
	Cuneus_R	9.43
	Lingual_R	7.20
	Occipital_Sup_R	5.91
	OUTSIDE	4.40
	Lingual_L	1.71
-26 -62 64	Parietal_Sup_L	88.89
	Precuneus_L	9.88
	OUTSIDE	1.23
-12 -50 -6	Lingual_L	70.32
	Cerebelum_4_5_L	23.74
	Fusiform_L	5.94
-6 -76 -30	Cerebelum_Crus1_L	52.63
	Cerebelum_Crus2_L	36.84
	Vermis_7	10.53
28 -52 -38	OUTSIDE	83.33
	Cerebelum_6_R	16.67
-2 4 62	Supp_Motor_Area_L	100.00
-28 -92 16	Occipital_Mid_L	100.00
-20 4 74	OUTSIDE	66.67
	Frontal_Sup_L	33.33

Figure A.3. Eye movements vs no eye movements. SPM(T) maps shown for corrected $p<0.05$. The SPM fixed effects design matrix is also shown. Note that realignment parameters were entered as covariates of no interest for each session.

The significant clusters were identified using "automatic anatomical labelling" software (Tzourio-Mazoyer et al, 2002) and pasted in table format on the right hand side. They include regions previously described and known to be associated with eye movements such as the FEFs and IPS. Some cerebellar activity is also seen. There is some asymmetrical activation present i.e. left FEF and right IPS were especially significant.

(ii) Fixation – The eye movement > no eye movement contrast was tested for the sessions where fixation was employed (1 and 2). Very similar regions as shown above were detected (figure A.4).

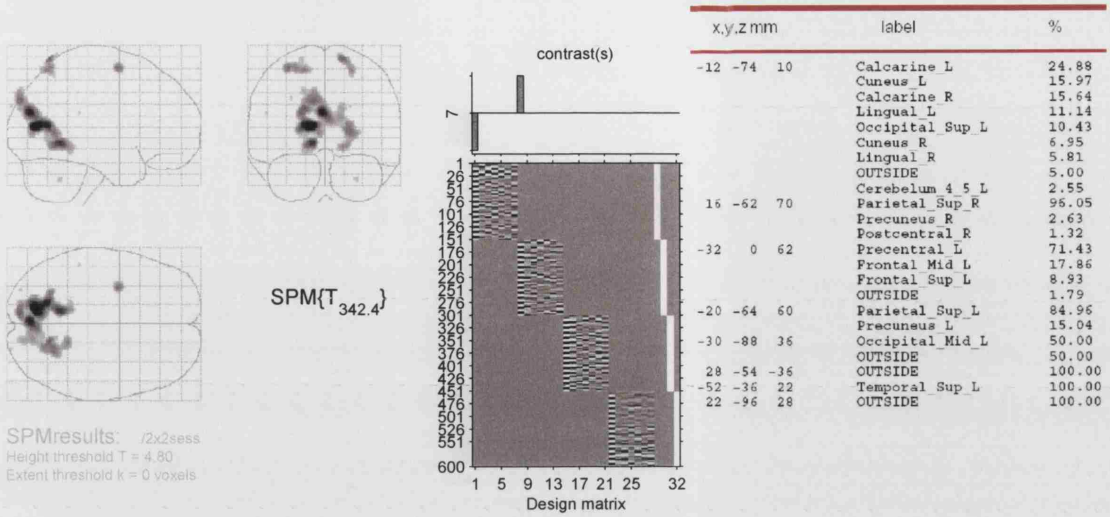

x,y,z mm	label	%
-12 -74 10	Calcarine_L	24.88
	Cuneus_L	15.97
	Calcarine_R	15.64
	Lingual_L	11.14
	Occipital_Sup_L	10.43
	Cuneus_R	6.95
	Lingual_R	5.81
	OUTSIDE	5.00
	Cerebelum_4_5_L	2.55
16 -62 70	Parietal_Sup_R	95.05
	Precuneus_R	2.63
	Postcentral_R	1.32
-32 0 62	Precentral_L	71.43
	Frontal_Mid_L	17.86
	Frontal_Sup_L	8.93
	OUTSIDE	1.79
-20 -64 60	Parietal_Sup_L	84.96
	Precuneus_L	15.04
-30 -88 36	Occipital_Mid_L	50.00
	OUTSIDE	50.00
28 -54 -36	OUTSIDE	100.00
-52 -36 22	Temporal_Sup_L	100.00
22 -96 28	OUTSIDE	100.00

Figure A.4. SPM(T) map (p<0.05 corrected) for eye movements > no eye movements in the presence of the visual fixation marker.

(iii) No fixation – The eye movement > no eye movement contrast demonstrated similar activation changes although to a lesser extent (figure A.5).

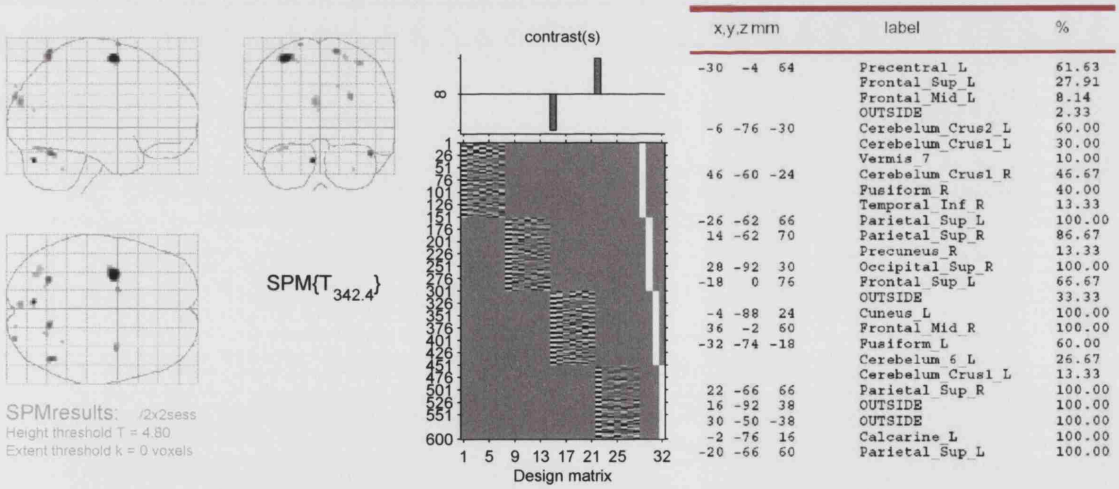

x,y,z mm	label	%
-30 -4 64	Precentral_L	61.63
	Frontal_Sup_L	27.91
	Frontal_Mid_L	8.14
	OUTSIDE	2.33
-6 -76 -30	Cerebelum_Crus2_L	60.00
	Cerebelum_Crus1_L	30.00
	Vermis_7	10.00
46 -60 -24	Cerebelum_Crus1_R	46.67
	Fusiform_R	40.00
	Temporal_Inf_R	13.33
-26 -62 66	Parietal_Sup_L	100.00
14 -62 70	Parietal_Sup_R	86.67
	Precuneus_R	13.33
28 -92 30	Occipital_Sup_R	100.00
-18 0 76	Frontal_Sup_L	66.67
	OUTSIDE	33.33
-4 -88 24	Cuneus_L	100.00
36 -2 60	Frontal_Mid_R	100.00
-32 -74 -18	Fusiform_L	60.00
	Cerebelum_6_L	26.67
	Cerebelum_Crus1_L	13.33
22 -66 66	Parietal_Sup_R	100.00
16 -92 38	OUTSIDE	100.00
30 -50 -38	OUTSIDE	100.00
-2 -76 16	Calcarine_L	100.00
-20 -66 60	Parietal_Sup_L	100.00

Figure A.5. SPM(T) map (p<0.05 corrected) for eye movements > no eye movements in the absence of visual fixation.

These experiments were chosen because they matched the original paradigm of the longitudinal study. The results suggest that eye movement induced BOLD activity should not be related to the deactivations observed in our study, because they occur in an unrelated network of regions. However, the ability to draw such conclusions is limited by the fact that the photic stimulus and eye

movement tasks served as baselines for each other. Also, eye movement comparisons were made between fMRI sessions making it difficult to account for intersessional effects. A further set of experiments was performed to address these issues as described below.

A.3.2.2 Eye movement effects (intrasessional)

Four visual fMRI experiments were performed with left sided photic stimulation. For each session there were three conditions divided into 20 second epochs: (A) Photic stimulation (used in two of the sessions), (B) Planned saccadic eye movements as described above, (C) A resting condition of darkness with no eye movements. The presentation order of the conditions was BACABACABACA etc. Hence the paradigm was similar to the photic stimulation paradigm used in the longitudinal study with the exception that the baseline (to photic stimulation) alternated between darkness (with no eye movements) and planned saccadic eye movements. This paradigm allowed us to make intrasessional comparisons between eye movements and a resting baseline. Crude fixation was used during two of the four fMRI sessions and as well as photic stimulation so that the four sessions could be analyzed as a 2x2 factorial fixed effects model (see table below).

		Photic stimulation	
		YES	NO
Crude Fixation	YES	1	2
	NO	3	4

(i) Any eye movement effects – eye movement effects across all four sessions were determined and found to activate very similar regions to the previous eye movement experiments (figure A.6).

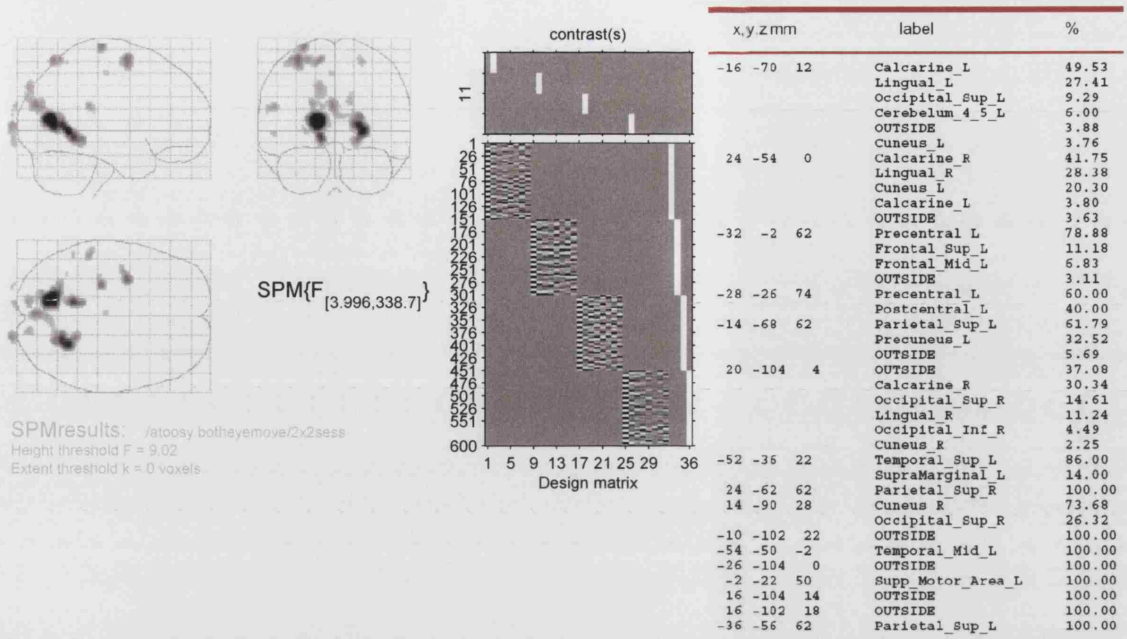

x,y,z mm	label	%
-16 -70 12	Calcarine_L	49.53
	Lingual_L	27.41
	Occipital_Sup_L	9.29
	Cerebelum_4_5_L	6.00
	OUTSIDE	3.88
	Cuneus_L	3.76
24 -54 0	Calcarine_R	41.75
	Lingual_R	28.38
	Cuneus_L	20.30
	Calcarine_L	3.80
	OUTSIDE	3.63
-32 -2 62	Precentral_L	78.88
	Frontal_Sup_L	11.18
	Frontal_Mid_L	6.83
	OUTSIDE	3.11
-28 -26 74	Precentral_L	60.00
	Postcentral_L	40.00
-14 -68 62	Parietal_Sup_L	61.79
	Precuneus_L	32.52
	OUTSIDE	5.69
20 -104 4	OUTSIDE	37.08
	Calcarine_R	30.34
	Occipital_Sup_R	14.61
	Lingual_R	11.24
	Occipital_Inf_R	4.49
	Cuneus_R	2.25
-52 -36 22	Temporal_Sup_L	86.00
	SupraMarginal_L	14.00
24 -62 62	Parietal_Sup_R	100.00
14 -90 28	Cuneus_R	73.68
	Occipital_Sup_R	26.32
-10 -102 22	OUTSIDE	100.00
-54 -50 -2	Temporal_Mid_L	100.00
-26 -104 0	OUTSIDE	100.00
-2 -22 50	Supp_Motor_Area_L	100.00
16 -104 14	OUTSIDE	100.00
16 -102 18	OUTSIDE	100.00
-36 -56 62	Parietal_Sup_L	100.00

Figure A.6. F contrast maps (p<0.05 corrected) denoting any effect of eye movement across all four sessions.

(ii) Any photic stimulation effects (figure A.7).

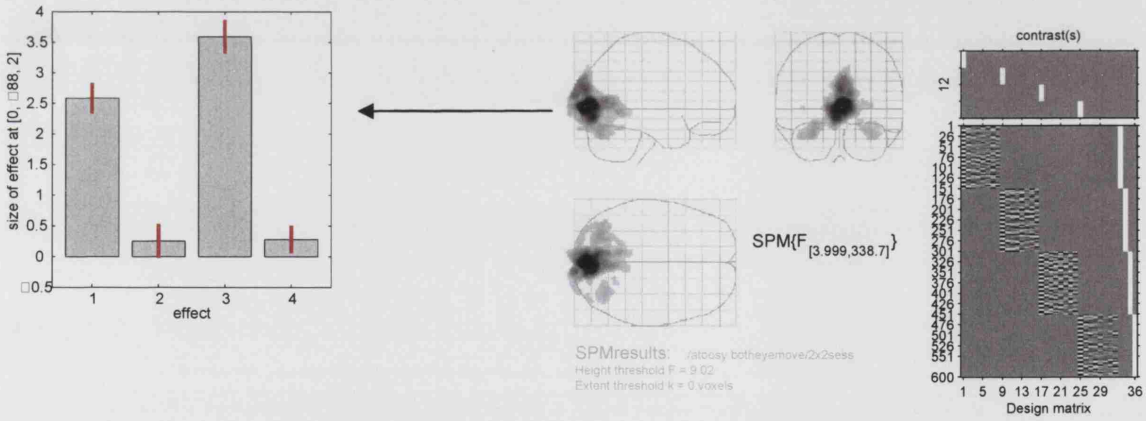

Figure A.7. SPM(F) map (p<0.05 corrected) for effect of photic stimulation. The PEs are shown for the global maximum (within the visual cortex). Sessions two and four had no photic stimulation and so had PEs close to zero as expected.

(iii) Effect of photic stimulation or fixation on eye movement (figure A.8).

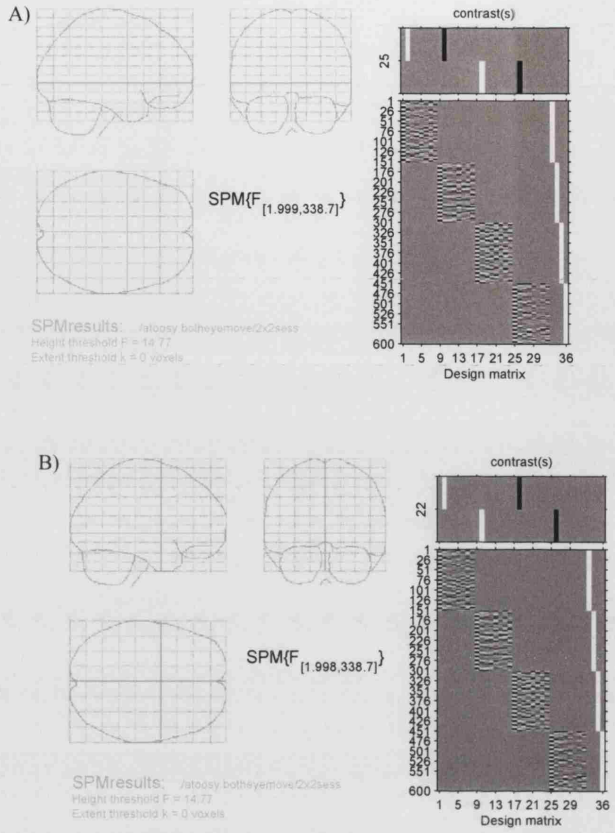

Figure A.8. A) shows the effect of photic stimulation on the activity associated with eye movements. B) shows the effects of the fixation marker on the fMRI response to eye movements.

These results demonstrate that the fMRI activity associated with eye movements were not affected by the presence of a fixation cross or photic stimulation.

A.3.3 FMRI group effect of eye movements (5 subjects)

Five subjects underwent the eye movement paradigm described in the previous section with photic stimulation but no fixation marker. A fixed effects conjuction analysis (Friston et al, 1999) was performed to show the common activations associated with eye movements (figure A.9).

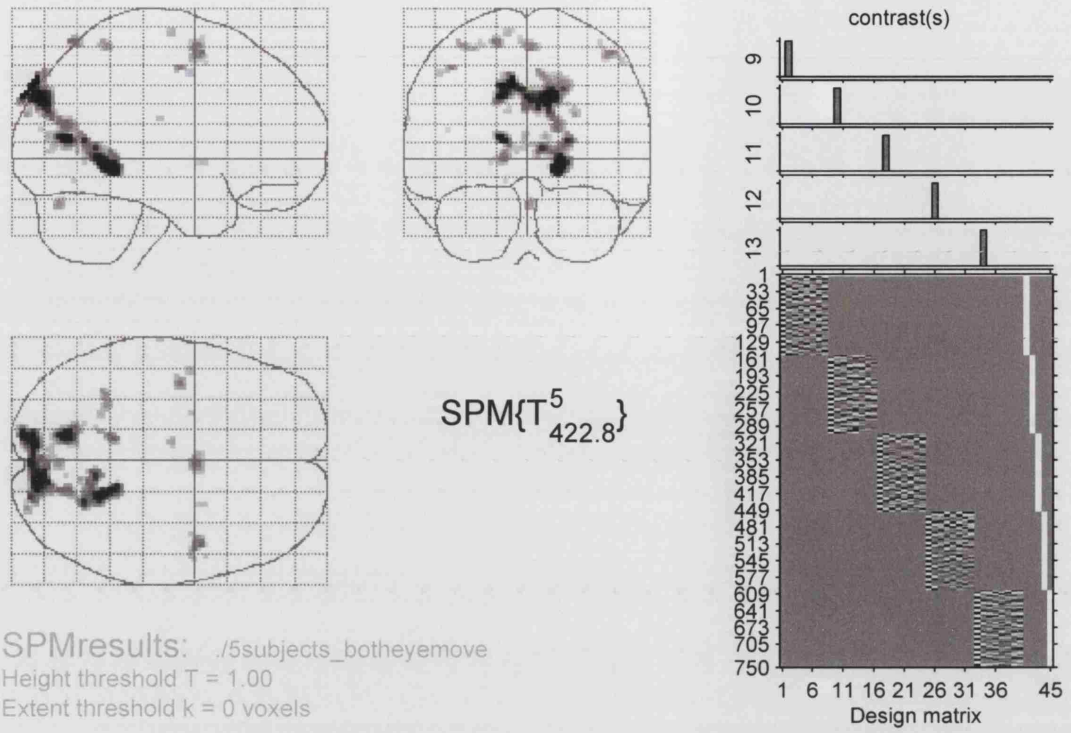

Figure A.9. Conjuction analysis across five subjects to show the 'typical' effects of eye movements. The significant areas (shown at p<0.0001 uncorrected) are very similar to the regions activated in the single subject experiments.

A.3.4 Control Baseline activity (Deactivation)

The group effect of 'deactivation' for the controls in the longitudinal study was examined in order to help make a qualitative comparison with the results from the eye movement experiments described above. The left sided visual fMRI experiments that had used the wholebrain protocol from 29 subjects were entered into a one sample t test in SPM99. Results are shown below.

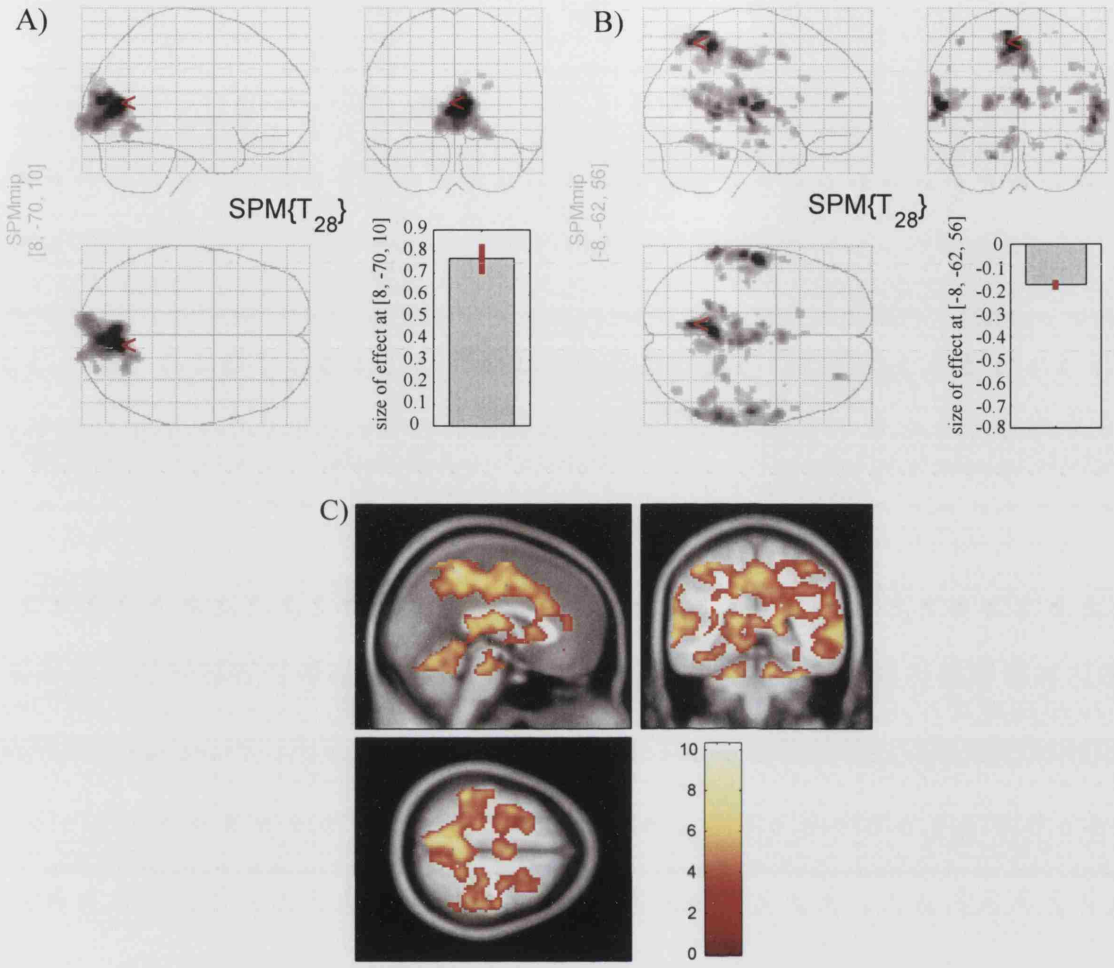

Figure A.10. SPM T contrast maps that show the activations and deactivations of the visual fMRI paradigm on 29 normal controls. A) Activations due to photic stimulation ($p<0.05$ corrected). The effect size is shown in the visual cortex. B) Deactivations from the photic stimulation paradigm ($p<0.05$ corrected). The effect size is shown for the precuneus. C) Section display (MNI [0,-38,57]) equivalent to B but at a lower threshold ($p<0.001$ uncorrected) for visual display purposes.

The deactivations seen in figure A.10B are mainly confined to the lateral temporal cortices and precuneus (interparietal sulcus) at $p<0.05$ corrected. Note that the intraparietal sulcus (IPS) is usually involved in eye movements and not the interparietal sulcus. The parameter estimate bar graphs show that the deactivation effect size is approximately four times lower than the activation effect size (shown in A). The regional pattern involved in the deactivation effects is also quite different to the eye movement related activation patterns observed in the previously described studies. At lower statistical thresholds (e.g. in C where $p<0.001$ uncorrected), more extensive brain regions emerge including cingulate regions, frontal and other parietal areas.

A.3.5 Conclusions

From the evidence provided above, it is most likely that eye movements do not contribute to the deactivation patterns seen in the control group especially in those areas which were focussed upon in the longitudinal study (as part of the *a priori* hypothesis). A particular limitation of the saccadic eye movement fMRI experiments relates to the self paced eye movements whereby the subjects were instructed to maintain a saccadic rate of 1-2 Hz. This was not formally monitored during the experiment because of practical limitations but the subjects were observed for eye movement compliance in pre-acquisition training sessions. For this reason, we do not consider this limitation to have significantly affected our conclusions.

A.4 References

Anderson, TJ, Jenkins, IH, Brooks, DJ, Hawken, MB, Frackowiak, RS, and Kennard, C. Cortical control of saccades and fixation in man. A PET study. *Brain.* 1994. **117 (Pt 5)**, 1073-84.

Corbetta, M, Akbudak, E, Conturo, TE, Snyder, AZ, Ollinger, JM, Drury, HA, Linenweber, MR, Petersen, SE, Raichle, ME, Van Essen, DC, and Shulman, GL. A common network of functional areas for attention and eye movements. *Neuron.* 1998. **21**(4), 761-73.

Friston, KJ, Holmes, AP, Price, CJ, Buchel, C, and Worsley, KJ. Multisubject fMRI studies and conjunction analyses. *Neuroimage.* 1999. **10**(4), 385-96.

Gagnon, D, O'Driscoll, GA, Petrides, M, and Pike, GB. The effect of spatial and temporal information on saccades and neural activity in oculomotor structures. *Brain.* 2002. **125**(Pt 1), 123-39.

Grosbras, MH, Leonards, U, Lobel, E, Poline, JB, LeBihan, D, and Berthoz, A. Human cortical networks for new and familiar sequences of saccades. *Cereb.Cortex.* 2001. **11**(10), 936-45.

Mort, DJ, Perry, RJ, Mannan, SK, Hodgson, TL, Anderson, E, Quest, R, McRobbie, D, McBride, A, Husain, M, and Kennard, C. Differential cortical activation during voluntary and reflexive saccades in man. *Neuroimage.* 2003. **18**(2), 231-46.

Pierrot-Deseilligny, C, Rivaud, S, Gaymard, B, Muri, R, and Vermersch, AI. Cortical control of saccades. *Ann.Neurol.* 1995. **37**(5), 557-67.

Tehovnik, EJ, Sommer, MA, Chou, IH, Slocum, WM, and Schiller, PH. Eye fields in the frontal lobes of primates. *Brain Res.Brain Res.Rev.* 2000. **32**(2-3), 413-48.

Tzourio-Mazoyer, N, Landeau, B, Papathanassiou, D, Crivello, F, Etard, O, Delcroix, N, Mazoyer, B, and Joliot, M. Automated anatomical labeling of activations in SPM using a macroscopic anatomical parcellation of the MNI MRI single-subject brain. *Neuroimage*. 2002. **15**(1), 273-89.